Thin Film Combinatorial Synthesis of Advanced Scintillation Materials

Jonathan Daniel Peak
University of Tennessee - Knoxville, jon.peak@gmail.com

Follow this and additional works at: https://trace.tennessee.edu/utk_graddiss

Part of the Other Materials Science and Engineering Commons, and the Semiconductor and Optical Materials Commons

Recommended Citation

To the Graduate Council:

I am submitting herewith a dissertation written by Jonathan Daniel Peak entitled "Thin Film Combinatorial Synthesis of Advanced Scintillation Materials." I have examined the final electronic copy of this dissertation for form and content and recommend that it be accepted in partial fulfillment of the requirements for the degree of Doctor of Philosophy, with a major in Materials Science and Engineering.

Philip D. Rack, Major Professor

We have read this dissertation and recommend its acceptance:

Charles L. Melcher, Claudia J. Rawn, Jason P. Hayward

Accepted for the Council:

Carolyn R. Hodges

Vice Provost and Dean of the Graduate School

(Original signatures are on file with official student records.)

To the Graduate Council:

I am submitting herewith a dissertation written by Jonathan Daniel Peak entitled "Thin Film Combinatorial Synthesis of Advanced Scintillation Materials." I have examined the final electronic copy of this thesis for form and content and recommend that it be accepted in partial fulfillment of the requirements for the degree of Doctor of Philosophy, with a major in Materials Science and Engineering.

Philip D. Rack , Major Professor

We have read this dissertation
and recommend its acceptance:

Charles L. Melcher

Claudia J. Rawn

Jason P. Hayward

Accepted for the Council:

Carolyn R. Hodges
Vice Provost and Dean of the Graduate School

(Original signatures are on file with official student records.)

THIN FILM
COMBINATORIAL SYNTHESIS OF
ADVANCED SCINTILLATION MATERIALS

A Dissertation Presented for the
Doctor of Philosophy
Degree
The University of Tennessee, Knoxville

Jonathan Daniel Peak
December 2010

to nadya

ACKNOWLEDGEMENTS

I would first like to thank my advisor Dr. Philip Rack for his guidance, mentoring and friendship, and also for the many priceless hours of discussion. During my graduate career I have admired the example he sets and have strived to meet it. Secondly, I would like to thank Dr. Charles Melcher. He has given me guidance and friendship along the way. He always treated me as one of his group members, for which I am thankful. I feel very fortunate to have had the opportunity to work with both of them. I would like to thank my additional committee members Dr. Claudia Rawn and Dr. Jason Hayward for their giving their time to read and advise on this dissertation. To Dr. Piotr Szupryczynski for lending his knowledge and giving helpful suggestions. To Merry Koschan for sharing her general crystal growth knowledge and making available her detailed laboratory notes that made the initial single crystal work possible. I would like to thank my past and present colleagues in both the Scintillation Materials Research Center and in Dr. Rack's research group, Ryan Rucker, Mathew Lassiter, Seyeoul Kwon, Yueying Wu, Jiyong Noh, Joo Hyon Noh, Siwie Tang, Paul Cutler, Kan Yang, Harold Rothfuss, Kurt Johanns and Yingfeng Guan. I have enjoyed working with them and have valued their feedback on my research. I would like to specifically mention Dr. Jung-Won Park for the time he spent introducing me to sputter deposition and thin film characterization during my first year at Tennessee and also Dr. Mariya Zhuravleva for giving her time to review sections of my research. Thank you to Dr. C.P. Wong for giving me my start in research as an undergraduate student.

I would like to thank Dr. Daryl Smith for his valued friendship and insight. He has been a mentor both in and out of the lab. I am also grateful to his wife Rachel for her friendship and the many home-cooked meals that always renewed my spirits during the writing process.

I would like to thank my lifelong friends Peg and Sam Feder as well as my Godparents Jan and Dan Davis. I consider them family. I will always cherish our many

discussions around the dinner table that lasted late into the night. I credit them with helping to develop my intellectual curiosity. I want to thank Samuel Vera, Anne Vera and also Andres Vera for accepting me into their family and treating me like a son and brother from the first time I met them. I want to express my gratitude to my grandparents, Bill and Anne Robinson. Their support made the start of my graduate career possible. To my darling sister Kristin, she brings joy to my life and those around her. I am proud to have her as a sister.

I would also like to thank my parents Ed and Joanne Peak for their love and support throughout my life. My parents ensured I had the help I needed during my early education. Without them I doubt I would have attended college, let alone completed the work presented here. Additionally, they instilled in me a value of education and the pursuit of knowledge. They made it possible for me to attend St. Xavier and the Georgia Institute of Technology, for which I will always be grateful. My father taught me the philosophical foundations of logical problem solving and my mother taught me to always look for the roundabout approach when the straight path will not work, both of which have been invaluable in my research.

Finally, I would like to thank Nadya Michelle Vera, the love of my life, for her support, trust and patience. She has believed in me and believed in us throughout my graduate career. I feel blessed to have her in my life and to be able to share *The Adventures of Muffin and Bubu* with her.

ad maiorem Dei gloriam

ABSTRACT

The development and application of a combinatorial sputtering thin film technique to screen potential scintillation material systems was investigated. The technique was first benchmarked by exploring the binary lutetium oxide-silicon oxide material system, which successfully identified the luminescence phases of the system, Lu2SiO5 (LSO) and Lu2Si2O7 (LPS). The second application was to optimize the activator concentration in cerium doped LSO. The successfully optimized cerium concentration in the thin film LSO of 0.34 atomic percent was much greater than the standard cerium concentration in single crystal LSO. This lead to an intensive study based on temperature dependent steady-state and lifetime photoluminescence spectroscopy to understand the different concentration quenching mechanisms involved in the bulk single crystal versus the thin film LSO. The results were used to develop configuration coordinate models which were employed to explain the observed concentration dependent behavior. The nature of single crystal LSO:Ce concentration quenching was determined to be due to radiative energy transfer, and ultimately self-absorption. For the thin films it was found self-absorption was not a dominant factor due to the thin dimension of the film and also its nano-crystalline nature. Instead, the photoluminescence excitation and emission spectra as a function of concentration demonstrated the concentration quenching behavior was due to an increase in defect-mediated non-radiative transitions with increasing cerium. The final application of the thin film screening technique was the exploration of the ternary Lu2O3-SiO2-Al2O3 material system doped with cerium. It was found that the presence of aluminum and silicon hindered LSO and Al5Lu3O12 (LuAG) emission, respectively. However, the presence of aluminum was found to increase LPS emission intensity. The percent of aluminum in the LPS phase was estimated at 2.5 atomic percent.

PREFACE

It has been said that characterizing a scintillator with photoluminescence is like hitting one key on a piano, while using ionizing radiation is like throwing the whole piano down the stairs. This aptly describes much of the work conducted in this dissertation. Photoluminescence excites the activator site directly, as opposed to exciting electrons across the host material's band gap, this allows for detailed probing of the luminescent behavior of the activator. The technique is even more illuminative when coupled with temperature dependent and time dependent measurements.

The Lu_2O_3-SiO_2 binary material system covered in chapter 2 served to initially develop the thin film combinatorial screening process and benchmark the technique. The results were both promising and relatively straightforward and concise.

At the start of this research it was not intended to characterize single crystal samples. As work progressed on the cerium concentration in thin film LSO, covered in chapter 4, it became apparent that a full understanding of the effects of cerium concentration in single crystal LSO was required. A single crystal material has the advantage that the luminescence behavior is not affected by grain boundaries, or in the case of thin film LSO:Ce, by substrate interactions. The single crystal work is covered in chapter 3. The work and conclusions in chapter 3 and 4 are based heavily on the application of theoretical models, such as the configuration coordinate diagram, to explain the complicated luminescent behavior of these materials. The precise nature of photoluminescence was invaluable to the work covered in these chapters.

The goal of the work conducted in chapter 5 was to both push the ability of the developed thin film combinatorial screening method by applying it to a complex pseudo ternary system and to explore a system that had not been previously explored. The results from this section were not clear-cut, but were promising nonetheless.

scientia ac labore

TABLE OF CONTENTS

Chapter   Page

LIST OF TABLES

LIST OF FIGURES

xiv

CHAPTER I
INTRODUCTION

The importance of radiation detection

The detection of ionizing radiation is critical in fields such as medical imaging, high-energy physics, geophysical exploration, interplanetary exploration, and security applications. One of the common methods of detecting ionizing radiation is to use a scintillating material. A scintillator is a material that absorbs and converts ionizing radiation, such as γ- or x-rays into visible light. The detection requirements of the above applications are stimulating the development of new scintillators and the refinement of existing scintillators. Although solid state detectors have shown potential for use in several applications the popularity of scintillator based detectors has continued to increase because of their high γ-ray detection efficiency and high count-rate capability [1]. A wide variety of scintillation materials are utilized, ranging from organic to inorganic; solid to gaseous; and single crystalline to amorphous. For γ-ray detection, inorganic scintillators are preferred due to their generally higher density and atomic number; both important for absorbing high energy particles.

Positron emission tomography (PET) is a medical imaging technique in which the patient is injected with a glucose analog, such as Fludeoxyglucose (FDG), that contains a positron emitting, radioactive isotope (flourine-18 in the case of FDG). As a positron decays it emits two 511 keV γ-rays that travel in opposite directions (close to 180 degrees). By time correlating the absorption of the emitted γ-rays by a scintillator-based

circular detector array the centroid, or origin, of the γ-ray can be used to produce an image. An area with high metabolic activity (i.e. an area with high uptake of the glucose analog) has high contrast; such as the brain, the kidneys, and cancer cells. In essence, PET provides metabolic information in comparison to nuclear magnetic resonance (MRI) or computed tomography (CT) which provide anatomic information. As such, it is common to use PET in combination with an anatomic based imaging technique.

Scintillators used in PET imaging need to fulfill many properties, namely: high density, atomic number, and light output, a fast decay time, acceptable energy resolution, an emission wavelength near 400 nanometers with minimal self-absorption, non-hydroscopic, rugged, and a reasonable production cost [2]. Inorganic single-crystal scintillators, such as cerium-doped lutetium oxyorthosilicate (Lu_2SiO_5:Ce or LSO), have proven superior at fulfilling these requirements.

Motivation

The common production methods of single-crystal scintillators are expensive and time-consuming processes such as the Czochralski and Bridgman crystal growth techniques [3]. The search for new scintillator materials can therefore be a long and expensive process as new material compositions are grown in a serial manner. In fact, only three scintillators have seen widespread commercial use in PET imaging: NaI, first demonstrated by Robert Hofstadter in 1948; $Bi_4Ge_3O_{12}$ (BGO), first commercially available in the late 1970's; and Ce doped Lu_2SiO_5, discovered by C. L. Melcher and J. S.

2

Schweitzer in 1993. Consequently, the need exists for a method to rapidly investigate and characterize new scintillator material systems. Additionally, it would be beneficial to be able to rapidly optimize activator and sensitizer concentrations in scintillator materials. To that aim, a combinatorial exploration method is investigated based on thin film processing, specifically reactive RF magnetron sputtering.

Phosphors

General info and basic mechanisms

Scintillators are considered a subset of phosphor materials. Additionally, it is helpful to have a general understanding of phosphor absorption and luminescence mechanisms before discussing scintillation. The word phosphor can broadly be defined as any "solid luminescent material"[4] and indeed includes all luminescent materials. However, in practice the term generally refers to a powder inorganic phosphor. Here we focus our discussion on solid-inorganic luminescent materials.

A phosphor is created by adding an activator to a host material. The host material is generally a compound material with a large band gap. The activator needs to have a ground state above the valence band and excited states below the conduction band, as depicted in figure 1. Commonly the activator is a dopant with a small concentration level; however some materials do not require a dopant, such as $Bi_4Ge_3O_{12}$. In the case of

3
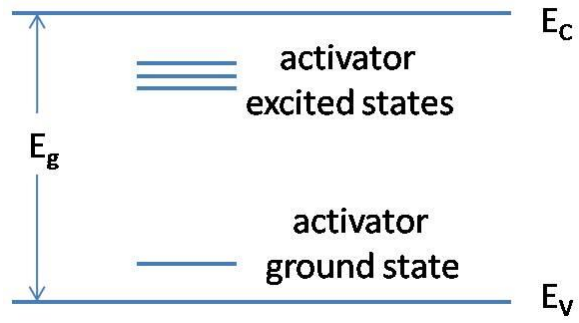
Figure 1. Band gap diagram depicting activator energy levels.

$Bi_4Ge_3O_{12}$, luminescence occurs due to optical transitions of the Bi^{3+} ion that is naturally present in the crystal. The absorption properties of the material are directly related to the electronic structure of the host and the activator. Incident photons with energies higher than the band gap of the host material will be absorbed by exciting an electron from the valence band to the conduction band which is then transferred to an activator site or returned to the ground state. Incident photons with energies close to the energy separation between the ground and excited state of the activator with be absorbed directly by the activator site by exciting an electron from the ground to the excited state of the activator.

The absorption and luminescent properties of the activator can be described more accurately with a configuration coordinate diagram, such as the one in figure 2. The y-axis is energy while the x-axis nuclear distance. Electrons move much faster than nuclear rearrangements therefore transitions (within a good approximation) take place in static surroundings (i.e. only in the vertical (y) direction). This assumption is called the Condon approximation. The two parabolas represent the ground and excited states. The horizontal lines within the parabolas represent vibrational states. An electron in a higher energy vibrational state will quickly decay to the lowest energy vibration state in its band. Therefore, particularly at low temperature, electrons are typically excited from the lowest energy vibrational level in the ground state. Incident photons with energy equal to the energy difference between the activator's ground state and its excited states will be absorbed. If the transition is from an inner, shielded orbital to an outer
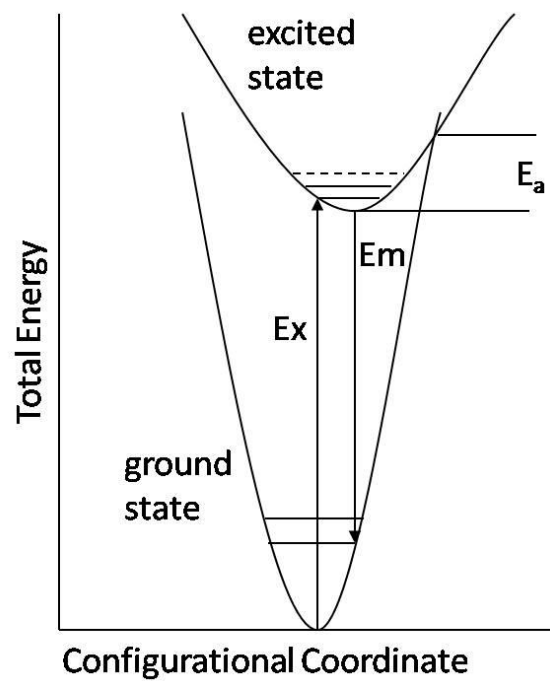
Figure 2. Configuration coordinate diagram.

orbital of the activator, such as the 4f-5d transition in Ce^{3+}, then the absorption peak tends to be a broad band. This is due to crystal-field and spin-orbit splitting. However, if the transition is between inner energy levels, such as f-f transitions in Eu^{3+}, then the absorption bands will be sharp peaks because they are shielded from effects by the host material by the outer energy levels of the activator.

An absorption spectrum for cerium doped Lu_2SiO_5 (LSO) is shown in figure 3. At 200 nm and shorter the absorption is due to the LSO host material. The peaks at 360, 300, and 265 nm are due to absorption by the cerium activator with excitation from the 4f ground state to the 5d excited states. The difference in peak height is due to the density of state functions of each vibrational state; the more overlap between the lowest energy vibrational state in the ground state and a vibrational state in the excited state, the higher the probability electrons will be exited to that level and the higher the absorption of the corresponding energy wavelength. Cerium does not exhibit f-f transitions so sharp peaks are not observed.

Just as electrons are excited from the lowest energy vibrational level in the ground state, electrons de-excite from the lowest energy vibrational level in the excited state. When the electron de-excites there is a specific probability the energy can be released as a photon, which is a radiative transition. The wavelength of the photon is again related to the energy difference between the excited state and a vibrational state in the ground state. However, because some energy is lost due to moving from a higher energy to a lower energy vibrational state in the excited band, the energy of the emitted
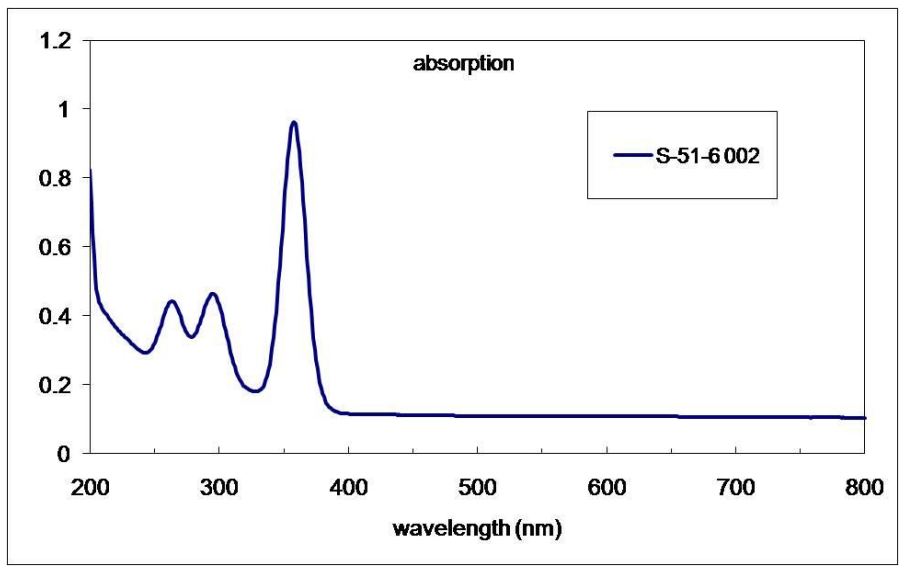
Figure 3. Measured absorption spectrum of Lu_2SiO_5.

photon is lower (the wavelength is longer) than the corresponding energy of the absorbed photon. This wavelength shift is called the Stokes shift. Additionally, when an electron de-excites there is a probability that the energy can be released as phonons, a so-called non-radiative transition. In terms of the configuration coordinate diagram this would occur when an electron has enough energy to transition from the excited state to the ground state by a pathway where the two parabolas cross. Generally, the ratio of non-radiative transitions to radiative transitions increases with increasing temperature.

Trivalent cerium

Ce^{3+} has the simplest electronic structure of the rare earth ions that exhibit broad band emission (which also includes Pr^{3+}, Nd^{3+}, Eu^{2+}, Sm^{2+}, Yb^{2+}) since it is a one-electron case. As mentioned above, transition occurs between the 5d excited state and the 4f ground state. The 4f ground state electrically shield by the $5s_25p$ orbitals reducing crystal field effects. Its electronic structure is dominated by spin-orbit coupling which splits it into the $F_{5/2}$ and the $F_{7/2}$ configurations, separated by about 2000 cm^{-1}. The $F_{5/2}$ and $F_{7/2}$ levels are further split due to reduced crystal field effects into a total of seven states, though for Ce^{3+} in many host materials these states are degenerate. The 5d configuration is not shielded and is strongly affected by crystal field effects which split it into 2 to 5 components that show a total separation on the order of 15,000 cm^{-1}. These 5d components can be further split into additional levels by spin-orbit coupling. For example, crystal field calculations of Ce^{+3} in octahedral sites of alkaline earth sulfide hosts have shown the lower 5d crystal field level is spin-orbit split into three levels with

two additional 5d levels spin-orbit split from the next higher 5d crystal field level [5-6].

The spectral position of the cerium emission band is influenced by three factors: The covalency (the nephelauxetic effect) which will decrease the energy difference between the 4f and 5d levels. The crystal field splitting of the 5d configuration; low symmetry will lower the lowest 5d level. And finally the Stokes shift, which is usually not very large, varying from a thousand to a few thousand wave numbers.

Gamma-radiation

Emission

In part, the focus of this dissertation is scintillators used for γ-ray detection in PET imaging so it is helpful to understand the origin of γ-rays in different sources. Or more specifically, gamma rays following beta decay. The two nuclear transmutations of interest in gamma ray emission are beta minus and beta plus decay. In beta minus decay, a neutron in the specie's nucleus transmutes to a proton with the emission of a negative beta particle and an antineutrino:

$$\prescript{A}{Z}{X} \rightarrow \prescript{A}{Z+1}{Y} + \beta^- + \bar{\nu} \quad (1.1)$$
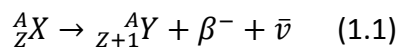
X and Y are the initial and final nuclear species, β is the beta particle (a fast moving electron, or e⁻), and $\bar{\nu}$ is an antineutrino. Antineutrinos (and their antiparticle, neutrinos) are elementary particles that have a low interaction probability with matter and are therefore extremely difficult to detect. For many of the radioisotopes that experience beta decay, the nucleus of the final species Y is in an excited state. The transition of the

excited nuclei to lower-lying nuclear levels takes place by the emission of a gamma-ray photon with energy essentially equal to the energy difference between the two levels. The gamma-ray emission is much faster than the parent level beta emission so half-life characteristics will be dominated by the beta decay. An example of this process is ^{137}Cs source, as diagramed in figure 4.

In beta plus decay a proton in the specie's nucleus transmutes to a neutron with emission of a positive beta particle and a neutrino:

$$^A_Z X \rightarrow \, ^A_{Z-1}Y + \beta^+ + v \quad (1.2)$$
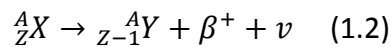
Instead of the beta particle being a fast moving electron, in this case it is a fast moving positron (e^+). Gamma ray emission can still occur with an energy characteristic of the final nuclear species; however, annihilation of the positron can also take place. When a positron interacts with an electron they annihilate one another following $E=mc^2$ and produce two 511 keV gamma rays that are opposed at almost 180 degrees. An example of beta plus decay is ^{22}Na which emits 1274 keV gamma rays characteristic of the final species energy level structure and 511 keV gamma-rays due to positron annihilation. ^{18}F decays to ^{18}O following beta plus decay. In this case, the decay only shows 511 keV gamma rays due to positron annihilation.

Interaction in matter

To understand the first step in scintillation, the absorption of incident ionizing radiation and the creation of electron-hole pairs, it is helpful to review the interaction
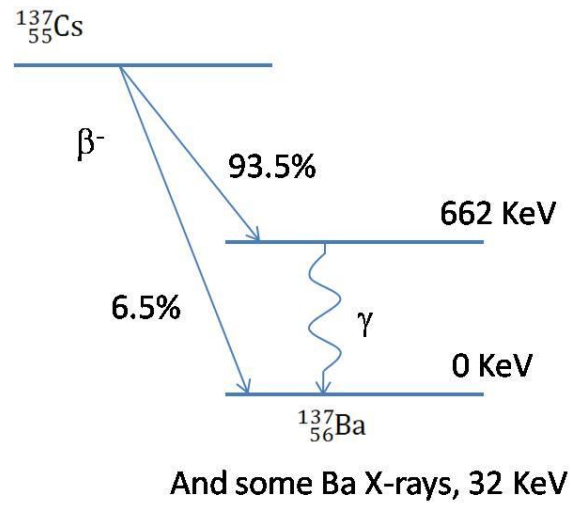
Figure 4. γ-ray emission from ^{137}Cs.

A 662 keV γ-ray along with Ba characteristic X-rays are emitted

mechanisms of γ-rays in matter. There are many known interactions of γ-rays in matter, however only three main types are important for radiation detection: photoelectric absorption, Compton scattering, and pair production [7]

Photoelectric absorption of a gamma ray is similar to the absorption mechanism of lower energy photons described above for phosphors. In this case the incident gamma ray absorbed by exciting an electron (i.e. creating a photoelectron) from a tightly bound inner shell. The hole left behind will quickly be filled by a higher shell electron generating one or more characteristic x-rays (or Auger electrons) that are then usually reabsorbed close to the original site, which is also by photoelectric (electron) absorption. Photoelectric absorption is the dominant model for low energy gamma rays (and x-rays). The probability of the mechanism increases with higher Z of the material.

Compton scattering is a collision interaction between an incident gamma-ray photon and an electron. It is the dominant absorption mechanism for the energy scale typical of radioisotopes (e.g. ^{137}Cs and ^{18}F). Energy transfer from the gamma-ray to the electron can vary widely, ranging from zero to a large percent of the gamma-ray's initial energy. The energy transferred can be calculated by solving simultaneous equations for conservation of energy and momentum:

$$h\acute{v} \; = \; \frac{hv}{1 + \frac{hv}{m_0 c^2}(1 - \cos\theta)} \qquad (1.3)$$

where m_0 is the rest mast of an electron (511 keV), and θ is the angle between the vector of the incident gamma-ray and its resulting vector after impacting an electron.

Since the probability of Compton scattering is dependent on the number of electrons in the material, probability of interaction increases linearly with Z.

For pair production to be energetically possible the energy of the incident photon must be twice the electron rest energy of 511 keV. Furthermore, the probability of this type of interaction remains very low until energies upwards of several MeV are involved. Pair production is not an important mechanism for the detection of the 511 keV gamma rays created by positron annihilation, but a short description is given in the interest of completeness. The pair production takes place in the coulomb field of the nucleus. In the transition the incident gamma ray disappears creating an electron and a positron. Energy from the gamma ray above 1.02 MeV is shared as kinetic energy between the newly created particles. The resulting positron will ultimately annihilate creating two 511 keV photons. The resulting positron annihilation can be an important effect in detectors of incident gamma-ray photons with energies above 1.02 MeV.

Scintillators

Scintillation

Scintillation can be described by three main processes. The first process is the absorption of incident ionizing radiation and the creation of electron-hole pairs. The second process involves the migration of holes and electrons to activator sites. The third process is the recombination of the holes and electrons at the activator site and photon

emission via the same mechanism as that described for phosphors. Lempicki et al. [8] have proposed a relationship for the overall quantum efficiency of the scintillation process:

$$\eta = \beta S Q \quad \text{(1.4)}$$

Where β is the efficiency of electron hole pair creation by incident γ-ray energy, S is the efficiency of the transfer of energy from electron hole pairs to luminescent centers, and Q is the quantum efficiency of the luminescent centers.

β represents the conversion efficiency of the energy of the γ-ray, E_γ, into electron hole pairs. Robbins [9] has shown than the minimum energy to produce an electron-hole pair is 2.3 times the energy of the band gap: $\xi_{min} = 2.3E_g$. So the maximum possible creation of electron-hole pairs is $E_\gamma/2.3E_g$. It follows that the conversion efficiency β will be given by:

$$\beta = \frac{n_{e-h}}{E_\gamma/2.3E_g} \quad \text{(1.5)}$$

where n_{e-h} is the number of electron-hole pairs actually produced by one γ-ray photon. β can also be expressed as:

$$\beta = \frac{2.3E_g}{\xi} \quad \text{(1-6)}$$

where ξ is the energy required to produce one electron-hole pair. β can be calculated from the band gap, the high frequency and static dielectric constants, and the optic longitudinal phonon energy. For well know scintillator materials β can be calculated with relative confidence, but for newer scintillators where the values are not well known there can be a high degree of uncertainty.

There is not an adequate model to calculate S, however it can have a large effect on overall efficiency. Additionally, this transfer process has been shown to be responsible for large performance variations among Ce-based scintillators [8]. It has been stated that developing a model for S could currently be the primary challenge in scintillator research [2]. Q can be measured with photoluminescence which excites the luminescent center directly. The band gap E_g can also be measured with additional optical spectroscopy.

Scintillators for Positron Emission Tomography

Important properties of scintillators for use in PET are summarized in table 1 for selected noteworthy scintillation materials. Additionally information regarding LSO is included below.

LSO is widely used in PET imaging because it fulfills many of the application's ideal scintillator properties, namely, high density, atomic number, and light output, a fast decay time, good energy resolution, an emission wavelength near 400 nanometers with minimal self-absorption, non-hydroscopic, rugged, and a reasonable production cost [2].

Table 1. Summary of selected scintillators.

	LSO	LuAG	BGO	NaI(Tl)
Density (g/cm3)	7.4	6.7	7.13	3.67
Effective Z	66	58.9	75	51
Hygroscopic	No	No	No	Yes
Rugged	Yes	Yes	Yes	No
Index of refraction	1.82	1.84	2.15	1.85
Peak wavelength (nm)	420	535	480	410
Decay time constant (ns)	40	50-60	300	230
Relative light output	75	20	15	100

LSO is not widely employed in geophysical exploration nor oil well logging mainly due to the drop in luminescent efficiency above 300K [10] that yields the material undesirable for higher temperature applications. The naturally occurring [176]Lu isotope gives LSO a background spectrum that does not fulfill the low signal to noise ratio required for some security applications.

LSO has a monoclinic structure (space group C2/c) with two distinct Lu sites with oxygen coordination numbers of 6 and 7. The trivalent Ce activator substitutes in the Lu^{3+} sites [11] and both sites are likely occupied which have similar crystal field splitting. The convolution of the two sites likely accounts for the single broad peak observed at room temperature instead of the characteristic double peak associated with the spin orbit splitting of the 4f levels. Additional broadening observed at higher concentrations have been associated with defect-mediated sites (i.e. vacancies) as well as interstitial sites [12]. LSO has a high density of 7.34 g/cm^3 and exhibits a fast decay time of ~40ns with a 28,000 photons/MeV light output for 512KeV gamma ray excitation.

Thin film sputter deposition

Plasma physics

A brief introduction to plasma physics as it pertains to physical vapor deposition (PVD) is given; a more in-depth discussion of plasma physics can be found elsewhere [13]. Sputtering is a form of PVD that employs a plasma, or more specifically a glow

discharge, to deposit material onto a substrate. A plasma is a partially ionized gas containing equal parts of positively and negatively charged gas particles in addition to a number of non-ionized gas particles. On earth plasma may seem to be a rare, fourth sate of mater. However, it is estimated that 99% of the matter in the universe is in the form of a plasma. Everyday examples of plasmas include the aurora borealis (northern lights), neon lights and the inside of fluorescent lights. Plasma densities range from 10^7 to 10^{20} species/cm^3. PVD typically employs glow discharges, a subset of plasmas that have an electron and ion density of ~10^8-10^{14} species/cm^3.

In a gas without an applied potential, the gas molecules are electrically neutral; at room temperature the gas will contain very few charged particles. Occasionally, an electron will be released by a gas particle due to absorption of incident radiation (such as a photon) or by a random high energy collision with another particle. If the gas is placed between two metal plates and a large DC voltage is applied (upwards of 100 V/cm) the free electrons with be accelerated rapidly towards the anode while gas ions will be accelerated slowly towards the cathode. Inelastic scattering between fast electrons and gas particles ionizes additional particles creating additional free electrons; this process quickly cascades to a self-sustaining plasma. The degree of ionization (f_i) follows: $f_i = n_e/(n_e + n_0)$ where n_e is the number of electrons and n_0 is the number of neutral atoms (or molecules). For a typical glow discharge at 10 mTorr n_0 is ~10^{14} and $f_i = 10^{-4}$.

In addition to DC biased discharges, AC (usually RF) discharges can also be sustained. The initial startup mechanisms for an RF discharge vary dramatically from DC discharge,

but the target quickly self-biases to a negative potential. Once this occurs the target (material to be sputtered) behavior is the same as for DC discharges. RF offers the advantage that insulating materials may be sputtered in addition to metals. In DC discharges the voltage required to sputter an insulating material (which essential makes the cathode a resistor) is prohibitively high. In RF discharges, due to the drop in impedance of a dielectric based capacitor with increasing frequency, the plasma passes current through dielectrics (insulating target materials) as a DC discharge does with a metal target. RF frequencies of 5 to 30 MHz are practical for sustaining sputtering plasmas, but the Federal Communications Commission has reserved 13.56 MHz for plasma processing and it is the most widely used.

Sputtering

In sputter deposition the voltage is applied between the target (i.e. source material) and the substrate in a low pressure, typically Ar, atmosphere (commonly 3 to 5 mtorr for RF systems). The target is negatively biased as the cathode while the substrate is positively biased (or grounded relative to the target). The glow discharge overall is charge neutral but sections may be charged positively or negatively. The main regions of a general glow discharge in a sputtering system are diagramed in figure 5a. In the Crookes space, or cathode dark space, there is relatively little ionization so this region appears dark. In the negative glow region visible emission is attributed to interactions between electrons and neutral species with attendant excitation and de-excitation. Additional regions lie beyond the negative glow region, however, during sputtering the substrate is commonly

placed in the negative glow region so these additional regions are not usually visible [13]. Most of the voltage drop is across the cathode dark space; Ar ions in this region are accelerated towards the target (cathode) and physically eject (or sputter) target atoms through momentum transfer. The distribution of the sputtered species typically follows a cosine shaped profile (figure 5b). The sputtered target material passes through the discharge region and is ultimately deposited atomistically on the substrate with a profile (if the substrate is held stationary) directly related to the sputtered cosine distribution. Modeling of the sputtered profile will be introduced in chapter 2.

In magnetron sputtering, magnets are added to the sputter source, typically behind the sputter target. The addition of magnets has several advantages, namely it increases the distance electrons travel which in turn increases the ionization rate. Subsequently, more current is drawn for the same applied voltage leading to higher deposition rates or lower voltage operation and the ability of reduced operating pressures because ions are more directed by the magnetic field. The main disadvantage of magnetron sputtering is the effects on target integrity. Specifically, a race track type ring develops on the target where the plasma is more intense. As the target wears the race track pattern can deepen and decrease sputtering yield. In production systems this is typically solved by periodically rotating the positions of the magnets to maximize target life.

Reactive sputtering involves injecting a small partial pressure of a reactive gas while sputtering from a metal target source in order to deposit a reacted compound. The sputter system used in this dissertation is set up to reactively sputter oxides and
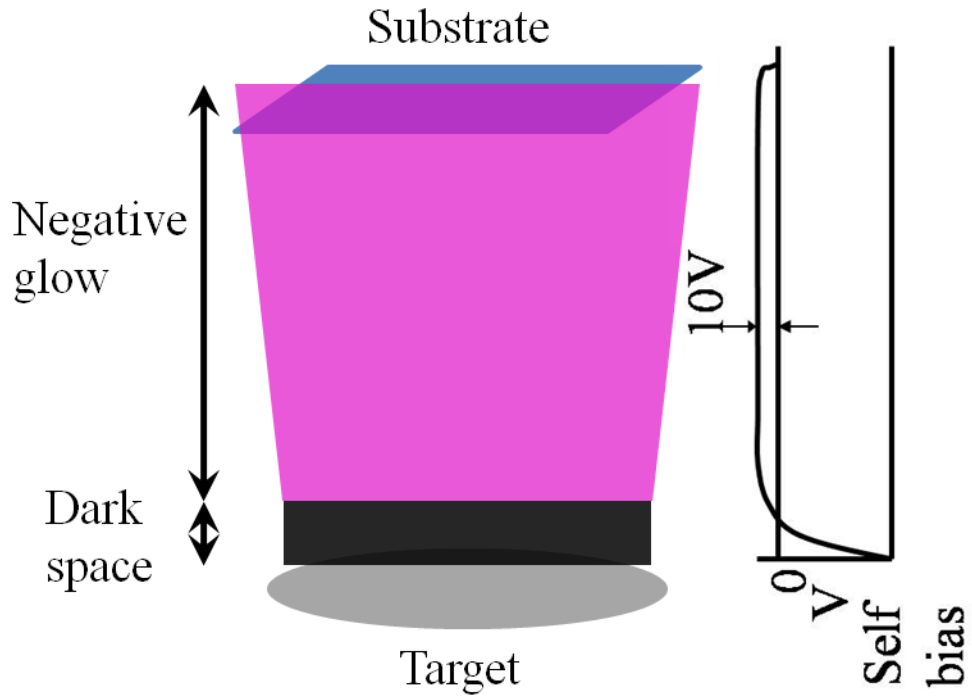
a.

$$I(\theta) = I\cos(\theta)$$
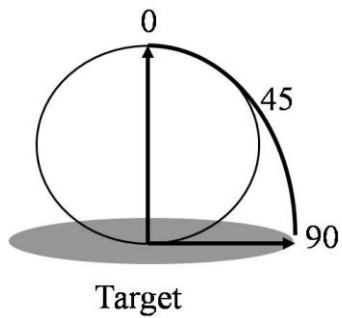
b.

Figure 5. Sputtering diagram.

(a) Diagram of plasma in a sputtering system. (b) Angular distribution of sputtering deposition.

nitrides. An important parameter for reactive sputtering is the hysteresis behavior between target self bias and reactive gas partial pressure. When the target self bias behavior is not changed by the injection of a reactive gas the target is said to be in metal mode. In metal mode deposition rates are relatively high. However, if not enough reactive gas is injected the species will not be fully reacted. If too much reactive gas is injected the target will go into covered mode, where the reacted compound forms on the surface of the target itself. When the target is in covered mode deposition rate is usually decreased dramatically. Ideally, enough gas is injected that the species is fully reacted, but the target stays in metal mode. A hysteresis plot for Lu at 200 W in argon and oxygen is shown in figure 6. Generally, a good starting point in achieving good film quality is a partial pressure that corresponds to the top shoulder on the way from metal to covered mode. Reactive sputter is further complicated when multiple materials are sputtered as each material has its own hysteresis plot. Additionally, the hysteresis will change slightly with changes in other parameters such as wear on the target and overall chamber conditions.

Several thin film processing methods, including sputtering, lend themselves to combinatorial compositions. There are three general combinatorial patterns as summarized in a convenient diagram by Koinuma and Takeuchi [14] reproduced in figure 7. The first generation of combinatorial patterns is the natural composition spread. This pattern arises out of the geometry of many processing equipment where the sources are offset from the substrate so that a thickness gradient is achieved if the
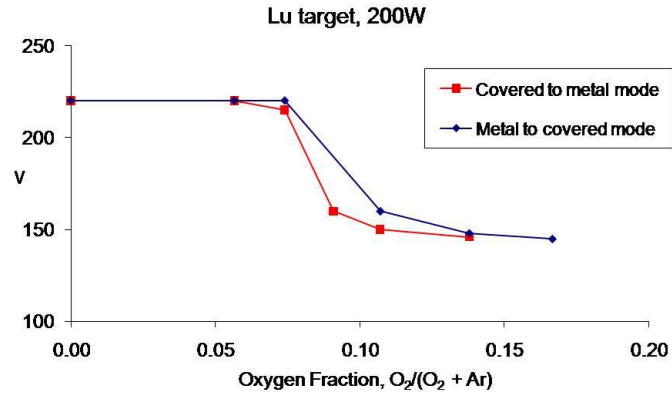
Figure 6. Lutetium metal to covered mode hysteresis
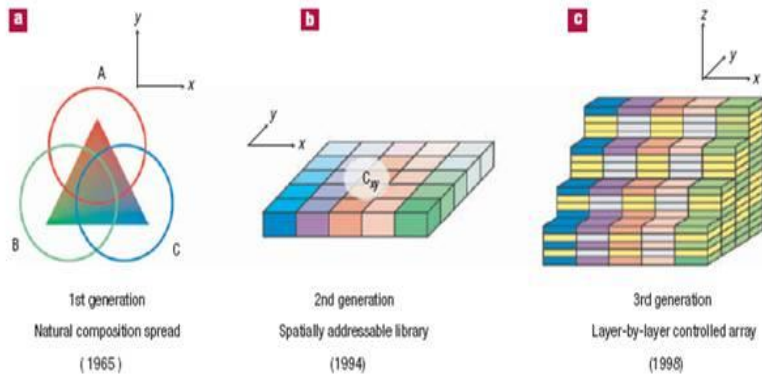
Figure 7. Methods of thin film combinatorial processing

substrate is not rotated during processing. Kennedy, et al. [15] first used this approach to look at ternary-alloy phase diagrams by source evaporation in 1965. A few years later, Hanak [16] was the first to apply this approach to sputter deposition. In a spatial addressable library masks are used so that each section is of a uniform composition. Xiang and Schultz et al. [17] have applied this approach for many material systems, among them superconducting materials. In a layer-by-layer array masks are combined with layer-by-layer deposition. Koinuma and Takeuchi [14] have pioneered this approach.

R.F. magnetron sputter system

AJA International ATC 2000 R.F. magnetron sputter system (diagramed in Figure 8a) was used for the sputter deposition processing in this dissertation. Figure 8b is a picture of the sputter chamber while co-sputtering Si and Lu. The system employs four 2" guns spaced evenly below the substrate holder, which can accommodate 4" or 6" substrates. Operating parameters include R.F. or D.C. substrate bias, still or rotating substrate, and a substrate heater up to 800°C. Inert gas (usually Ar or Ar+H) is injected at the target surface, while reactive gasses are injected at the substrate. Base pressure of the system is below 10^{-9} torr with common processing pressures of 3 to 5 mtorr. By controlling gun power and tilt angle, substrate rotation, and system atmosphere a wide range of compositions can be generated. Substrate temperate and substrate bias have a smaller effect on film composition but can play a large role in film morphology.
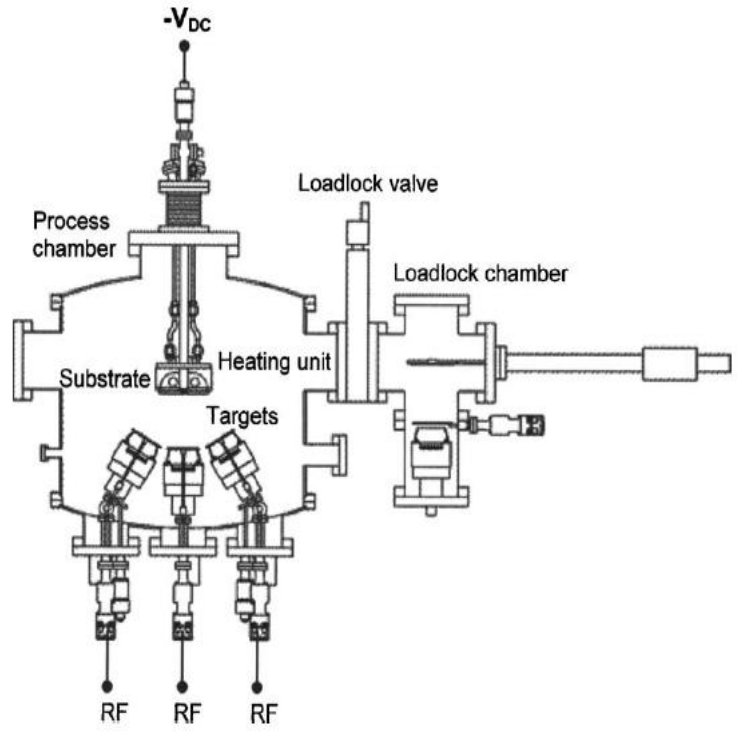
a.
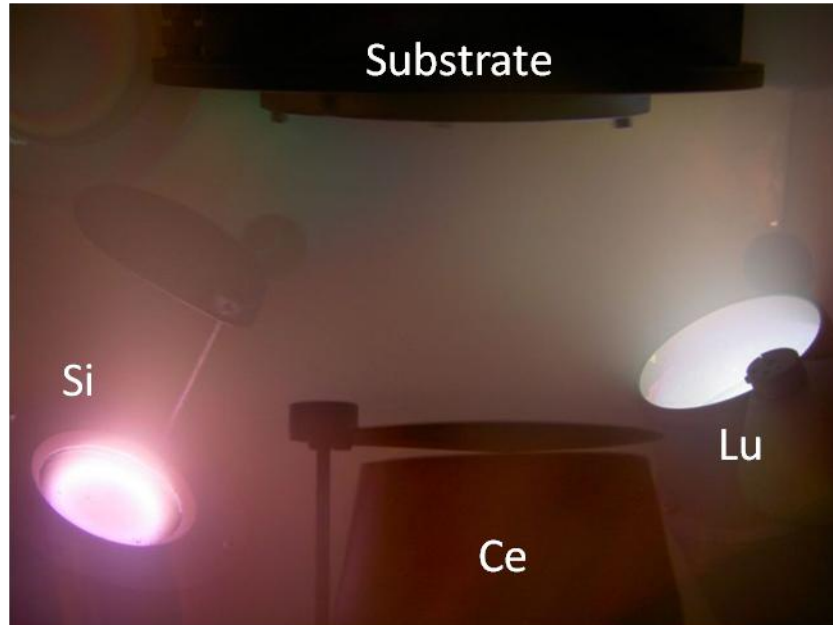
b.

Figure 8. Diagram (a) and image (b) of sputter system.

Thin film scintillators

There has not been a large volume of work published investigating the use of thin film processing to screen potential scintillators. Lee, et al. [14] have investigated thin filmLSO:Ce deposited via pulsed laser deposition. They found, when normalized for thickness, the films had a relative radioluminescence brightness twice that of bulk single crystal LSO:Ce. However, they did not observe the characteristic 4f spin-orbit peak split in the emission spectrum, even down to 75 degrees Kelvin, which was attributed to peak broadening due to film stress.

Milbrath et al. [18] have also explored thin films produced by vapor deposition to screen scintillator materials, specifically in $CaF_2(Eu)$, $CeCl_3$ and CeF_3. The hydroscopic CeCl3 films were coated with a protective polymer/oxide barrier and they showed emission spectra and decay times were consistent with the single crystal values. However, thin film $CaF_2(Eu)$ had a lower light output (alpha particle excitation) than single crystal $CaF_2(Eu)$; they proposed this was due to the polycrystalline nature of the thin film. This work was followed up by Matson et al. [19] with the study of a CeCl3-CeBr3 composition gradient. The samples exhibited relatively low light yield and red-shifted emission that was attributed to perturbation of the Ce sites due to structural defects in the films.

In addition to vapor deposition synthesis, liquid phase epitaxy has been used to study thin and thick film single crystal scintillators. For instance, $Y_3Al_5O_{12}$ (YAG) and $Lu_3Al_5O_{12}$ (LuAG) [20-22] have been grown and differences between the luminescent spectra and

decay time of bulk single crystals and single crystal films were attributed to anti-site defects that are present in the bulk single crystal but not in the single crystal films. Martin et al. [23] grew LSO:Tb, LSO:Tb, Ce and $Lu_{2-x}Y_xSiO_5$:Ce single crystal films via liquid phase epitaxy for X-ray imaging. They showed LSO:Tb films had better absorption efficiency and conversion efficiency compared to LuAG:Eu and more efficient 550 nm emission, but less efficient 715 nm emission than $Gd_3Ga_5O_{12}$:Eu.

The development and processing of the thin film combinatorial scintillator samples presented here was based on work conducted by Fowlkes, Deng, Rack and Fitz-Gerald on combinatorial investigations of thin film luminescent materials [24-27]. The application of their research to the work conducted here will be introduced in chapter 2.

CHAPTER II
BINARY MATERIAL SYSTEM

Sections of this chapter have been published previously by Philip Rack, Jim Fitz-Gerald, Charles Melcher, and myself. [28-29]. Of the work presented in this chapter Jim Fitz-Gerald performed the backscatter-electron and cathodoluminescence imaging; Philip Rack and Charles Melcher provided direction, funding of the research, discussion and motivation.

Introduction

In this chapter the lutetium oxide (Lu_2O_3) – silicon oxide (SiO_2) material system doped with cerium is investigated by the thin film combinatorial process. Additionally, the relevant prior work and development of the exploration process are described. The thin film samples were investigated to determine the phases of the material system that exhibit scintillation properties and the results were compared to the results of bulk crystal samples. It was found that the emission spectra of the thin film materials have similar characteristics compared to the bulk crystals. Additionally, x-ray diffraction measurements have been correlated to the anticipated phases of the Lu_2O_3-SiO_2 equilibrium phase diagram and the intensity of the luminescence emission spectra have been correlated with the corresponding phases of the system, specifically LSO and LPS.

Background

The development of the thin film combinatorial scintillator exploration process presented in this dissertation was based on work conducted by Fowlkes, Deng, Rack and Fitz-Gerald on combinatorial investigations of thin film ultraviolet emitting materials [24-27]. Deng, et al. [24] initially looked at gadolinium doped $Y_3Al_5O_{12}$ (YAG) compositions. Their first step was to optimize the YAG sputter parameters which was done by reactively co-sputtering an un-doped gradient composition ranging from Y_2O_3 to Al_2O_3 on to a silicon substrate. Energy dispersive X-ray spectroscopy (EDS) was used to determine sample composition. Deposition parameters were adjusted to deposit a Al/Y ratio of 5/3 in the center of the substrate. The next step in the process was to deposit uniform YAG with a gadolinium composition gradient. This was done by depositing seven alternating layers of YAG and a gadolinium thickness gradient. Two samples were used to achieve the desired range of 1-12 at% gadolinium (first sample 1.5-6.5 at%, second sample 3.5-12.5 at%). A post-deposition anneal was performed at 1000 °C for 10 hours to diffuse the gadolinium into the YAG layers and to crystallize the amorphous as-deposited film. Luminescence intensity was characterized by cathodoluminescence and plotted versus gadolinium at%. They found the highest intensity luminescence occurred at 5.5 at% gadolinium above which emission intensity decreased dramatically due to concentration quenching. This work was followed up by an investigation [25] that optimized sputtering parameters (O_2 partial pressure, substrate temperature and substrate bias voltage) to achieve the highest

cathodoluminescence efficiency. It was found that high substrate temperature (400-600 °C) and high substrate bias (150 V) improved efficiency, however high O_2 partial pressure decreased efficiency.

Fowlkes, et al. [26] optimized the gadolinium dopant concentration in Y_2O_3 thin films. The brightness was found to increase up to 8.3 at% gadolinium, above which intensity decreased dramatically. They also demonstrated the use of a sputtering model to simulate the composition profile of deposited thin films. The thickness profile (and ultimately concentration profile after annealing) is dependent on the spatial profile of the sputtering flux and the processing chamber's geometry. These factors were incorporated into the sputter model using the standard surface source evaporation equation:

$$\frac{d\bar{M}_S}{dA_S} = \frac{\bar{M}_T(n+1)cos^n\phi\,cos\theta}{2\pi r^2} \quad (2.1)$$

where M_s is the mass deposited at the substrate (s), A is the area of the substrate, M_T is the total mass sputtered from the target (T), n is the degree of forward peaking of the sputter flux, r is the distance from the center of the target surface to the substrate position, ϕ and θ are the angles between a line extended from the center of the target surface to a point on the substrate and the target surface normal and the substrate surface normal, respectively (geometry is diagramed in figure 9). The modeling work was followed by a detailed investigation on the effect of sputter processing parameters
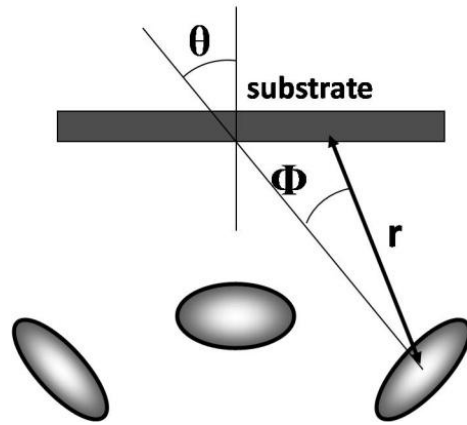
Figure 9. Illustration of sputtering geometry.

on the morphology of gadolinium doped Y_2O_3 thin films and, in turn, the effect of film morphology on cathodoluminescence intensity [27]. While the research by Fowlkes, Deng, Rack and Fitz-Gerald was a solid starting point, extensive work was undertaken to adapt the combinatorial technique to scintillation materials.

Experimental procedure

Thin film deposition

Thin film deposition was performed using elemental cerium, lutetium, and silicon targets in an Ar-O_2 atmosphere onto 100mm substrates using an AJA International ATC 2000 R.F. magnetron sputter system. Three of the system's four R.F. sputtering sources were used. The lutetium and silicon targets (50mm diameter) were mounted 180 degrees from one another while the cerium target was mounted ninety degrees from both targets; similar to the positions used by Deng, et al [24] for gadolinium doped YAG deposition. The substrate was positioned 7cm above the plane of the sputtering targets.

Before depositing Lu_2O_3-SiO_2 gradients, deposition rates and metal-to-covered mode hysteresis curves were measured. All thickness measurement samples were deposited onto silicon test substrates (100) in an argon atmosphere [25 SCCM flow (SCCM denotes standard cubic centimeter per minute at STP)] at 3 mTorr. Lutetium was deposited at power settings of 50, 100, and 200 W. Silicon was deposited at power settings of 100 and 200 W. A straight line was drawn on the silicon wafer with a thick marker before

deposition to act as a lift-off mask. After deposition, lift-off was performed by removing the ink mask with methanol leaving an uncoated line across each sample. Sample thickness was measured using a profilometer to scan across the coated and un-coated regions. Cerium was deposited at 25 W. Initial rate tests showed cerium rates as high as 1.34 nm/min (measured using profilometry). However, subsequent rate tests showed rates ranging from 0.06 − 0.178 (measured using atomic force microscopy). The drastic decrease in cerium sputter rate is attributed to oxidation of the target and subsequent sputtering performed in covered or oxide-mode (when a reacted layer forms on the surface of the target that decreases sputter rate). The deposition rates are summarized in table 2. Oxygen hysteresis curves were measured for the lutetium and silicon curves and are plotted in figures 10a and 10b. Based on these results, silicon and lutetium reactive co-sputtering was performed at 3 mTorr with and oxygen partial pressure of 7.4% [O_2 flow rate = 2 SCCM, Ar flow rate = 25 SCCM].

Lu_2O_3-SiO_2 gradients with a constant cerium doping concentration were deposited by alternating four layers of constant cerium thickness between five layers of Lu_2O_3-SiO_2 gradients, as shown in figure 11. To sputter Lu_2O_3-SiO_2 gradient layers, the lutetium and silicon targets were powered with 200 W and 110 W, respectively, for 15 minutes. For each Lu_2O_3-SiO_2 layer the substrate was aligned with the Lu-Si sputtering target axis (figure 8b in chapter 1) and held stationary during the deposition. Each cerium doping layer was sputtered at 25 W in an argon atmosphere at a pressure of 3 mTorr for 201 seconds while rotating the substrate at 20 revolutions per minute to produce a uniform

Table 2. Deposition rates for Lu, Si and Ce.

Element	Power	Voltage	Deposition Rate
Lu	50 W	115 V	2.51 nm/min
Lu	100 W	157 V	4.62 nm/min
Lu	200 W	218 V	8.36 nm/min
Si	200 W	335 V	5.67 nm/min
Si	100 W	220 V	1.67 nm/min
Ce	25 W	93 V	0.06 -0.17 nm/min
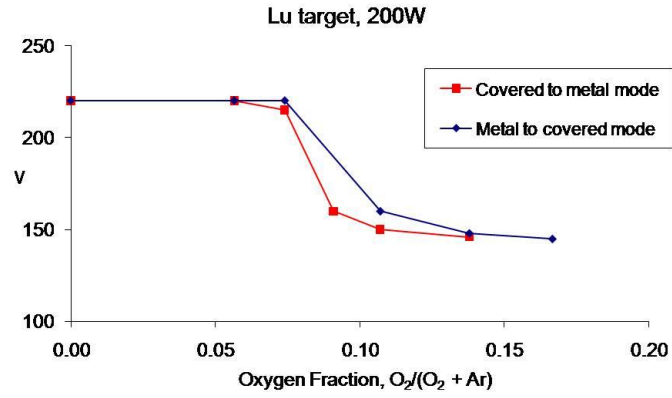
a.
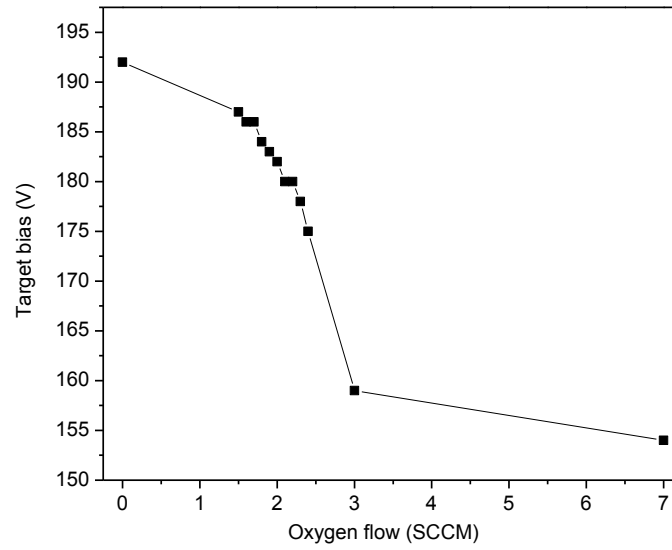
b.

Figure 10. Hysteresis plot for (a.) lutetium and (b.) silicon metal to covered mode.
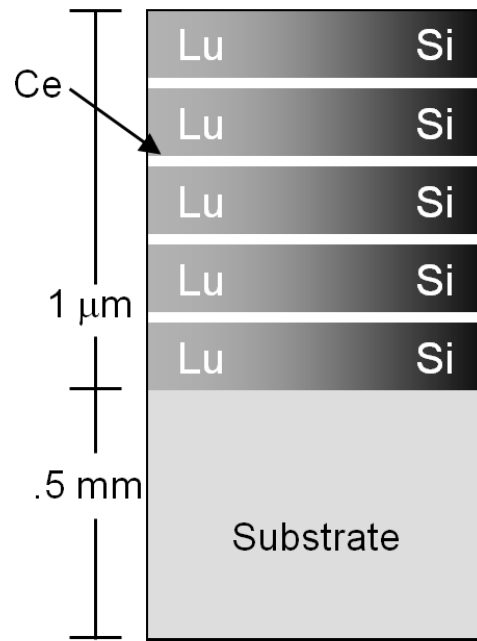
Figure 11. Diagram of as deposited profile parallel to Lu_2O_3-SiO_2 gradient.

profile. Based on Lu, Si, and Ce sputtering rates, the estimated cerium concentration in the Lu_2O_3-SiO_2 films is 0.3 atomic percent.

Characterization

Secondary-electron microscopy (SEM) was performed using a Hitachi 4300, backscatter-electron imaging was done on a JEOL 6700F and cathodoluminescence imaging was measured with a Gatan MonoCL3. X-ray diffraction (XRD) was measured from 10 to 60 degrees 2-theta with a step size of 0.02 degrees at 2 seconds per step using a Philips X'Pert diffractometer with a copper anode to investigate sample structure and composition. Photoluminescence emission and excitation spectra were measured using a Hitachi F-4500 spectrophotometer at a scan rate of 240nm/min. The photomultiplier tube voltage, the excitation slit and emission slit were uniform for all measurements. X-ray excitation measurements were performed using a Source 1 X-ray CMX003 X-ray tube at 31 kV with an Acton Research Corporation Spectra Pro 2150i spectrometer. A 15 mm by 6.6 mm guard was placed over the samples to ensure a fixed emission area of 100 mm^2.

Experimental Results

Films were initially deposited on silicon (001) substrates. Later samples were deposited on alumina (Al_2O_3) substrates (surface roughness less than 26 nm, grain size less than 1μm) to reduce film-substrate diffusion and allow higher annealing temperatures.
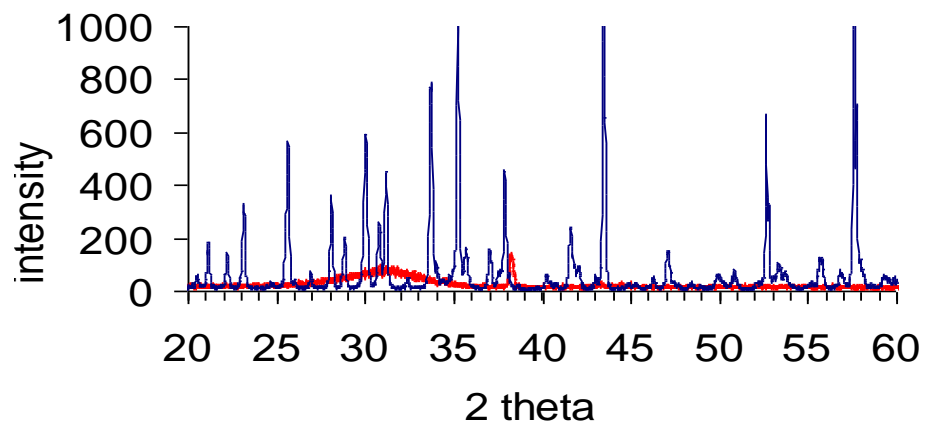
Figure 12. XRD spectra of as-deposited and annealed film.

Red line is spectrum of as-deposited film and blue line is spectrum of annealed film.

The XRD spectra of an as-deposited and annealed film on a silicon wafer are plotted in figure 12 and confirms that the film is amorphous as-deposited and crystalline after annealing. Cross-sectional SEM images of an un-doped film deposited on silicon before and after annealing at 1200 °C for 10 hours in air are shown in figures 13a and 13b. Comparing the as-deposited film in figure 13a to the annealed film in 13b it is apparent that film-substrate diffusion has occurred. The original film-substrate boundary is still visible in figure 13b at 0.79 μm below the film surface; however diffusion is seen to extend over 0.15 μm into the substrate. In an attempt to minimize diffusion, a doped film was deposited on a silicon substrate with a 0.52 μm layer of SiO_2 between the film and the substrate to act as a diffusion barrier. SEM images of this sample before and after annealing at 1200 °C for 10 hours in air are shown in figure 14a and b. In figure 14a the SiO_2 layer and each of the five individual layers of the Lu_2O_3-SiO_2 gradient are visible. However, large scale diffusion is again observed in figure 14b.

To minimize the film/substrate interdiffusion, the next step was to try alumina substrates. Successive rounds of annealing revealed that higher annealing temperatures of 1400 °C and a nitrogen atmosphere increased film emission intensity greatly. SEM image of the as-deposited Lu_2O_3-SiO_2 gradient/Ce multilayer film structure is shown in figures 15a and 15b before and after annealing at 1400 °C in nitrogen. Each individual Lu_2O_3-SiO_2 gradient layer is again observed and each layer is close to the target value of 200nm (at the center of the substrate) for a total film thickness of approximately 1 μm (measured ~0.96 μm). The thickness of the annealed film (figure 15b) increased from

0.79 microns

SE   S4300N WD13.7mm 10.0kV x30k   1um

a.

0.94 um   .79 um

SE   S4300N WD13.4mm 10.0kV x35k   1um
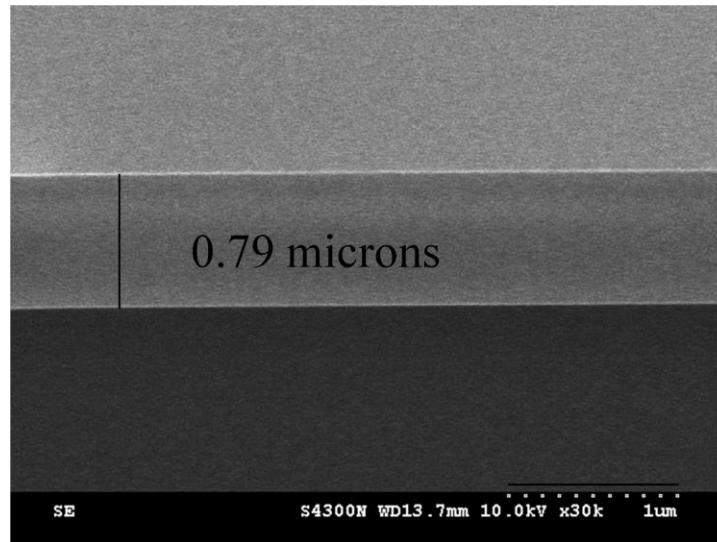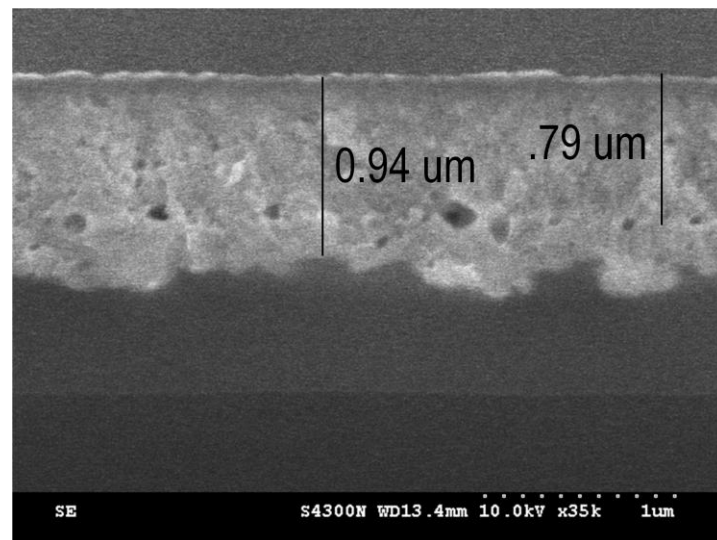
b.

Figure 13. SEM images of (a) as-deposited and (b) annealed films on a silicon substrate.
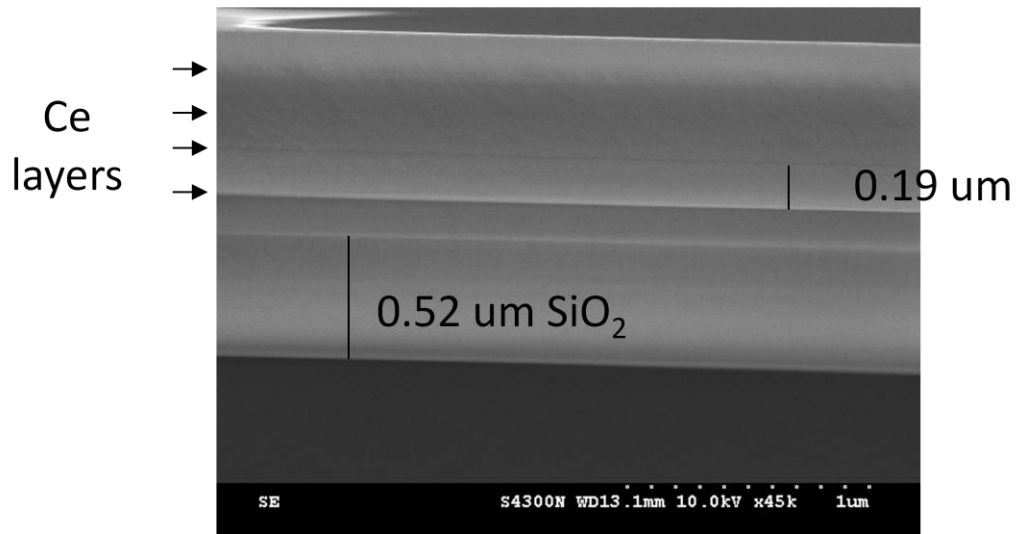
a.
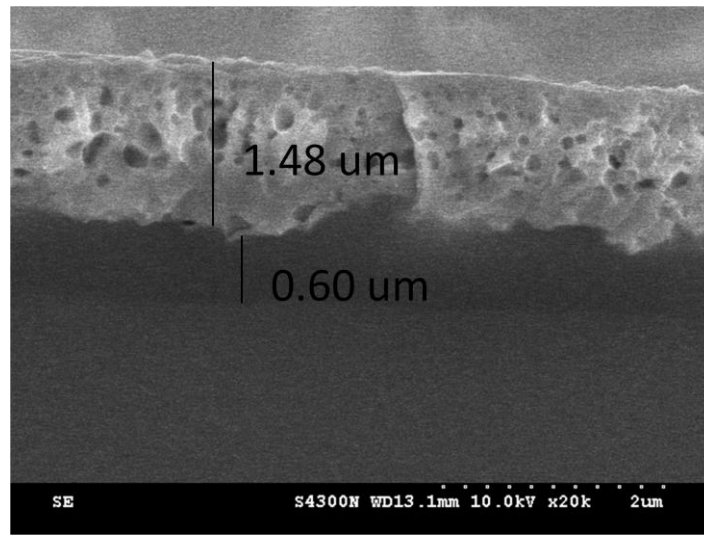
b.

Figure 14. SEM images of (a) as-deposited and (b) annealed films on a silicon substrate with a 0.52 μm SiO_2 diffusion barrier.

a.

1.41 μm
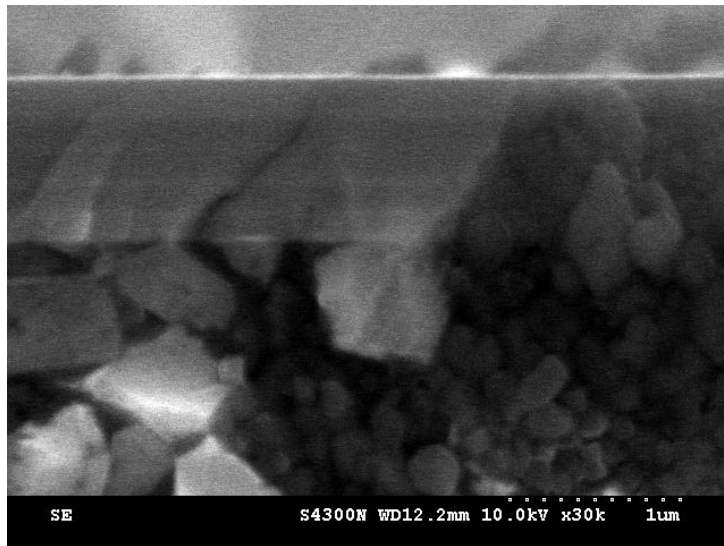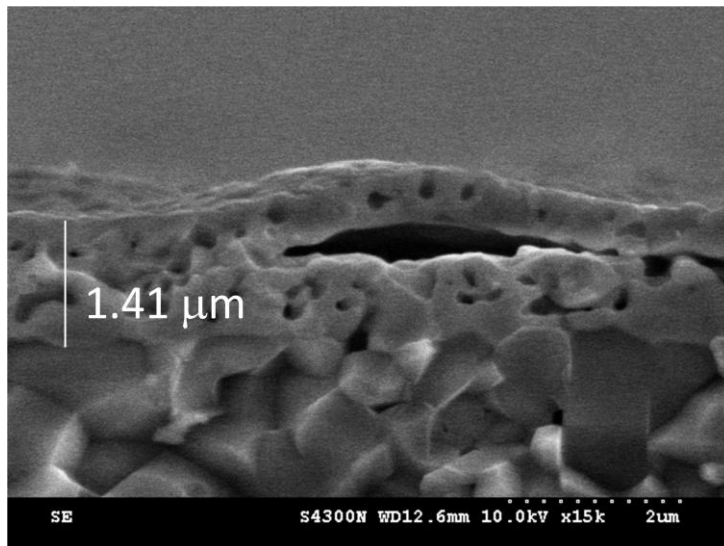
b.

Figure 15. SEM images of (a) as-deposited and (b) annealed films on an alumina

substrate.

~1 μm to 1.41 μm but there appears to be less diffusion between the film and alumina substrate. XRD spectra were measured at five locations along the Lu_2O_3-SiO_2 gradient on alumina substrate; at 1cm, 3cm, 5cm, 7cm, and 9cm from the Lu_2O_3 rich end of the film. The XRD spectra at each position across the Lu_2O_3-SiO_2 gradient are plotted in figure 16; the phases present are labeled with patterned/colored vertical lines identified in the legend. XRD peaks for the Lu_2O_3 ((400) peak), Lu_2SiO_5 (LSO, (-402) peak), and $Lu_2Si_2O_7$ (LPS, (110) peak) compounds present in the Lu_2O_3-SiO_2 material system are plotted in figure 17a along with integrated intensities of the peaks plotted in figure 17b to give a more straight forward presentation of the compounds present at each position. By comparing the peak locations and the ratio of the peak heights of the various phases, the composition was estimated at the five locations along the substrate. Figure 18 shows the estimated compositions for positions 1, 3, 5, 7, 9 (based on Lu_2O_3 substituted for Yb_2O_3 in the known Yb_2O_3-SiO_2 phase diagram [30]).

XRD results also showed the presence of $Al_5Lu_3O_{12}$ (LuAG) peaks (figure 16) suggesting some degree of film-substrate diffusion. To investigate potential film-substrate diffusion further cross-sectional backscatter-electron and cathodoluminescence imaging was performed and is shown in figures 19a and 19b. The significance of these images is presented in the discussion.

Photoluminescence measurements were taken at 2 cm, 4 cm, 6 cm, and 8 cm from the Lu_2O_3 rich end of the substrate. The excitation (420 nm emission wavelength) and
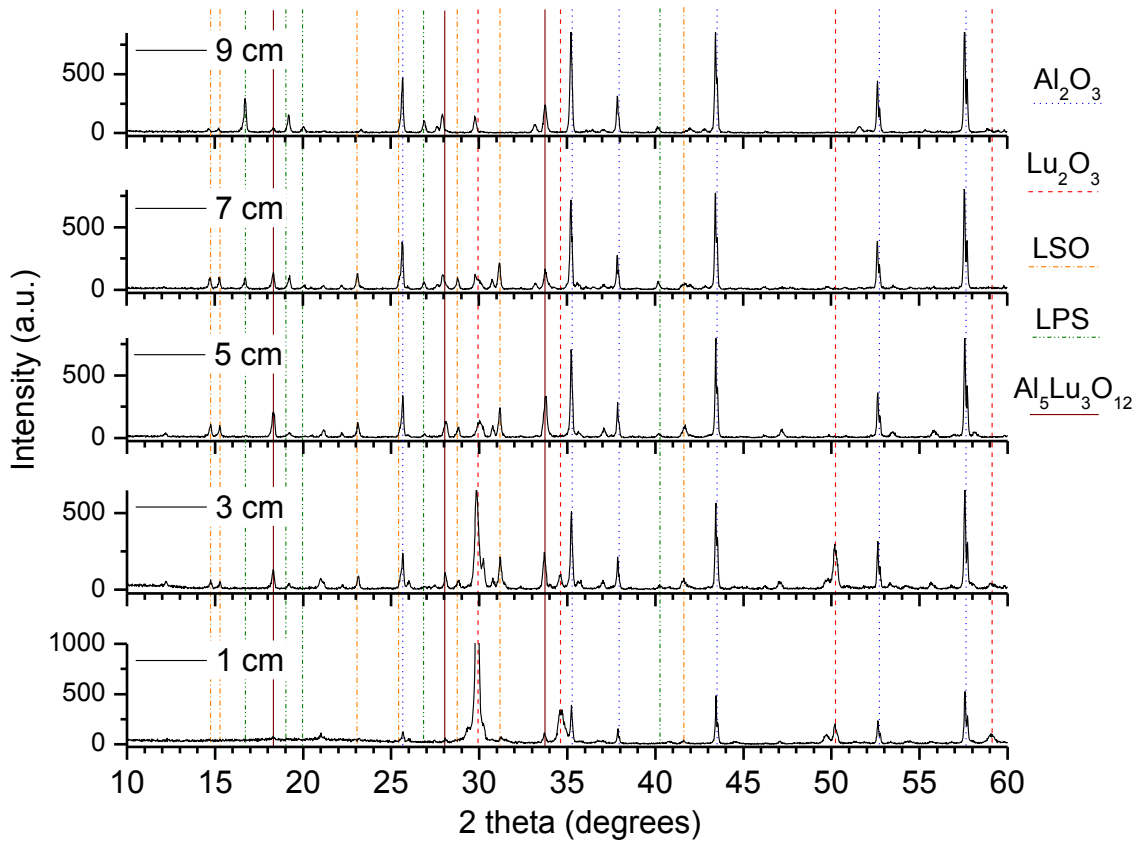
Figure 16. Labeled XRD spectra at positions across the Lu_2O_3-SiO_2 gradient.
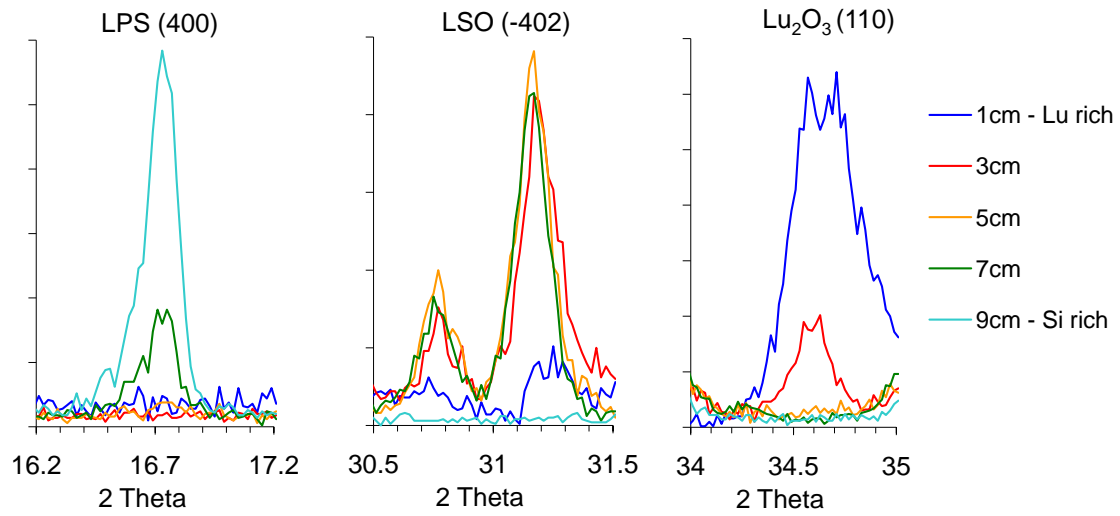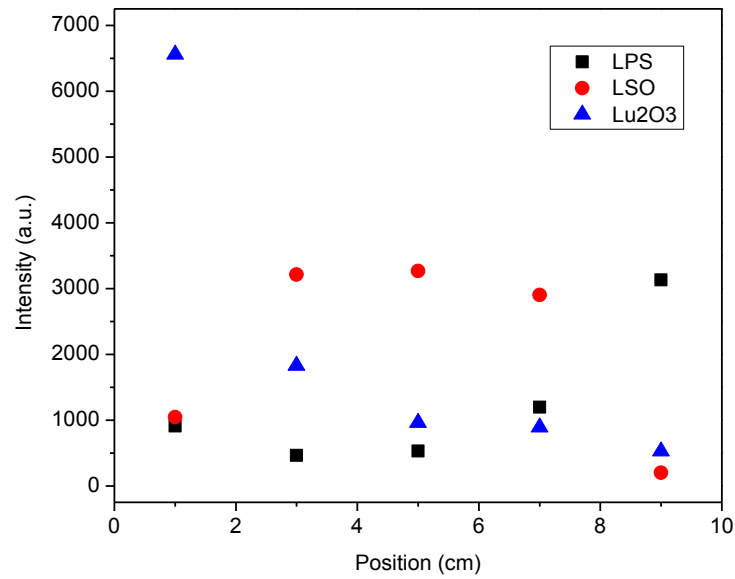
Figure 17. LPS, LSO and Lu_2O_3 (a) XRD spectra and (b) integrated intensities.
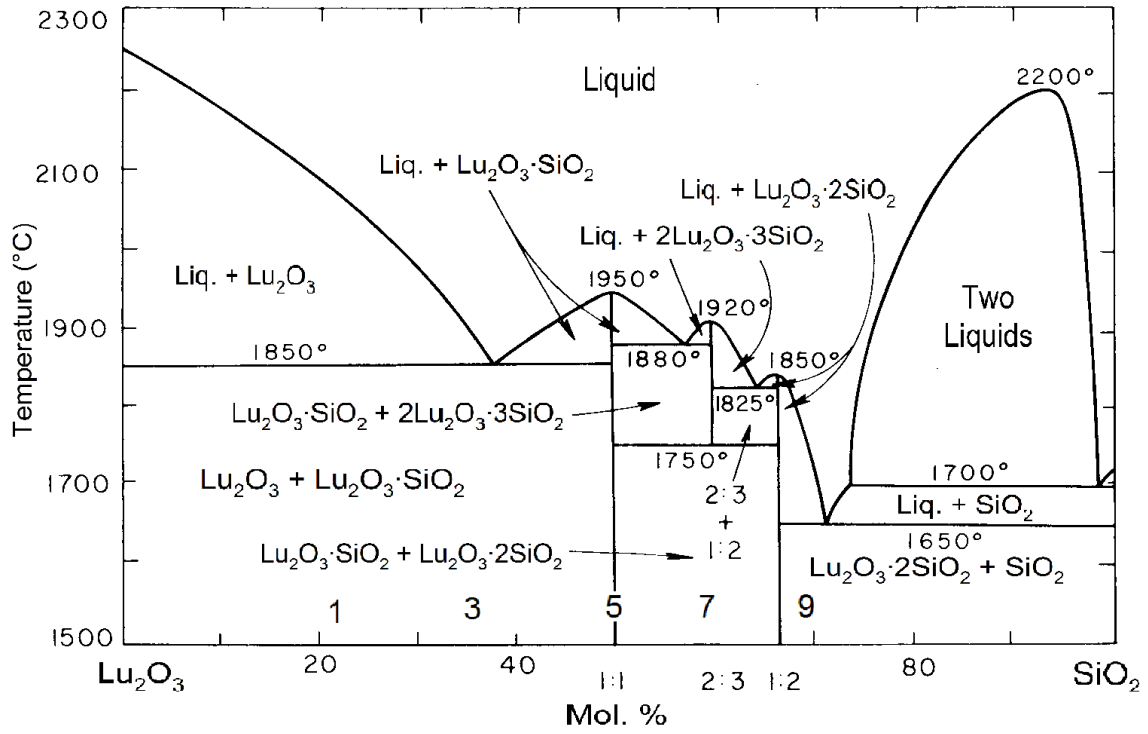
Figure 18. Estimated compositions for positions 1, 3, 5, 7, 9 based on Lu_2O_3 substituted for the known Yb_2O_3-SiO_2 phase diagram.

Yb_2O_3-SiO_2 phase diagram [30].
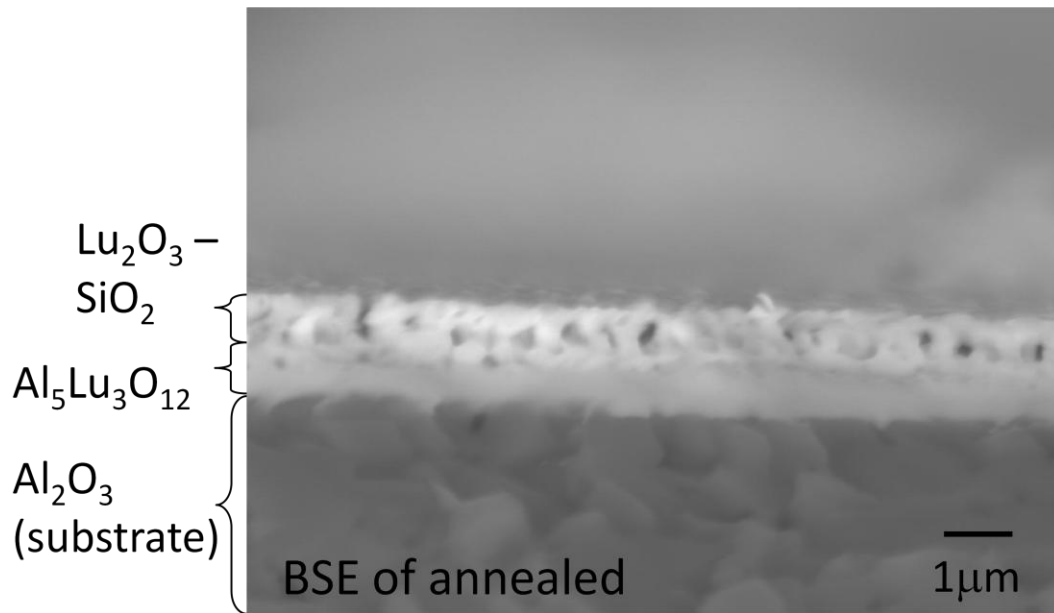
a.
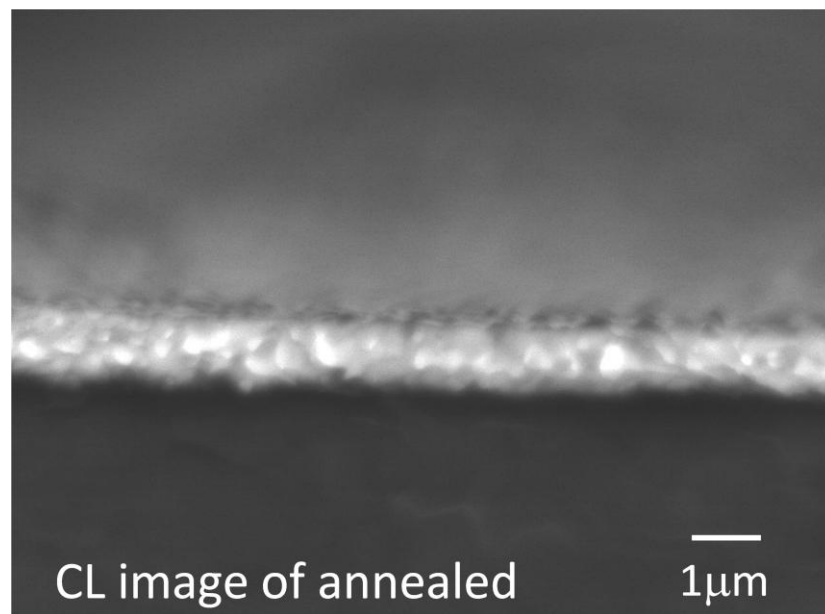
b.

Figure 19. (a) Backscatter-electron and (b) CL images of annealed Lu_2O_3-SiO_2 film on alumina substrate.

emission spectra (360 nm excitation wavelength) of single crystal LSO are plotted in figure 20a for comparison. Figure 20b shows the excitation (400 nm emission wavelength) and emission spectra (357 nm excitation wavelength) at the four positions along the sample. Figure 20c plots the integrated emission intensity at each position. Position 4 cm which has the highest LSO concentration (mixed with a small amount of Lu_2O_3) was found to exhibit the highest photoluminescence intensity.

X-ray excited emission (radioluminescence) measurements of the Lu_2O_3-SiO_2 gradient on alumina substrate were taken at 1 cm, 3 cm, 4 cm, 6cm, 7 cm, and 9 cm. Selected spectra (for clarity) are plotted in figure 21a. Integrated emission intensity from 370 nm to 500 nm are plotted in figure 21b. The background spectra of the alumina substrate is plotted along with the spectra measured at position 4 cm for comparison in figure 21c. A large portion of the emission is from the alumina substrate itself, but characteristic cerium doped LSO emission at 400 nm is also present. As with photoluminescence emission, position 4 cm exhibited the highest emission intensity.

Discussion

The annealed film thickness on an alumina substrate increased from 0.96 μm to 1.41 μm. Some of the increase in thickness can be attributed to the creation of voids in the film. However, the backscattered-electron image in figure 19a reveals the presence of a reaction or interdiffusion layer between the film and the Al_2O_3 substrate. Additionally,

49
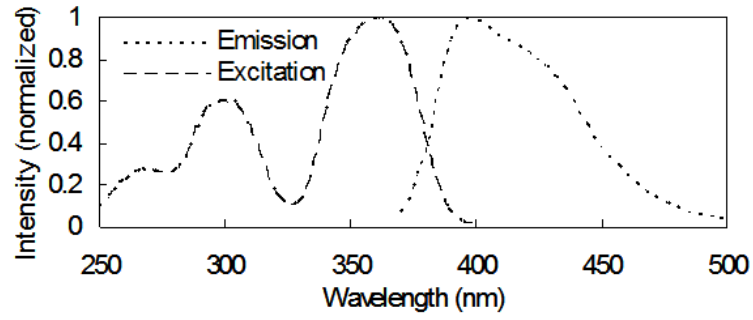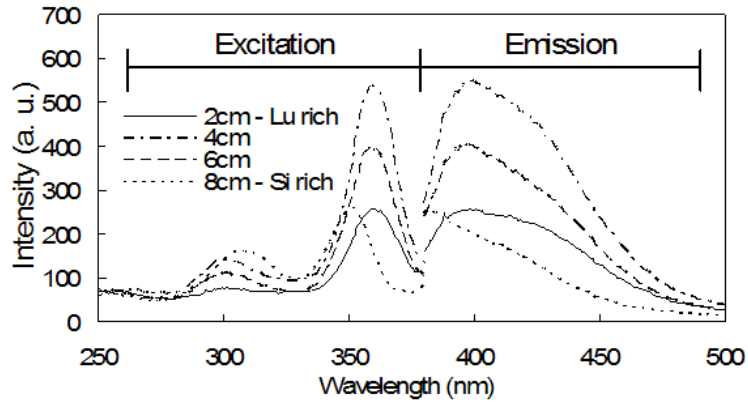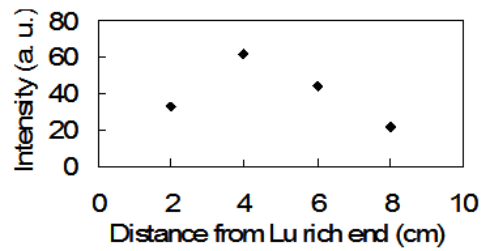
Figure 20. Photoluminescence results for (a) single crystal LSO and (b, c) Lu_2O_3-SiO_2 gradient thin film.
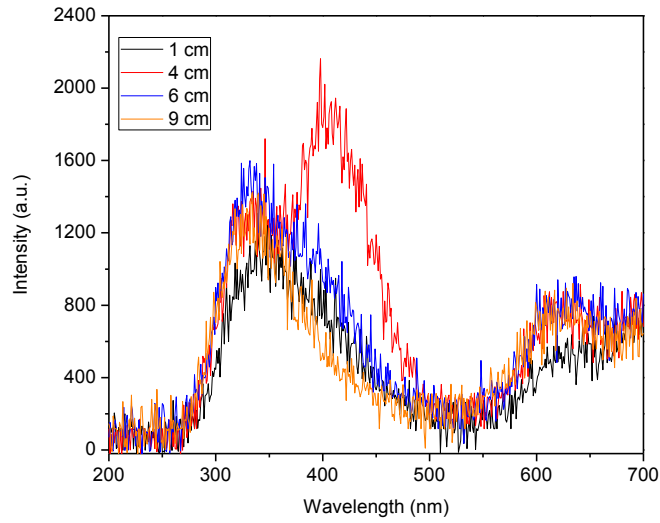
a.
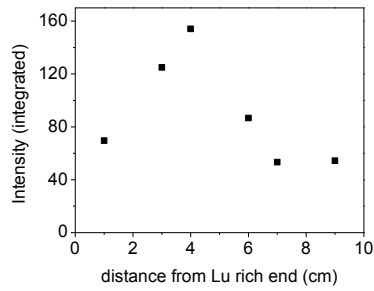
b.
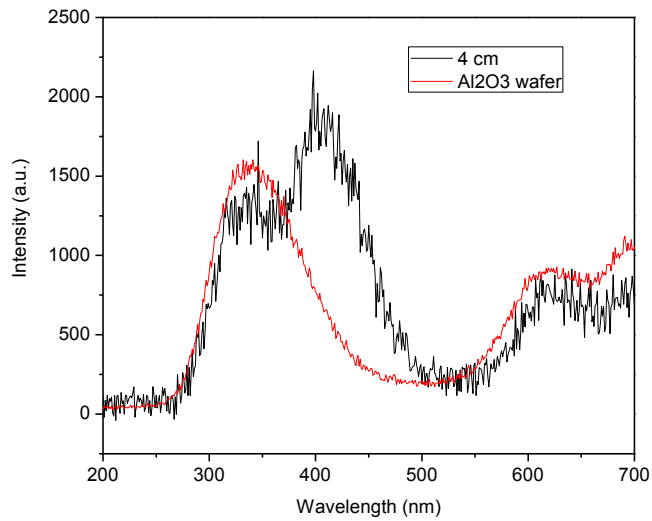
c.

Figure 21. Radioluminescence results for Lu_2O_3-SiO_2 gradient thin film.

the XRD spectra revealed the presence of LuAG. The LuAG is attributed to reaction or interdiffusion with the Al_2O_3 substrate and is labeled as such in figure 19a. Importantly, the cathodoluminescence image in figure 19b shows the diffusion layer does not exhibit luminescence for the present level of cerium concentration (~0.3 at%). The effects of higher cerium concentrations on LSO:Ce thin films are investigated in chapter 5. Rack, et al. [28] extensively characterized LSO:Ce thin films on alumina substrates with cross-sectional X-ray energy dispersive spectroscopy (EDS); the results confirmed diffusion between the substrate and the film seen in the Lu_2O_3-SiO_2 gradient film and additionally showed diffusion was limited to the film-substrate interface.

Delamination of the film after annealing was observed and is attributed to differences in the coefficient of thermal expansion between the film and the substrate. However, film delamination has been shown to increase photoluminescence intensity as it enhances light scattering otherwise inhibited by internal reflection of the light produced in the film [8]

LSO exhibits photoluminescence excitation peaks at 265 nm, 300 nm and 360 nm, LPS has excitation peaks at 300 nm and 350 nm and Lu_2O_3 does not exhibit cerium luminescence. The excitation spectra in figure 20b follow the peak positions expected by the composition positions in the phase diagram in figure 18. Position 2 cm is dominated by the non-luminescent Lu_2O_3 phase with only a small amount of LSO and correspondingly shows week luminescence. Position 8 cm is dominated by LPS and shows a shift in the excitation spectrum towards 350 nm. Positions 4 cm and 6 cm with

higher LSO compositions show more intense excitation spectra with the main peak centered at 360 nm.

The radioluminescence results showed a similar intensity trend compared to the photoluminescence results. However, the radioluminescence emission is complicated by the alumina substrate background emission. As seen in figure 21c, the alumina substrate exhibits a broad emission band centered are 340 nm. It is possible that this emission is exciting the cerium doped LSO and LPS phases (excitation peaks at 350 nm and 360 nm, respectively) present in the thin film. It cannot be conclusively stated that the film emission is due to X-ray excitation.

Conclusion

The thin film combinatorial technique successfully screened the binary Lu_2O_3-SiO_2 material system, identified the phases present and correlated the phases to the exhibited luminescence spectra. There are numerous physical differences between thin film and single crystal bulk samples, namely the morphology and sample thickness, however the thin film photoluminescence spectra matched the single crystal spectra. Additionally, emission intensity for the LSO and LPS phases were in line with expectations based on single crystal behavior. Ultimately, the photoluminescence provided an accurate comparison and proved to be a valuable metric. XRD of the thin film also showed good results and clearly followed the expected phase diagram. The

combination of XRD and photoluminescence can be employed to rapidly and successfully screen combinatorial thin film scintillation material libraries.

SEM imaging is not directly required for screening scintillation material systems, but it is helpful to confirm as deposited thickness (and therefore help confirm composition) and morphology of annealed samples. Photoluminescence and XRD are invaluable at each measurement location; SEM imaging can be employed on an as-needed basis, which will increase the speed of the screening process.

The work by Deng, et al. and Fowlkes, et al. was performed using silicon substrates, however their post deposition annealing was conducted below 900 °C. The higher annealing temperature required by an inorganic, oxide-based scintillator requires a substrate able to withstand higher annealing temperatures. The alumina substrates are an improvement compared to silicon substrates, but a more robust substrate would be ideal. Additionally, an alternative substrate may simplify radioluminescence characterization, increasing its value as a useful metric.

The thin film combinatorial screening technique exhibits promise for rapidly synthesizing and characterizing scintillator libraries. The successful screening of a binary system, by extension, suggests the technique would prove beneficial in screening solid solutions, such as $(Lu_{1-x}Y_x)_2SiO_5$, or ternary material systems, such as Lu_2O_3-SiO_2-Al_2O_3, which is the topic of chapter 5.

CHAPTER III
ACTIVATOR CONCENTRATION IN A SINGLE CRYSTAL

The photoluminescent intensity, the relative light output and the low temperature photoluminescence spectra as a function of cerium concentration have been published previously in a condensed form by Philip Rack, Charles Melcher, and myself [31]. Of the work presented in this chapter Charles Feigerle helped perform the Raman shift measurements, Merry Koschan grew the selected cerium doped LSO single crystals; Philip Rack and Charles Melcher provided direction, funding of the research, discussion and motivation.

Introduction

The thin film combinatorial screening technique was applied to binary material systems in chapter 2. The next goal is to apply the technique to optimize activator concentration in a known scintillator. To do this, cerium doped LSO was chosen because of the successful screening of the $Lu_2O_3 - SiO_2$ material system in chapter 2 and because cerium doped single crystal LSO has been widely characterized.

At the onset of the work covered in this dissertation its scope was not intended to include characterization of single crystal samples, but rather to focus on the cerium concentration dependent behavior of thin film LSO. As work progressed on the cerium doped LSO thin films, it became apparent that to properly understand the observed

behavior a thorough understanding of the concentration dependent behavior of single crystal LSO was required. Surprising little work [12] had been conducted on this aspect of single crystal LSO necessitating the work covered in this chapter.

In this chapter single crystal LSO samples with a range of cerium concentrations are investigated. The effect of cerium on the excitation and emission line shapes, temperature quenching behavior and decay times are explored. Temperature dependent photoluminescence measurements were used to measure the electron-phonon coupling and calculate the configuration coordinate diagram of the cerium site. Additionally, Raman shift measurements were made to correlate the electron-phonon coupling values to the phonon values of the host LSO crystal.

Background

LSO is in the group of oxyorthosilicates $RE_2(SiO_4)O$ (RE = rare earth) that exhibits two different monoclinic structures. Oxyorthosilicates with the smaller rare earth elements, Dy to Lu (including LSO) have the monoclinic structure of space group C2/c with two distinct RE sites with oxygen coordination numbers of 6 and 7 [32]. The larger rare earths, La to Tb (including Ce) form the monoclinic structure of space group $P2_1/c$.[33]. The trivalent Ce activator substitutes in the Lu^{3+} sites [11] and both sites are likely occupied which have similar crystal field splitting. The convolution of the two sites has been attributed to the single broad peak observed at room temperature instead of the

characteristic double peak associated with the spin orbit splitting of the 4f levels. Additional broadening observed at higher concentrations has been associated with defect-mediated sites (i.e. vacancies) as well as interstitial sites [12]. LSO has a high density of 7.34 g/cm^3 and exhibits a fast decay time of ~40ns with a 28,000 photons/MeV light output for 512KeV gamma ray excitation.

At low temperature LSO exhibits two distinct excitation and emission spectra that have been designated Ce1 and Ce2 [10]. The emission spectrum shows peaks at 400 and 420 nm with excitation peaks at 265 nm, 300 nm and 360 nm. A less intense set of peaks is observed with an emission at peak at 460 nm (with a distinct shoulder) and excitation at 324 nm and 373 nm.

Emission Probability

In chapter 1 the concept of spontaneous absorption and emission was introduced. However, the rate of these transitions was not elaborated. A first order rate of emission (after a short pulse of incident radiation) is governed by:

$$\frac{dN_e}{dt} = -N_e P_{eg} \quad (3.1)$$

where N_e is the number of luminescent ions in the excitation state, *t* is time, and P_{eg} is the probability for spontaneous emission from the excited to the ground state. Theoretical calculation of the spontaneous emission probability, P_{eg}, can be found elsewhere [34]. The critical aspect is P_{eg} is independent of temperature. Integrating equation (3.1) yields:

$$N_e(t) = N_e(0)e^{-P_{eg}t} \quad (3.2)$$

Which is commonly written as:

$$N_e(t) = N_e(0)e^{-t/\tau_R} \quad (3.3)$$

where $\tau_R = P_{eg}^{-1}$ and is the radiative decay time (or lifetime). This relation also holds for excitation by ionizing radiation (although due to additional mechanisms, outlined in equation (1.4), the decay time value may not be the same as the photo excited value). Decay profiles with multiple decay times are possible, but generally the decay time constants in fits with more than three components have untraceable physical meaning. For a one component decay, the population of the excited state decreases to $1/e$ after time τ_R. The decay profile of LSO with 0.095 at% cerium at 26 K along with a least-squares fit of equation (3.3) is plotted as an example in figure 22. The value of $\tau_R = 32.9$ ns is essentially the intrinsic decay time of cerium for 400 nm emission. For cerium, it can be derived that the intrinsic decay time for a specific transition is proportional to the emission wavelength as $\tau \sim \lambda^2$ [35]. While the radiative decay time is temperature independent, a decrease in measured decay time values at elevated temperature is commonly seen due to an increase in the non-radiative recombination rate and a corresponding decrease in the luminescence efficiency.

Temperature quenching

Luminescence efficiency is dependent on the radiative and non-radiative recombination rates as described by:

$$\eta(T) = \frac{I(T)}{I(0)} = \frac{W_R}{W_R + W_{NR}} = \frac{\tau(T)}{\tau_R} \quad (3.4)$$

58
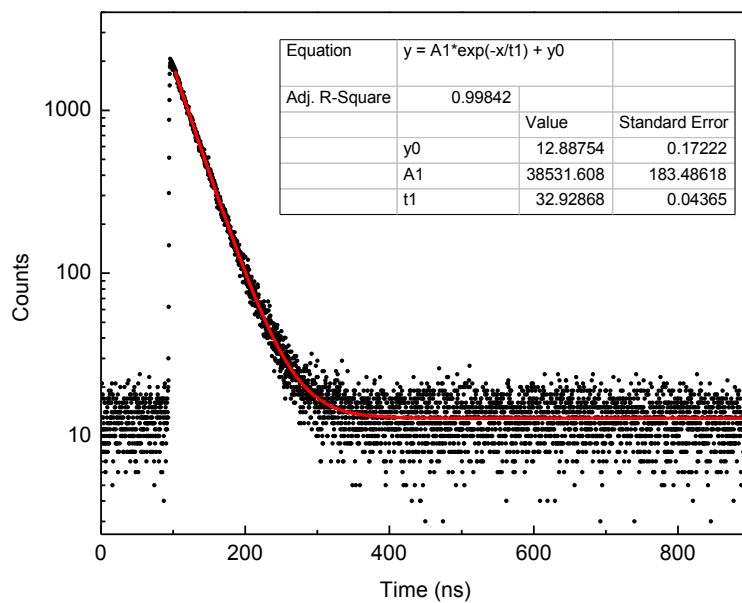
Figure 22. Photoluminescence decay profile for LSO with 0.095 at% cerium (S-51) with fit of equation (3.3).

where $\eta(T)$ is the luminescence efficiency at temperature T, W_R and W_{NR} are the radiative and non-radiative recombination rates. $I(T)$ is the intensity at temperature T, $I(0)$ is the intensity when W_{NR} is close to zero (at low temperature). Because the radiative rate is related to the spontaneous emission probability (P_{eg}), the radiative rate is temperature independent and proportional to the inverse of the radiative lifetime (τ_R). Hence, the decay time as a function of temperature, $\tau(T)$, can be used to calculate the luminescence efficiency (assuming $\tau(T)$ is not increased by energy transfer or traps that increase its observed value). The non-radiative recombination rate follows an Arrhenius relationship:

$$W_{NR}(T) = W(0)\exp\left(\frac{-E_a}{k_b T}\right) \quad (3.5)$$

where T is temperature, E_a is the activation energy, k_b is the Boltzmann constant and $W(0)$ is a constant on the order of the vibrational frequency of the host lattice. Solving for $I(T)$ yields:

$$I(T) = \frac{I(0)}{1+A exp\left(\frac{-E_a}{k_b T}\right)} \quad (3.6)$$

where

$$A = \frac{W(0)}{W_R} \quad (3.7)$$

Fitting equation (3.6) to the integrated emission intensity versus temperature yields the thermal activation energy, E_a, which potentially gives insight into the nature of the non-radiative pathway.

Experimental procedure

Cerium concentrations in single crystal LSO

Three single crystal samples (grown at the Scintillation Materials Research Center) with a wide composition range were measured. For photoluminescence and Raman shift measurements, three 5 mm single crystal LSO cubes were cut from boules grown via the Czochralski technique with cerium concentrations in the melt of 0.02, 0.1 and 1.0% Ce relative to Lu (equivalent atomic concentrations 0.005, 0.025 and 0.25%, respectively). For absorption measurements 10 mm square by 1 mm thick samples were cut from the same vertical locations (along the growth axis) of the boule and polished. While dopant concentrations in crystal growth are commonly stated relative to the ion they replace in the crystal (e.g., Lu in LSO), from this point forward all concentrations are reported as a percent of the total number of atoms (at%). The atomic percent (at%) cerium in the samples measured were calculated based on the reported distribution coefficient of 0.22 for cerium in LSO [36] following:

$$C_S = C_0 k (1 - g)^{(k-1)} \quad (3.8)$$

where C_0 is the concentration in the melt, C_S is the concentration in the crystal, k is the distribution coefficient and g is the fraction of melt grown. A curve calculated for a cerium concentration of 0.1 % of lutetium sites in the melt is plotted in figure 23 and the cerium concentrations of the samples are summarized in table 3.
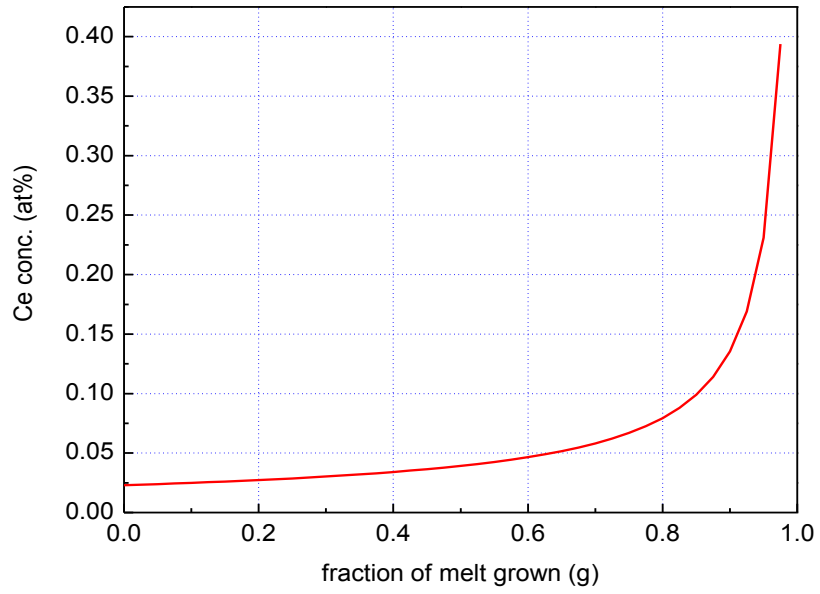
Figure 23. Cerium concentration as a function of melt grown.

Table 3. Cerium concentrations of single crystal samples.

Sample	Ce in melt (% of Lu sites)	Ce in crystal (at %)
S-74	0.02	0.0015
S-51	0.1	0.0095
S-75	1	0.078

Characterization

Room temperature photoluminescence emission and excitation spectra were measured using a Hitachi F-4500 spectrophotometer at a scan rate of 240 nm/min. The photomultiplier tube voltage along with the excitation slit and emission slit were uniform for all measurements. Temperature dependent steady-state photoluminescence emission and excitation spectra were measured using a Horiba Jobin Yvon Flouralog-3 Spectrofluorometer. Photoluminescence life-time measurements were made with the addition of an R-928 hub and NanoLED excitation sources with time-correlated single photon counting capability. The NanoLED excitation sources are wavelength specific with Gaussian shaped emission profiles centered at the stated wavelength of the source with a half-width half-max of roughly 10 nm. The NanoLED sources can be mounted directly to the sample chamber or to the excitation monochromator. For all of the life-time measurements the NanoLED sources were mounted to the excitation monochromator. Temperature dependent stead-state and life-time photoluminescence measurements were made using an ARS model CS202 cryostat integrated with the Horiba spectrophotometer and a Lake Shore 331-S temperature controller. Room temperature absorption measurements were measured using a Carrie 5000 spectrophotometer with the spectra corrected/normalized to a sample thickness of 1 mm. Relative light output measurements of the single crystals were made using a Hamamatsu model R877 photomultiplier tube with a loose fitting Teflon cap to increase light collection. Samples were placed directly on the

photomultiplier tube and excited with 662 keV gamma rays from a 10 μCi ^{137}Cs source. Raman shift measurements were performed using a Horiba Jobin-Yvon T64000 Raman spectrometer with excitation by an unpolarized 514.5 nm laser.

Results

Photoluminescence

Normalized excitation (397 nm emission) and emission (357 nm excitation) spectra measured at 40 K are plotted in figure 24. An increase in the intensity of the two high energy peaks (265 nm and 300 nm) relative to the lower energy excitation peak and broadening of the low energy excitation peak are observed with increasing cerium concentration. The emission peak profile is similar over the cerium composition range. Excitation at 265 nm and 300 nm exhibit similar line profiles compared to 357 nm excitation, albeit at lower intensity. Excitation and emission spectra for cerium concentrations of 0.0015 at% (S-74) and 0.078% (S-75) at 200 K at wavelengths selected to exhibit Ce1 and Ce2 [10] are plotted in figure 25a and b (additional relevant plots in figures A-1 to A-3 of the appendix). At low temperature (figure 24), there is very little overlap between the excitation and emission. However, as the temperature is raised, temperature induced homogeneous broadening occurs and spectral overlap increases. Additionally, the degree of overlap increases with increasing cerium concentration. Ce1 emission overlaps the excitation spectra of Ce1 and Ce2 suggesting some degree of

65
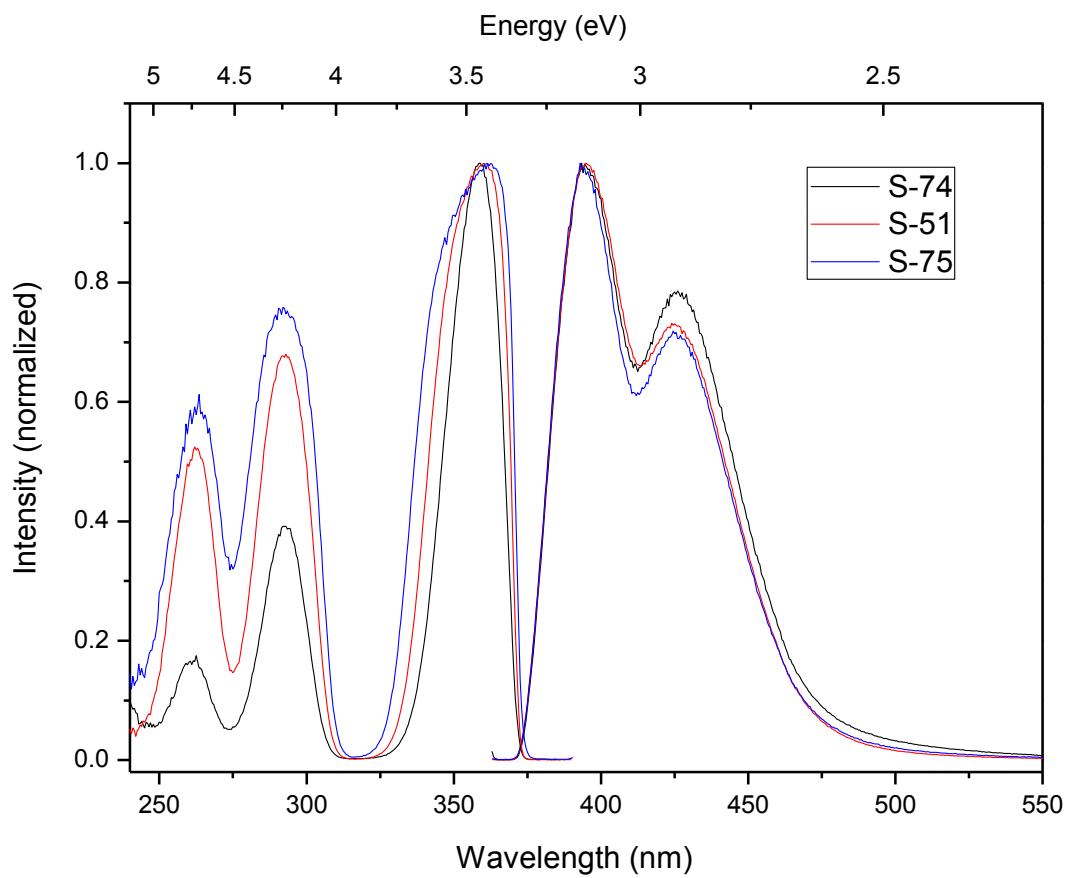
Figure 24. Normalized excitation (397 nm emission) and emission (357 nm excitation) PL line spectra at 40K.
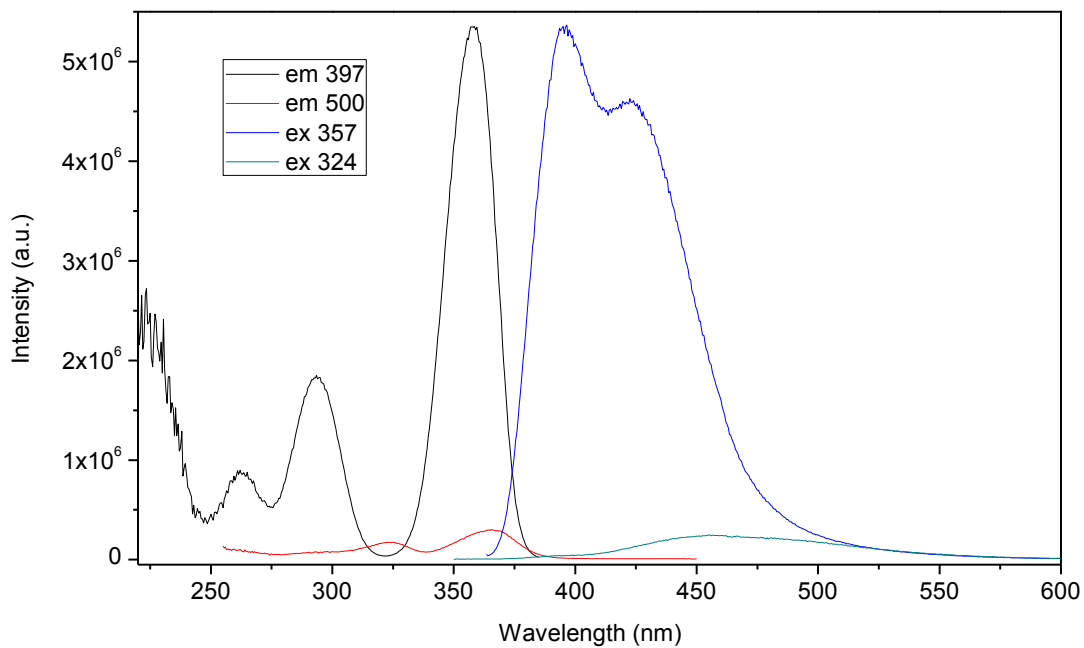
a.
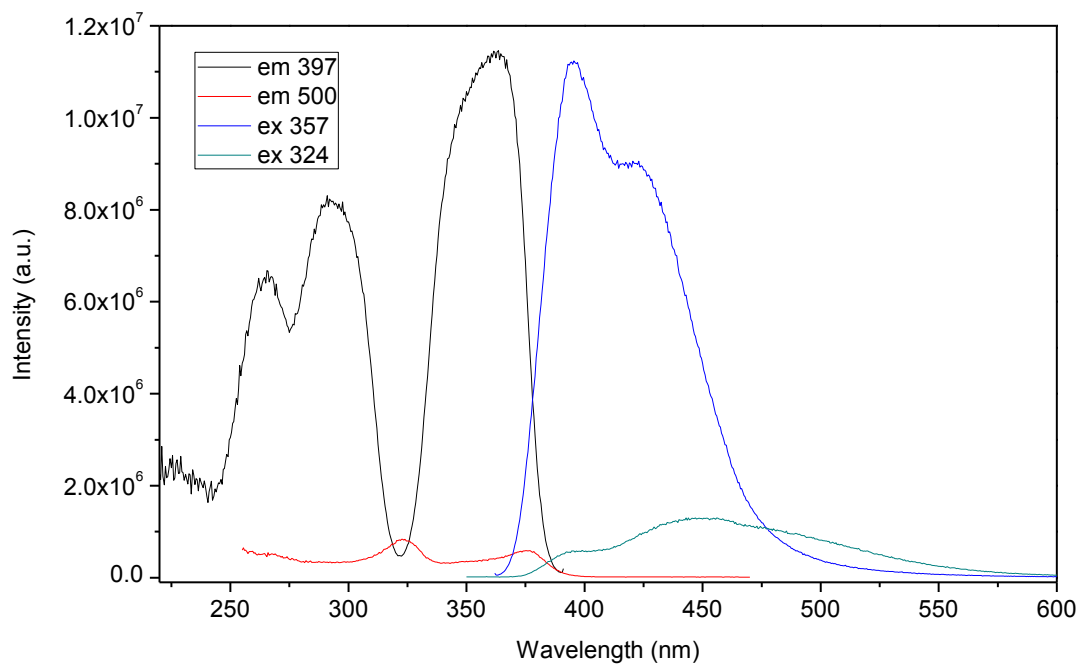
b.

Figure 25. Ce1 and Ce2 emission and excitation spectra at 200 K for (a) low and (b) higher cerium single crystal samples.

radiative Ce1 to Ce1 and Ce1 to Ce2 energy transfer. The absorbance spectra of the three samples are plotted in figure 26. The absorbance is related to the transmittance by:

$$A_{abs} = \log_{10} T = \log_{10}\left(\frac{I}{I_0}\right) \quad (3.9)$$

where A is the absorbance, T is the transmittance and I_0 and I are the intensity of light before and after passing through the material, respectively. The full-width at half-max of the peaks for low (S-74) and medium (S-51) cerium samples do not appear to be broadening relative to one another, but there is a dramatic increase in the percent absorbance of incident light with increasing cerium concentration.

The photoluminescence decay time constants at 360 nm excitation and 400 nm emission for high and low cerium samples versus temperature are plotted in figure 27. The time constants for the 0.095 at% cerium (S-51) sample lie between the high and low concentrations (not shown in figure 27 for clarity, but included in figure A-4 of the appendix). The time constant at 29 K for all of the samples was close to the intrinsic cerium lifetime for 400 nm emission. The time constant increases with temperature up to 240 K; this increase is indicative of energy transfer. Additionally, the increase is larger for higher cerium concentrations, which corresponds with the observed increase in the spectral overlap seen in figure 25a. At room temperature, quenching and a corresponding increase in the non-radiative decay rate (W_{NR}) noticeably shortens the decay time. For the mid and high cerium samples the room-temperature decay is once
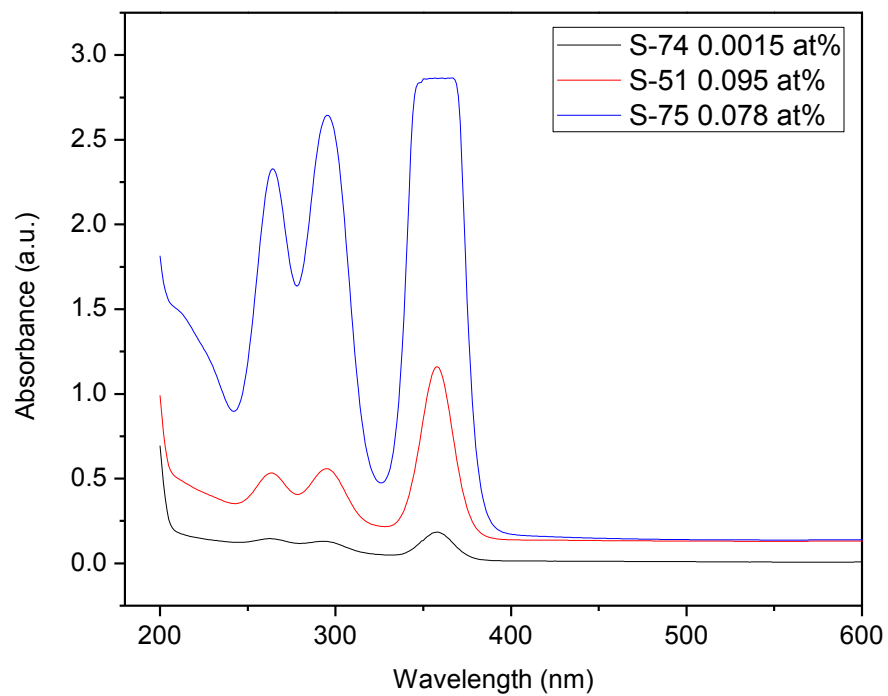
Figure 26. Absorbance spectra for the three single crystal samples.
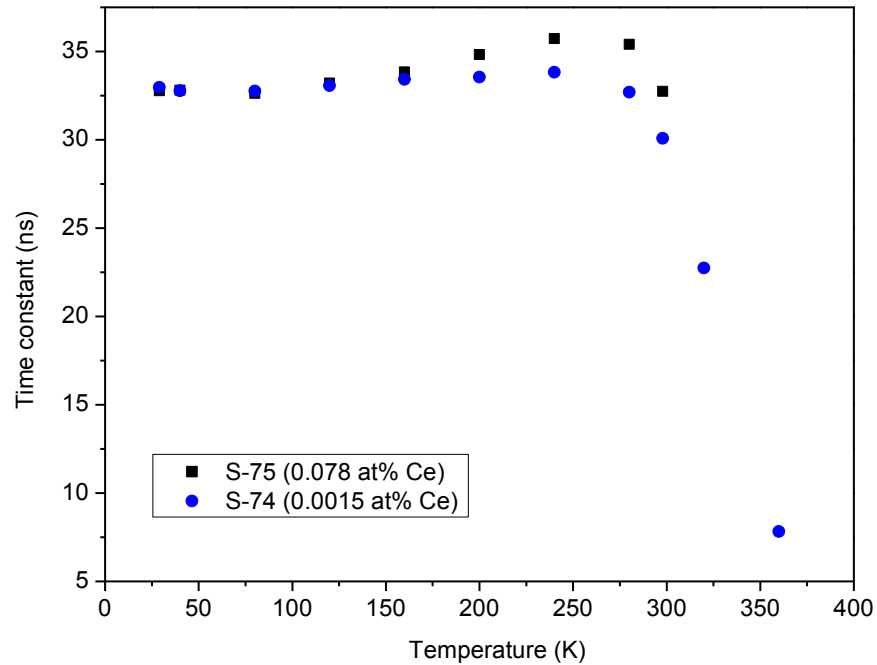
Figure 27. Photoluminescence decay time constants plotted versus temperature.

again (perhaps coincidently) close to the intrinsic lifetime value. The Ce2 emission spectra does not overlap the Ce1 nor the Ce2 excitation spectra, so radiative Ce2 to Ce1 or Ce2 to Ce2 transfer is not possible. However, the possibility of non-radiative Ce2 to Ce1 energy transfer still remains. The emission spectra for 324 nm excitation for the middle cerium concentration sample (S-51) at selected temperatures between 40 K and 600 K is presented in figure 28. Upon initial inspection the observed shift from Ce2 to Ce1 emission wavelengths is suggestive of energy transfer, but this shift could also be caused by Ce2 temperature quenching and temperature dependent homogenous broadening of the Ce1 excitation spectrum. The nature of the peak shift was investigated by comparing the integrated emission intensity between 390-395 nm (mostly Ce1 emission) for 324 nm excitation to the integrated intensity between 322-324 nm for the Ce1 excitation spectrum (397 nm emission). The results are plotted in figure 29. The two curves are nearly identical suggesting the shift observed in figure 28 is due to broadening of the Ce1 excitation spectrum and subsequently direct excitation of the Ce1 site rather than Ce2 to Ce1 energy transfer. Similar results were also seen for 373 nm excitation and for the low and high cerium samples.

Mao, et. al. [37] investigated the effect of excitation energy (γ-ray, x-ray and ultraviolet) and incident angle on the emission spectra of LSO and LYSO (among others). For LSO, they found that PL measured with an incident excitation angle of 80° showed less internal absorption of the emission spectra (thus, less radiative energy transfer) versus a geometry that excited one side of the sample and measured emission from a side at
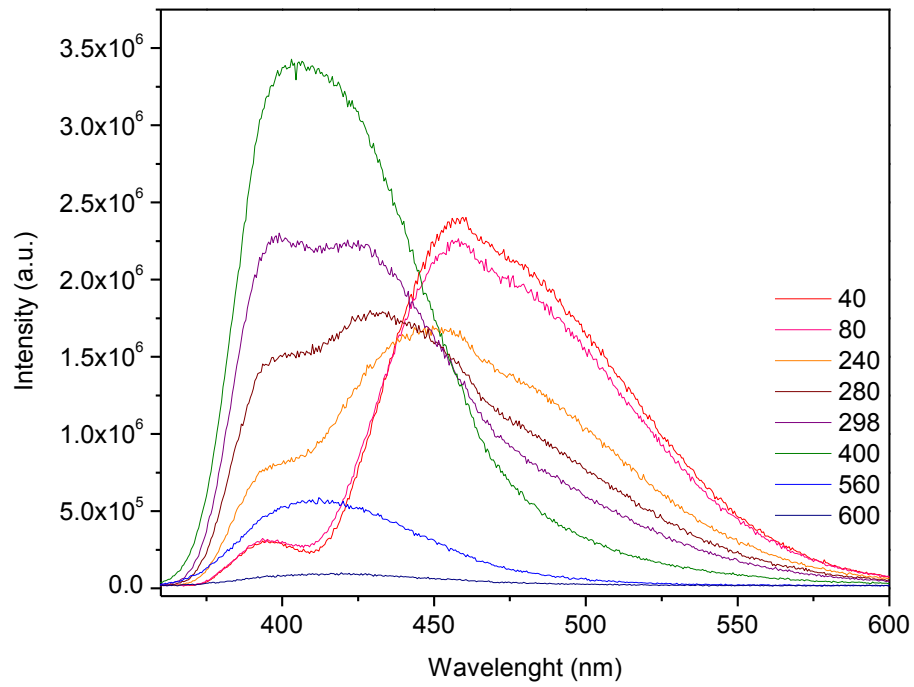
Figure 28. Photoluminescence Ce2 emission spectra (324 nm excitation) for selected temperatures for the middle cerium concentration sample (S-51).
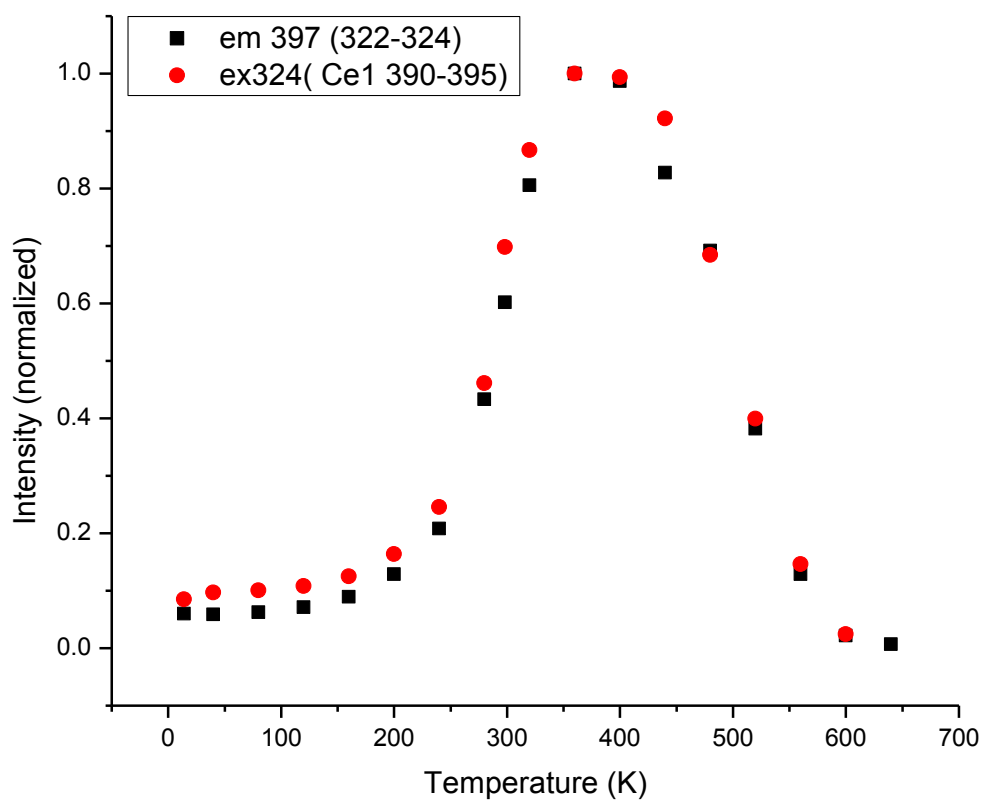
Figure 29. Integrated intensity between 390-395 nm (mostly Ce1 emission) for emission at 324 nm excitation and integrated intensity between 322-324 nm for the Ce1 excitation spectrum (397 nm emission).

90°, which showed a red shifted emission with a profile similar to γ-ray and x-ray excitation. The decrease in high energy emission was attributed to self-absorption and an increase in lower energy emission was attributed to Ce2 emission. Furthermore, irradiating the sample for an extended period of time decreased the Ce2 emission, which they suggested implies Ce2 emission is defect related.

Emission for x-ray excitation (radioluminescence, or RL), 190 nm and 360 nm excitation at different cerium concentrations are plotted in figure 30. In PL with an incident angle of 60° at ~360 nm excitation we see Ce1 dominated emission with little, if any, Ce2 emission. In PL with an incident angle of 60°at 323 nm excitation (in figure 25) Ce1 and Ce2 emission is observed, the Ce1 emission increases with temperature (up to ~ 400 K, figure 28) due to temperature induced homogeneous broadening of the Ce1 excitation spectra. In PL with an incident angle of 60° at ~190 nm excitation (exciting to the CB of LSO) of the high cerium sample (figure 30) emission with Ce1 and Ce2 components is observed. X-ray excitation of low cerium LSO exhibits emission similar to 357 nm excitation with little, if any, Ce2 component. The higher cerium samples show red shifted emission and significant Ce2 contribution. These cerium dependent observations, along with Mao, et al's [37] angle dependent results, give a good understanding of room temperature emission in single crystal LSO:Ce. At very low cerium concentrations there is little self-absorption and little Ce2 preset, hence x-ray excited emission is very close to UV excited emission. At higher cerium concentrations self-absorption increases along with Ce2 emission. This is not conveyed in PL emission
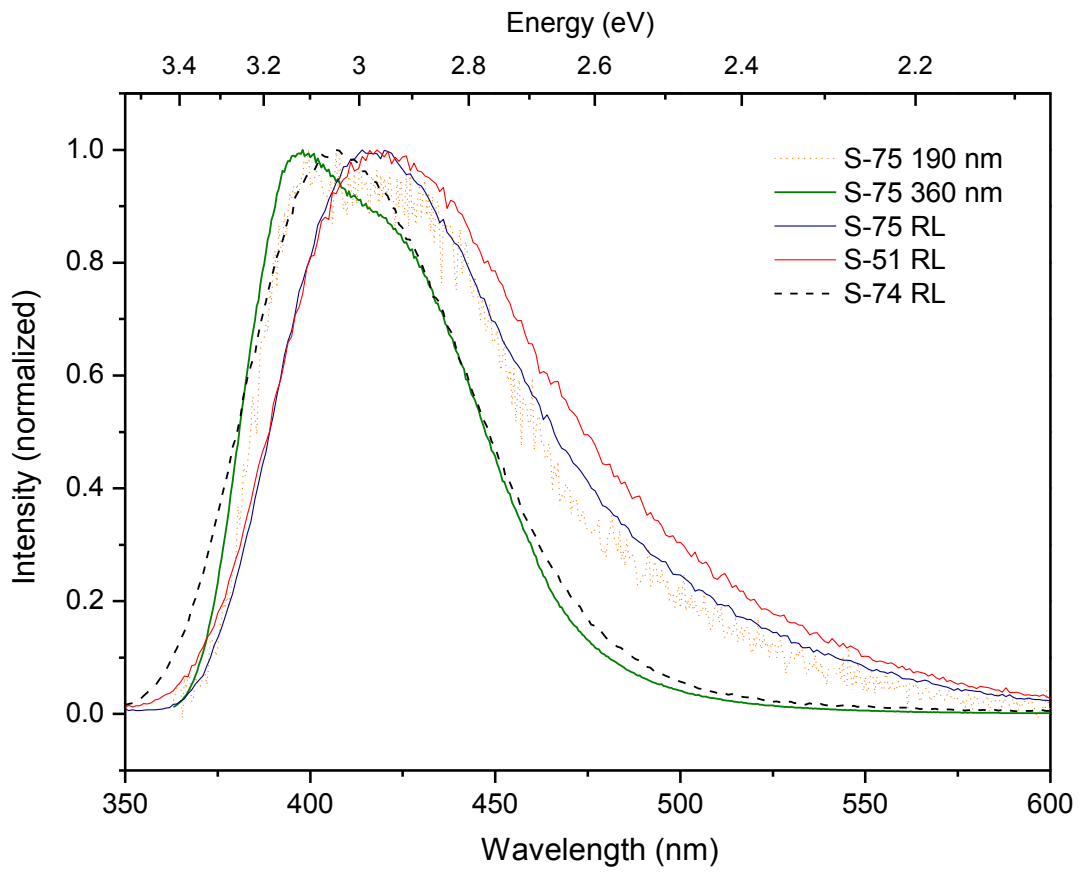
Figure 30. Emission spectra for different excitation sources.

with an incident angle of 60° at ~360 nm excitation because there is very little self-absorption and the Ce2 is not excited directly, but an increase in Ce2 emission at low temperature is observed with increasing cerium. The low self-absorption also explains the relatively small increase in the decay time seen in figure 27. At 190 nm excitation the Ce1 and Ce2 is excited but there is very little self-absorption giving an emission that resembles a combination of 360 nm excitation and x-ray excitation.

Integrated emission intensity (357 nm excitation) and relative light output (Cs^{137} source) versus cerium concentration are plotted in figure 31. For the three single crystal samples measured, S-51 with a Ce concentration of 0.0095 at% (0.025 % in the melt) exhibited the highest PL and gamma excited emission. S-74, the lowest single crystal Ce concentration sample of 0.0015 at% (0.005% in the melt) showed similar relative emission intensity for both photo- and gamma-ray excitation sources. S-75, the highest single crystal Ce concentration sample with 0.078 at% (0.25% in the melt) exhibited a large relative difference between PL and gamma excitation. The light emitted due to Cs^{137} excitation occurs throughout the sample whereas light emitted by photo excitation will be closer to the surface. Based on the above observations and the change in relative emission with excitation sources, the dominant quenching mechanism in single crystal LSO appears to be concentration quenching due to radiative self-absorption.
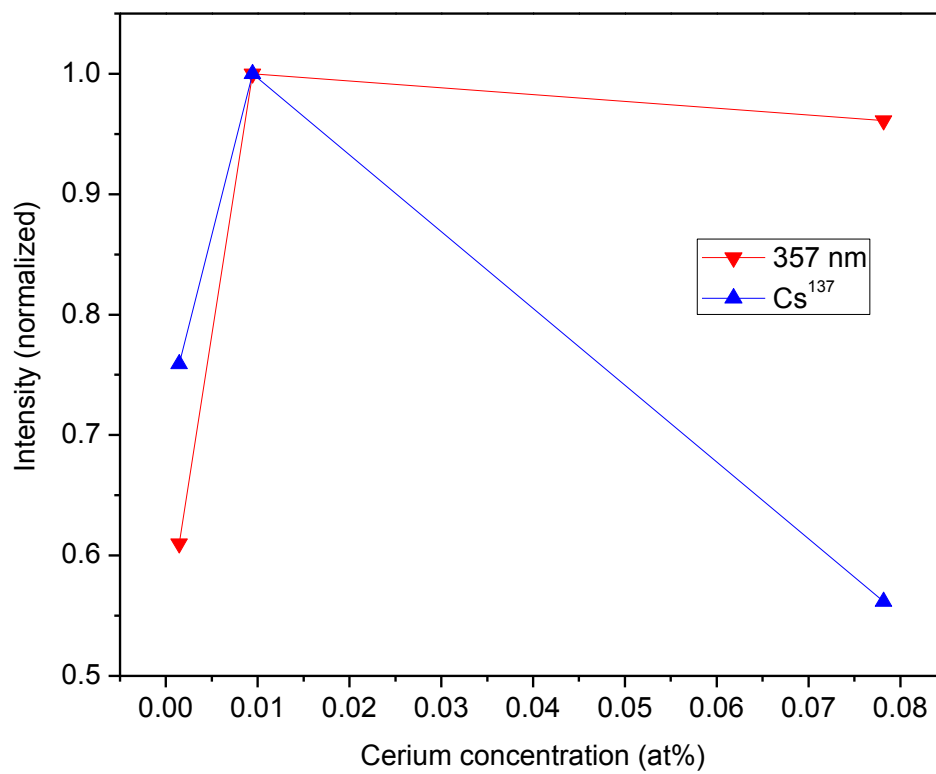
Figure 31. Relative emission intensity versus cerium concentration.

Temperature dependence

As discussed above, luminescence intensity generally decreases with temperature due to an increase in the non-radiative recombination rate. The emission spectra (for 357 nm excitation) measured at selected temperatures between 14 and 600 K are plotted for the middle cerium concentration (S-51, 0.0095 at%) sample in figure 32 as an example of the quenching behavior observed. Integrated photoluminescence intensity versus temperature for the three single crystal samples for Ce1 and Ce2 excitation and emission spectra are plotted in figure 33a-d along with a least squares fit to equation (3.6). E_a and A values, fit error, and with wavelengths of integration are reported in table 4. Ce1 emission values are similar to values reported for x-ray excitation [38], but lower than those reported for γ-ray excitation [12, 39]. Ce2 temperature quenching activation energies have not been reported, but the onset of quenching agrees with previous observations of Ce2 temperature dependent behavior [10, 40]. The fitted curves are in reasonable agreement with the recorded values, but there are discrepancies. In figure 33b (Ce1 emission) the middle and high cerium samples show a gradual decline in luminescence intensity before dropping off above room temperature while in figure 33a (Ce1 excitation) they are relatively flat up to 280 K. This discrepancy can be explained by the increase in broadening with cerium and temperature for the excitation spectrum that is not seen in the emission (Figure 24). The integrated excitation intensity is constant, but due to broadening the peak intensity is decreasing.
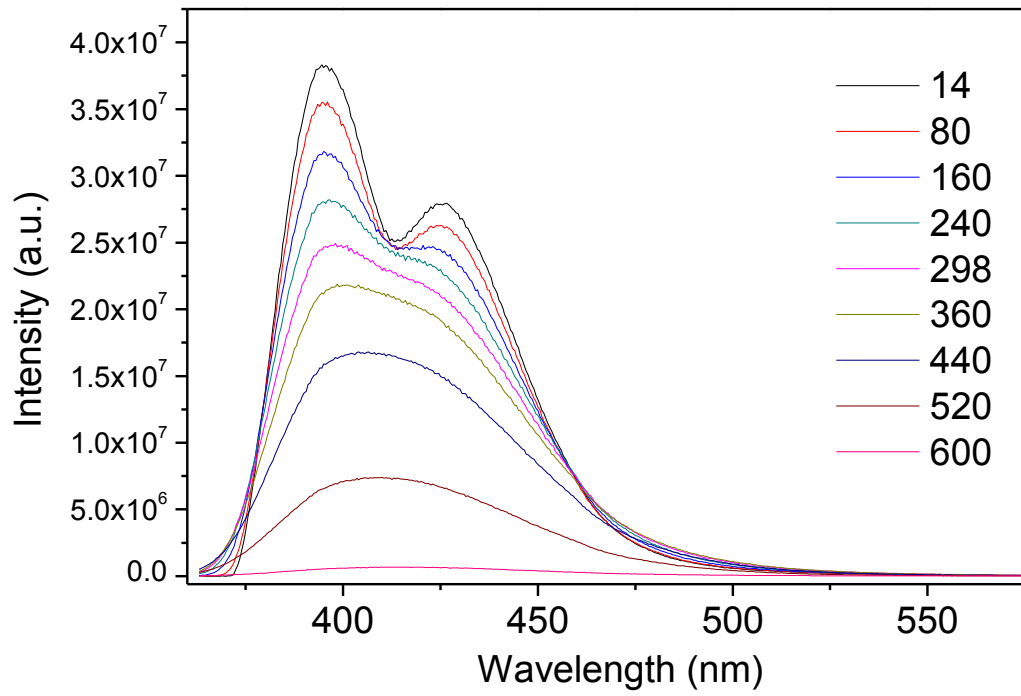
Figure 32. Emission spectrum for 357 nm excitation at selected temperatures for the middle cerium concentration single crystal LSO sample.
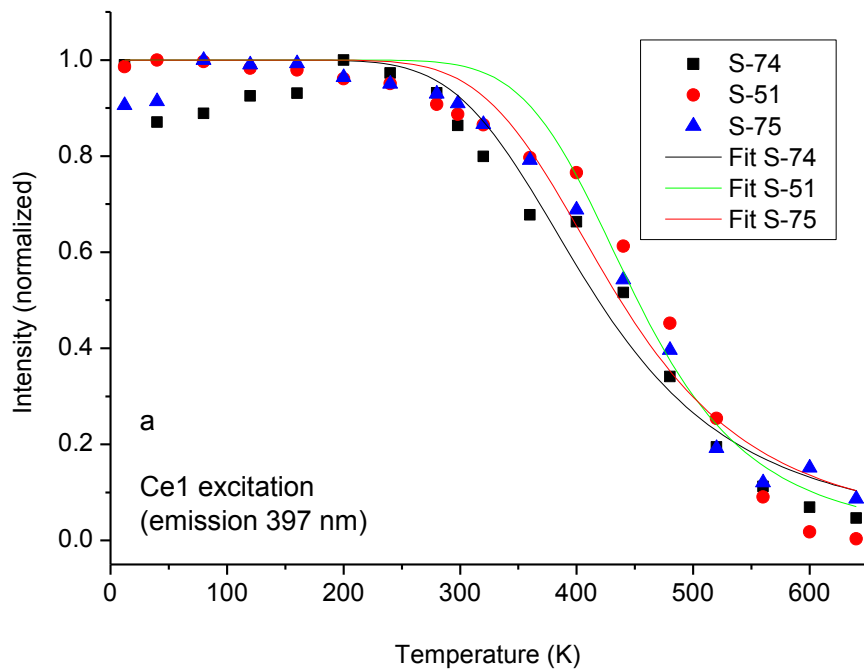
a.
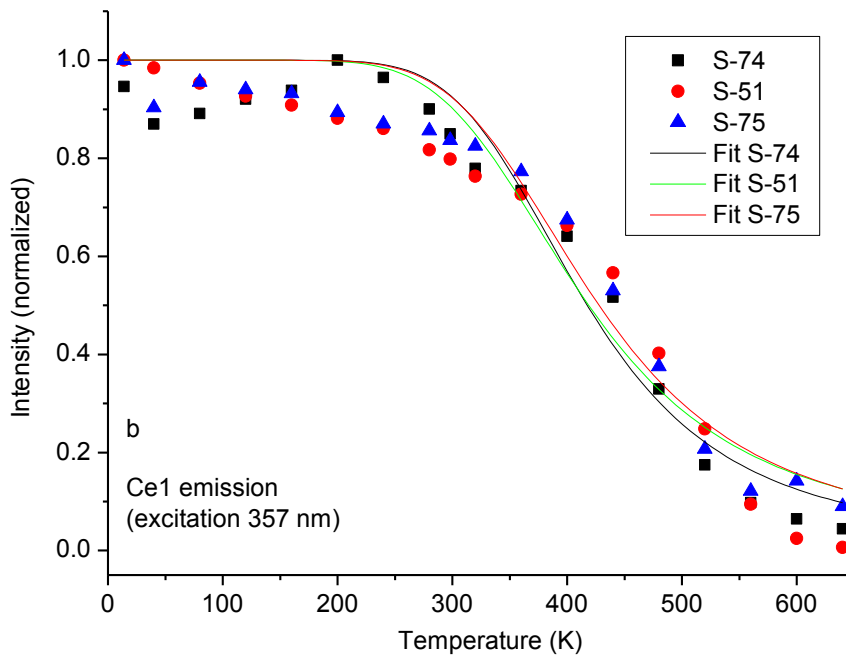
b.
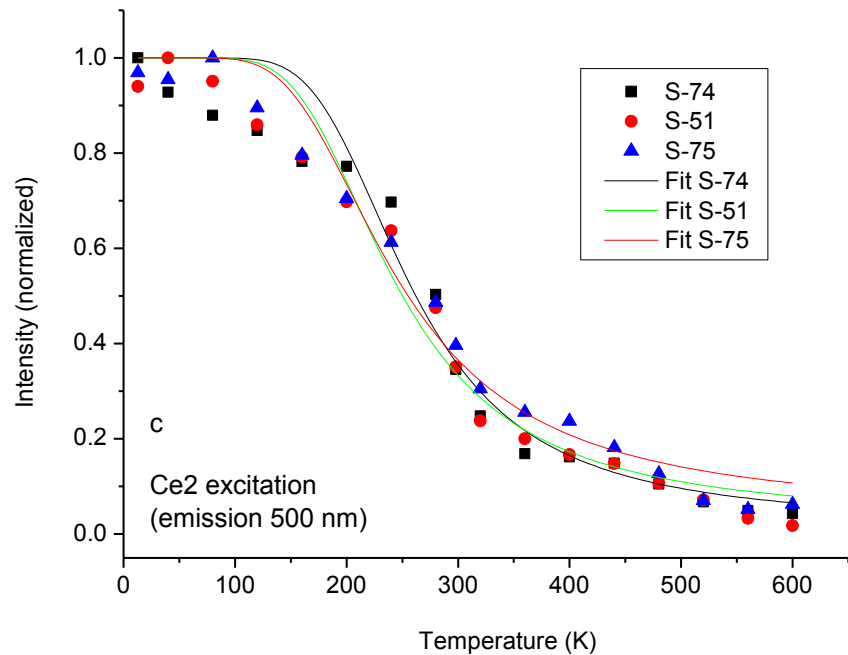
c.
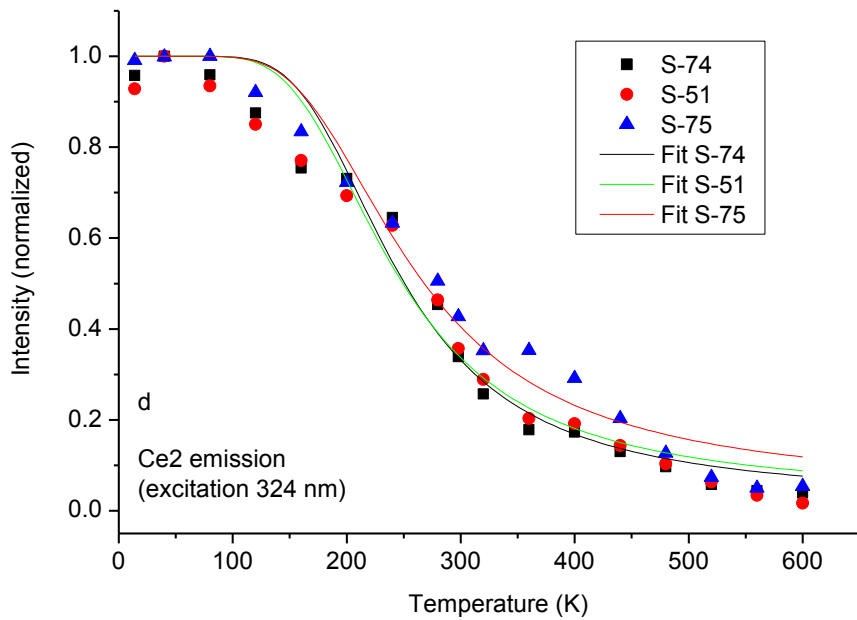
d.

Figure 33. Temperature dependence of integrated luminescence intensity.

a) Excitaion intensity at 397 nm emission, b) emission intensity are 357 nm excitation, c) excitation intensity at 500 nm emission, d) emission intensity at 324 nm emission.

Table 4. Single crystal LSO thermal quenching activation energies.

		S-74 0.0015 at%	(+/-)	S-51 0.0095 at%	(+/-)	S-75 0.078 at%	(+/-)
em 397 nm (Ce1)	E (meV)	225.0	(29.1)	342.1	(48.9)	257.2	(25.4)
(Int. 330-390 nm)	A	512	(404)	6510	(8032)	920	(607)
ex 357 nm (Ce1)	E (meV)	230.3	(31.3)	202.4	(34.9)	215.6	(28.8)
(Int. 363 to 600)	A	603	(512)	273	(259)	347	(266)
em 500 nm (Ce2)	E (meV)	106.5	(15.2)	90.4	(10.6)	81.1	(7.5)
(Int. 321.5-325.5)	A	111.6	(68.8)	66.0	(29.2)	39.9	(12.2)
ex 324 nm (Ce2)	E (meV)	92.1	(10.7)	85.8	(10.5)	83.8	(7.9)
(Int. 500-505)	A	71.1	(31.8)	54.5	(23.8)	37.6	(11.6)

Because the excitation is at a specific wavelength (357 nm) the decrease in peak intensity will be exhibited in the emission intensity. This can be confirmed by plotting the peak intensity values versus temperature (figure 34); the two curves are virtually identical. Figure 33b-d show little change with cerium concentration. While figure 33a and table 4 show an increase in the integrated Ce1 excitation's thermal quenching activation energy for the middle cerium concentration, which is not seen in the integrated Ce1 emission (fitting just the activation to peak intensity values is not accurate because it does not account for temperature induced homogenous broadening of the spectra). For S-75, the high cerium concentration sample, the relative emission intensity decreased due to some degree of concentration quenching (as mentioned above and [31]) which could be exhibited in the temperature quenching profile for Ce1 excitation. An excitation source and measurement geometry that maximized self-absorption would likely affect the quenching profile of the high cerium sample to a greater degree than the mid and low cerium samples. The relatively flat values of the PL thermal quenching activation energies give further evidence to self-absorption being the dominant mechanism of the concentration quenching. The mid cerium concentration sample, S-51, appears to balance the increase in intensity due to additional activator (cerium) sites with the decrease in emission intensity due to self-absorption.
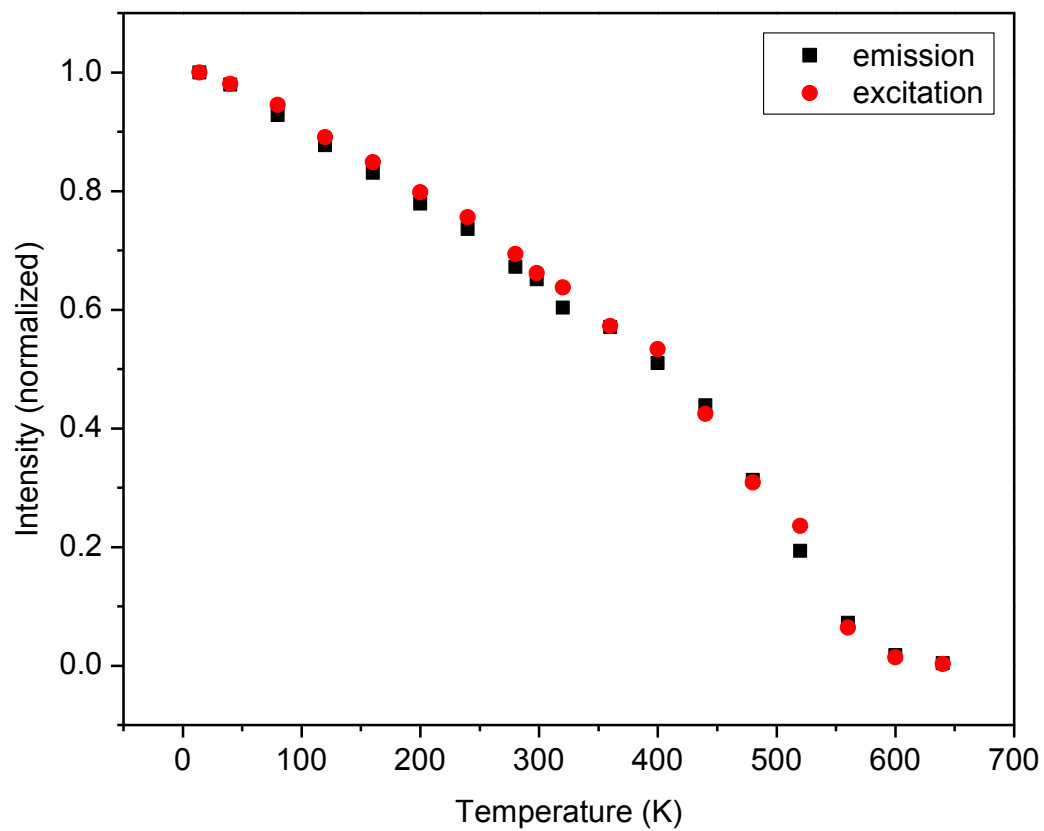
Figure 34. Normalized peak intensity values for Ce1 excitation (397 nm emission) and emission (357 nm excitation) versus temperature.

Configuration coordinate diagram and electron-phonon coupling

The activator site and the host crystal itself have many normal modes of vibration. The multiple modes can complicate the analysis of transitions and therefore it is helpful to make the assumption that there is one representative mode dominant for the activator site. Commonly this is the "breathing mode", where the ionic environment expands radially out from the activator site. The distance from the activator to the nearest neighbors is Q, or the configuration coordinate (CC). The configuration coordinate diagram was introduced in chapter 1 (figure 2) and is again shown in figure 35a. The parabolas in the diagram represent the vibrational frequencies of the one representative mode (commonly the breathing mode) for the ground and excited states. The phonon energy, $\hbar\omega$, corresponds to the energy difference between the vibrational states (diagramed in figure 35b) within the parabola. The ionic potential energy of the ground state as a function of Q, $E^{(a)}(Q)$ (the shape and position of the ground state parabola), can be expressed as [34]:

$$E^{(a)}(Q) = E_0^{(a)} + \frac{1}{2}M\omega_a^2(Q - Q_0^{(a)})^2 \quad (3.10)$$

where M is an effective ionic mass and ω_a is the vibrational frequency of the ground state. $E_0^{(a)}$ is the energy at the equilibrium configuration coordinate value, $Q_0^{(a)}$. It is convenient to set $E_0^{(a)}$ as the zero energy. With $E_0^{(a)}$ set as the zero energy, the ionic potential of the excited state, $E^{(b)}(Q)$, is:
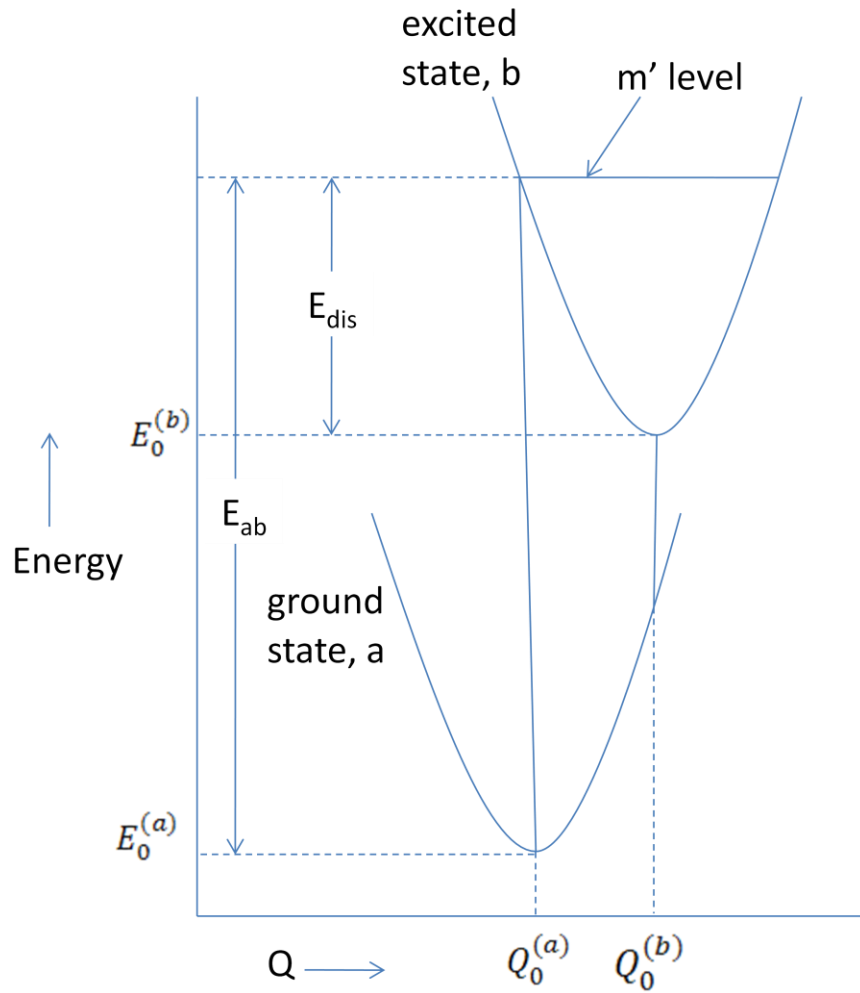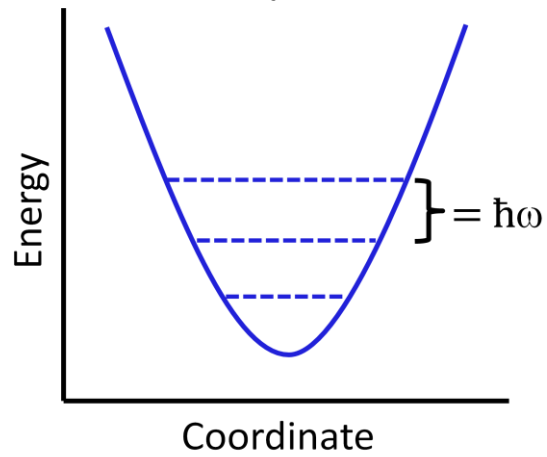
Figure 35. a) Configuration coordinate diagram and b) visualization of phonon energy, $\hbar\omega$.

$$E^{(b)}(Q) = E_{ab} - \frac{1}{2}M\omega_b^2\left(Q_0^{(b)} - Q_0^{(a)}\right)^2 + \frac{1}{2}M\omega_b^2\left(Q - Q_0^{(b)}\right)^2 \quad (3.11)$$

E_{ab} is the peak absorption energy (from the bottom of the ground state to the absorption level of the excited state), ω_b is the vibrational frequency of the ground state and $Q_0^{(b)}$ is the equilibrium configuration coordinate of the excited state. The difference of the electron-lattice coupling between the ground and excited states is commonly characterized by the Huang-Rhys parameter, S, a dimensionless constant defined as:

$$S = \frac{1}{2}\frac{M\omega^2}{\hbar\omega}\left(Q_0^{(b)} - Q_0^{(a)}\right)^2 = \frac{E_{dis}}{\hbar\omega} \quad (3.12)$$

Where E_{dis} is the energy difference between m' and the bottom of the excited state, $Q_0^{(b)}$. m' is the vibrational level where the vertical line from the bottom of the ground state, $Q_0^{(a)}$, intersects the parabola of the excited state. E_{dis} and m' are both shown in figure 35. Furthermore,

$$E_{dis} = S\hbar\omega = \left(m' + \frac{1}{2}\right)\hbar\omega \quad (3.13)$$

The greater S, the greater the degree of electron-lattice coupling. The shape of the spectra is strongly dependent on the electron-lattice coupling. S is related to the Stokes Shift (SS) by,

$$SS = 2S\hbar\omega \quad (3.14)$$

The assumption of the CC diagram with one representative mode is generally an accurate description of systems that exhibit a large Stokes shift and show medium to strong phonon coupling (a Huang-Rhys Parameter >5). Like LSO:Ce, these systems exhibit broad, Gaussian shaped excitation and emission line spectra.

In low coupling materials the vibrational frequency, ω, (and the electronic structure) can be measured from the phonon peaks in the low temperature spectra [41]. For higher coupling materials ω can be found from the temperature dependence of the bandwidth measured as either the half-width at half-max (HWHM) or as the full-width at half-max (FWHM):

$$H(T) = H(0) \left[coth \left(\frac{\hbar\omega}{2kT} \right) \right]^{\frac{1}{2}} + A \quad (3.15)$$

Where H(T) is the HWHM at temperature, T, H(0) is the HWHM at absolute zero, and k is the Boltzmann constant. A is a constant and is set to zero if the sample follows Condon approximation. For a Gaussian line shape the FWHM can be written as:

$$W(T) = \hbar\omega \left[8S \ln 2 \coth \left(\frac{\hbar\omega}{2kT} \right) \right]^{\frac{1}{2}} \quad (3.16)$$

W(T) is the FWHM at temperature T. Peak width versus temperature for the absorption or excitation gives ω for the ground state; for the emission it gives ω for the excited state. The 360 nm normalized excitation peak (400 nm emission) at selected temperatures for the medium cerium concentration (0.01 at%) is plotted in figure 36 as
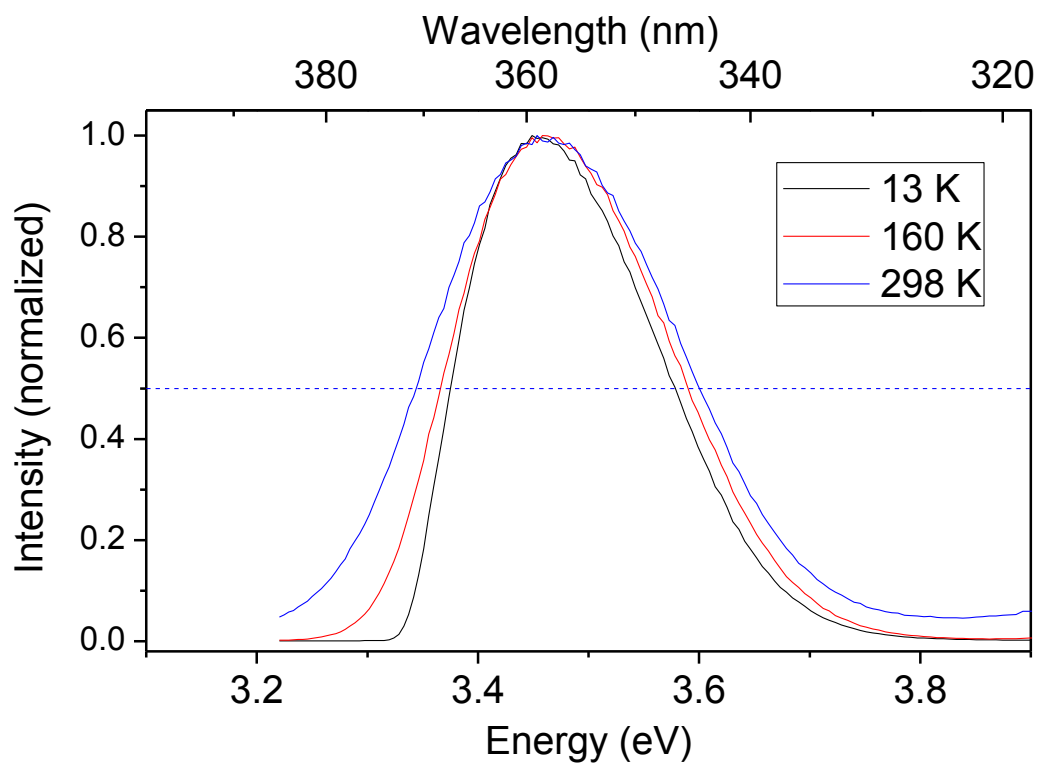
Figure 36. Example of the half-width half-max of the peak broadening with temperature.

an example of the phonon dependent thermal broadening that is observed in the single crystal LSO:Ce samples.

Electron-phonon coupling

As briefly discussed, it is not possible to completely remove or to fully quantify the effects of self-absorption, and in turn Ce2 emission, on the Ce1 emission profile of the single crystal LSO:Ce samples. The effects can be minimized by exciting at a wavelength that does not directly excite Ce2, using a geometry that minimizes self-absorption and using a sample with very low cerium concentration. The possibility of self-absorption and Ce2 emission complicate fitting Gaussian peaks to LSO:Ce emission and measuring half-width at half-max (HWHM or similarly, full-width at half-max, FWHM) values. It is still beneficial to look at LSO:Ce emission, but these caveats need to be kept in mind. Fitting of the excitation spectra is a little more straightforward. However, as seen by Cook, et al [42] the low energy excitation peak does not fit a simple single Gaussian profile. Because of these considerations, two methods were used for measuring the HWHM values: (1) a least-squares Gaussian fit of the peaks and (2) manually measuring the values from the data.

Gaussian fits of the excitation spectra of S-74 and S-51 at 13 K are plotted in figure 37. A two peak Gaussian fit was required for the low energy peak (labeled 1 and 2). For the S-

a.
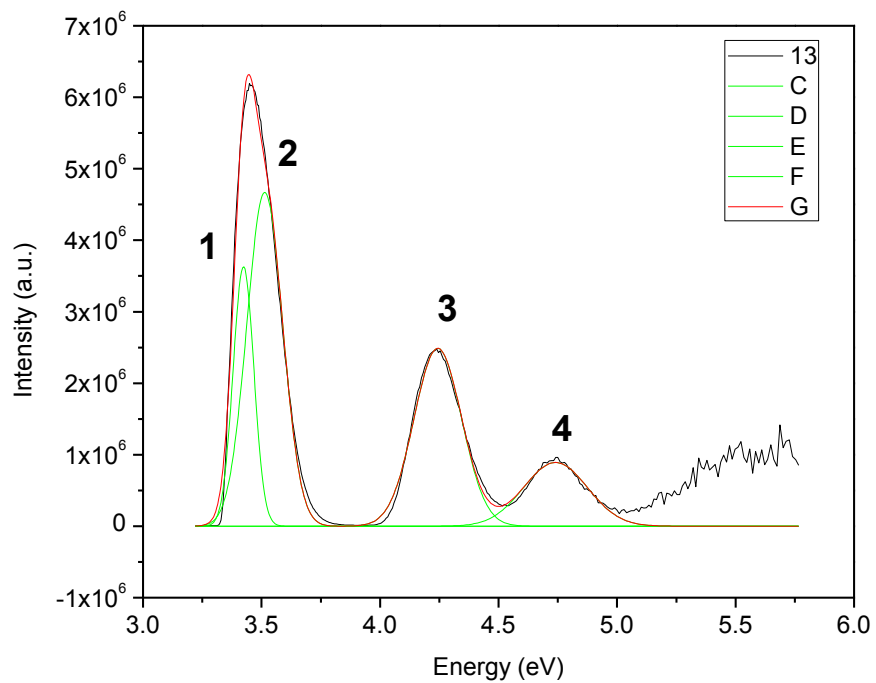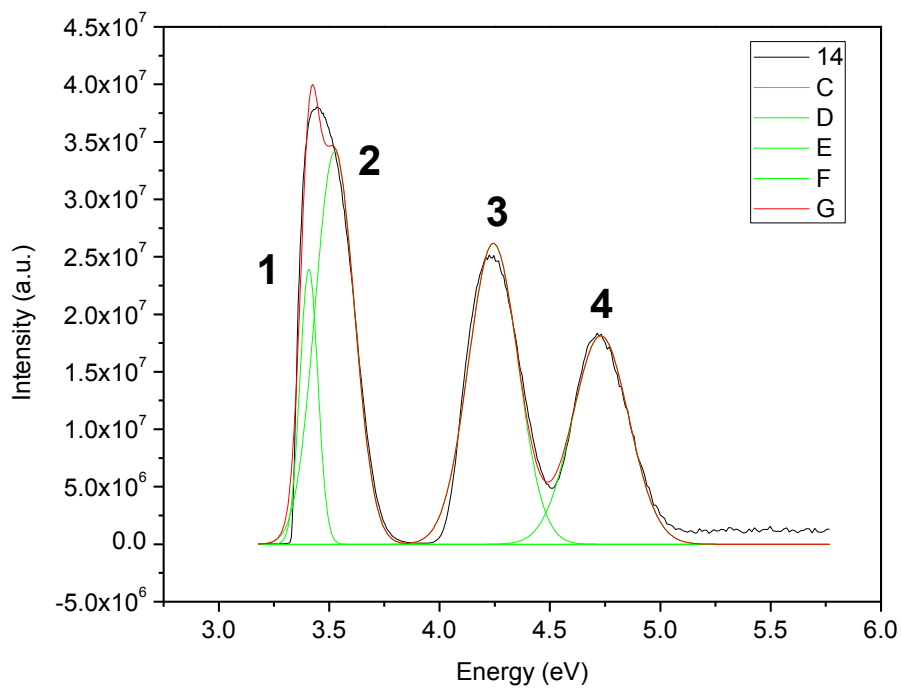
b.

Figure 37. Excitation (397 nm emission) spectra at low temperature with the addition of amplitude based Gaussian peak fits for (a) S-74 and (b) S-51.

51 (figure 37b) and S-75 excitation spectra even two peaks did not accurately fit the broad low energy peak. Cooke, et al [42] similarly reported that two Gaussian peaks were required for fitting the low energy peak of the absorption spectra of LSO:Ce at low temperatures. They proposed the second peak was due to Ce2 absorption. This is not likely the case because the second peak is seen in the Ce1 excitation spectrum, the peak intensity is too high compared to the peak intensity for the PL excitation spectrum of Ce2 emission and the peak wavelength values are (close, but) not the same. Additionally, this explanation does not account for the fact that a two peak Gaussian does not fit the low energy peaks of the higher cerium concentration samples. The double peak is possibly attributable to two closely spaced 5d crystal field split levels or that the spin-orbit levels of the lowest 5d level are not fully degenerate. Several calculations of the energy levels of cerium in LSO have been performed [43-46]. Kuznetsov, et al. [45] suggested that the 5d $1e_2$ crystal field level for the seven oxygen-coordinated cerium site was degenerate. It is possible the 5d $1e_2$ is not fully degenerate but close in energy to the 5d $1e_1$ level. The spin-orbit splitting of the 5d levels for LSO:Ce have not been determined. Crystal field calculations of Ce^{+3} in octahedral sites of alkaline earth sulfide hosts [5-6] have shown the lower 5d crystal field level is spin-orbit split into three levels. The two cerium sites in LSO are both distorted octahedral sites (7 and 6 coordinated respectively) and this energy layout does match the higher energy Ce1 excitation peaks, but more precise crystal field calculations would be needed for confirmation. However, this explanation does not evidently account for the broadening

of the low energy peak seen at higher cerium concentrations. It also possible (as mentioned above) that the Gaussian shape of the peak is distorted by inhomogeneous broadening with increasing cerium concentration.

A Gaussian fit of the Ce1 emission spectrum of S-51 at 13 K is plotted in figure 38. The emission was fit with two peaks having an energy separation of 1953 cm^{-1}, in agreement the characteristic 4f spin orbit split for cerium of ~2000 cm^{-1} [47]. In figure 39 the emission spectrum at 298 K is plotted with two slightly different fitting methods. In figure 39a the fit was performed allowing each value to float freely. The R^2 value is high (>0.999) and overall it looks like an excellent fit. However, the peak height ratio of peak 1 to peak 2 has reversed from the ratio in figure 38. The peak height ratio should be constant with temperature because the excited electron de-excites from the bottom of the 5d level to either the $4f_{7/2}$ or the $4f_{5/2}$ and the radiative recombination rates are temperature independent; the non-radiative transition is temperature dependent but it occurs from the 5d level and in this case cannot preferentially quench one radiative pathway over the other. Following this argument, the fit in figure 39b was performed with the peak height ratio fixed to the value from the fit in figure 38. The fit is still reasonable (R^2 >0.99) and the peak split is a more reasonable 2034 cm^{-1} compared to 1727 cm^{-1} for figure 39a. The peak split values for all temperatures and most samples are plotted in figure A-5 of the appendix. However, the issue still remains that the extent of self-absorption is not known. A large degree of self-absorption could lead to a
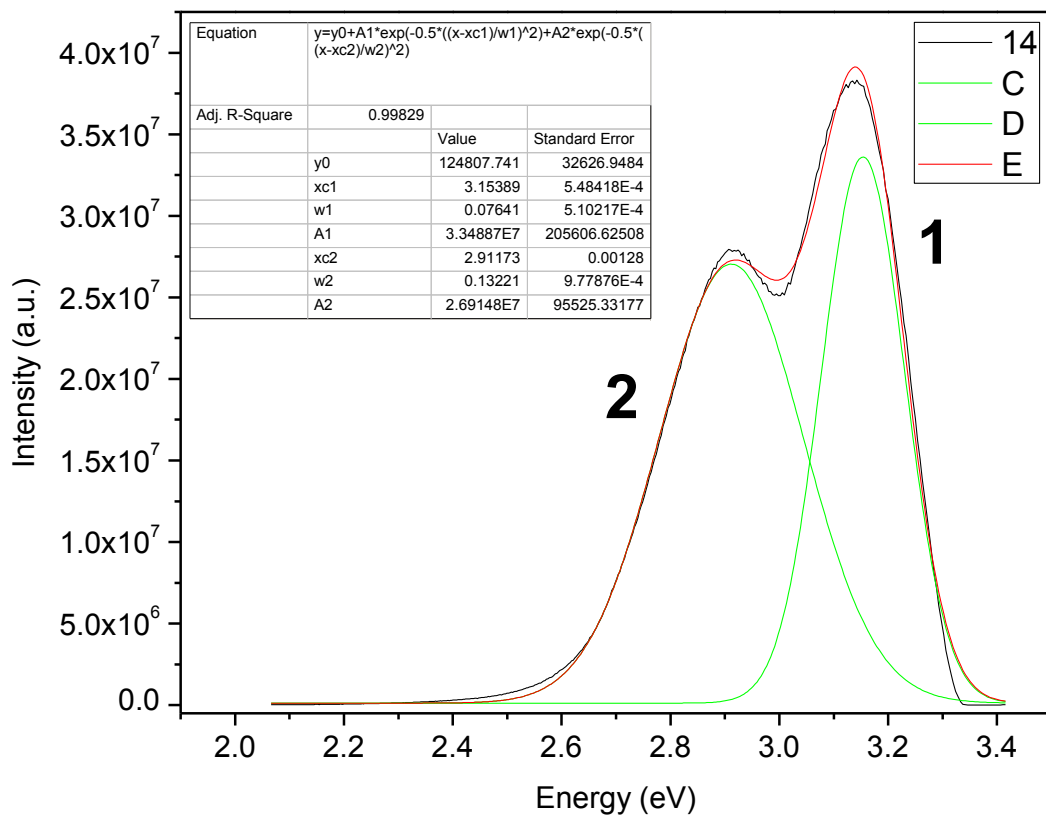
Figure 38. S-51 Ce1 emission spectrum at 14 K with a 2 peak Gaussian fit.
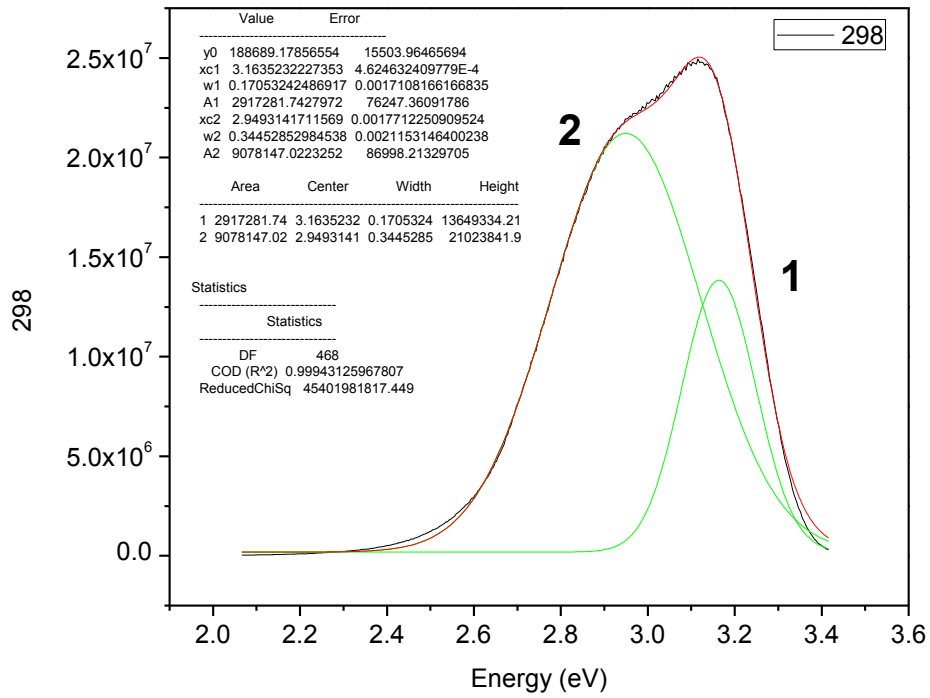
a.
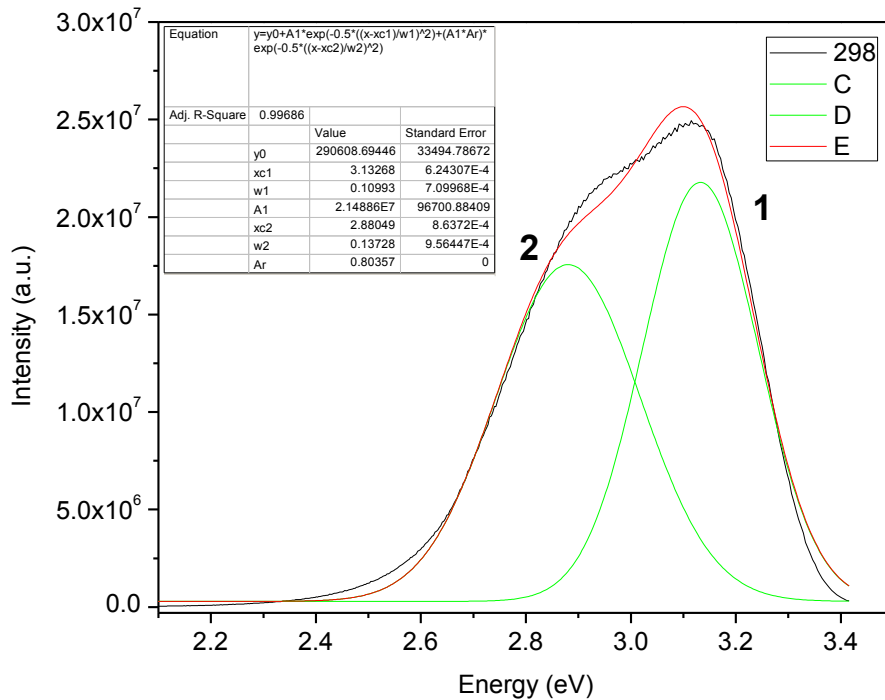
b.

Figure 39. S-51 emission spectrum at 298 K a) fit with "floating" peak ratios, b) fit with peak ratios from the fit in figure 38.

peak profile like that in figure 39a, but Ce2 peaks would have to be added. Three-peak Gaussian fits of LSO emission have been performed [38, 48] with two peaks assigned to Ce1 and one peak assigned to Ce2. This is not accurate however, because as is evident in figure 28, Ce2 emission also exhibits the characteristic two-peak cerium emission (additionally, the fitted Ce2 emission peak position did not match the emission peak position for Ce2 excitation). An attempted four-peak Gaussian fit is plotted in figure A-7 of the appendix.

Because of the multi-peak issues in the excitation spectrum, the potential self-absorption and Ce2 peaks in the emission spectrum HWHM values were also measured manually from the recorded data. The half-max energy position was found using a six-point linear interpolation to remove artifacts caused by the step size of the raw data recorded by the instrument (an example is plotted in figure A-8 of the appendix).

The FWHM versus temperature, measured using the two methods, for the higher energy emission peak (peak 1 in figure 38) of the low cerium sample (S-74, 0.002 at%) are plotted in figure 40a and b along with least-squares fit of equation (3.15) in figure 40b and of equation (3.16) in figure 40a. The FWHM versus temperature for low the cerium sample (S-74, 0.002 at%), measured with Gaussian fits of the excitation spectra, are plotted in figure 41. The values for each sample and method are summarized in table 5. The $\hbar\omega$ values for emission peak 1 are similar between the two methods and range between 0.0225 eV for the fit based method and 0.0263 eV for the manual method. For emission peak 2, the fit method gives a value of 0.0815 eV whereas the
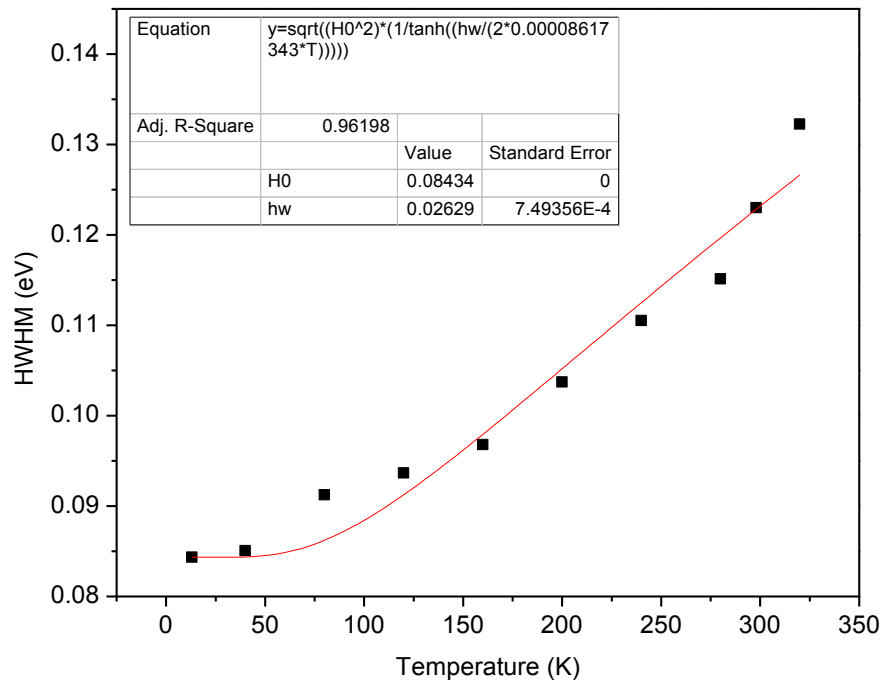
a.
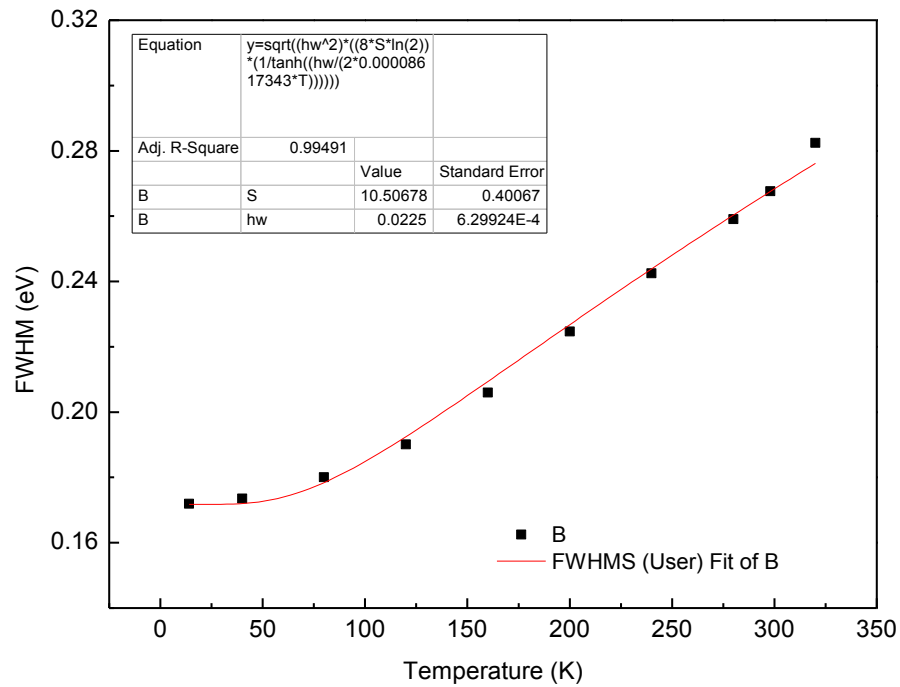
b.

Figure 40. FWHM versus temperature and comparison of different fitting methods.
a) Values from two peak Gaussian fit with the ratio of the peak amplitudes fixed, fit with
equation (3.16). b) Values manually measured from data, fit with equation (3.15).
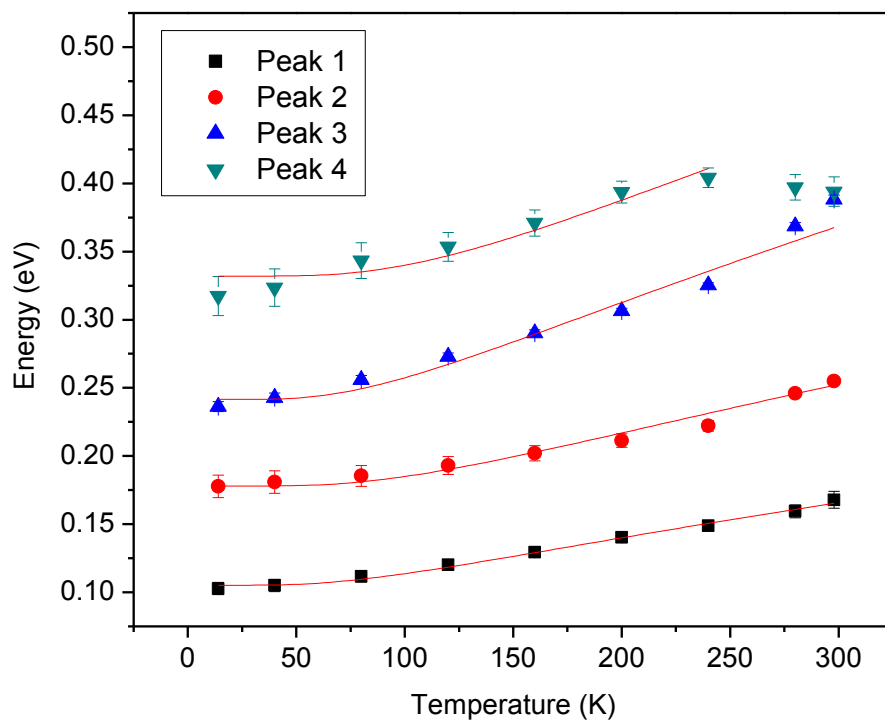
Figure 41. The FWHM versus temperature for the low cerium sample (S-74, 0.002 at%), measured with Gaussian fits of the excitation spectra

Corresponding plots for the medium and high cerium samples are given in figures A-9a and b in the appendix.

Table 5. Values from fits of HWHM (or FWHM) versus temperature.

a) Values from Gaussian Fits:

Spectra		Emission (357 nm ex)		Excitation (397 nm em)			
	Peak	1	2	1	2	3	4
S-74	S	10.5	2.67	4.10	7.20	18.7	19.1
	$\hbar\omega$ (eV)	0.0225	0.0815	0.0221	0.0282	0.0237	0.0323
	ω (10^{13} s^{-1})	3.42	12.38	3.35	4.28	3.60	4.90
	R^2			0.993	0.968	0.948	0.924
S-51	S	7.9	2.6	7.2	3.3	19.5	21.9
	$\hbar\omega$ (eV)	0.0276	0.0816	0.0144	0.0519	0.0263	0.0289
	ω (10^{13} s^{-1})	4.19	12.40	2.18	7.88	3.99	4.38
	R^2			0.980	0.846	0.981	0.979
S-75	S	10.2	2.1	12.7	0.6	14.2	61.8
	$\hbar\omega$ (eV)	0.0228	0.0919	0.0119	0.1343	0.0357	0.0232
	ω (10^{13} s^{-1})	3.47	13.96	1.81	20.39	5.41	3.52
	R^2			0.985	-0.086	0.942	0.954

b) Values from manual method:

	Spectra	Emission		Excitation
	Method	manual		manual
	Peak	1	2	1
S-74	H(0)	0.0843	0.1659	0.0997
	$\hbar\omega$ (eV)	0.0263	0.0300	0.0332
	ω (10^{13} s^{-1})	3.99	4.55	5.05
	R^2	0.962	0.945	0.0997
S-51	H(0)	0.0935		0.1042
	$\hbar\omega$ (eV)	0.0318		0.0259
	ω (10^{13} s^{-1})	4.83		3.93
	R^2	0.969		0.994
S-75	H(0)	0.08683		0.1081
	$\hbar\omega$ (eV)	0.0311		0.0229
	ω (10^{13} s^{-1})	4.71		3.48
	R^2	0.993		0.996

manual method gives a value of 0.0300 eV. Since both peaks emit from the bottom 5d level they should have similar $\hbar\omega$ values. Ce2 emission contributions around 460 nm would inadvertently broaden peak 2 and narrow peak 1 in a Gaussian fit, which is likely the case for the Gaussian based values. The low energy broadening would have less affect on the manual method and indeed these values show better agreement to one another and to the behavior predicted by the configuration coordinate model. For the excitation spectrum, the FWHM measured from Gaussian peak fits in figure 41 for the low cerium sample give phonon values ranging from 0.0221 eV to 0.0323 eV and exhibits reasonable agreement between peaks 1 and 2. However, for the higher cerium concentrations (table 5a) the fits yield unreasonable S parameters and poor R^2 values. The fits to manually measured excitation HWHM values (table 5b) with equation (3.15) yield excellent R^2 values and show more reasonable results at higher cerium concentrations. For these reasons the emission and excitation phonon values measured with the manual method and fit with equation (3.15) are considered to have the highest confidence and are summarized in table 6. The phonon energies are converted from electron-volts (eV) to wavenumbers (cm^{-1}) in table 7.

Raman shift spectroscopy

After the phonon energy responsible for the thermal broadening of the PL spectra was measured for the cerium activator the values were compared to reported values for the host LSO measured by Raman spectroscopy [49-50]. The phonon structure, like the crystal structure, is complicated and exhibits a multitude of peaks. However, the host

Table 6. Single crystal LSO phonon values with high confidence.

		Emission	Excitation
S-74	H(0)	0.0843	0.0997
0.0015 at%	$\hbar\omega$ (eV)	0.0263	0.03323
	ω (10^{13} s^{-1})	3.99	5.05
S-51	H(0)	0.0935	0.1042
0.0095 at%	$\hbar\omega$ (eV)	0.0318	0.02585
	ω (10^{13} s^{-1})	4.83	3.93
S-75	H(0)	0.0868	0.1081
0.078 at%	$\hbar\omega$ (eV)	0.0311	0.02294
	ω (10^{13} s^{-1})	4.71	3.48

Table 7. Phonon values reported in wave numbers.

		Emission	Excitation
S-74 0.0015 at%	$\hbar\omega$ (cm^{-1})	212.0	268.0
S-51 0.0095 at%	$\hbar\omega$ (cm^{-1})	256.4	208.5
S-75 0.078 at%	$\hbar\omega$ (cm^{-1})	250.4	185.0

LSO exhibits a Raman active Bg mode phonon with a value of 268 cm^{-1} ($\hbar\omega$ = 0.0332 eV) which has been attributed to an Lu cation site [49-50]. This corresponds to the phonon energy in table 7 measured for the excitation of the low cerium sample (S-74, 0.002 at%) to within three significant figures.

Further work conducted by Ricci et al. [51] looked at the Raman shift of Lu$_{1.8}$Y$_{0.2}$SiO$_5$ with and without the addition of cerium. They found that a broad band at 266 cm^{-1} for Lu$_{1.8}$Y$_{0.2}$SiO$_5$ was composed of two bands, a Lorentzian shaped band at the LSO value of 268 cm^{-1} and Gaussian shaped band at 264.5 cm^{-1}. The Gaussian band was attributed to a convolution of the LSO band and the contribution of a similar band at 254 cm^{-1} for pure YSO. Additionally, using polarized sources they found the 264.5 cm^{-1} band progressively shifted towards the LSO band with an increase in cerium concentration while no other bands showed a shift.

Encouraged by Ricci et al.'s results Raman shift measurements were performed on the three single crystal LSO:Ce samples in an attempt to further elucidate the phonon coupling relationship between the host LSO and the cerium activator. The Raman shift spectra are plotted in figure 42 for the low (42a), medium (42b) and high (42c) cerium samples. The 268 cm^{-1} peak is highlighted. The spectra did not exhibit a shift in the 268 cm^{-1} peak nor any of the additional peaks present. The spectra for the low and high cerium samples are virtually identical. The changes in intensity between the middle
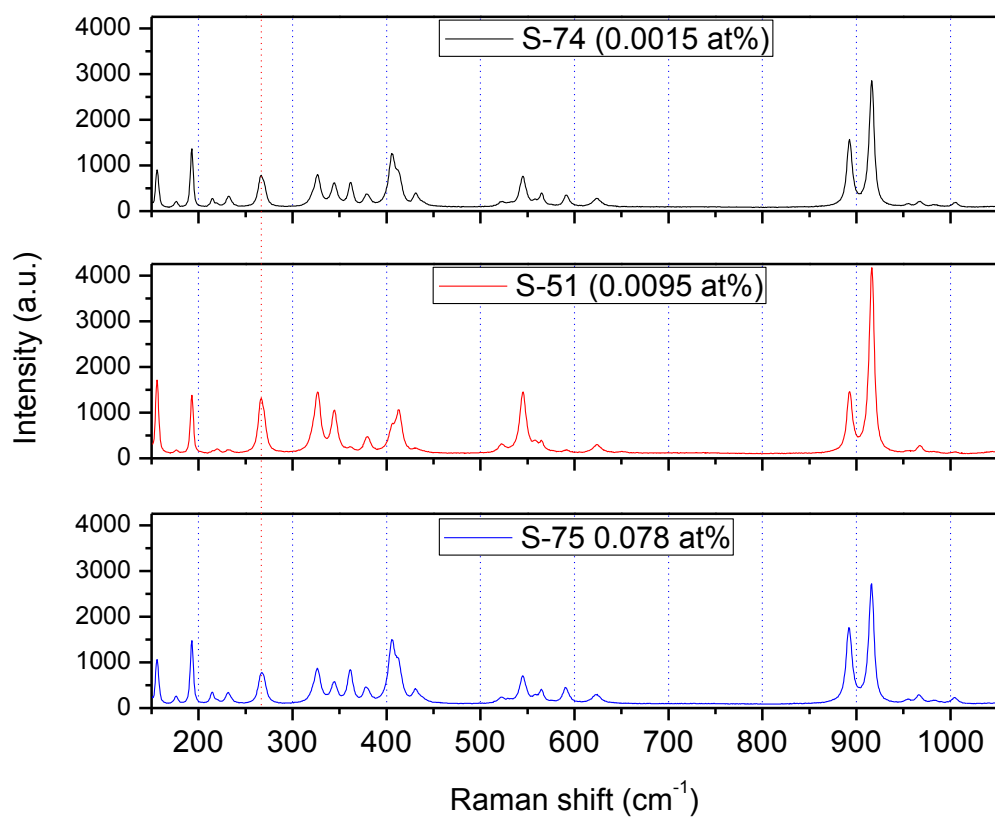
Figure 42. Single crystal LSO Raman shift results.

cerium concentration (0.01 at% sample in relation to the low (0.002 at%) or high (0.08 at%) samples is attributed to orientation of the single crystal samples during measurement (due to single crystal nature of the samples there is some degree of intrinsic polarization of the shifted emission due to crystallographic orientation).

Configuration coordinate diagram

Configuration coordinate diagrams of the dominant Ce1 emission, calculated from the measured PL spectra and phonon values, for the low (S-74, 0.002 at%), medium (S-51, 0.01 at%) and high cerium (S-75, 0.08 at%) samples are plotted in figures 43, 44 and 45, respectively. A significant change in the diagrams is observed with increasing cerium concentration as the ground state broadens and the excited state narrows. The ground and excited states were calculated using equations (3.10) and (3.11). The Stokes Shift (SS) was measured from the experimental PL spectra, while the Huang-Rhys Parameter was calculated from the phonon energies and the Stokes Shift using equation (3.14). The sample dependent values (peak positions, etc.) used in the calculations are summarized in table 8. The highest 5d parabola, 5d $4e_1$, is portrayed as dashed because the energy value is taken from absorption measurements [52]. The configuration coordinate model generally assumes one dominant "breathing mode" vibration based on an effective mass, M, which was assumed to be coordinated with 7 oxygen atoms. Using different values for the effective mass will change the coordinate (x-axis) values, Q, but it will not
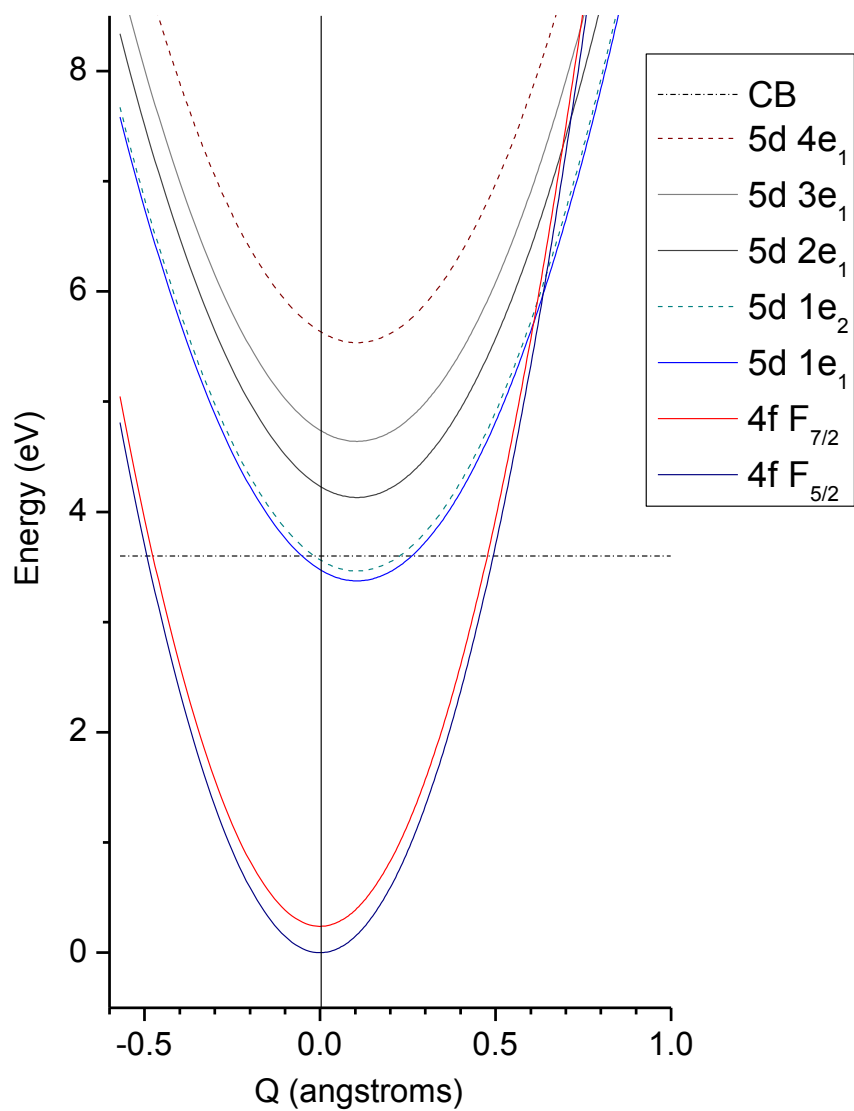
Figure 43. Configuration coordinate diagram for low cerium concentration (S-74) single crystal LSO.
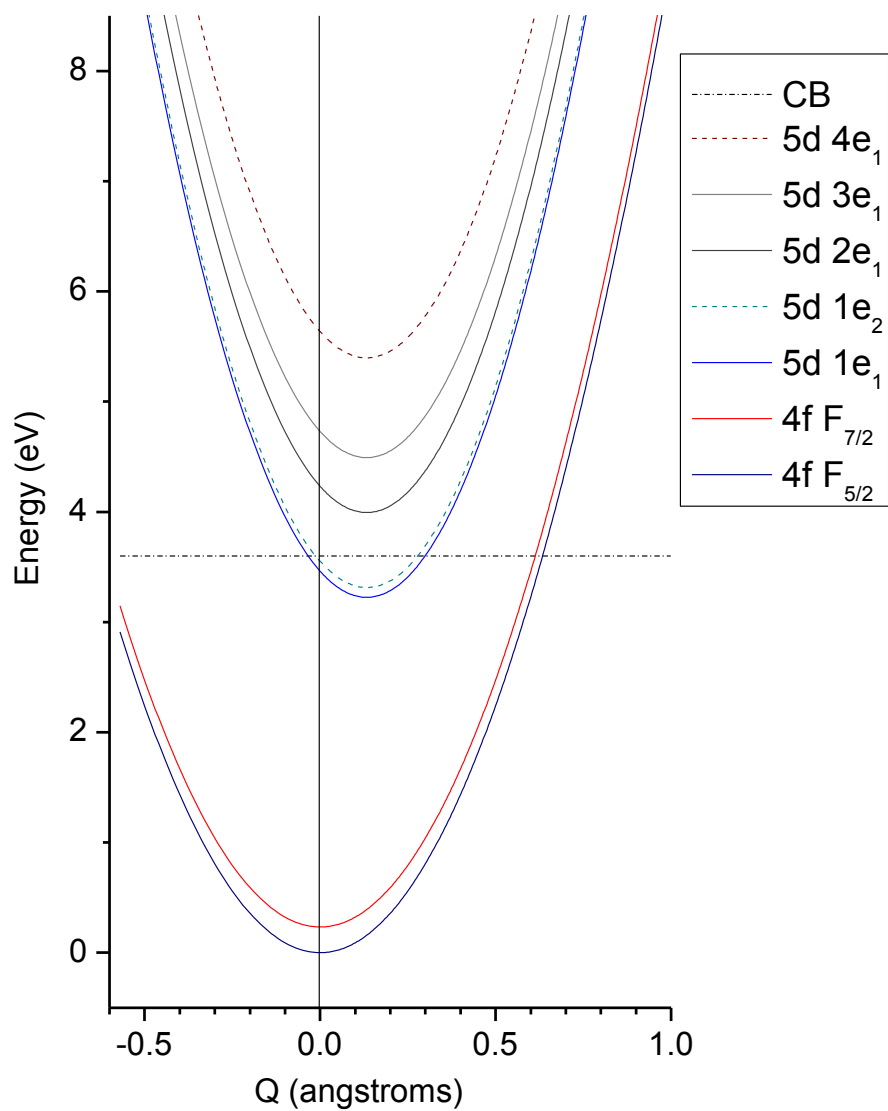
Figure 44. Configuration coordinate diagram for medium cerium concentration (S-51) single crystal LSO.
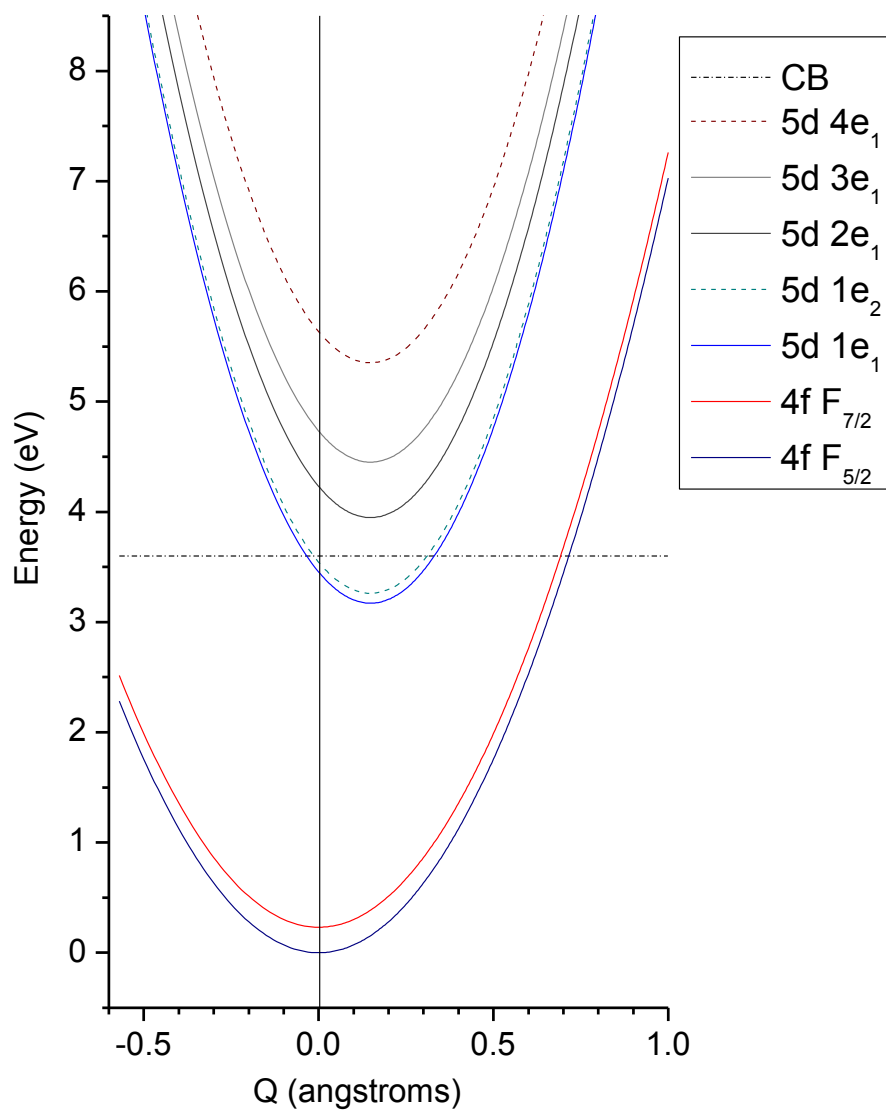
Figure 45. Configuration coordinate diagram for high cerium concentration (S-75) single crystal LSO.

Table 8. Values used to calculate the configuration coordinate diagrams.

		S-74	S-51	S-75
		0.0015 at%	0.0095 at%	0.078 at%
Excitation				
Peak (eV)	1	3.475	3.462	3.455
	2	4.232	4.232	4.232
	3	4.740	4.730	4.734
ω (10^{13} s^{-1})		5.05	3.93	3.48
Emission				
Peak (eV)	1	3.150	3.147	3.145
	2	2.910	2.914	2.914
ω (10^{13} s^{-1})		3.99	4.83	4.71
Stokes Shift (eV)		0.325	0.315	0.310
S		4.89	6.10	6.75

change the positions and shapes of the parabolas relative to one another. Diagrams calculated using an effective mass of 6 oxygen atoms yielded ground and excited parabolas that were equally broadened. The effective mass could actually be set to 1, but the Q coordinate would scale only relative change and not represent physical distance. Additionally, because the effective mass is assumed the actual Q values are less important for comparison than the relative shapes of the parabolas between both the ground and excited states and between different cerium concentrations. Since the measured emission wavelength was not used in the calculations it can be compared to the energy distance between the bottom of the 5d to the intersection of the 4f $F_{5/2}$, to gauge the accuracy of the model. For the low the cerium sample (S-74), the 4f $F_{5/2}$ emission is 3.15 eV; measured from the S-74 CC diagram the value is 3.21 eV; a difference of 60 meV. Because the value from the CC diagram does not include the vibrational state interactions it is expected to be slightly larger than the measured value. Considering this, the values exhibit excellent agreement.

The cerium ground state parabolas are assigned to the 4f $F_{5/2}$ and $F_{7/2}$ spin orbit split levels. The excited state parabolas are assigned to the five 5d crystal field split levels following designations used in LSO:Ce energy level calculations [45]. The energy separation of the excited state parabolas correspond reasonably well with calculated 5d crystal field split levels [45] for seven oxygen coordinated cerium in LSO ([CeO_7]), the measured values did not match six oxygen coordinated cerium ([CeO_6]). Excitation/emission-measured, absorption-measured and calculated 5d energy values

are given in table 9 along with assigned designations and the total 5d crystal field splitting (Δ). The energy level designations for the calculated and absorption-measured values are retained from [45]. For the excitation/emission values the 5d $1e_2$ has been assigned to the high energy peak for the two peak Gaussian fits of the low energy excitation peak (figure 37, peak 2). The 5d $1e_2$ is portrayed as dashed because it appears to be semi-degenerate with 5d $1e_1$, following the calculated values.

From the CC diagrams it is evident that the dominant non-radiative de-excitation pathway does not take place via a transition from the excited state to the ground state by a pathway where the two parabolas cross as the required energy is much greater than the measured thermal quenching activations energies (table 4). A possible non-radiative pathway is the conduction band of the host LSO. Evidence for a conduction band based non-radiative pathway is supported by photoconductivity measurements of LSO:Ce [53-54] which put the conduction band in an energy range above the bottom 5d level consistent with the activation energy (E_a) values measured above. This places the higher energy 5d levels above the conduction band which could possibly quench their emission. However, Raukas [53] calculated that the excited electron transitions to the lowest 5d level faster than it has time to travel through the conduction band, preventing non-radiative de-excitation. It has also been proposed that the Ce2 site sits higher in the bang gap with the bottom 5d level closer to the conduction band and ultimately responsible for the lower quenching temperatures observed for Ce2 emission [53, 55]. The proposed Ce2 5d to conduction band energy distances correlate with the measured

Table 9. LSO:Ce 5d energy level designations.

	Calculated [45]		Absorption [52]	Excitation/ emission
	[CeO$_6$]	[CeO$_7$]		
5d 1e$_1$	4.3	3.5	3.48	3.47
5d 1e$_2$	4.6	--	4.2	3.56
5d 2e$_1$	5.2	4.2	4.7	4.23
5d 3e$_1$	7.6	5.6	5.63	4.74
5d 4e$_1$	8.1	5.8	--	5.63*
5d Δ	3.8	2.3	2.15	2.16

*Value from experimentally measured absorption [52].

Ce2 PL quenching activation energies reported in table 4.

The energy value of the conduction band in the CC diagrams (figures 43, 44 and 45) was placed by adding the quenching activation energy for the low cerium sample (S-74) of 225 meV to the energy of the bottom of the 5d, 3.373 eV, which yielded a value of 3.598 eV (relative to the bottom of the 4f ground state). The CC diagrams give a qualitative depiction of the fine line LSO:Ce follows for luminescence emission. In host materials where the bottom of the cerium 5d configuration is above the conduction band luminescence is quenched (for example, cerium in Lu_2O_3 [54]). The conduction band is placed at 3.598 eV on the CC diagrams of the medium (S-51) and high (S-75) samples (figures 44 and 45) under the assumption that the energy value of the conduction band relative to the 4f ground state will be independent of cerium concentration. The energy difference between the conduction band and the bottom 5d level can be measured and compared to the thermal quenching energies (E_a). The results of the comparison are presented in table 10. The two values for the middle sample (S-51) are remarkable similar and within the error of the E_a value. This suggests that even at a higher concentration of cerium (compared to the low cerium, S-74, sample) a single luminescent center is still an accurate model of the system. The values for the high cerium sample (S-75) are less consistent. The increase in self-absorption, demonstrated above, for the higher cerium concentration is responsible for the discrepancy. The self-absorption leads to a lower quenching value than what would be predicted by the CC diagram. It is possible that the higher cerium concentration creates an additional defect

Table 10. The calculated distances to conduction band compared to experimentally measured E_a values for single crystal LSO at different cerium concentrations.

	Bottom of 5d (5d $1e_1$)	Distance to conduction band	E_a (error)
S-74 0.0015 at%	3.373	-	0.225 (.029)
S-51 0.01 at%	3.224	0.375	0.342 (.049)
S-75 0.08 at%	3.171	0.427	0.257 (.025)

(units in eV)

related non-radiative pathway, though this would be expected to be observed in a decrease in the decay time with temperature; which is the opposite of what is exhibited (Figure 27). However, it is also possible that a single luminescent center begins to break down as an accurate model of the system at higher cerium concentrations due contributions of additional luminescent sites in the PL spectra, such as the presence of Ce2.

Discussion

Cerium concentration

There is little conclusive published work [12, 31] that specifically reports the effects of cerium concentration on single crystal LSO. This is understandable considering the many factors that lead to varying performance of single crystal samples, even among samples cut from the same boule [56]. A general range of 0.025 to 0.0625 percent cerium in the melt is considered a standard/optimized doping concentration [36]. However, the cerium concentrations of grown single crystals are much lower due to the relatively low distribution coefficient of 0.22. While both monoclinic, LSO and cerium-oxyorthosilicate have different space groups which likely leads to the low solubility of cerium in LSO and makes crystal growth of LSO with high cerium concentrations difficult (> 0.25 atomic % in the melt). As evident in the plot of intensity versus cerium concentration (figure 31) the ideal cerium concentration must strike a balance between increasing activator sites

(increasing emission) and increasing self-absorption (decreasing emission). In the middle cerium concentration (0.095 at%) the onset of substantial self-absorption has already occurred. A more accurate representation of the self-absorption affecting the results in figure 31 would be to set the low cerium (0.0015 at%) values equal to one another, thereby exhibiting the relative decrease in emission of the middle cerium (0.095 at%)

The broadening in the 360 nm excitation peak with relative increases in the peaks at 265 nm and 300 nm with increasing cerium concentration (figure 24) could be attributable to several factors. One possibility is an increase in simple inhomogeneous broadening. Slight variations in the cerium positions will increase with increasing cerium due to increased stress in the crystal. Variations from the equilibrium position will lead to shifts in the spectrum and a general broadening of the spectrum. Comparing the absorbance spectra (figure 26) it is likely that the low cerium sample is not absorbing all of the incident excitation light. On the other hand, the higher cerium samples absorb all of the incident ~360 nm light and consequently a larger portion of the ~265 nm and ~300 nm incident light leading to increased emission by 265 nm and 300 nm excitation. A final possibility is a change in the overlap of the wave functions of corresponding vibrational states with increasing cerium. This is supported by the expanding of the ground state parabola and a contracting of the excited state parabola that is observed for increasing cerium in the CC diagrams in figures 43-45, which will be discussed in further detail below.

Phonon values

The measured Raman shift results suggest that at low cerium concentrations the cerium cation couples to the vibrations of the host LSO crystal. At higher cerium concentrations this coupling appears to break down. At an infinitely dilute concentration the system behavior is expected to follow the predicted theory. As concentration increases the addition of internal stresses and introduced defects are expected to contribute to behavior that deviates from the predicted theory. The Raman results also support the argument that the phonon value of 268 cm^{-1} measured for the low cerium sample actually is the dominant vibrational mode of the cerium activator. The phonon values for the medium and high cerium samples are likely not the values of the actual dominant phonon mode, but rather a value that represent the convolution of multiple strong phonon modes. As dopant concentration is increased and the number of defects and stresses increase in the material it follows that the additional defects and stresses would add complexity to the vibrational modes coupling with the cerium site. The Huang-Rhys values (*S* in table 8) for the samples are close to 5 and above, which places the cerium activator in a regime of strong to medium lattice-coupling. This implies the cerium site will be strongly affected by the phonons of the host crystal lattice, adding credence to the notion that internal stresses and defects in the lattice will affect the activator site.

Configuration coordinate diagram

The shape of the CC diagrams are predominately governed by the phonon energies of electron-phonon coupling values measured from the homogeneous thermal broadening. The observed changes in the electron-phonon coupling values and the corresponding large shifts in the parabola widths of the CC diagrams were surprising. Initial qualitative inspection of the single luminescence center CC model suggests it accurately depicts the behavior of the low cerium sample and breaks down for higher cerium concentrations. However, upon closer inspection the CC model explains the observed behavior of the system even at higher cerium concentrations. The ground state broadens with increasing cerium signifying a broadening of the wave functions of the vibrational state and increased absorption probability which is reflected in the broadening observed in the excitation spectrum (figure 24). This also accurately represents the demonstrated increase in self-absorption. The excited state unexpectedly narrows with increasing cerium concentration, but this is again reflected in the emission spectra plotted in figure 24. The position of the conduction band accurately explains the thermal quenching energies (E_a) observed for the low and medium cerium concentration samples. The discrepancy between the values of the high cerium sample can solidly be explained by the demonstrated concentration quenching due to self-absorption. As mentioned above, the measured phonon values for the medium and high cerium samples may not be the actual phonon modes of the cerium site, but they do accurately represent the observed cumulative behavior when the

116

systems are described using a CC model with one luminescence site and a single "breathing mode" vibration.

Nature of Ce2

Unfortunately, a concrete conclusion was not obtained regarding the structural nature of the Ce2 luminescence site. Calculations of the cerium electronic structure suggest Ce1 is 7 oxygen coordinated and have found less energy is required to put cerium in the 7 coordinated site [43-46]. Electron paramagnetic resonance spectroscopy measurements of LSO:Ce have also suggested cerium prefers the 7 coordinated site [57]. Additionally, the presently measured energy values were in better agreement with calculated energy values for 7 oxygen coordinated cerium [45]. Therefore, it is concluded the 7 oxygen coordinated site exhibits Ce1 luminescence. However this does not specifically explain the nature of Ce2. It is still possible that the 6 coordinated site exhibits Ce2 luminescence or that it exhibits Ce1 luminescence and Ce2 luminescence it due to interstitial cerium; evidence exist for both scenarios [10-12].

Summary

The effect of cerium concentration on single crystal LSO was investigated with temperature dependent steady state and time resolved luminescence spectroscopy. The results were used to determine the thermal quenching activation energies and the

phonon energies responsible for the thermal broadening of the luminescence spectra. The measured electron-phonon coupling values where shown to correspond to a Raman active Lu cation of the host LSO for small cerium concentrations. The measured phonon values were used to calculate CC diagrams of the luminescence centers. The nature of single crystal LSO:Ce concentration quenching was determined to be due to radiative energy transfer, and ultimately self-absorption. The observed broadening of the excitation spectra and narrowing of the emission spectra with increasing cerium was explained via a CC model. A combination of the CC model and concentration quenching explained the measured thermal quenching activation energies.

CHAPTER IV
ACTIVATOR CONCENTRATION IN A THIN FILM

The cross-sectional scanning electron image, the photoluminescence intensity and the low temperature photoluminescence spectra as a function of cerium concentration have been published previously by Philip Rack, Charles Melcher, and myself [31]. Of the work presented in this chapter Charles Feigerle helped perform the Raman shift measurements, Allen Patchen helped perform the wavelength dispersive spectroscopy measurements and Joo Hyon Noh helped calibrate the sputtering model. Philip Rack and Charles Melcher provided direction, funding of the research, discussion and motivation.

Introduction

In addition to using thin film combinatorial screening to explore binary material systems it would be advantageous to apply the technique to optimize the activator concentration in a known scintillator. To this end, cerium doped Lu_2SiO_5 (LSO) was chosen. In this chapter the effect of cerium concentration on the luminescence quenching mechanisms of thin film LSO will be discussed. The elucidation of the cerium concentration dependent behavior of single crystal LSO conducted in chapter 3 is used as a foundation to enable an accurate investigation of the thin film LSO. The required phenomenological and theoretical background is covered in chapter 3.

Figure 46 is an image taken of the single crystal and thin film cerium doped LSO samples under excitation by 366 nm ultra-violet (UV) lamp. Figure 46 gives a good qualitative
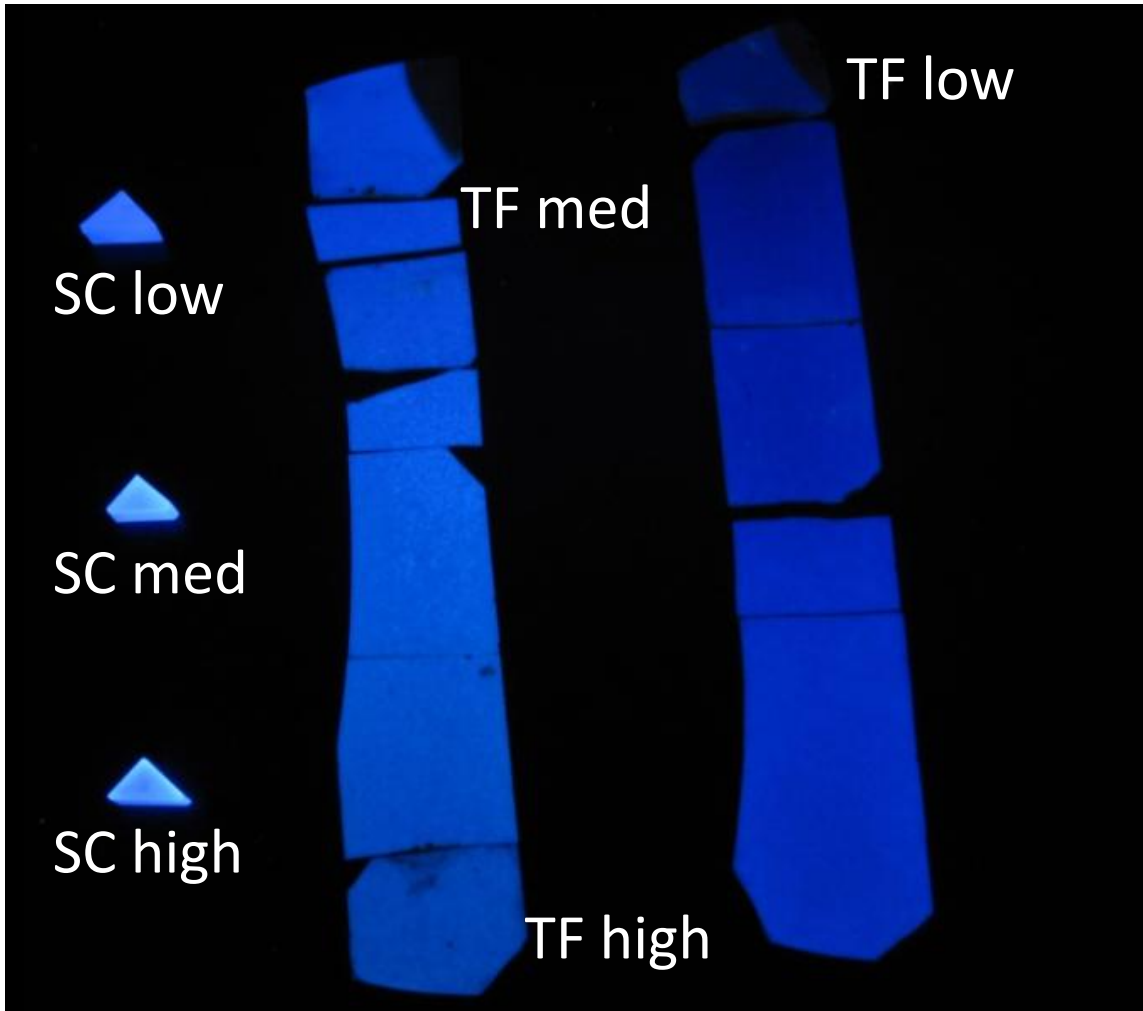
Figure 46. Image of the thin film and single crystal LSO:Ce samples under a 366 nm UV light.

understanding of the respective emission intensities based on cerium concentration. The medium (0.0095) single crystal LSO sample is noticeably brighter than the high (0.078 at%) and low (0.0015 at%) single crystal samples and the medium (0.34 at%) thin film is noticeably the brightest of the thin film compositions. The qualitative analysis of figure 46 is supported by the results from quantitative measurements of the emission intensity for the samples, which are plotted versus cerium concentration in figure 47. Figure 47 is the integrated (370-470 nm) room temperature PL emission (360 nm excitation) for thin film and single crystal samples along with relative light output (^{137}Cs excitation) for the single crystal samples. The intriguing result is that the thin film exhibits a peak emission intensity at a higher cerium concentration than the single crystal LSO (0.34 at% cerium compared to 0.01 at%, respectively). The desire to understand the observed thin film LSO concentration quenching illustrated in figure 47 and the discrepancy between the ideal cerium concentrations for thin film and bulk single crystal LSO prompted much of the research covered in this chapter.

Experimental procedure

Thin film deposition

The processing procedure for LSO:Ce thin films with a cerium concentration gradient was similar to the procedure used for the deposition of the Lu_2O_3-SiO_2 gradient samples investigated in chapter 2. The key modification was rotating the substrate during
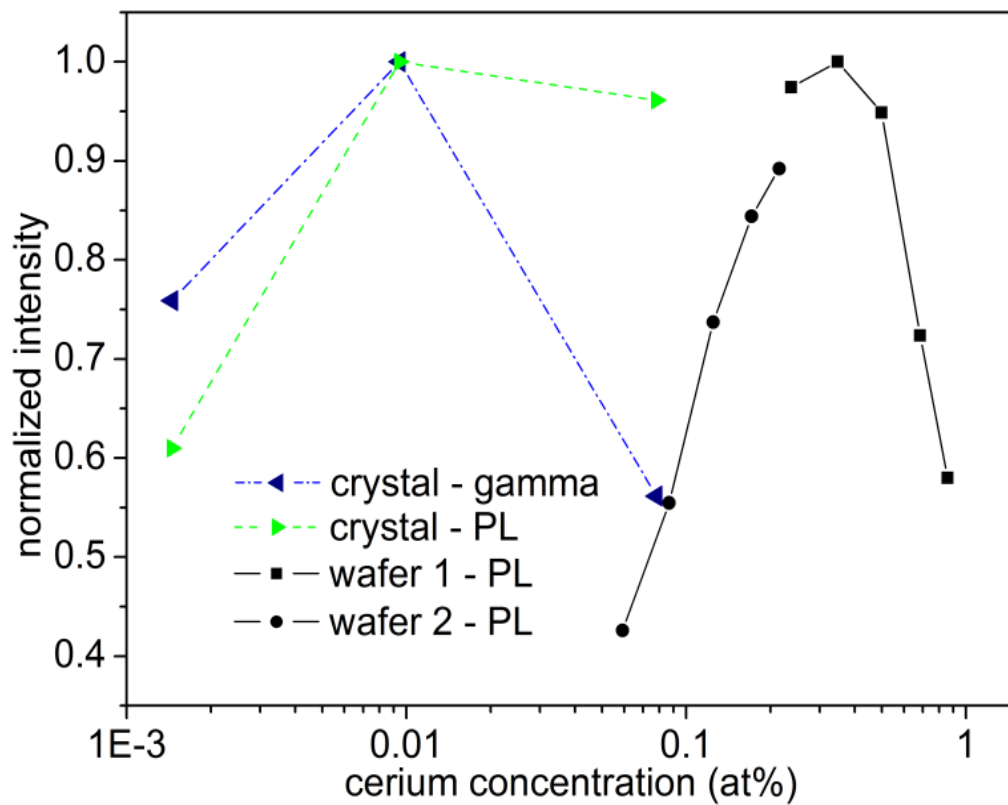
Figure 47. Relative emission intensity versus cerium concentration for thin film and bulk single crystal LSO.

lutetium silicon reactive co-sputtering (thus depositing uniform LSO as opposed to a Lu_2O_3-SiO_2 gradient as in chapter 2) and holding the substrate stationary during cerium sputtering (thus depositing a cerium thickness gradient as opposed to uniform cerium as in chapter 2). However, for completeness and accuracy the main procedure is covered below. Additionally, some processing values, such as power settings and sputtering time, were adjusted due to wear on the targets and changes in the sputter chamber/system conditions.

Samples were reactively sputter deposited from elemental cerium, lutetium and silicon targets in an Ar-O_2 atmosphere onto 100mm diameter polished alumina substrates using an AJA International ATC 2000 R.F. magnetron sputter system. Three individual R.F. sputtering sources (50mm diameter) were used. The cerium and silicon targets were mounted at azimuths of 90 and 180 degrees, respectively, in reference to the lutetium target. To sputter LSO, the substrate was rotated at 20 revolutions per minute while co-sputtering lutetium and silicon at R.F. power settings of 200 watts and 114 watts in an atmosphere of argon and oxygen maintained at 3 mTorr with an oxygen partial pressure of 7.4 % (O_2 flow rate = 2 sccm, Ar flow rate = 25 sccm). The cerium was deposited with a specific orientation so-as to create a cerium thickness gradient along one axis of the substrate. The cerium was sputtered at 25 watts in an argon atmosphere at a pressure of 3 mTorr with the substrate stationary. Thin film LSO with a cerium thickness gradient was deposited by alternating five layers of LSO with constant thickness and four layers of cerium with a thickness gradient. The five LSO layers were

sputtered for 930 seconds each. To achieve the desired range of Ce concentration, two samples were sputtered: 1) a low Ce concentration sample with four Ce layers sputtered for 104 seconds each and 2) a high Ce concentration sample with four Ce layers sputtered for 416 seconds each. Figure 48a illustrates a cross-section schematic of the as-deposited multi-layer thin film structure cut parallel to the Ce gradient, and figure 48b shows an SEM image of the as-deposited structure. Each individual LSO layer is clearly observed and each layer is close to the target value of 200nm for a total film thickness of approximately 1μm (measured ~0.96 μm).

Samples were annealed in nitrogen at 1400 °C for a total of 10 hours to crystallize the film and to diffuse the cerium into the Lu-Si-O films. This diffusion step is adequate to homogenize the films perpendicular to the substrate (in the thickness dimension which equates to ~200 nm for the top and bottom layers and ~100 nm for the middle 3 layers) but not sufficient to alter the gradient along the axis of the sputtered cerium thickness gradient (100 mm). Emission intensity was found to vary critically with annealing temperature and conditions. To assure uniform annealing conditions the samples were first annealed for 5 hours at 1400 °C then cooled, rotated 180 degrees and annealed a second time, again for 5 hours at 1400 °C. This annealing procedure was found to yield repeatable emission intensity values. X-ray diffraction (XRD) of the annealed samples confirmed crystalline LSO and showed no discernable cerium oxides.
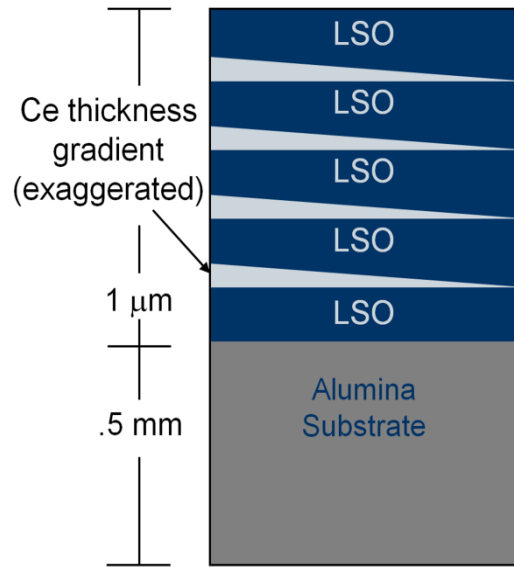
a.
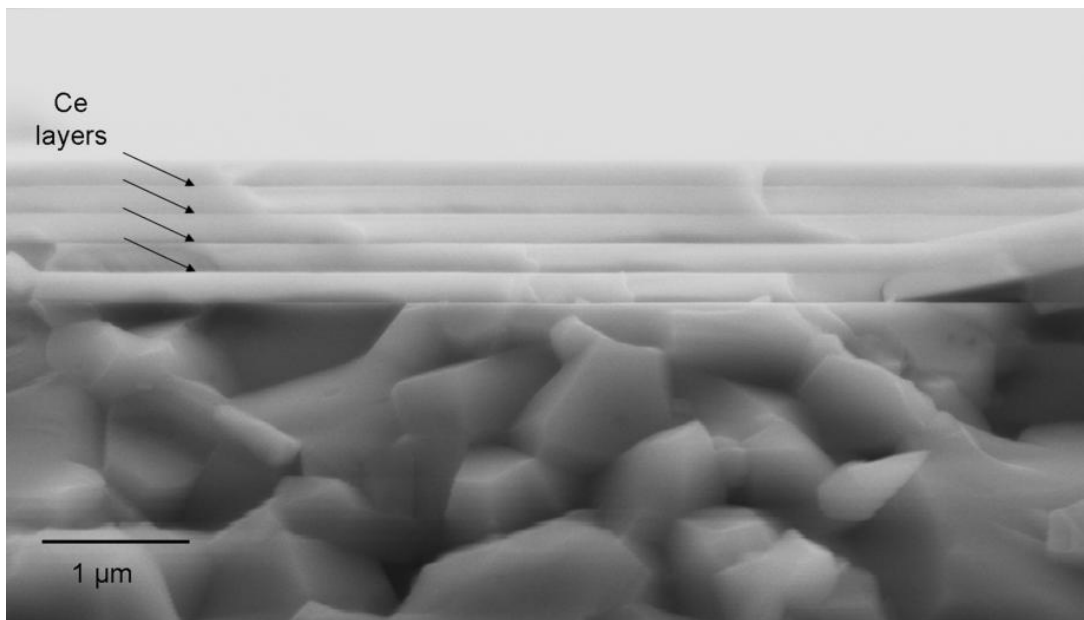
b.

Figure 48. a) A cross-section schematic of the as-deposited multi-layer thin film structure cut parallel to the Ce gradient, and b) an SEM image of the as-deposited structure.

Characterization

Scanning electron microscopy was performed using a Hitachi 4300 scanning electron microscope to confirm as-deposited thickness. Film composition was measured using wavelength dispersive spectroscopy (WDS) on a Comeca 100 electron probe microanalysis (EPMA) system at an accelerating voltage of 15 keV. Concentrations of all elements were taken at the middle and each end of the cerium gradient for each sample. For each location along the cerium gradient, concentration was measured at three comparable points to gauge measurement accuracy and film uniformity. Photoluminescence (PL) emission and excitation spectra were measured using a Hitachi F-4500 spectrophotometer at a scan rate of 240 nm/min. The photomultiplier tube voltage along with the excitation slit and emission slit were uniform for all measurements. Low temperature PL measurements were measured with the addition of an ARS cryostat with a Lakeshore 331-S temperature controller for four samples with cerium concentrations of 0.86, 0.34, 0.23 and 0.06 at% from 40 to 420 K. PL lifetime measurements were made using a Horiba Jobin Yvon Flouralog-3 Spectrofluorometer with the addition of an R-928 hub and NanoLED excitation sources (introduced in the procedure section of Chapter 4) with time-correlated single photon counting capability. Temperature lifetime photoluminescence measurements were made using an ARS model CS202 cryostat integrated with the Horiba spectrophotometer and a Lake Shore 331-S temperature controller for three samples with high (0.86 at%) , medium (0.34 at%) and low (0.06 at%) cerium concentrations between 27 to 320 K. XRD peaks were

measured from 10 to 60 degrees 2-theta with a step size of 0.02 degrees at 2 seconds per step using a Philips X'Pert diffractometer for three positions (1, 5 and 9 cm along cerium gradient) on the low cerium wafer and five positions on the high cerium wafer (1, 3, 5, 7 and 9 cm along cerium gradient). Peak matching and semi-quantitative analysis [58] of the measured XRD spectra were performed using PANalytical B.V. X'Pert HighScore software. Raman shift measurements were performed using a Horiba Jobin-Yvon T64000 Raman spectrometer with excitation by an unpolarized 514.5 nm laser.

Model of sputtered composition

A sputtering model based on previous work by Fowlkes, et al. [26] was introduced in chapter 2. This model was used to simulate the cerium composition profile of the LSO:Ce films. The model uses the standard surface source evaporation equation (equation 2.1) to incorporate the spatial profile of the sputtering flux and the processing chamber's geometry to determine the thickness profile expressed as the dM_s/dA_s (and ultimately concentration profile after anneal), where M_s is the mass sputtered on to the substrate and A_s is the area of the substrate. The forward peaking value, n, in the sputtering model was calibrated for the ATC 2000 RF sputter system by fitting modeled thickness profiles to sputtered nickel and SiO_2 thickness gradients. A value of n=6 and was found to yield accurate results. A gun tilt of 29.7 degrees for the system was measured. The cerium sputtering rate for use in the model was obtained using the WDS results for measurements near the center of each wafer. The sputter rates for the high and low cerium wafers were consistent at 0.06 nm/min.

Results

General

The measured and modeled cerium concentrations versus substrate position along the cerium gradient axis (in line with the cerium sputter source) are plotted in figure 49. The error bars represent the measured cerium concentration standard deviation of 0.02 %. The concentrations of lutetium and silicon were essentially constant across both samples and consistent with the LSO stoichiometry (Lu/Si=2.05 +/- 0.14). For both gradient samples the measured and modeled cerium concentration profiles were in good agreement. Aluminum concentrations of less than 0.1% were measured and are attributed to the substrate and film-substrate interdiffusion (Monte Carlo simulations of the electron penetration depth at 15 keV showed the interaction was nominally limited to the 1 μm thick LSO films).

The XRD spectrum of thin film LSO with a cerium concentration of 0.35 at% is plotted in figure 50 with the peaks of the phases presented highlighted. As with the thin film Lu_2O_3 to SiO_2 gradient samples, $Al_5Lu_3O_{12}$ (LuAG) peaks were again present. Semi-quantitative analysis of the XRD spectra taken at a total of eight positions along the two cerium gradients estimated an overall average LuAG concentration of 9.7 at% with a standard deviation of 2.3 at% (with 90.3 at% LSO) and did not exhibit a correlation with
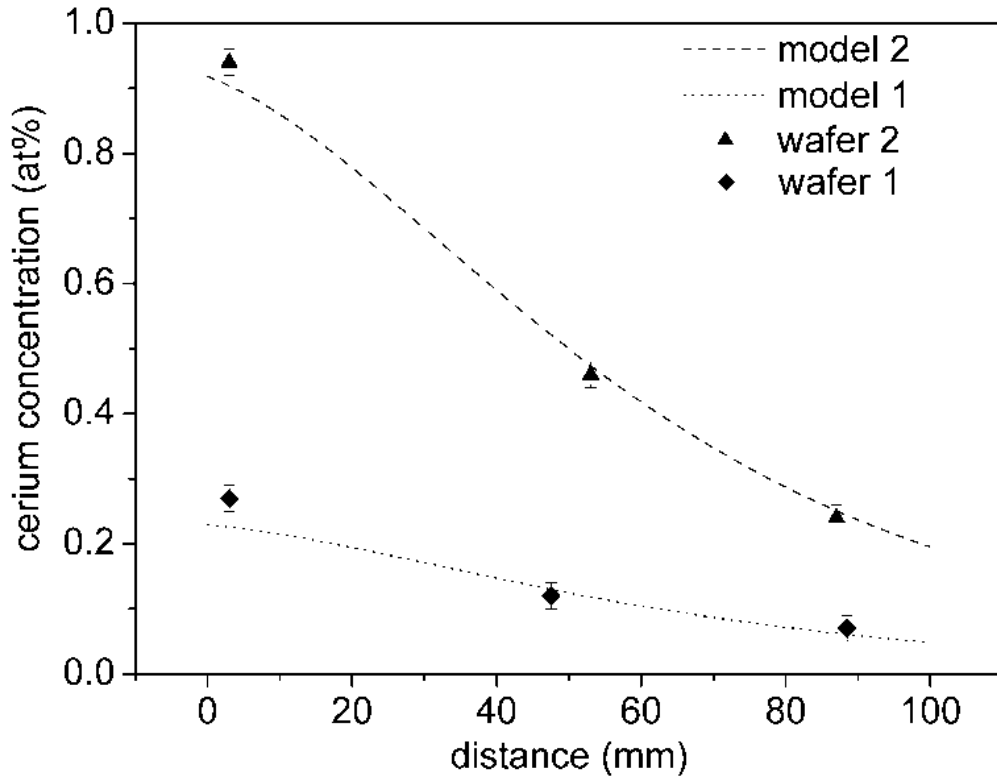
Figure 49. Measured and modeled cerium concentrations versus substrate position along the cerium gradient axis.
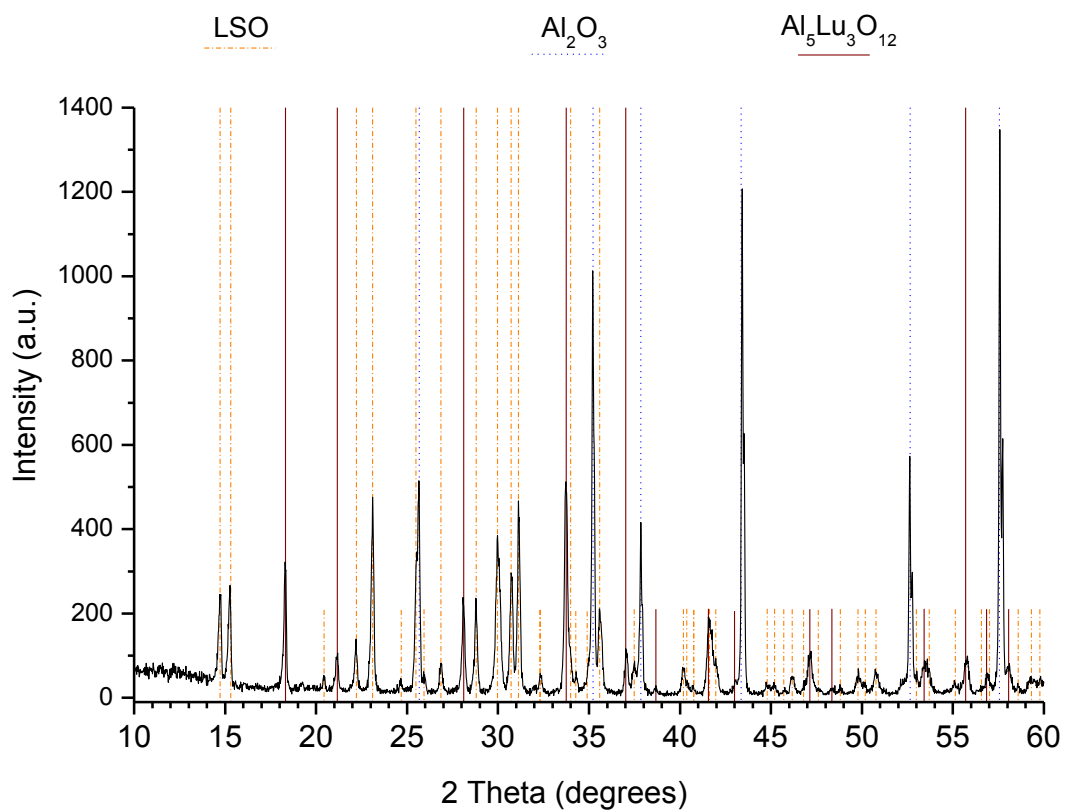
Figure 50. XRD spectrum of thin film LSO with a cerium concentration of 0.35 at%.

measurement position. The spectra showed no discernable cerium-oxide based compounds nor additional Lu, Si or Al based compounds.

Photoluminescence spectra

Normalized excitation (400 nm emission wavelength) and emission (360 nm excitation wavelength) PL spectra of the thin film samples measured at 40 K for selected cerium concentrations are plotted in figure 51. The broadening with cerium concentration observed in the excitation spectrum of bulk single crystal LSO (figure 24) is seen to a lesser extent in the thin film LSO. The higher energy 265 nm and 300 nm peaks show lower relative intensity and the region between the 300 nm and 360 nm peaks shows a higher relative intensity. The emission spectra exhibit low energy broadening. The excitation and emission spectra for the low cerium (0.06 at%) and high cerium (0.86 at%) samples are plotted in figure 52a and b, respectively. Following the Ce1 and Ce2 site designation [5-6, 21], emission at 400 nm and excitation at 360 nm was intended to excite Ce1; emission at 500 nm and excitation at 325 nm was intended to excited Ce2. In comparison to the single crystal samples (figure 25), the overlap between the excitation and emission spectra is noticeably decreased, even in the higher cerium (0.86 at%) spectra. This suggests the Ce-Ce radiative energy transfer that dominated the single crystal LSO emission behavior should be less of a factor in the thin film LSO:Ce. The Ce2 characteristic spectral profile is noticeable absent, indicating cerium is not present in the Ce2 site or, if it is present, is not actively luminescent. Additionally, the higher cerium (0.86 at%) excitation spectrum for 500 nm emission exhibits a low intensity

131
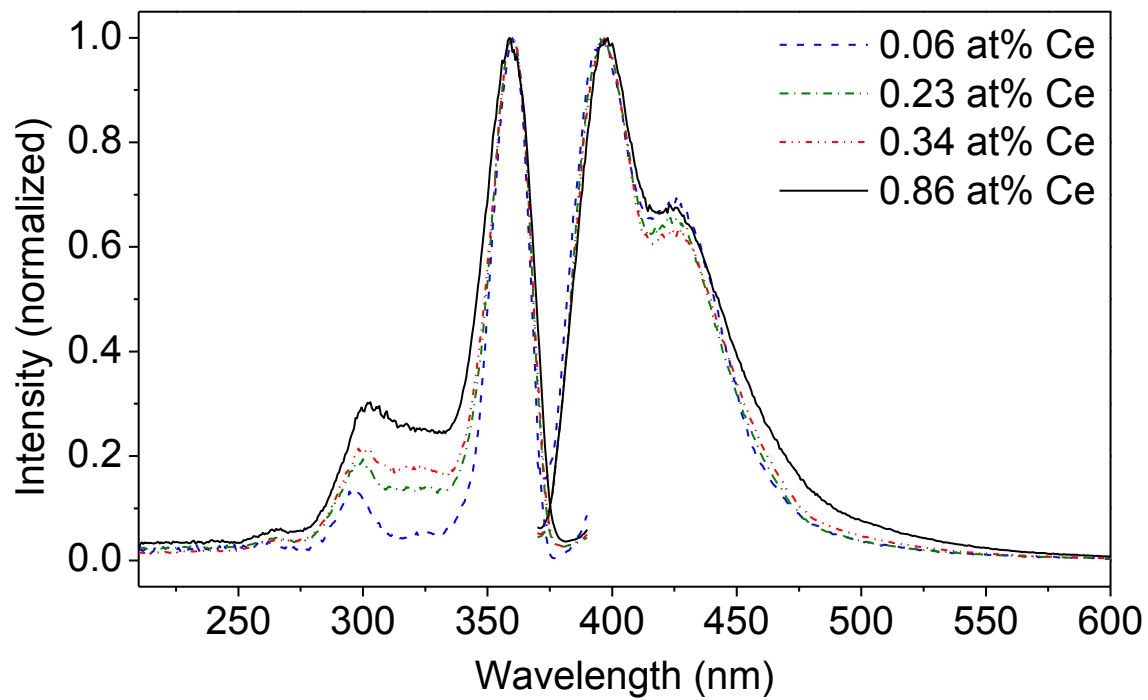
Figure 51. Normalized PL spectra of thin film LSO measured at 40 K for selected cerium concentrations
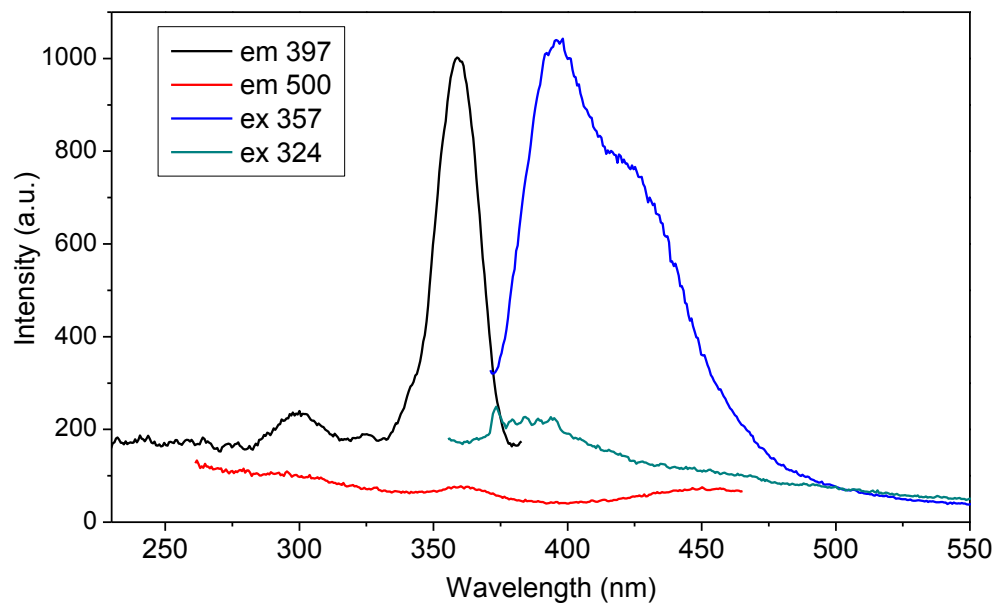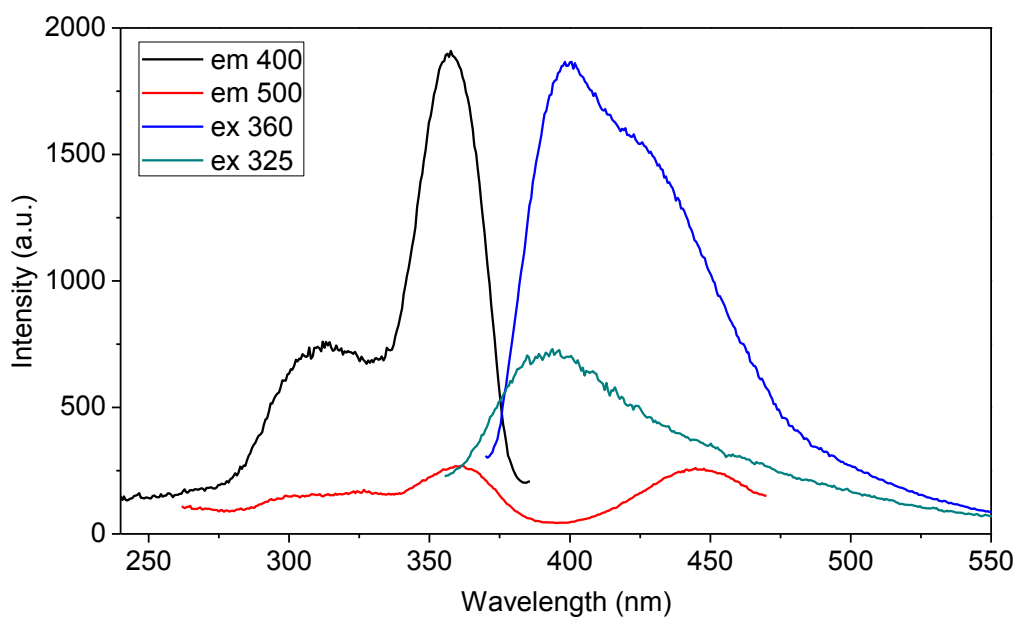
Figure 52. PL spectra at 200 K for thin film LSO with cerium concentrations of a) 0.06 at% and b) 0.86 at%.

Corresponding plots at 40 K are given in figure A-10 of the appendix.

peak at 450 nm. This peak is attributed the excitation band for the corresponding 500 nm emission of cerium doped LuAG [59] which is also present in the XRD and may alter the emission line for 360 nm excititation (plotted in figure 51).

Temperature dependent photoluminescence

Excitation (400 nm emission) and emission (360 nm excitation) spectra for thin film LSO with a cerium concentration of 0.34 at% at selected temperatures are plotted in figure 53. At room temperature the intensity is roughly 30 % of the low temperature spectra in comparison to the single crystal samples (figure 32) which exhibited a room temperature intensity close to 80 % of the low temperature value. Additionally, the thin film samples' emission was quenched at 400 K, compared to 600 K for the single crystal LSO. Integrated excitation (336 – 475 nm) and emission (380 – 460 nm) intensity versus temperature for selected cerium concentrations are plotted in figure 54a and b, respectively. As cerium concentration is increased there is an observed increase in temperature induced quenching. In figure 55 the high (0.86 at%) and low (0.06 at%) samples' emission intensity values are plotted versus temperature along with a least-squares fit of equation (3.6). The temperature quenching activation energy values [obtained by fitting equation (3.6) to the plots in figure 54a and b] for the Ce1 characteristic excitation and emission are reported in table 11. As mentioned previously, the thin film samples did not exhibit the characteristic Ce2 emission so Ce2 quenching values are not included. The Ce1 values are plotted versus cerium concentration in figure 56 and decrease with increase concentration. The single crystal LSO results
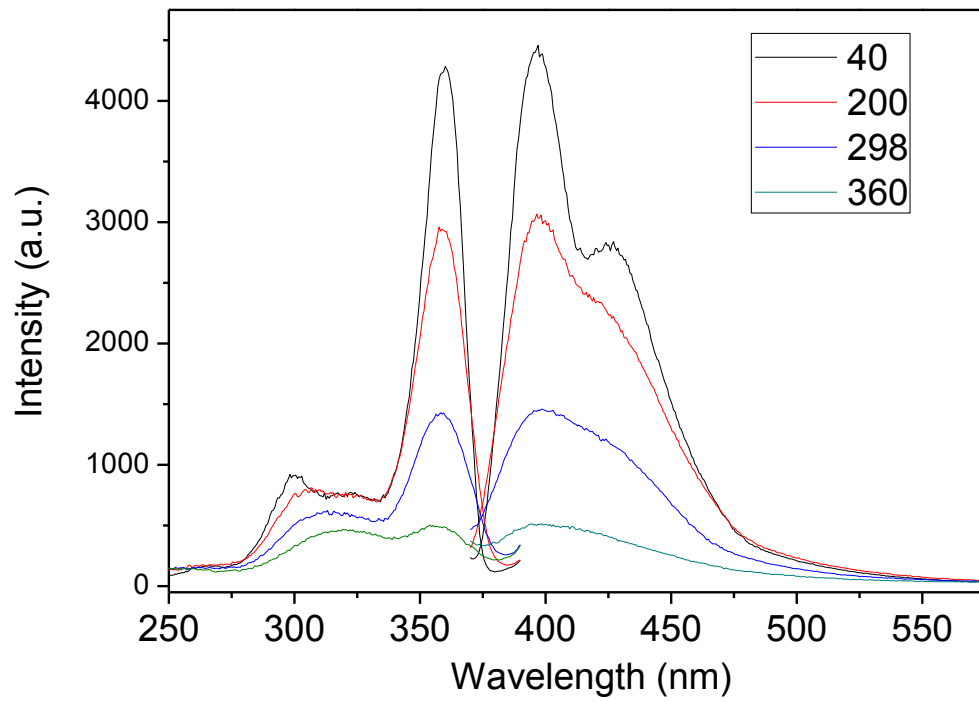
Figure 53. Excitation (400 nm emission) and emission (360 nm excitation) spectra for thin film LSO with a cerium concentration of 0.34 at% at selected temperatures.
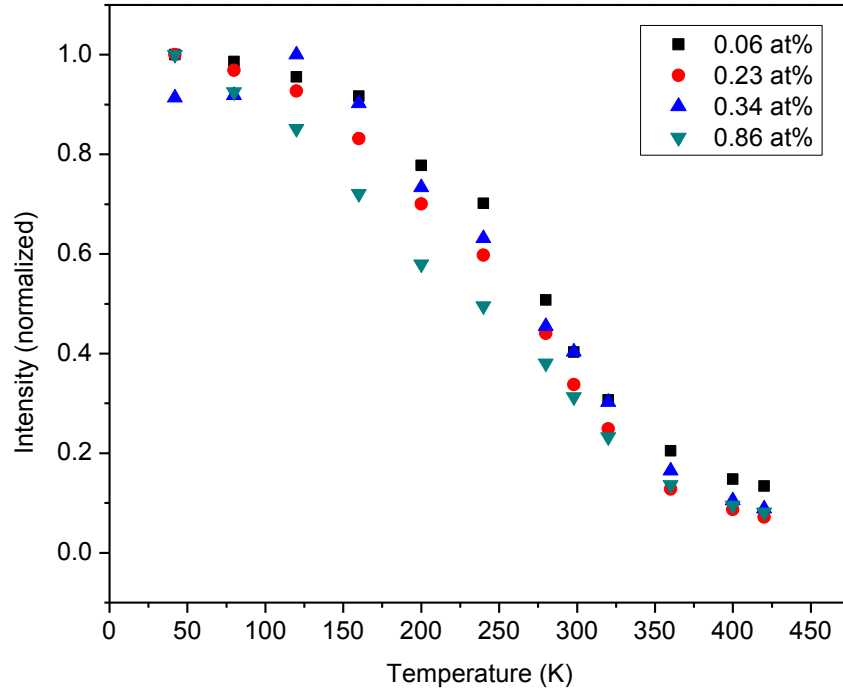
a.
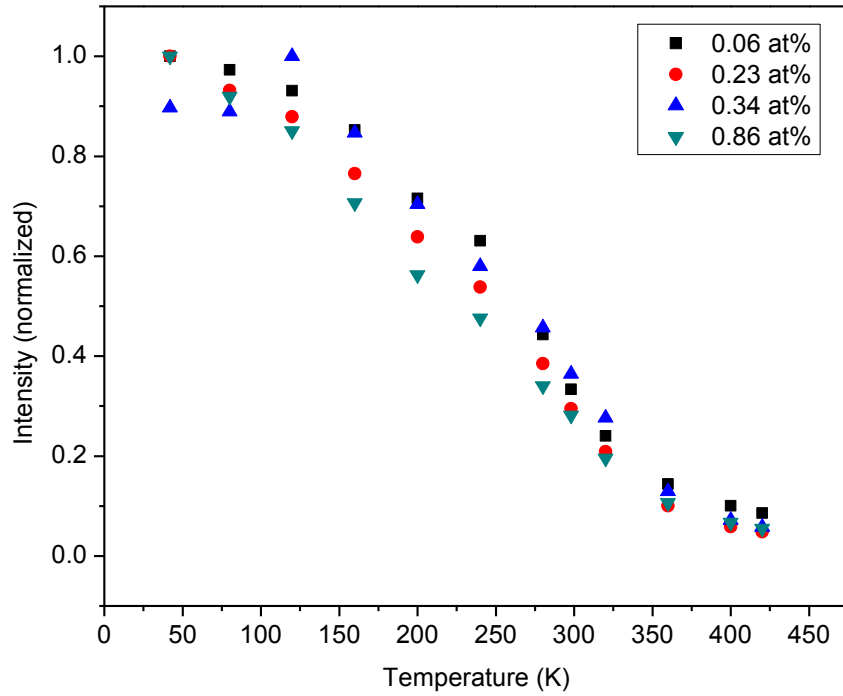
b.

Figure 54. Integrated excitation (336 – 475 nm) and emission (380 – 460 nm) intensity versus temperature for selected cerium concentrations.
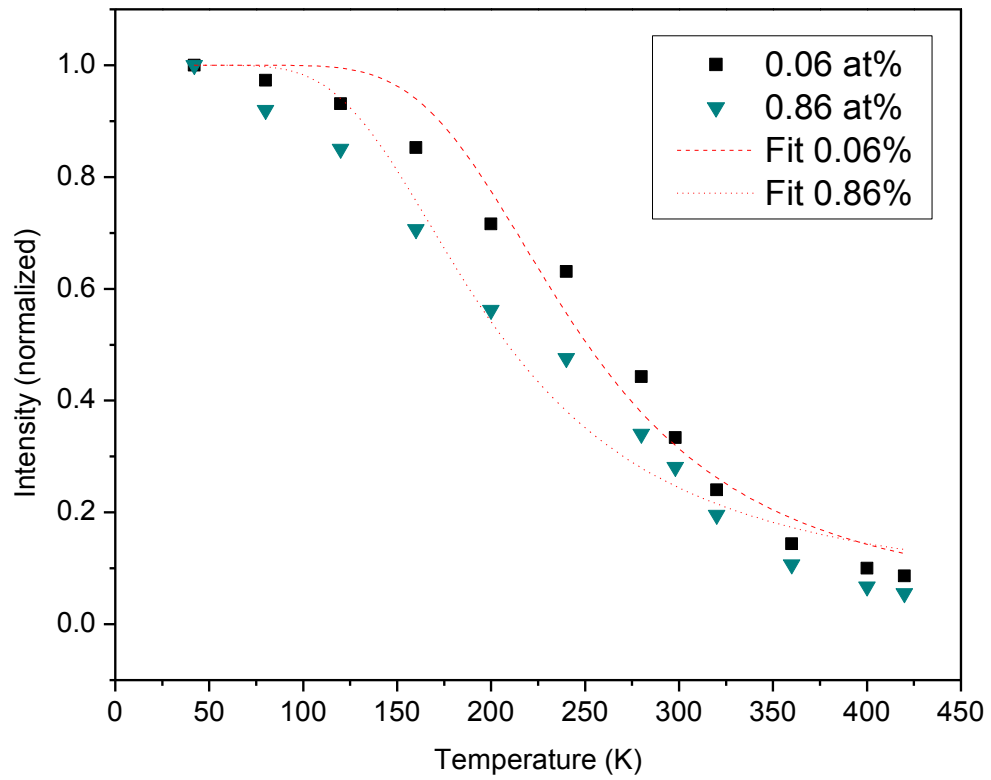
Figure 55. Integrated emission (380 – 460 nm) intensity versus temperature for cerium concentration of 0.06 and 0.86 at% along with fits of equation (3.6).

Table 11. Thin film LSO:Ce temperature quenching activation energy values.

a.

Sample ID		A6-1	+/-	B6-1	+/-
Cerium		0.06 at%	+/-	0.23 at%	+/-
em 400 nm	E (meV)	114	9.9	98.8	12.5
(Int. 336-375 nm)	A	131	53	104	57
ex 360 nm	E (meV)	104.2	12.2	84.1	12.7
(Int. 380 to 460)	A	123	65	73	43

b.

Sample ID		B6-3	+/-	B6-9	+/-
Cerium		0.34 at%	+/-	0.86 at%	+/-
em 400 nm	E (meV)	106.8	13.4	64.2	8.5
(Int. 336-375 nm)	A	119	67	32	13
ex 360 nm	E (meV)	101	16	67	9.2
(Int. 380 to 460)	A	111	76	41	19
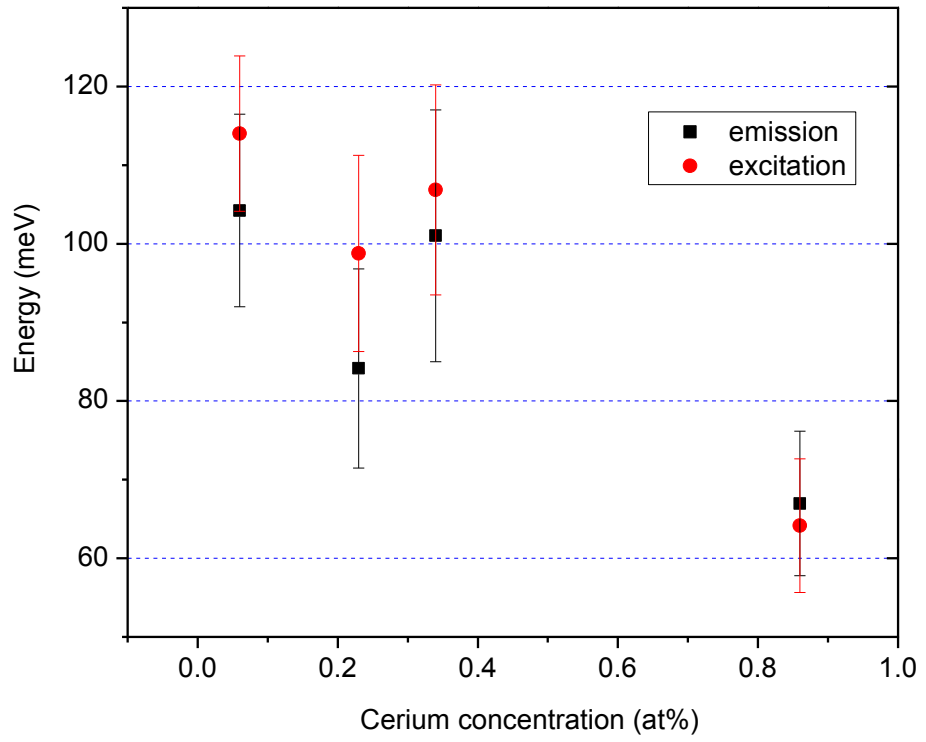
Figure 56. Thermal quenching activation energies plotted versus cerium concentration.

(figure 33) showed excellent agreement with equation (3.6), while the thin film samples exhibit less of a sigmoidal shape. Equation (3.6) models one radiative rate (W_R) and one non-radiative rate (W_{NR}) (or one radiative and one non-radiative pathway) and gives the thermal activation energy (E_a) for the non-radiative rate (or pathway). The temperature quenching behavior of the thin films can be explained by the presence of a distribution of activator sites with defect related non-radiative pathways in the material that are increasingly activated by increasing temperature. A visualization of this model is diagramed in figure 57 with the activator situated between the conduction and valence bands (labeled CB and VB, respectively). As temperature is increased, an electron in the excited state is able to reach higher energy non-radiative pathways. It is not implied that each activator has multiple quenching pathways (though possible), but rather that each activator has a different quenching activation energy corresponding to a different defect-based non-radiative pathway, leading to the distribution of non-radiative pathways throughout the film. The exact nature of these defect-related pathways are not specifically determined but possible defects include oxygen vacancies, cerium near grain boundaries, or non-radiative cerium sites.

Temperature dependent photoluminescence decay time

The room temperature photoluminescent decay profiles at 360 nm excitation and 400 nm emission for the low (0.06 at%) and high (0.86 at%) cerium thin film samples are plotted in figure 58 with the time at 1/e intensity indicated. The decay time profile for the high cerium sample is noticeably shorter. The PL decay profile at 27 K (360 nm
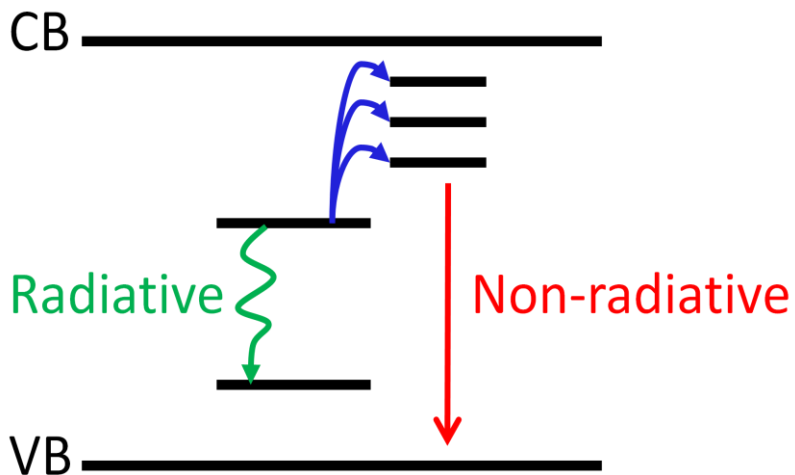
Figure 57. Diagram of multiple non-radiative pathways with increasing thermal quenching activation energies.
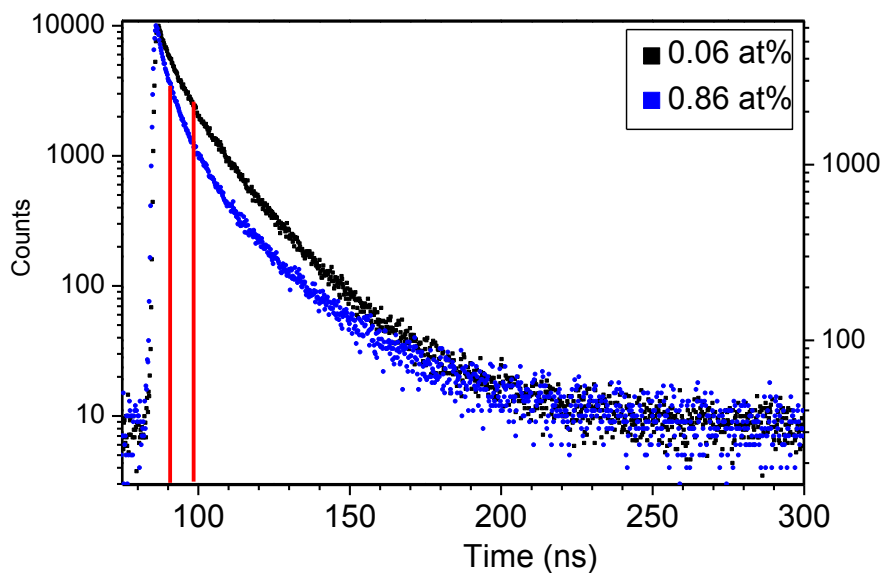
Figure 58. Room temperature photoluminescent decay profiles at 360 nm excitation and 400 nm emission for the low (0.06 at%) and high (0.86 at%) cerium thin film LSO samples.

excitation, 400 nm emission) for the medium (0.34 at%) cerium concentration is plotted in figure 59 along with a fit of equation (3.3) utilizing three decay-time constants. The longest time-constant of 32.4 ns is attributed to the cerium center and is close to the intrinsic decay time for 400 nm emission. The faster two components at 15.7 ns and 4.8 ns are not attributed to specific electron transition pathways. Similar to the "straightening" of the steady-state PL temperature quenching profile, the additional time-constants are simply fitting the behavior exhibited by a distribution of non-radiative pathways throughout the material. Because the time constants do not represent specific pathways it is more demonstrative to look at the integration of the emission pulse time-profile. Since the measured decay time, $\tau(T)$, is related to the luminescence efficiency by equation (3.4), the plot should be expected to show a trend with cerium concentration similar to the temperature quenching plots: the luminescence efficiency should decrease with increasing cerium. The normalized integrated intensity of the emission pulse shape is plotted for high (0.86 at%) medium (0.34 at%) and low cerium (0.06 at%) concentrations versus temperature in figure 60. For comparison, the time constants and amplitude weighted ratios for a three component fit of the decay time profile for the medium cerium concentration at each measured temperature are plotted in figure 61a and b. The single crystal LSO samples exhibited an increase in the decay time with temperature and cerium concentration (figure 27) indicating (radiative) energy transfer. The thin film samples exhibit the opposite behavior. In figure 60 the area under the pulse shape decreases with

142

Equation	y = y0 + A1*exp(-(x-x0)/t1) + A2*exp(-(x-x0)/t2) + A3*exp(-(x-x0)/t3)	
Adj. R-Square	0.99972	
	Value	Standard Error
y0	17.15204	0.33519
x0	86.6	0
A1	2218.25479	103.85237
t1	4.75916	0.14545
A2	3046.71977	151.59
t2	15.67855	0.89559
A3	4938.17194	231.40253
t3	32.41507	0.42063
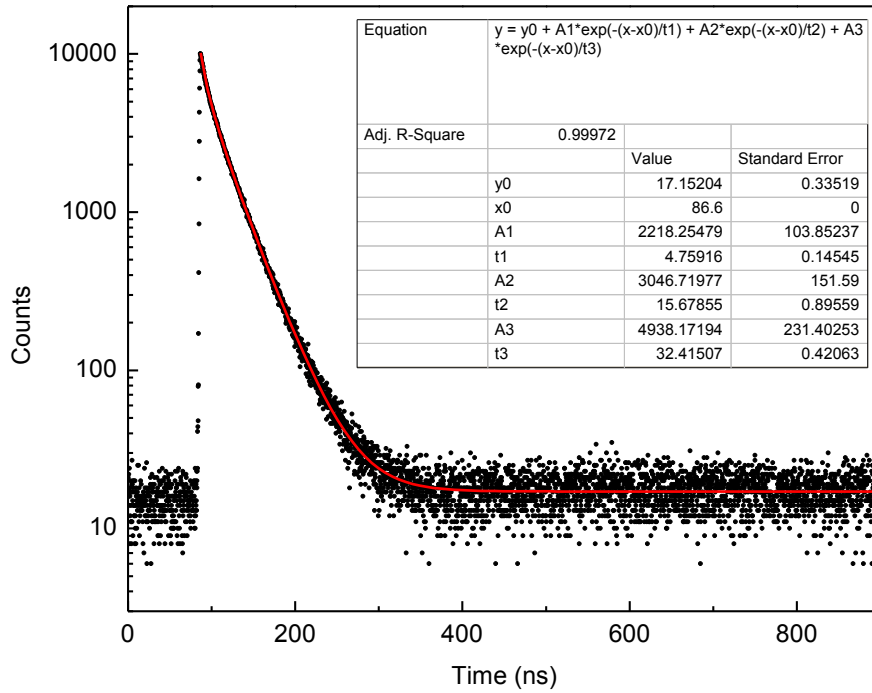
Figure 59. The PL decay profile at 27 K (360 nm excitation, 400 nm emission) for the medium (0.34 at%) cerium concentration sample with a 3-component decay fit.
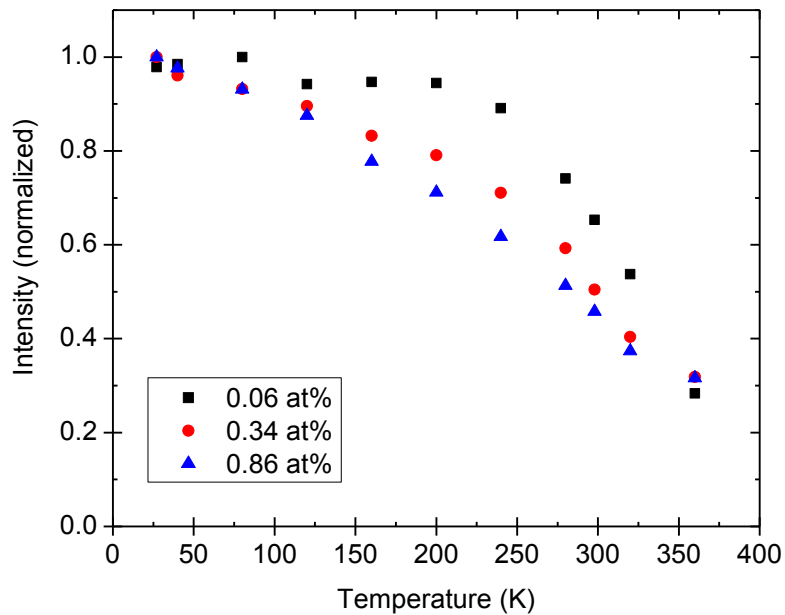
Figure 60. The normalized integrated intensity of the emission pulse shape for high (0.86 at%) medium (0.34 at%) and low cerium (0.06 at%) concentrations versus temperature.

143
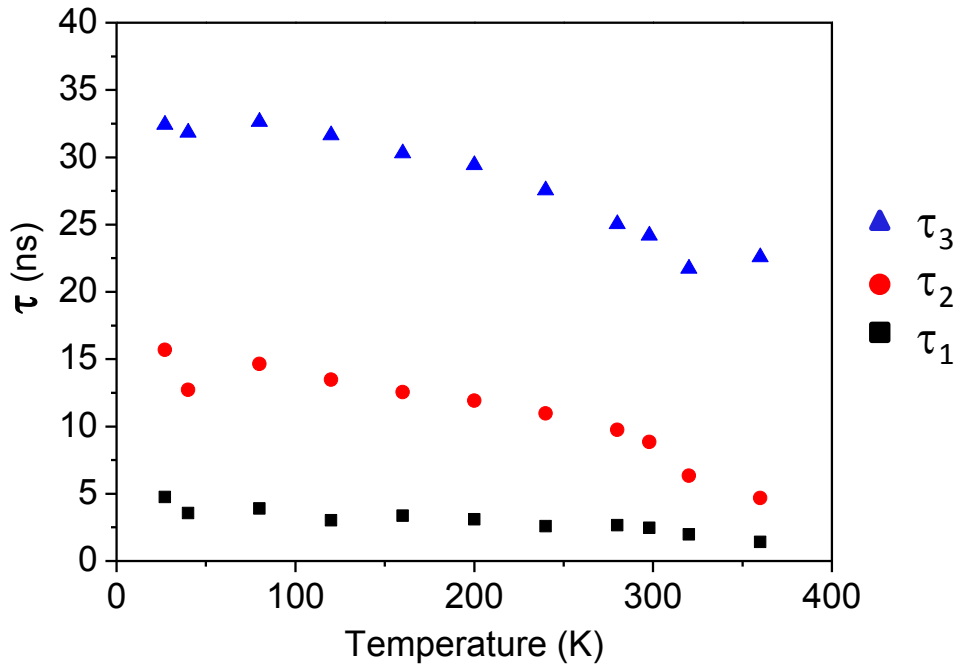
a.
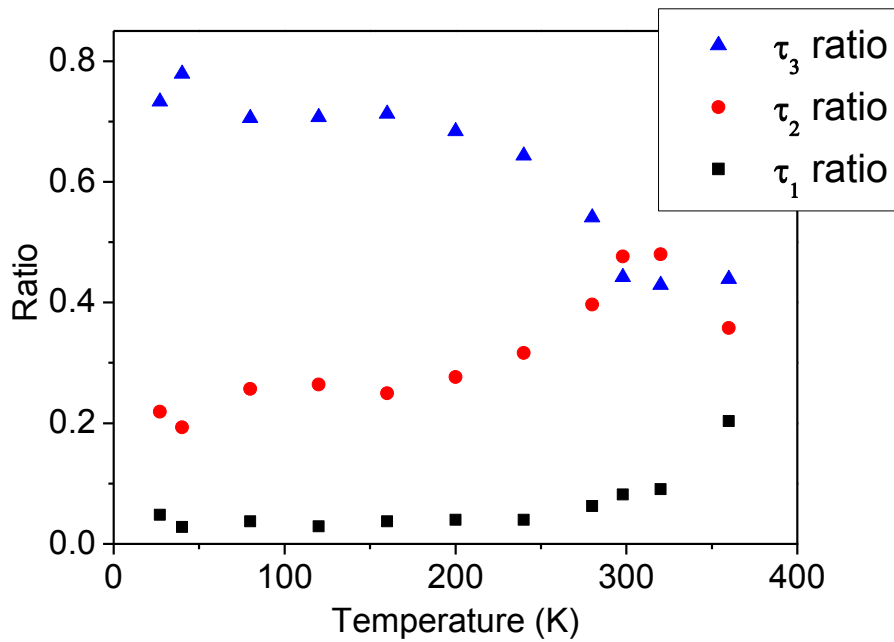
b.

Figure 61. a) The time constants and b) the amplitude weighted ratios for a three component fit of the decay time profile for the medium (0.34 at%) cerium concentration sample.

increasing temperature and cerium concentration. Plotting the decay time values for decay profiles fitted with exponential decay functions yields similar results (as plotted in figure 61a). The decrease in the radiative energy transfer suggested by the decrease in the spectral overlap for the thin films (figure 52) is confirmed by the continuously decreasing profiles of figure 60 and figure 61a. Furthermore, the thin film temperature quenching plots (figure 54 and figure 55) suggested an increase in the number of non-radiative pathways with increasing cerium concentration, which is also confirmed by the decrease of the decay time profiles with increasing cerium for the time-dependent measurements.

Cerium electron-phonon coupling

In chapter 3 the phonon energy responsible for the homogeneous thermal broadening of the PL spectra and the degree of lattice coupling was measured for bulk single crystal LSO:Ce using both Gaussian peak fits and manually measuring the values from the spectra. For several reasons it was found the manual measurements were more accurate.

While the PL spectra of the thin film LSO samples do not appear to be complicated by Ce2 emission or self-absorption and the excitation peak is narrower, the additional phases present due to film-substrate diffusion made Gaussian fitting impractical. Gaussian fitting was attempted, but unsuccessful. However, the low energy side of the 360 nm emission peak and the high energy side of the 400 nm excitation peak did not

exhibit any signs of being influenced by overlapping peaks. Therefore, half-width half-max (HWHM) values for the thin film samples were measured manually from the spectra. The half-max energy position was found using a six-point linear interpolation to remove artifacts caused by the step size of the raw date recorded by the instrument (an example is plotted in figure A-7 of the appendix). The energy values for the thin film samples' peaks changed very little with temperature, therefore a linear interpolation was again used to remove step size artifacts.

In figure 62 the low energy excitation peak (centered at 360 nm) for 400 nm emission of the low cerium (0.06 at%) thin film sample is plotted in electron-volts (eV) for selected temperatures to demonstrated the observed phonon-induced thermal broadening. The measured HWHM values for the excitation and emission of the low cerium (0.06 at%) sample are plotted versus temperature in figure 63a and b, respectively, along with least squares fits to equation (3.15). The measured HWHM values for the excitation and emission of the high cerium (0.86 at%) sample are plotted versus temperature in figure 64a and b, respectively, again with least squares fits to equation (3.15). The HWHM values for the middle cerium concentration samples are plotted in figures A-11 and A-12 of the appendix. For the fits A was set to 0, following the Condon approximation. The measured HWHM values were in good agreement with equation (3.15). The results for the thin film phonon energies are reported in table 12a along with the peak positions, the measured Stokes shift, and the Huang-Rhys parameter (S) [from equation (3.14)]. The single crystal results are included for comparison in table 12b.
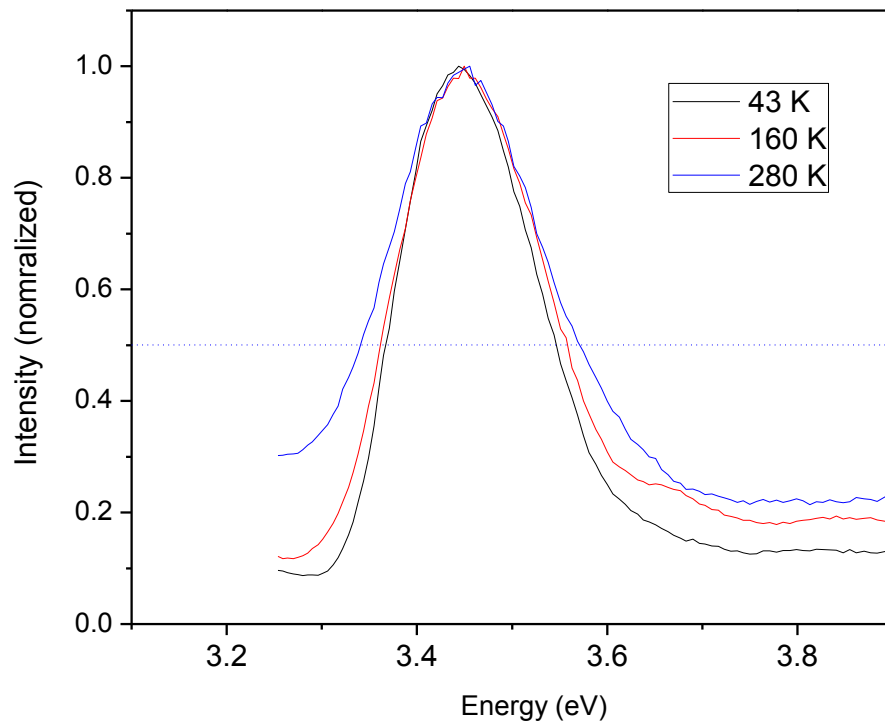
Figure 62. The low energy excitation peak (centered at 360 nm) for 400 nm emission of the low cerium (0.06 at%) thin film sample is plotted in electron-volts (eV) for selected temperatures to demonstrated the observed phonon-induced thermal broadening.
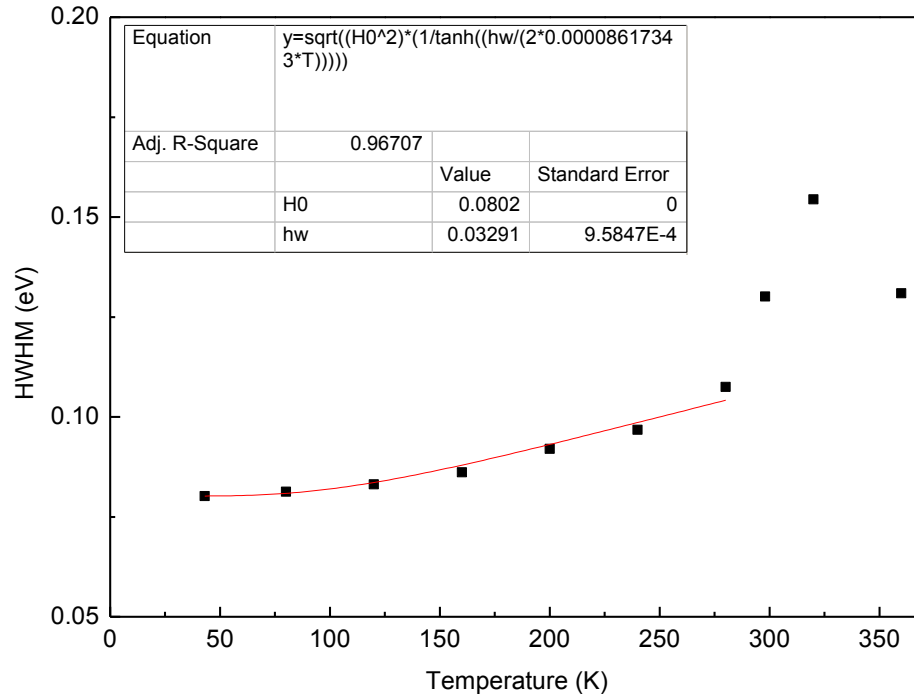
a.
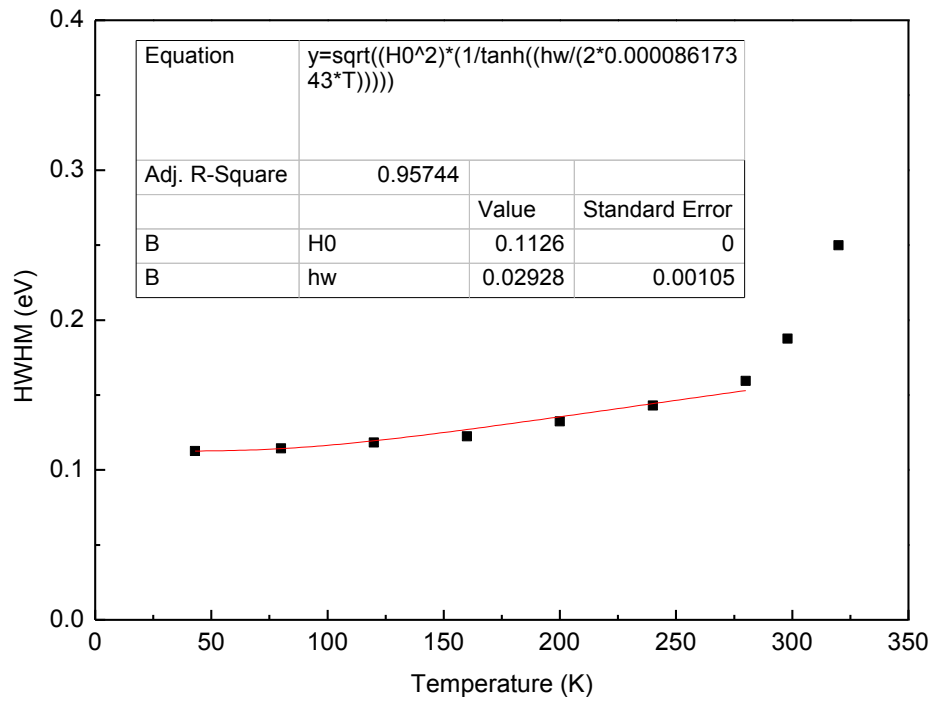
b.

Figure 63. The measured HWHM values for the a) excitation and b) emission of the low cerium (0.06 at%) sample plotted versus temperature with a fit to equation (3.15).

Equation	y=sqrt((H0^2)*(1/tanh((hw/(2*0.00008617343 *T))))))		
Adj. R-Square	0.99436		
		Value	Standard Error
B	H0	0.10066	0
B	hw	0.03119	3.48828E-4

a.

Equation	y=sqrt((H0^2)*(1/tanh((hw/(2*0.0000861 7343*T))))))		
Adj. R-Square	0.99297		
		Value	Standard Error
B	H0	0.1165	0
B	hw	0.03229	3.66713E-4
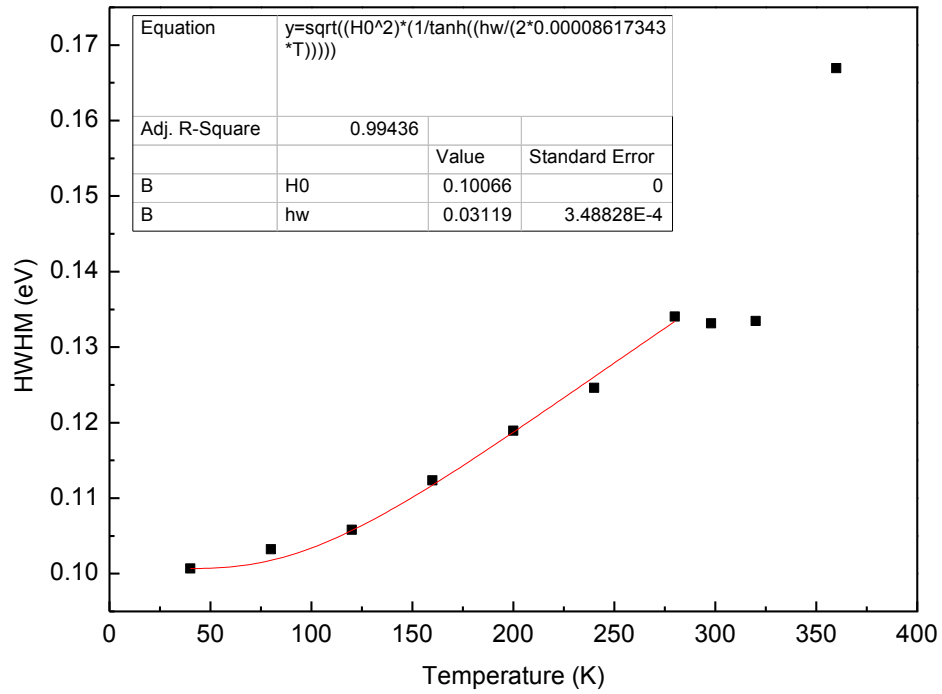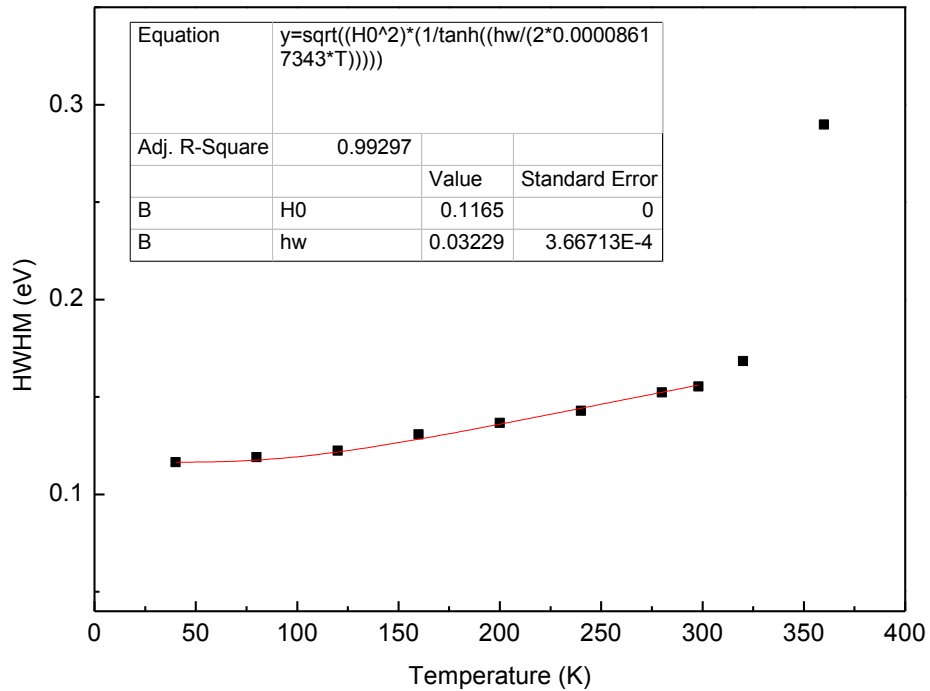
b.

Figure 64. The measured HWHM values for the a) excitation and b) emission of the high cerium (0.86 at%) sample plotted versus temperature with a fit to equation (3.15).

Table 12. The phonon energies along with the peak positions, the measured Stokes shift, and the Huang-Rhys parameter (S) for the a) thin film and b) single crystal samples

a.

	A6-1 0.06 at%	D6-1 0.23 at%	D6-3 0.34 at%	D6-9 0.88 at%
em peak (eV)	3.133	3.128	3.123	3.114
ex peak (eV)	3.444	3.444	3.444	3.456
SS (eV)	0.3115	0.3162	0.321	0.3424
S	4.73	5.51	5.78	5.49
H(0) excitation (eV)	0.0802	0.081	0.0897	0.1007
$\hbar\omega$ (eV)	0.03291	0.02868	0.02779	0.03119
ω (10^{13} s^{-1})	5	4.36	4.22	4.74
H(0) emission (eV)	0.1126	0.1112	0.1094	0.1165
$\hbar\omega$ (eV)	0.02928	0.02986	0.02889	0.03229
ω (10^{13} s^{-1})	4.45	4.53	4.39	4.9

b.

	S-74 0.0015 at%	S-51 0.0095 at%	S-75 0.078 at%
em peak (eV)	3.159	3.151	3.159
ex peak (eV)	3.475	3.462	3.455
SS (eV)	0.316	0.311	0.296
S	4.76	6.02	6.45
H(0) excitation (eV)	0.0843	0.0935	0.0868
$\hbar\omega$ (eV)	0.03323	0.02585	0.02294
ω (10^{13} s^{-1})	5.05	3.93	3.48
H(0) emission (eV)	0.0997	0.1042	0.1081
$\hbar\omega$ (eV)	0.0263	0.0318	0.0311
ω (10^{13} s^{-1})	3.99	4.83	4.71

Raman shift spectroscopy

In table 13 the phonon energies for cerium 4f ground state (from the excitation spectrum) are converted from electron-volts (eV) to wave numbers (cm^{-1}) giving values of 265.4, 224.1 and 251.6 cm^{-1} for the low, med and high thin film LSO:Ce samples, respectively. As with the bulk single crystal, the lowest cerium (0.06 at%) thin film sample shows a cerium electron-phonon coupling energy very close to the Raman active 268 cm^{-1} Lu cation Bg mode for the host LSO. The measured Raman spectra (with a un-polarized excitation source) for the low (0.06 at%), medium (0.34 at%) and high (0.86 at%) thin film LSO samples are plotted in figure 65 with the 268 cm^{-1} peak highlighted. As with the single crystal samples, the thin film LSO:Ce samples did not exhibit a shift in the 268 cm^{-1} phonon peak. Additionally, the baseline intensity increased dramatically for the higher cerium concentrations. An increase in the baseline noise is generally attributed to an increase in the fluorescence of the sample at wavelengths higher than the excitation source (which was 514.4 nm). The dip at 750 cm^{-1} is due to an artifact in the repositioning of the monochromator that arises when the signal to noise ratio is low. The peak positions of the thin film samples are similar to the single crystal samples, though the relative intensities change slightly. This is attributed to the natural pseudo-polarization of the emission of the single crystal samples due to their oriented crystal structure.

Table 13. Thin film LSO:Ce cerium 4f phonon energies converted to wave numbers.

Sample		Emission	Excitation
A6-1 0.06 at%	$\hbar\omega$ (cm^{-1})	236.2	265.4
D6-1 0.23 at%	$\hbar\omega$ (cm^{-1})	240.8	231.3
D6-3 0.34 at%	$\hbar\omega$ (cm^{-1})	233.0	224.1
D6-9 0.86 at%	$\hbar\omega$ (cm^{-1})	260.4	251.6
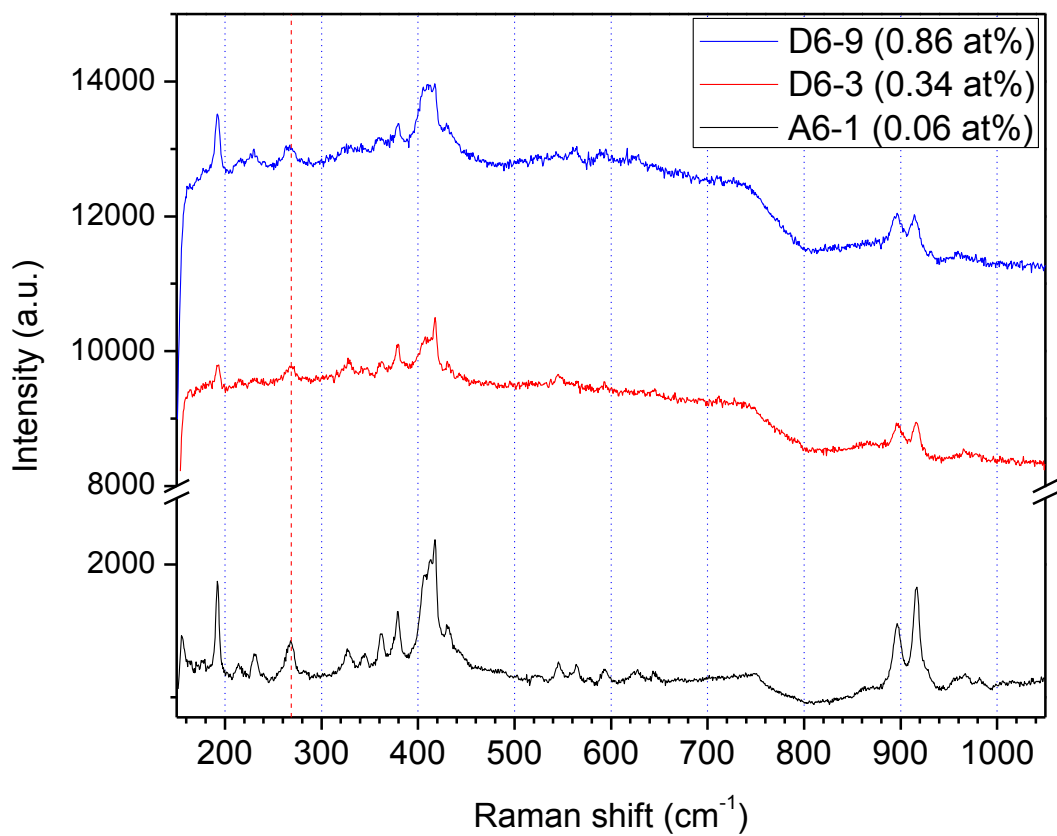
Figure 65. Raman shift measurements of thin film LSO at three cerium concentrations.

Configuration coordinate diagrams

Configuration coordinate diagrams, calculated from the measured PL spectra and phonon values, for four cerium concentrations in thin film LSO:Ce are plotted in figures 66-69. A significant change is observed between the low cerium (0.06 at%) diagram in figure 66 and the higher cerium diagrams, figures 67-69. However, the higher cerium concentrations of 0.23%, 0.34 % and 0.86 % (figures 67, 68 and 69, respectively) exhibit only subtle changes with increasing cerium concentration. As for the single crystal diagrams, the ground and excited states were calculated using equations (3.10) and (3.11). The Stokes Shift (SS) was measured from the experimental PL spectra, while the Huang-Rhys Parameter was calculated from the phonon energies and the Stokes Shift using equation (3.14). The sample dependent values (peak positions, etc.) used in the calculations are summarized in table 14. The highest 5d parabola, 5d $4e_1$, is portrayed as dashed because the energy value is again taken from absorption measurements [52]. The configuration coordinate model generally assumes one dominant "breathing mode" vibration based on an effective mass, *M,* which was again assumed to be coordinated with 7 oxygen atoms. Using different values for the effective mass will change the coordinate (x-axis) values, *Q*, but it will not change the positions and shapes of the parabolas relative to one another. Because the effective mass is assumed the actual Q values are less important for comparison than the relative shapes of the parabolas between both the ground and excited states and between different cerium concentrations.
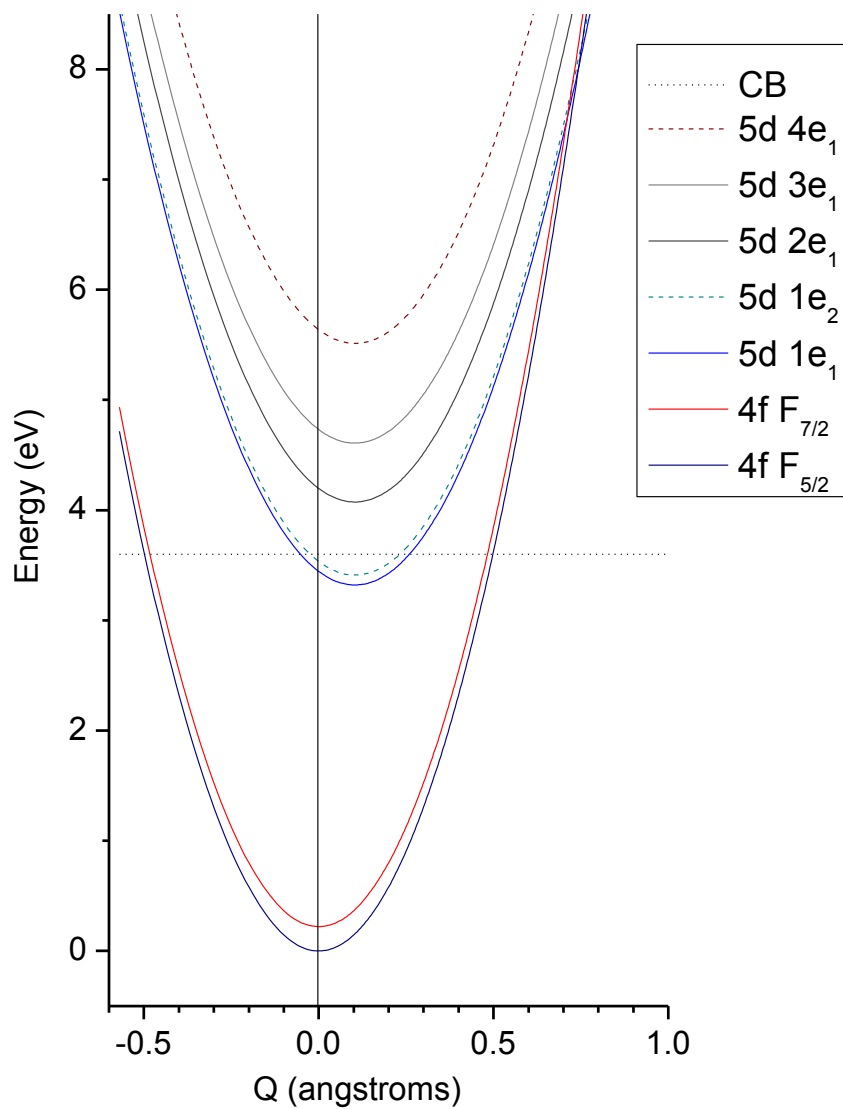
Figure 66. Calculated configuration coordinate diagram for thin film LSO with a cerium concentration of 0.06 at%.
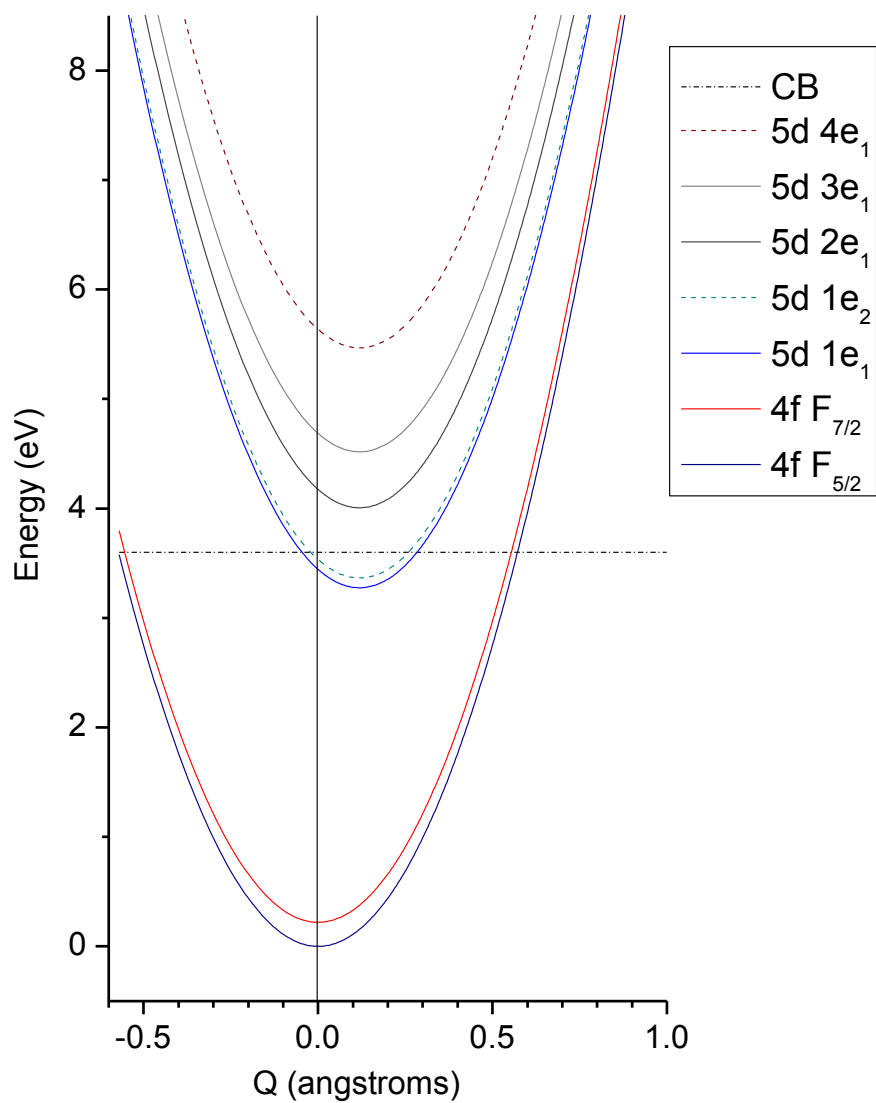
Figure 67. Calculated configuration coordinate diagram for thin film LSO with a cerium concentration of 0.23 at%.
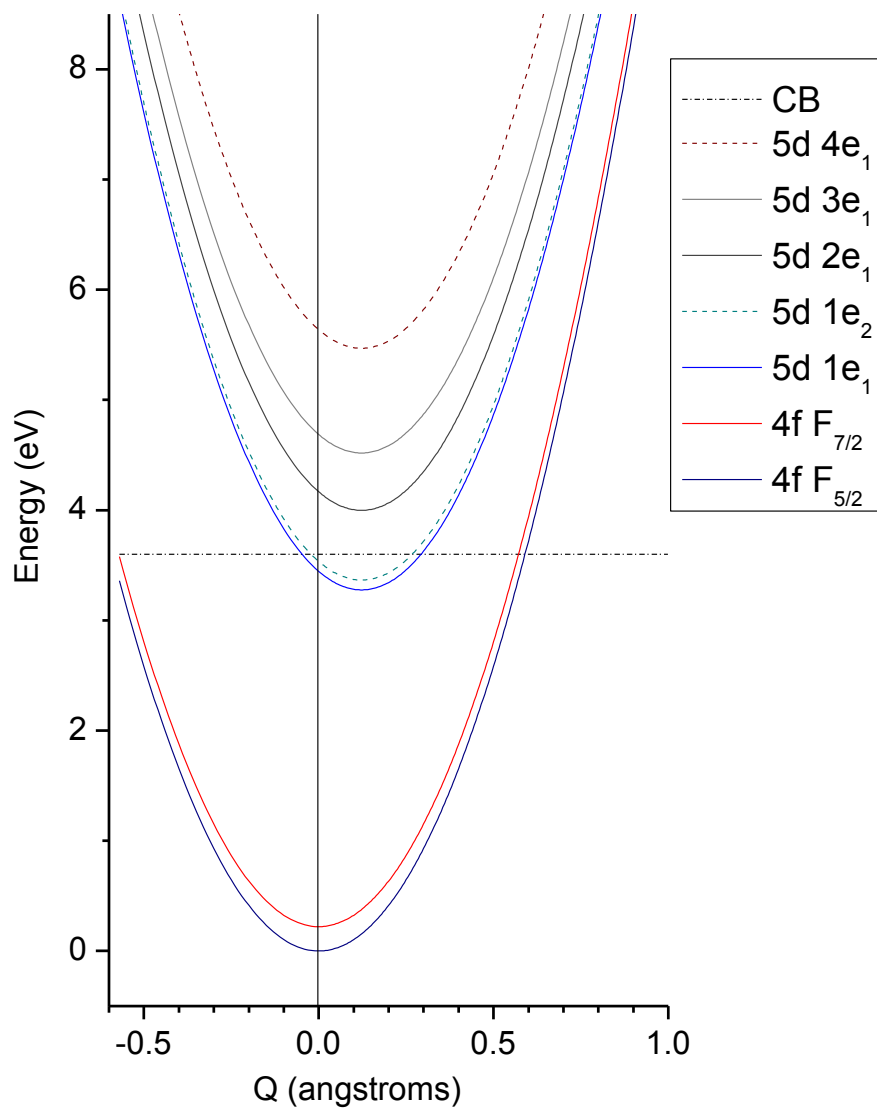
Figure 68. Calculated configuration coordinate diagram for thin film LSO with a cerium concentration of 0.34 at%.
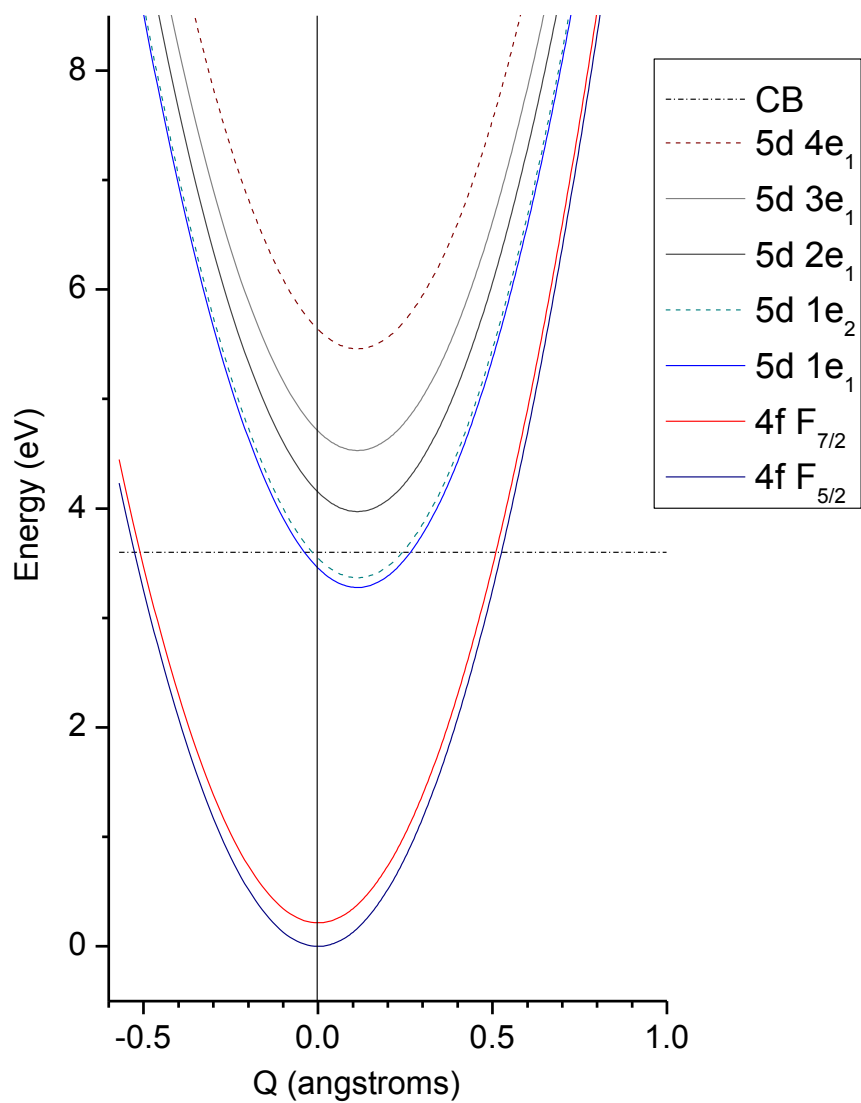
Figure 69. Calculated configuration coordinate diagram for thin film LSO with a cerium concentration of 0.86 at%.

Table 14. Values used to calculate the thin film configuration coordinate diagrams.

Sample ID		A6-1	D6-1	D6-3	D6-9
Cerium		0.06 at%	0.23 at%	0.34 at%	0.86 at%
Excitation					
Peak (eV)	1	3.444	3.444	3.444	3.456
	2	4.197	4.175	4.166	4.149
	3	4.731	4.686	4.686	4.707
ω (10^{13} s^{-1})		5.00	4.36	4.22	4.74
Emission					
Peak (eV)	1	3.133	3.133	3.133	3.123
	2	2.912	2.912	2.912	2.908
ω (10^{13} s^{-1})		4.45	4.53	4.39	4.90
Stokes Shift (eV)		0.311	0.311	0.311	0.332
S		4.73	5.43	5.60	5.33

As discussed in chapter 3, since the measured emission wavelength was not used in the calculations it can be compared to the energy distance between the bottom of the 5d to the intersection of the 4f $F_{5/2}$, to gauge the accuracy of the model. For the low the cerium thin film sample (A6-1), the 4f $F_{5/2}$ emission is 3.13 eV; measured from the A6-1 CC diagram the value is 3.16 eV; a difference of 33 meV. Because the value from the CC diagram does not include the vibrational state interactions it is expected to be slightly larger than the measured value. As with the single crystal samples, the values exhibit excellent agreement.

The designations of the parabolas follows the designations made for single crystal LSO in chapter 3. The cerium ground state parabolas are assigned to the 4f $F_{5/2}$ and $F_{7/2}$ spin orbit split levels. The excited state parabolas are assigned to the five 5d crystal field split levels following designations used in LSO:Ce energy level calculations [45]. The energy separation of the excited state parabolas correspond reasonably well with calculated 5d crystal field split levels [45] for seven oxygen coordinated cerium in LSO ($[CeO_7]$), the measured values did not match six oxygen coordinated cerium ($[CeO_6]$). Excitation/emission-measured, absorption-measured and calculated 5d energy values given in table 9 are included with the addition of the corresponding thin film values in table 15. The energy level designations for the calculated and absorption-measured values are retained from [45]. The 5d $1e_2$ is again portrayed as dashed because it appears to be semi-degenerate with 5d $1e_1$, following the calculated values.

Table 15. Cerium 5d energy level designations for bulk single crystal and thin film LSO.

| | Calculated [45] | | Absorption | Singe crystal | Thin film |
	[CeO$_6$]	[CeO$_7$]	[52]	[this work]	[this work]
5d 1e$_1$	4.3	3.5	3.48	3.47	3.44
5d 1e$_2$	4.6	--	4.2	3.56	3.53
5d 2e$_1$	5.2	4.2	4.7	4.23	4.20
5d 3e$_1$	7.6	5.6	5.63	4.74	4.73
5d 4e$_1$	8.1	5.8	--	5.63*	5.63*
5d Δ	3.8	2.3	2.15	2.16	2.19

*Value from experimentally measured absorption [52].

161

From the CC diagrams for the single crystal samples it was determined the conduction band was the most likely non-radiative pathway. Assuming the position of the conduction band would not change for polycrystalline samples it was again placed at 3.598 eV (relative to the bottom of the 4f ground state) in the thin film diagrams. This value was calculated in chapter 3 by adding the quenching activation energy for the single crystal low cerium sample (S-74) to the energy of the lowest 5d configuration (for S-74). The energy difference between the conduction band and the bottom 5d level was measured and compared to the thermal quenching energies (E_a). The results of the comparison are presented in table 15. The calculated distances are similar the measured and calculated values for the low and medium single crystal samples. However, they are much greater than the measured thermal quenching values (E_a). This difference is due to the presence of defect related non-radiative pathways demonstrated above. Additionally, the calculated distances in table 16 suggests that the thin film samples would exhibit quenching energies comparable to the single crystal samples if the defect-related pathways were removed.

Discussion

Excitation intensity near 325 nm

The nature of the increase in intensity observed in figure 51 between the 300 nm and 360 nm excitation peaks with increasing cerium concentration could possibly be

Table 16. The calculated distances to conduction band compared to experimentally measured E_a values for thin film LSO at different cerium concentrations.

	Bottom of 5d (5d $1e_1$)	Distance to conduction band	E_a (error)
A6-1 0.06 at%	3.321	0.278	0.114 (.010)
D6-1 0.23 at%	3.275	0.323	0.099 (.013)
D6-3 0.34 at%	3.276	0.322	0.107 (.013)
D6-9 0.86 at%	3.277	0.321	0.064 (.009)

attributed to several factors. The PL peaks in the thin film samples are less distinct compared to the single crystal. This is most evident in comparing $F_{7/2}$ and $F_{5/2}$ emission peaks at 40 K for the single crystal samples in figure 24 with that of the thin film samples in figure 51. This is probably an effect of inhomogeneous broadening due to the polycrystalline structure of the thin film, which would also increase the 325 nm region of the excitation spectrum. However, a close inspection of the region in question for cerium concentrations equal to or less than 0.34 at% yields the presence of a small peak, which could not be cause by the observed inhomogeneous broadening. Placing this peak between 320 and 325 puts it in the region of the higher energy 324 nm excitation peak for Ce2, but characteristic Ce2 emission is not observed in figure 52. It is possible energy transfer is occurring from the excited Ce2 site to Ce1 and emitting at 400 nm. Since the peak is present in the excitation spectrum even at low temperatures, if energy transfer was taking place the low temperature decay time for 325 nm excitation would differ from the decay time for 360 nm excitation. The PL decay curves for both 325 nm and 360 nm excitation at 400 nm emission for the high cerium sample at 40 K are plotted in figure 70. The two curves are virtually identical, which rules out assigning the 325 nm peak to Ce2. Therefore, the 325 nm peak is not attributable to the LSO film nor the small amount of LuAG present due to film-substrate diffusion. While some cerium-silicates exhibit luminescence [60-62] they are not likely the source because the cerium concentration is too low (0.06 at % in the low concentration sample). Of the additional phases possible (based on the composition of the film and

Figure 70. The PL decay profiles for both 325 nm and 360 nm excitation at 400 nm emission for the high cerium (0.86 at%) sample at 40 K.

substrate) cerium doped $LuALO_3$ (LuAP) is the only one with a luminescence excitation near 320 nm [63-65]. LuAP emission intensity and decay time values exhibit relatively little change from 200 K to over 600 K [64-65], therefore the PL decay time for 325 nm excitation (400 nm emission) should be longer than the decay time for 360 nm excitation (400 nm emission), since the LSO decay times have greatly decreased by room temperature. The decay curves for 325 nm and 360 nm excitation of the high cerium sample (0.86 at%) at 298 K are overlaid in figure 71. The decay curve for 325 nm excitation is noticeably longer confirming that LuAP appears to be present in amounts below the detection limits of XRD. Because LuAP emission remains intense to over 600 K [64-65], its contribution to the excitation profile can be gauged by looking at the spectra at elevated temperatures. The excitation (400 nm emission) spectra of the high cerium sample (0.86 at%) is plotted for selected temperatures between 40-400 K in figure 72. The excitation spectrum at 400 K exhibits a broad low intensity peak from 290 nm to 380 nm which is comprised of the LuAP peak at 320 nm and the mostly quenched LSO:Ce peak at 360. From this spectrum it is apparent that the LuAP contribution is very small, as would be expected if its presence is on an order too low to measure with XRD. The convolution of the 300 and 360 nm LSO peaks with the ~321 nm LuAP peak is enough to account for the higher intensity for the 325 nm region of the thin film samples versus the single crystal LSO.
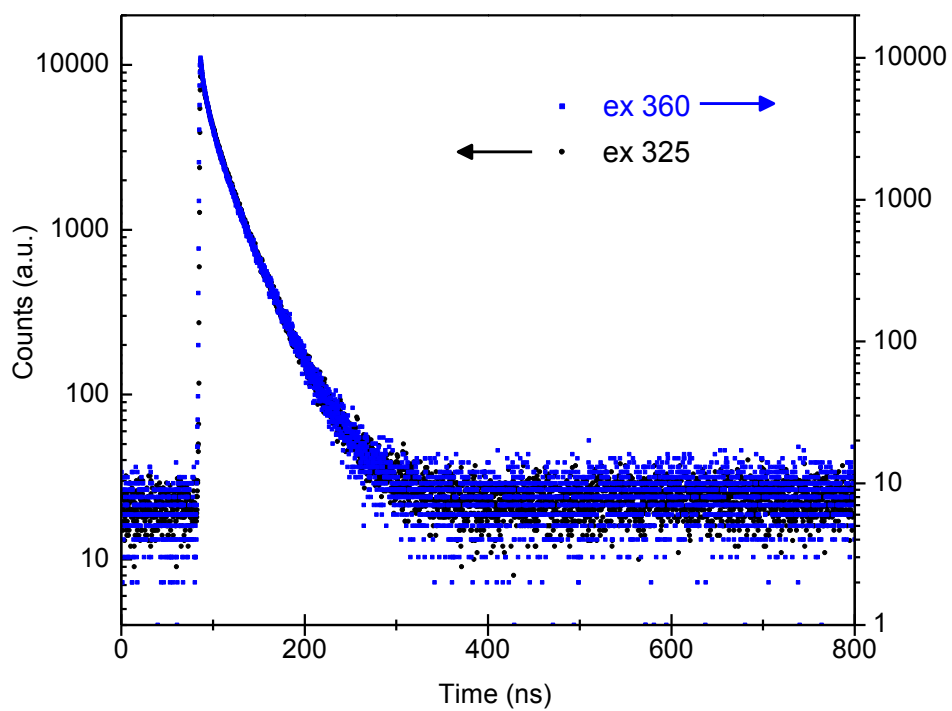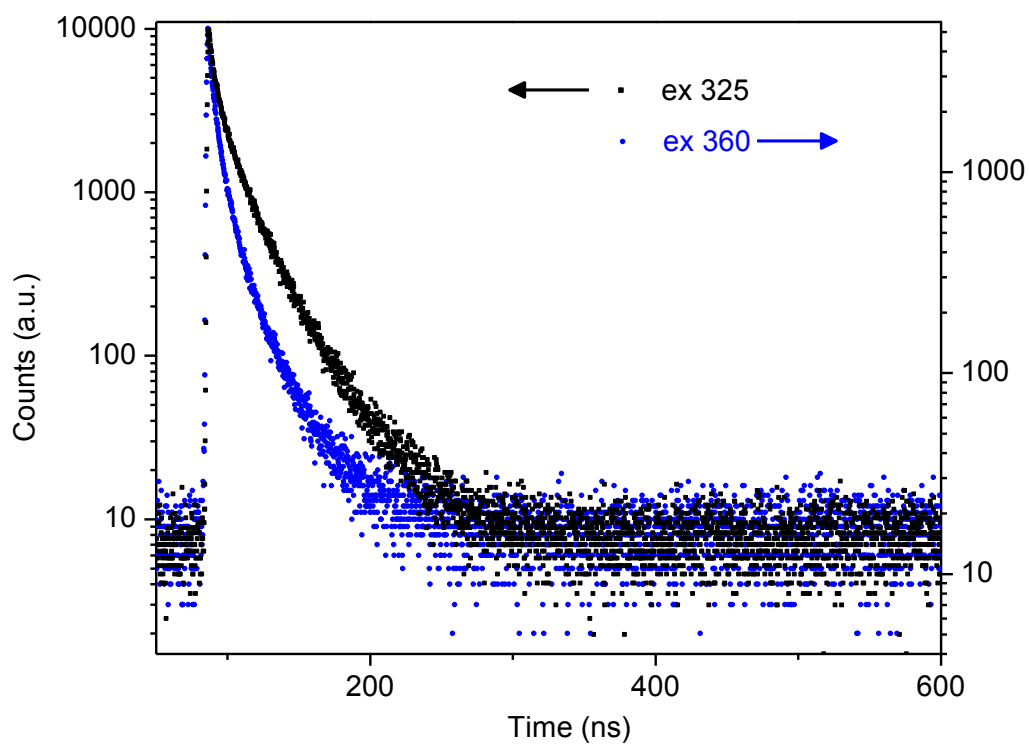
Figure 71. The PL decay profiles for both 325 nm and 360 nm excitation at 400 nm emission for the high cerium (0.86 at%) sample at 298 K.
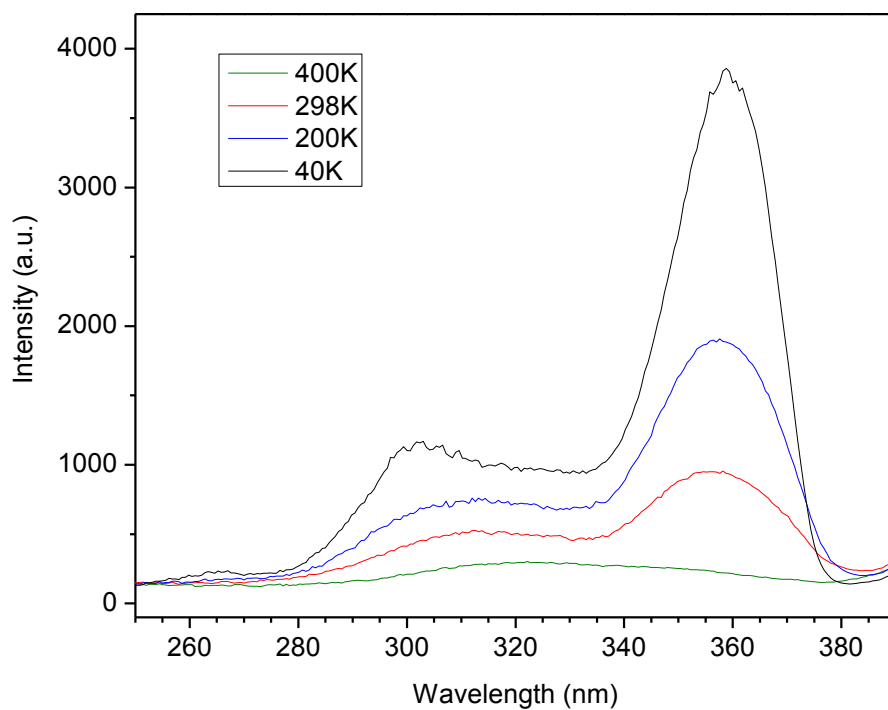
Figure 72. The excitation (400 nm emission) spectrum of the high cerium sample (0.86 at%) plotted for selected temperatures between 40-400 K.

Phonon values and configuration coordinate diagrams

Similar to the single crystal LSO results, the measured Raman shift results for the thin films suggest that at low cerium concentrations the cerium cation couples to the vibrations of the host LSO. As discussed in chapter 3, the stresses induced by the cerium in the single crystal LSO strongly affect the activator site's phonon modes, which was apparent in the dramatic broadening of the ground state CC parabola and subsequent PL spectra. For the thin film LSO, the phonon values, and in turn the CC diagrams, exhibit less change with increasing cerium concentration compared to the single crystals. The minimal broadening with increasing cerium of the calculated CC diagrams for the thin films accurately reflect the minimal broadening with cerium observed in the PL spectra. This suggests either less stress is induced by the addition of the cerium activator or the stresses induced affect the activator to a lesser extent. It would be expected that a nano-crystalline structure would accommodate the induced internal stresses of an activator, such as cerium, easier than a single crystal structure with long range order. The stresses in the thin film will not be compounded, so to speak, throughout the material but rather will "reset" or be relieved at each grain boundary. Additionally, the Huang-Rhys parameters (table 12) are moderately lower for the thin film samples suggesting the phonon modes of the host LSO do have a lesser affect on the activator site. Ultimately, it appears to be a combination of less induced internal stresses and the stresses that are induced affecting the activator to a lesser extent.

The placement of the conduction band in the CC diagrams of the single crystal samples corresponded with the measured thermal quenching activation energies. Using the conduction band placed on the CC diagrams of the thin films to estimate the thermal quenching activation energies (table 16) yields values similar to the single crystal LSO, but higher than the measured values (table 11). Instead, the dominant quenching pathways are attributed to defect-mediated non-radiative transitions that were shown to be present by the temperature dependent stead-state and lifetime PL results.

As was also the case for the single crystal samples, the measured phonon values for the higher cerium samples may not be the actual phonon modes of the cerium site, but they do accurately represent the observed cumulative behavior when the systems are described using a CC model with one luminescence site and a single "breathing mode" vibration.

Cerium concentration

The peak emission intensity of the thin film samples at 0.35 at% is in reasonable agreement with reported results of 0.5 at% for LSO:Ce prepared via sol-gel processing [66]. However, this is higher than the results in chapter 3 for single crystal LSO:Ce. This is attributable to several factors: the low solubility of cerium in single crystal LSO, the dimensionality effects of a thin film versus a bulk crystal and non-active cerium in the polycrystalline thin film. Due to the different space groups of LSO and cerium oxyorthosilicate, cerium doping at even low concentrations in single crystal LSO causes

170

significant effects in the optical properties of the crystals, as seen in chapter 3. As discussed above, the nano-crystalline thin film structure likely better accommodates any localized stress due to the ionic mismatch of Lu and Ce. This is also reflected by the lesser degree of change seen in the thin film CC diagrams.

In addition to these previously discussed issues, the presence of non-active Ce^{4+} in the thin film LSO:Ce could artificially raise the peak concentration value and serve as non-radiative recombination sites. X-ray photoelectron spectroscopy (XPS) and X-ray absorption near edge structure spectroscopy measurements of sol-gel LSO:Ce films and powders, respectively [67] revealed the presence of Ce^{4+}, however a Ce^{3+}/Ce^{4+} ratio was not specifically quantified. XPS measurement were attempted on the above thin film LSO:Ce samples, but were unsuccessful due to significant sample charging. It is possible that the vapor deposited films could also contain an appreciable amount of Ce^{+4}. Cerium could also preferentially segregate to the grain boundaries or to the surface in the thin film samples during the post-deposition annealing process. Cerium located at grain boundaries would not likely be active due to defects and again serve as non-radiative pathways. Because cerium is highly oxyphilic, cerium at the surface or at grain boundaries could be preferentially oxidized to the +4 state due to enhanced oxygen in the near surface region as well as rapid oxygen diffusion along grain boundaries. Thus the active cerium concentration could be lower and consistent with the optimum single crystal values, but non-active cerium in the polycrystalline thin films artificially increases the observed peak cerium concentration.

Additionally, dimensionality effects can influence the optimum cerium concentrations. Because the dominant single crystal quenching mechanism is due to self-absorption (shown in chapter 3), the optimum concentration is a convolution of the excitation efficiency and the subsequent self-absorption. The bulk crystal probe depth is much larger than the thickness of the thin film thus self-absorption in the thin films is minimal relative to the single crystals. Likewise, the thin film is not thick enough to absorb all of the incident excitation light so additional cerium adds absorption centers without causing as large a corresponding increase in self-absorption. This will raise the ideal cerium concentration to a level where an additional quenching mechanism dominates the luminescence behavior; in this case, defect-mediated non-radiative pathways.

Ce2

As discussed in chapter 3, there is strong evidence that Ce1 is 7 oxygen coordinated. The exact nature of Ce2 was not concluded, but it follows that it is either due to 6 oxygen coordinated cerium or interstitial cerium defects, both of which are higher energy sites. Due to the nature of single crystal (Czochralski) growth cerium (at sufficiently high concentrations) is forced into non-energetically favorable available sites. The polycrystalline nature of the thin films apparently provides additional sites for the cerium to ocupy, such a grain boundaries, that are absent in the single crystals. So it is possible that cerium occupies these additional sites that require less energy instead of sitting in the Ce2 sites. The concentration of cerium in these sites will increase with concentration just as the observed non-radiative pathways increase with concentration.

172

However, the quenching temperatures for the Ce1 were roughly 200 K lower compared to single crystal LSO:Ce. If this relation is also true for the Ce2 site as well, with an observed quenching temperature around 80 K in single crystal LSO:Ce, the Ce2 site could quite possibly just be quenched in the thin film LSO:Ce.

Conclusion

Relying on the knowledge of single crystal LSO gained in chapter 3 and the results above, a clear picture of the cerium concentration-dependent behavior of thin film LSO emerges. Single crystal LSO experienced concentration quenching due to self-absorption at relatively low cerium concentrations that was driven by a broadening of the configuration coordinate diagram (and PL spectra) and changes in the phonon modes affecting the cerium luminescence center. The thin film LSO does not follow the single crystal concentration quenching mechanism because the 1 μm thick thin film is less susceptible to self-absorption. Additionally, the nano-crystalline nature of the film more easily accommodates the stresses induced by the cerium activator reducing the excitation spectrum broadening that is responsible for the increase in self-absorption. With the self-absorption quenching mechanism removed the ideal cerium concentration is increased to a level where additional quenching mechanisms begin to dominate the luminescence behavior. In this case, as seen in the above results, the mechanism that dominates is an increase in defect mediated non-radiative pathways. As the cerium

concentration in the thin film LSO increases, naturally the number of defects increase, such as cerium near grain boundaries, interstitial atoms, vacancies, etc. This trend continues until enough cerium is present to precipitate out cerium-based phases that can act to quench emission. However, due to the still relatively low cerium in the thin film LSO (maximum 1.0 at%) and the absence of cerium phases in the XRD patterns, second phase precipitation is not a dominant factor in the quenching observed. Thus defect mediated non-radiative pathways are suggested as the dominant concentration quenching mechanism in the poly-crystalline thin film LSO:Ce samples.

Summary

Thin films with a cerium thickness gradient were sputter deposited with cerium concentrations ranging from 0.06 to 0.88 atomic percent. The thin film samples showed peak photoluminescence emission intensity at a cerium concentration of 0.35 atomic percent, which was higher than the optimum value found for single crystal samples of ~0.01 at%. In chapter 3 it was shown the dominant single crystal mechanism was concentration quenching due to self-absorption. For the thin films it was found self-absorption was not a dominant factor due to the thin dimension of the film and also its nano-crystalline nature. For the thin film LSO:Ce, photoluminescence excitation and emission spectra as a function of concentration demonstrated the concentration

quenching behavior was instead due to an increase in defect-mediated non-radiative

transitions with increasing cerium.

CHAPTER V
TERNARY MATERIAL SYSTEM

Of the work presented in this chapter Allen Patchen helped perform the wavelength dispersive spectroscopy measurements and Joo Hyon Noh helped calibrate the sputtering model. Philip Rack and Charles Melcher provided direction, funding of the research, discussion and motivation.

Introduction

In chapter 2, the binary Lu_2O_3-SiO_2 material system was explored and in chapter 4 the cerium activator concentration in thin film Lu_2SiO_5 was optimized. In this chapter the combinatorial thin film screening process is applied to more complex pseudo-ternary material systems (actually quaternary systems considering the activator), specifically the cerium doped Lu_2O_3-Al_2O_3-SiO_2 system.

This system was chosen because both the Lu_2O_3-SiO_2 and the Lu_2O_3-Al_2O_3 material systems contain well known scintillators. Additionally, this ternary system is not well known and the possibility of luminescence or scintillation properties have not been reported. The Lu_2O_3-SiO_2 system contains the scintillating phases Lu_2SiO_5 (LSO) and $Lu_2Si_2O_7$ (LPS), which were introduced and discussed in more detail in the binary system exploration in chapter 2. The Lu_2O_3-Al_2O_3 material system contains several phases that exhibit scintillation: $Lu_3Al_5O_{12}$ (LuAG) and $LuAlO_3$ (LuAP).

Background

The Lu_2O_3-SiO_2-Al_2O_3 ternary system has been minimally investigated [68]. Of the known phases present in the Lu_2O_3-SiO_2-Al_2O_3 ternary system cerium doped LSO has already been introduced. Cerium doped LPS exhibits photoluminescence properties similar to LSO, but with the excitation and emission shifted to higher energies with excitation peaks at 350 and 305 nm and characteristic cerium emission at 380 nm and 415 nm. LPS has a monoclinic structure with space group C2/m, a density of 6.23 g/cm^3 and a light yield of 26,300 photons/MeV with a reasonably fast decay time of 38 ns [69-71]. LuAG:Ce also exhibits good scintillation properties with a density of 6.73 g/cm^3, a decay time of 50-60 ns, a light output ranging from 6,800 to 18,450 photons/MeV, an excitation peak near 450 nm and an emission peak near 500 nm [20, 59, 72-73]. LuAP is an additional known scintillator [74] in the system, however because it does not congruently melt [75-76] it is not expected to be observed in significant quantities.

Experimental procedure

Sputter deposition

Samples were reactively sputter deposited from elemental cerium, lutetium, aluminum and silicon targets in an Ar-O_2 atmosphere onto 100mm diameter polished alumina substrates using an AJA International ATC 2000 R.F. magnetron sputter system. All four

of the individual R.F. sputtering sources (50mm diameter) were used. The cerium, silicon

and aluminum targets were mounted at azimuths of 90, 180 and 270 degrees,

respectively, in reference to the lutetium target.

Prior to sample deposition, rate measurements were conducted by depositing individual

oxides (Lu_2O_3, SiO_2 and Al_2O_3) onto silicon test wafers (100 orientation) and measuring

film thickness via reflectometry using a Filmetrics F-20 Optical Reflectometer.

Additionally, thickness measurements for Lu_2O_3-SiO_2-Al_2O_3 reactive co-sputtering were

measured by cross-sectional scanning electron microscopy (SEM) imaging using a

Hitachi 4300 scanning electron microscope. The results of the thickness measurements

are summarized in table 17.

Lu_2O_3-SiO_2-Al_2O_3 ternary gradients with cerium doping were deposited by alternating

four layers of uniform cerium thickness between five layers of Lu_2O_3-SiO_2-Al_2O_3 ternary

gradients producing a layered structure similar to the binary Lu_2O_3-SiO_2 structure

diagramed in figure 11. To sputter Lu_2O_3-SiO_2-Al_2O_3 ternary gradient layers, the lutetium

and silicon targets were both powered with 200 W and the aluminum target was

powered with 180 W. Each layer was sputtered for 10 minutes (for a total sputter time

of 50 minutes) in an atmosphere of argon and oxygen maintained at 3 mTorr with an

oxygen partial pressure of 9.1 % (O_2 flow rate = 2.5 sccm, Ar flow rate = 25 sccm). For

each Lu_2O_3-SiO_2-Al_2O_3 ternary layer the substrate was aligned to a consistent position

and held stationary during the deposition. Each cerium doping layer was sputtered at 25

W (101 V target self-bias) in an argon atmosphere at a pressure of 3 mTorr for 5 minutes

Table 17. Measured sputtering rates.

Material	Power (W)	Target self-bias (V)	O_2 partial presure (%)	Measured rate (nm/min)
SiO2	200	223	8.3	5.4
Lu2O3	200	224	7.7	12
Al2O3	180	443	8.8	5.2
Co-sputter all three	same as above	same as above	9.1	23.5

while rotating the substrate at 20 revolutions per minute to produce a uniform profile. Based on Lu, Si, Al and Ce sputtering rates, the estimated cerium concentration in the Lu_2O_3-SiO_2-Al_2O_3 film is 0.3 atomic percent.

Characterization

Film composition was measured using wavelength dispersive spectroscopy (WDS) on a Comeca 100 electron probe microanalysis (EPMA) system. Concentrations of all elements were taken at four locations on the substrate, as diagramed in figure 73. The substrate orientation in figure 73 is retained for all subsequent 2D substrate figures with the aluminum rich section at the top and the lutetium and silicon rich sections at the left and right of the figure, respectively. For each location, concentrations were measured at four comparable points to gauge measurement accuracy and film uniformity, at an accelerating voltage of 15 keV. To ensure the alumina substrate was not altering the measured aluminum values, measurements were also conducted with an accelerating voltage of 5 keV. Backscatter electron (BSE) images were taken using a Hitachi 4300 scanning electron microscope. Photoluminescence (PL) excitation and emission spectra were measured using a Horiba Jobin Yvon Flouralog-3 Spectrofluorometer. The sputter deposition model discussed in chapters 2 and 4 was used extensively to calculate film thickness and composition at positions not measured using WDS.

X-ray diffraction (XRD) peaks were measured from 10 to 66 degrees 2-theta with a step size of 0.02 degrees at 2 seconds per step using a Philips X'Pert diffractometer for nine
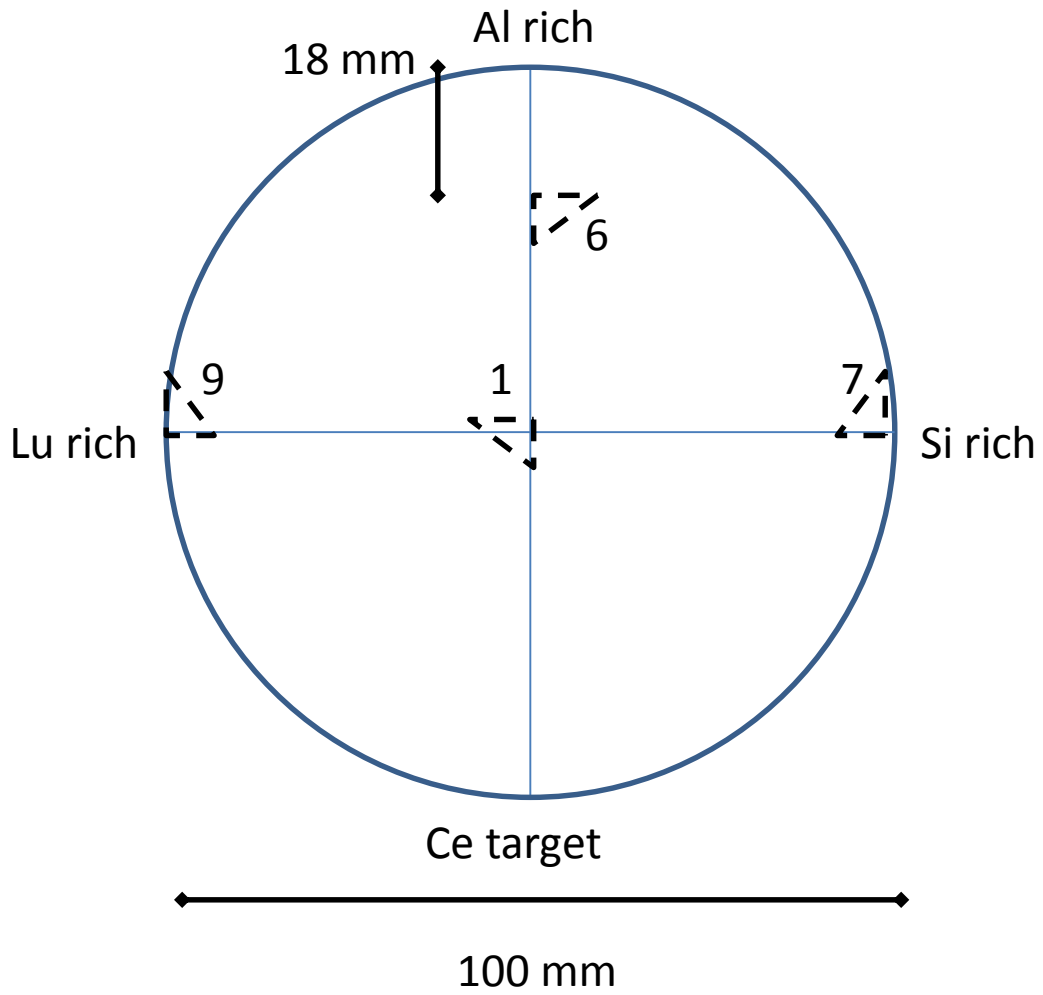
Figure 73. The locations of WDS measurements.

locations on the substrate, as diagramed in figure 74. Position numbering is retained from figure 73. Peak matching and semi-quantitative analysis [58] (when possible) of the measured XRD spectra were performed using PANalytical B.V. X'Pert HighScore software. Semi quantitative analysis requires using either a standard or measured Reference Intensity Ratio (RIR) for each phase, however there is not a published RIR for LPS. Therefore, an RIR ratio for LPS was obtained using the XRD spectrum from the 7 cm position of the Lu_2O_3-SiO_2 gradient in chapter 2, which was previously found to have an LSO-LPS ratio close to 1. This method yielded an RIR value of 1.8 for LPS which matches the standard value for LSO. Considering the chemical composition and the crystal structures of LSO and LPS are similar this value appears reasonable.

Results

Composition

A composition model was calculated based on the measured deposition rates. The atomic percent (on the substrate) of each target material (Lu, Al, Si) is plotted in figure 75a and total film thickness is plotted in figure 75b. Cerium concentration was not included in the model. The WDS measured atomic concentrations for the positions on the film diagramed in figure 73 are summarized in table 18.
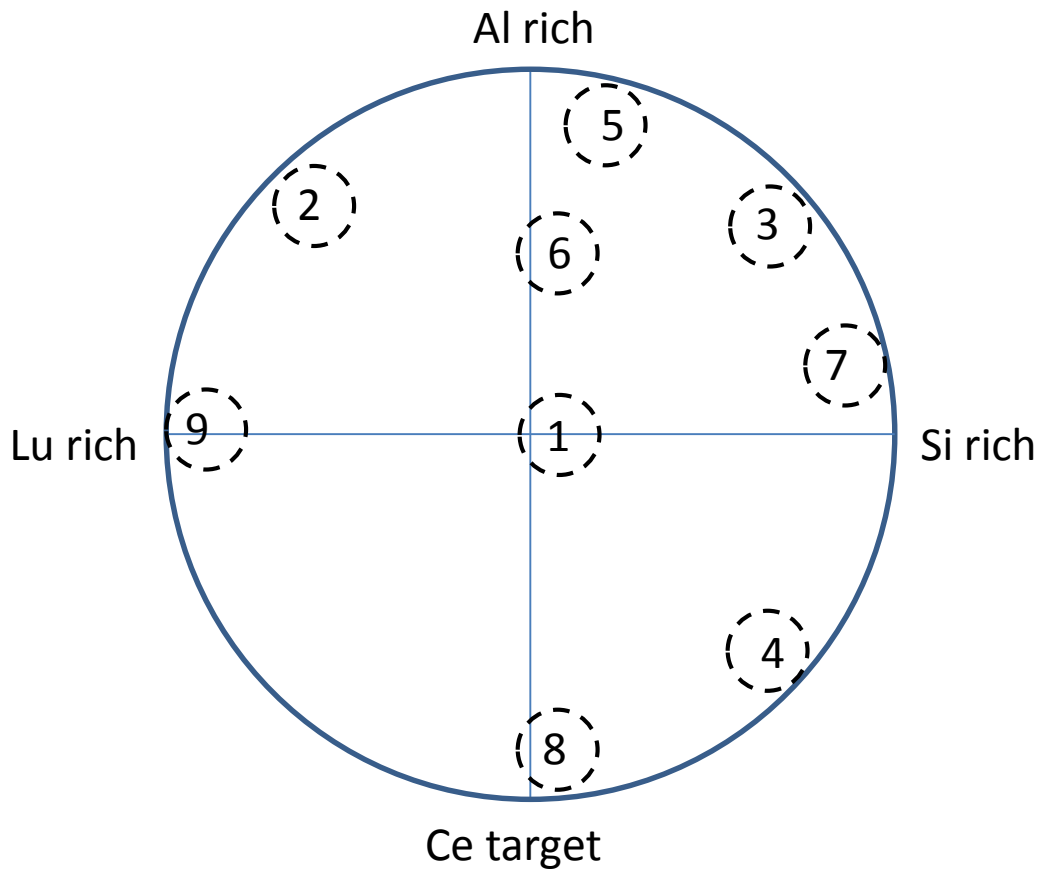
182

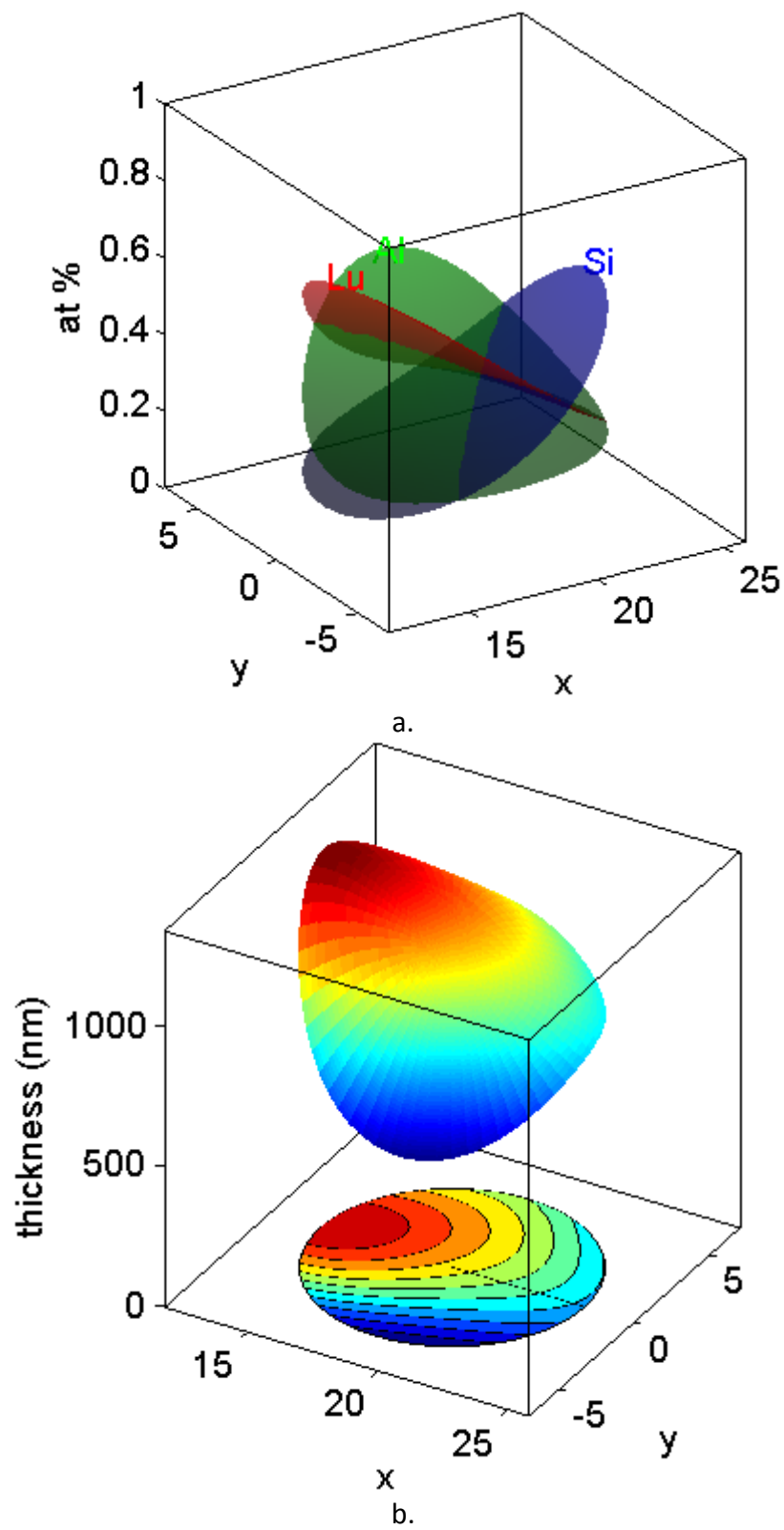Figure 74. The locations of XRD measurements.

Figure 75. Model based on deposition rates: a) atomic percent, b) film thickness.

Table 18. WDS results in atomic percent.

Location	Lu	Al	Si	Ce	O
1	20.88	12.83	5.09	0.18	61.02
6	13.94	21.87	3.38	0.13	60.68
9	32.14	5.84	1.56	0.14	60.31
7a	2.44	32.20	4.43	0.04	60.89
7b	5.93	16.30	14.69	0.16	62.94

The concentration of silicon in the WDS results was lower than expected. This is potentially due to oxidation of the target during processing and is addressed further in the discussion. The composition model was recalculated to fit the WDS measured composition values. The atomic percent of each target material (Lu, Al, Si) from the revised composition model is plotted in figure 76a. The corresponding film thickness is plotted in figure 76b. Due to the change in the silicon sputtering rate and the additional complexities of a ternary system the modeled concentration values exhibit less agreement with the WDS results than the cerium profile results in chapter 4, though the results are still reasonable. The WDS concentration values at an accelerating voltage of 5 keV (versus 15 keV in table 18) yielded similar results with the exception of the cerium concentration (5 keV is too low of an accelerating voltage to measure cerium peaks) and the aluminum-silicon ratio. The ratio increased by 8.7%, which suggests less silicon is present near the surface. The change in cerium atomic percent between locations 1, 6 and 9 is due to the respective change in film thickness at each location. Position 7 exhibited a large degree of phase separation with regions of varying concentrations. BSE imaging was performed to confirm the phase separation. The BSE image of position 7 is shown in figure 77a. BSE images of positions 1, 6 and 9 are shown in figure 77b, c and d, respectively. At position 7 (figure 77a) large regions of distinct contrast are observed. The measured concentration of the lighter colored, high areas are labeled 7a in table 18 and the lower dark colored areas are labeled 7b. In each of these larger sections, smaller
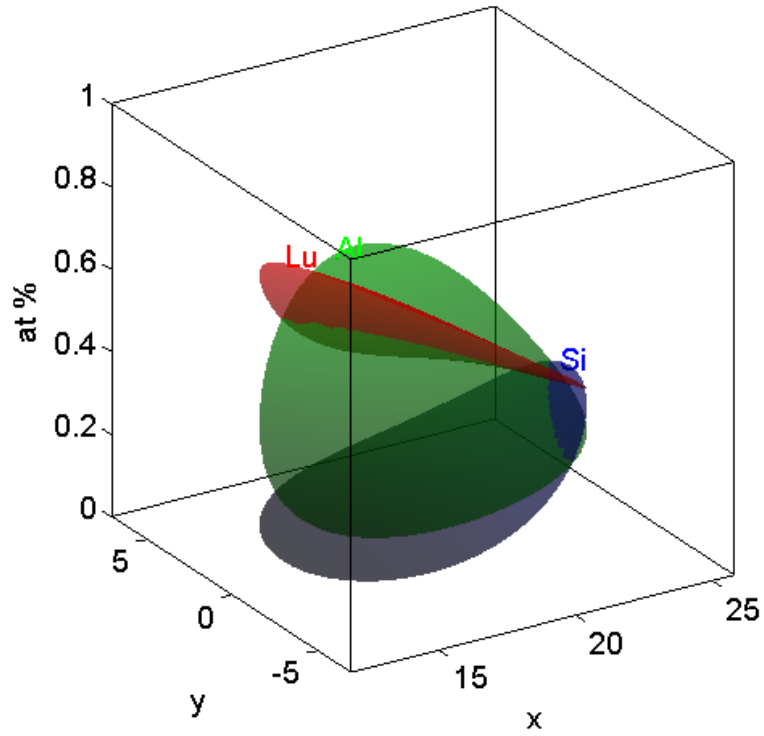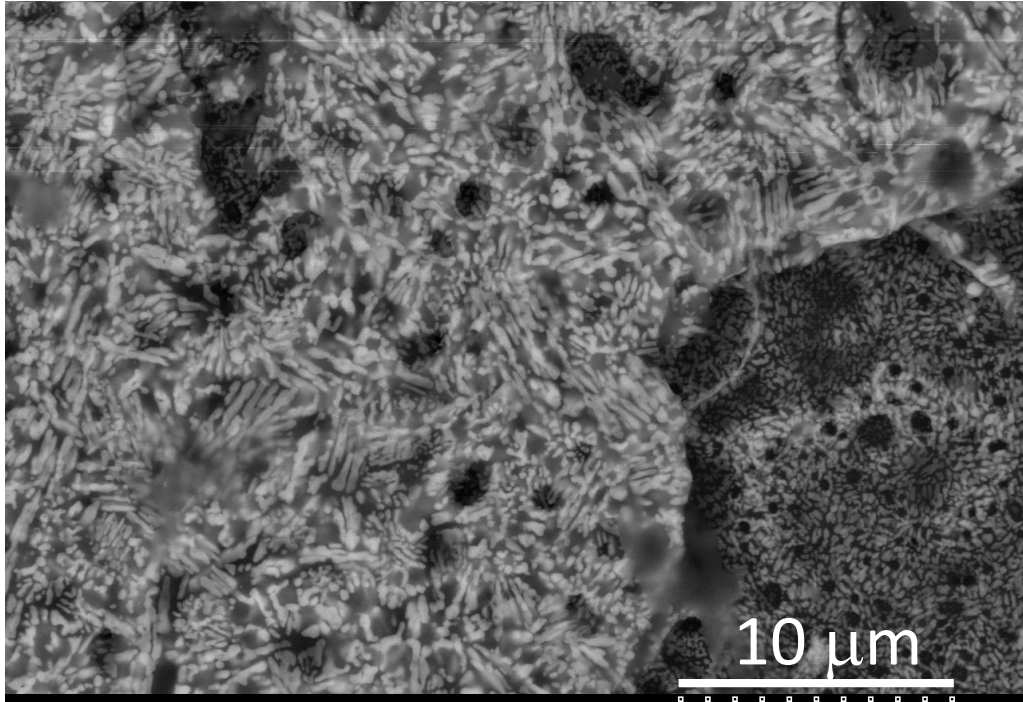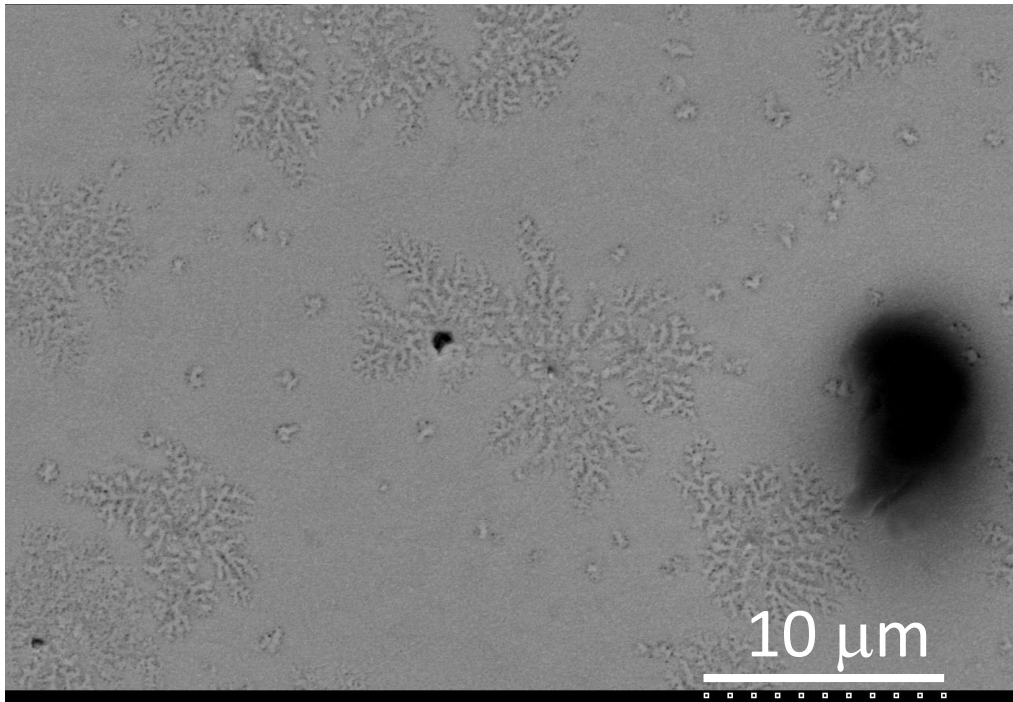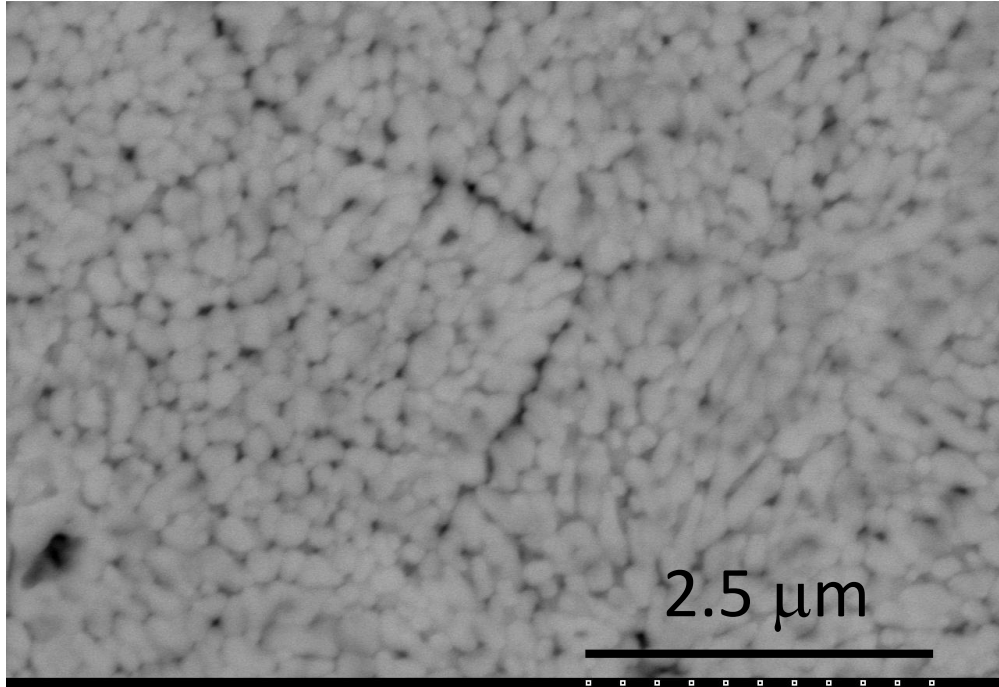
a.
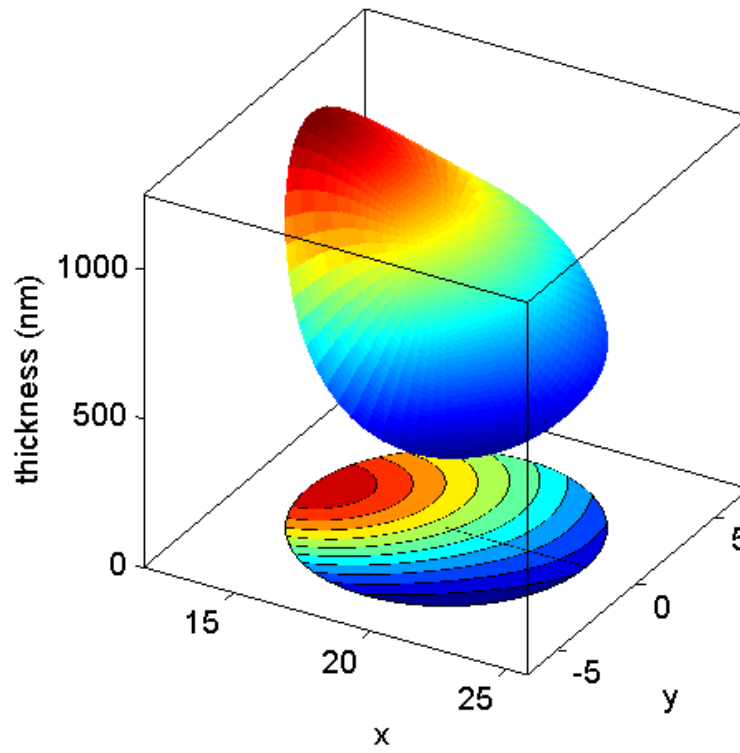
b.

Figure 76. Revised model based on WDS results: a) atomic percent, b) film thickness.
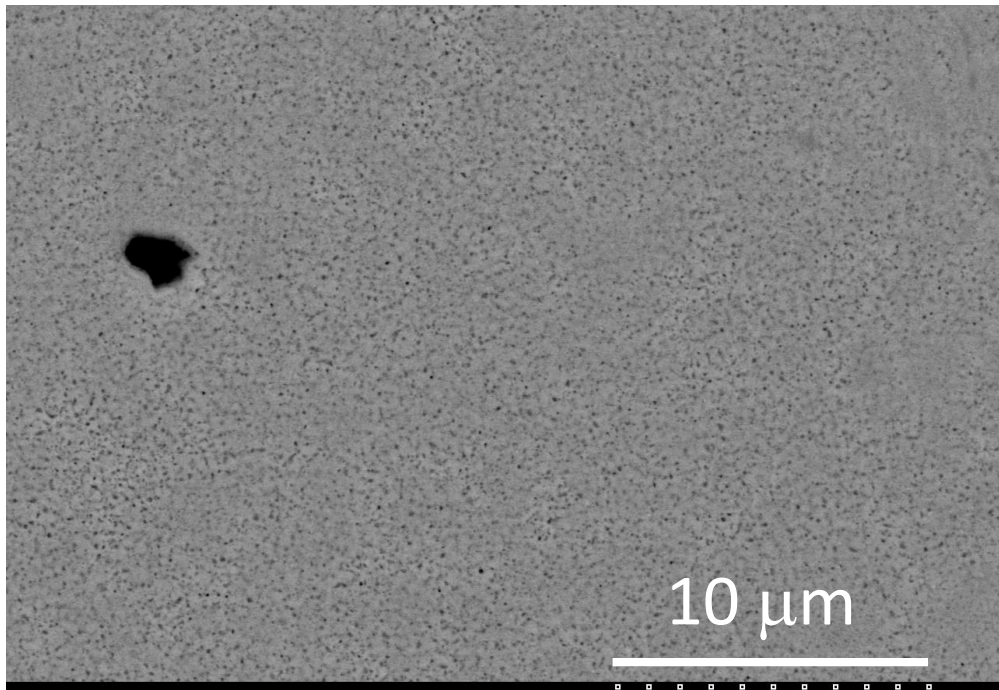
a.

b.

2.5 μm

c.

10 μm

d.

Figure 77. BSE images of the film at locations a) 7, b) 1, c) 6 and d) 9.

compositions are visible which are attributed to further phase separation. The other positions imaged did not exhibit noticeable phase separation.

Selected XRD spectra are plotted and labeled in figure 78. Semi-quantitative analysis was able to be performed on locations that contained some combination of LSO, LPS and LuAG phases. The potential percentage of Al_2O_3 in the sample was not able to be measured due to the alumina (Al_2O_3) substrate. The primary phases present at each location and their relative weight percentages are reported in table 19a along with the weight percent of each element from the composition model. The WDS results from table 18 are converted to weight percent and reported in table 19b with the addition of oxygen. None of the locations exhibited a unique Lu-Al-Si-O phase. LPS, LSO and LuAG were the most abundant phases. Lu_2O_3, $Lu_4Al_2O_9$ and Al_2SiO_5 were also present in select locations.

Photoluminescence

The PL excitation and emission spectra were measured at thirty-five locations on the sample. The as-measured emission intensities (integrated over 200 nm) versus measurement position are plotted as a 2D color-contour map in figure 79. The as measured values were normalized to a film thickness of 1 μm and the un-measured areas were filled in using interpolation. The results are plotted in figure 80 with the locations of WDS and XRD measurements identified by numbers corresponding to tables 18 and 19. Figure 80 enables a rapid identification of the areas with high emission
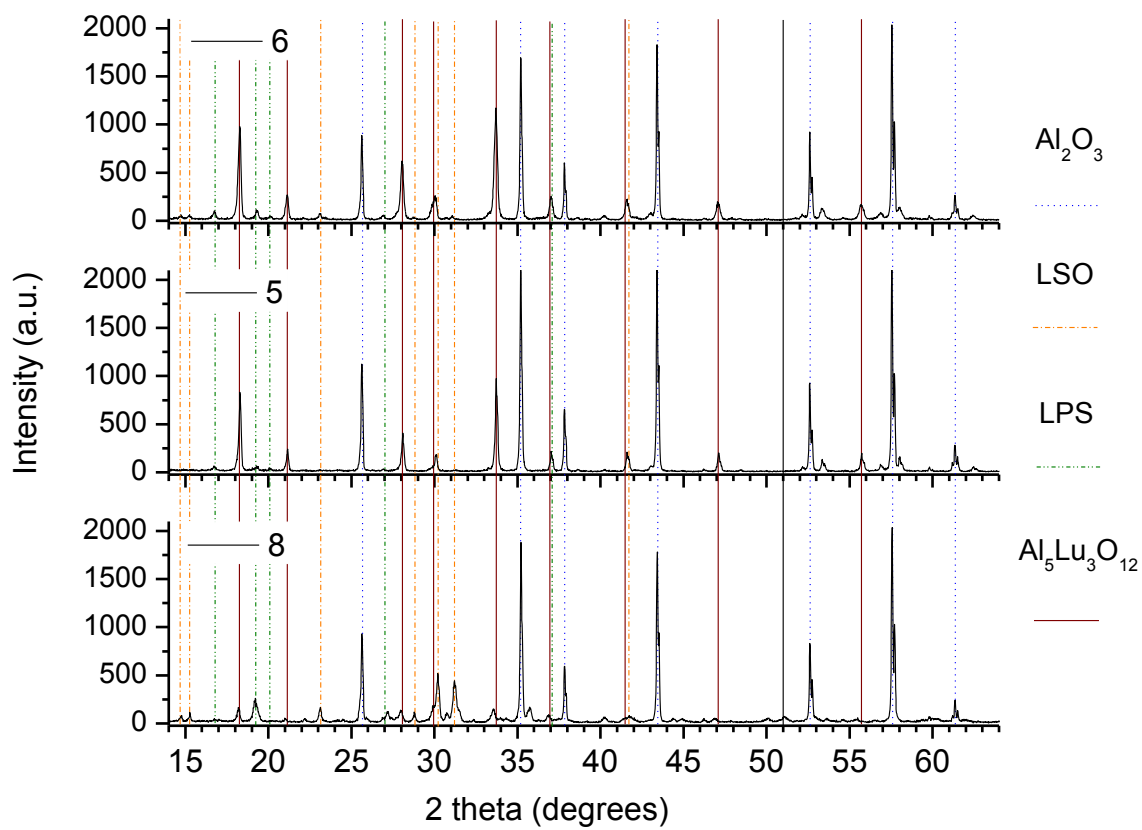
190

Figure 78. XRD spectra at selected locations.

Table 19. a) The primary phases present at each location with their relative weight percentages and the weight percent of each element from the composition model. b) The WDS results from table 18 (with the addition of oxygen) converted to weight percent.

a.

Location	Phases from XRD (rel. wt%)			wt% from model			
	1st	2nd	3rd	Lu	Al	Si	O
1	LSO (42)	LPS (33)	LuAG (25)	73.0	7.2	1.6	18.2
2	LuAG	$Lu_4Al_2O_9$		75.3	6.9	0.6	17.2
3	LPS (83)	LuAG (18)		58.9	13.2	3.8	24.1
4	LPS (71)	LSO (29)		70.2	6.7	3.6	19.6
5	LPS (69)	LuAG (31)		59.8	15.1	1.6	23.5
6	LPS (44)	LuAG (34)	LSO (22)	68.5	9.8	1.7	20.0
7	LPS	Al_2SiO_5		61.5	9.9	5.3	23.3
8	LSO (49)	LPS (39)	LuAG (12)	75.7	5.1	2.0	17.2
9	Lu_2O_3	$Lu_4Al_2O_9$		82.1	3.0	0.4	14.4

b.

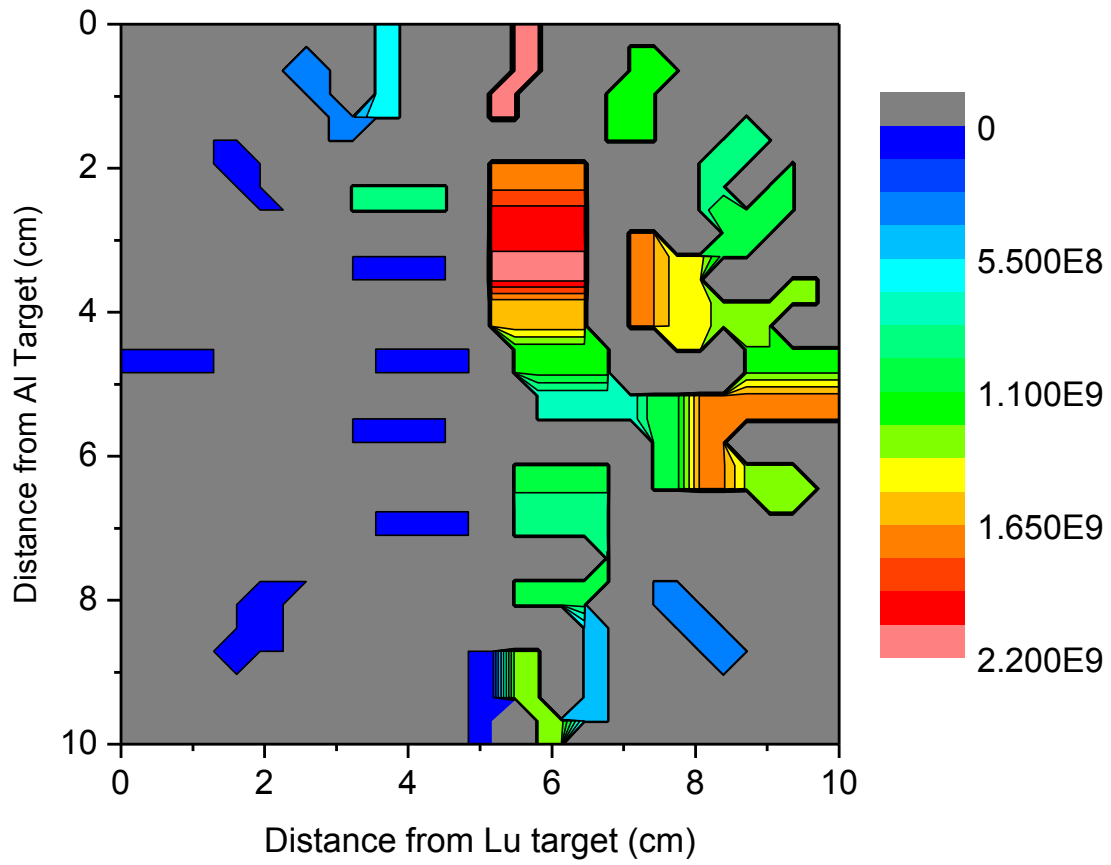|	wt% from WDS				
Location	Lu	Al	Si	O	Ce
1	68.2	6.5	2.7	18.2	0.5
6	56.7	13.7	2.2	22.6	0.4
7a	17.4	35.3	5.1	39.6	0.2
7b	32.2	13.7	12.8	31.3	0.7
9	78.2	2.1	0.6	13.3	0.3

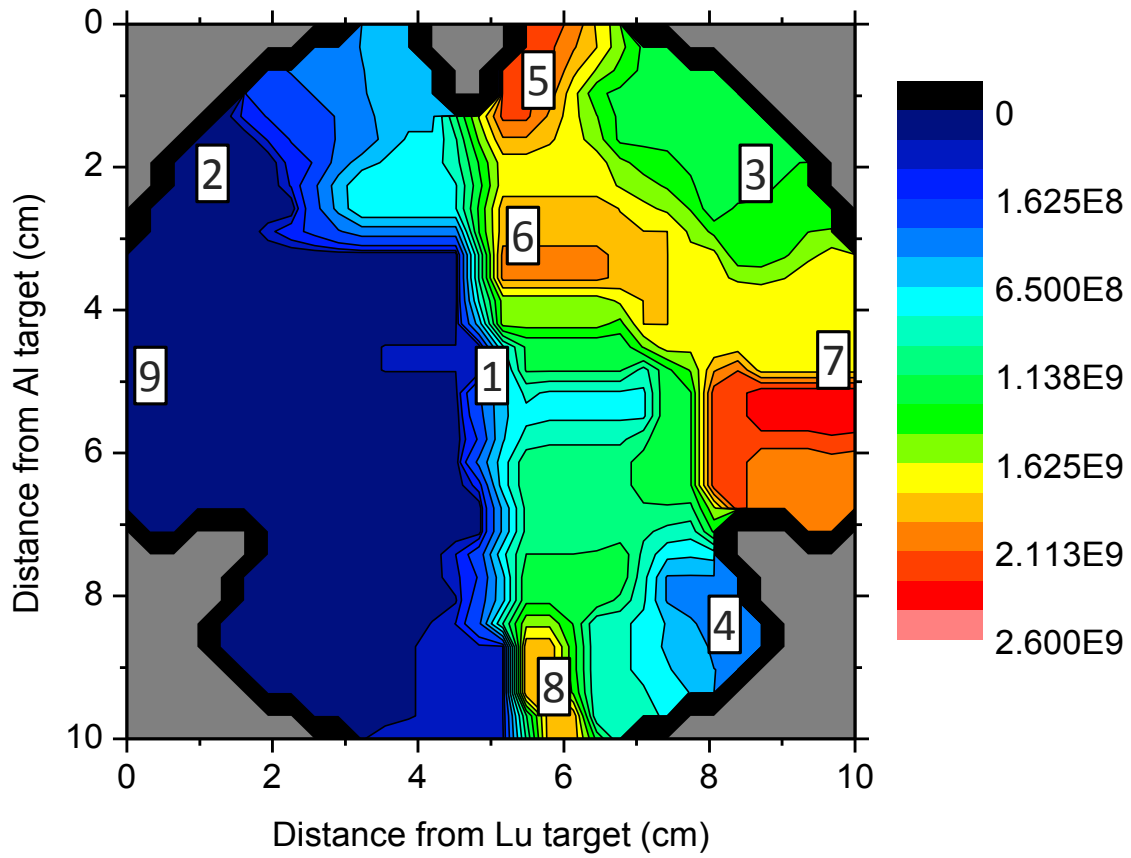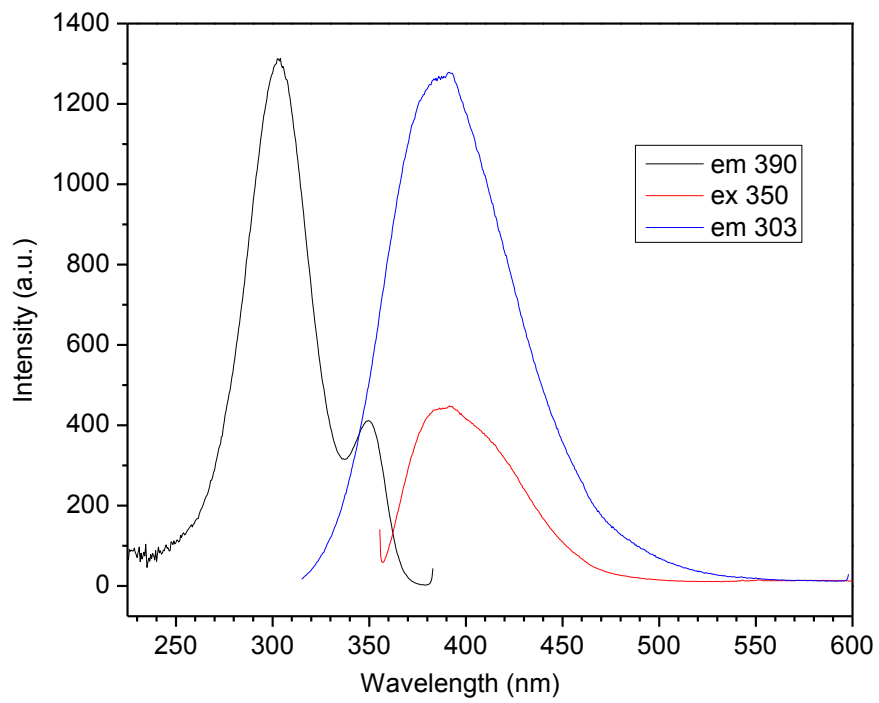Figure 79. Integrated PL emission intensity: measured positions.

Figure 80. Integrated PL emission intensity: thickness corrected and interpolated.

intensity that warrant further interest, which are locations 5, 6, 8 and just below location 7. The PL excitation and emission spectra for locations 5, 6, 8 and 7 (just below) are plotted in figure 81a-d. All of the spectra exhibit two dominant excitation peaks. Interestingly, moving from location 5 (figure 81a, high aluminum) to location 8 (figure 81d, low aluminum) the relative intensities of the excitation peaks change. As the aluminum concentration is decreased the higher energy excitation peak decreases and the low energy excitation peak increases. Location 8 exhibits characteristic LSO PL spectra (see figure 20a and b for reference). Locations 6 (figure 81b) and just-below-7 (figure 81c) exhibit spectra very close to characteristic LPS PL spectra, with location 6 exhibiting the highest peak emission intensity. The emission spectrum of location 5 is also similar to LPS, as are the excitation peak positions, but the relative excitation peak intensities are altered. None of the measured locations exhibited characteristic LuAG:Ce PL excitation (peak at 450 nm) and emission (peak at 500 nm). As expected, Lu_2O_3, $Lu_4Al_2O_9$ and Al_2SiO_5 phases did not appear to luminesce.

Discussion

Silicon concentration

The silicon concentration in the ternary sample was measured (via WDS) to be roughly half of the expected concentration based on the measured sputtering rates. This appears to be due to the silicon target slowly transitioning into covered mode (thus

195

a.

b.

196
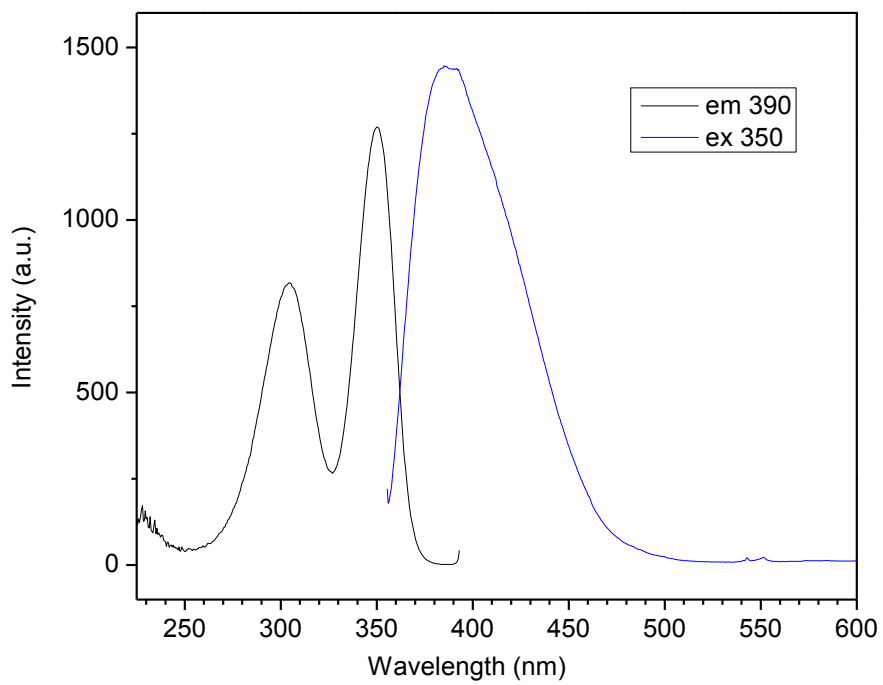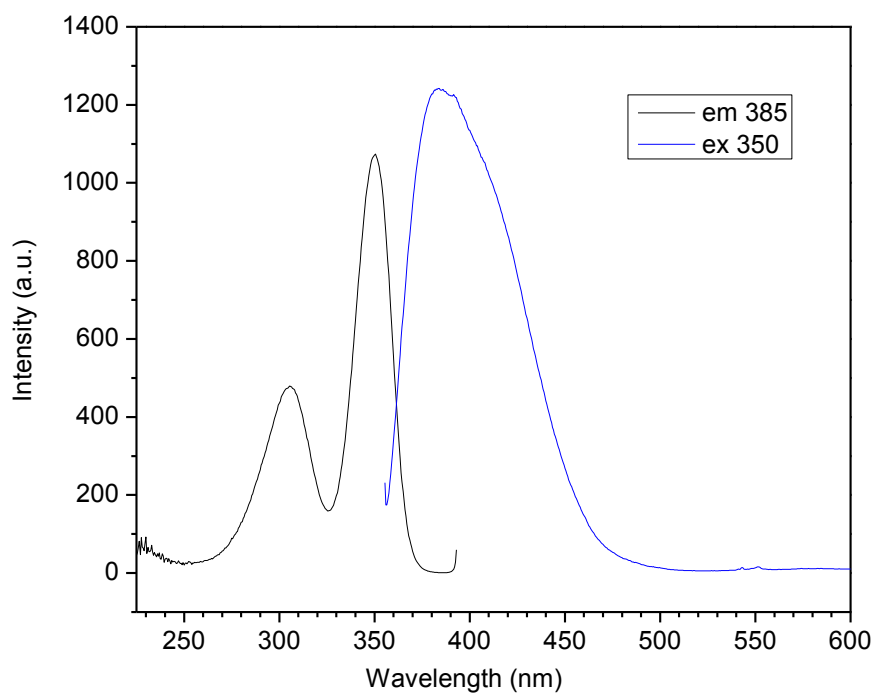
c.

d.

Figure 81. PL excitation and emission spectra for positions in figure 80 that exhibited high integrated emission intensity: a) 5, b) 6, c) just below 7 and d) 8.

197

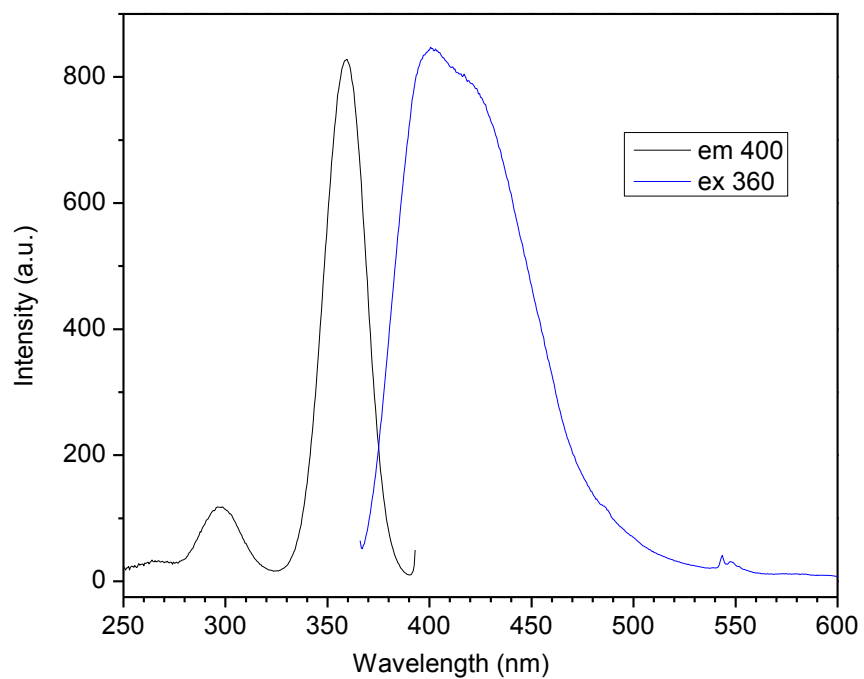greatly reducing the sputtering rate) during sample deposition. For the Lu_2O_3-SiO_2-Al_2O_3 ternary co-sputtering thickness measurements of 15 minutes it was found that oxygen partial pressures higher than the metal to covered mode transition values of the individual targets were able to be used without affecting the self-bias voltages on the targets. The steady self-bias voltages suggested the deposition rates remained unchanged. This was confirmed by the measured co-sputtering deposition rate. These results led to the assumption that with multiple targets sputtering the increased number of ionized species in the chamber was acting to getter the oxygen and preventing oxidation of the target surfaces. Additionally, the individual silicon sputtering rate was measured before and immediately after sample deposition and yielded consistent rates. However, the WDS results reveal that the silicon deposition rate must have decreased during the 50 minutes worth of sputtering during the sample processing. The most reasonable explanation for the discrepancy is that the additional sources did not act to getter enough oxygen to support the higher oxygen partial pressure. In turn the rate of the transition to covered mode transition for the silicon target was merely abated. Therefore, it was not seen in the 15 minute thickness measurement but was a factor in the longer 50 minute sample processing. This also brings into question the aluminum-silicon ratio in the WDS measurements as exhibited by the change in the ratio between 5 keV and 15 keV. The silicon content near the surface appears to be less than near the substrate, again due to the oxidation of the

198

silicon target. Fortunately, the combinatorial method proved to be somewhat robust and the lower silicon concentration still provided intriguing results.

Compositions of high intensity phases

Of the locations that contained the LSO phase and exhibited characteristic LSO PL excitation and emission spectra location 8, demonstrated the highest emission intensity, even before correcting for thickness. Additionally, location 8 contains the lowest percentage of aluminum out of all the locations that contain the LSO phase. This strongly suggests that the presence of aluminum in LSO is detrimental to luminescence intensity.

Surprisingly, neither characteristic LuAG:Ce emission (450 nm excitation, 500 nm emission) nor substantial emission near 500 nm was observed. Referencing table 19, most of the locations that contained LuAG, contained higher relative percentages of LPS. In these locations it is likely the higher concentration LPS dominates the luminescent behavior of the location. Location 2 was the only area where LuAG was the dominant phase. However, $Lu_4Al_2O_9$ was also present which does not appear to be luminescence and possibly quenched the LuAG:Ce emission.

The area just below position 7 exhibited high thickness-corrected luminescence intensity. BSE images of this region region also showed extensive phase separation (figure 77a). The phase separation in this region appears to enhance the emission intensity. This could be due to several factors. The phase separation could act to

increase the out-coupling of light produced in the film. Additionally, the multiphase structure would lower the melting temperature of LPS which could lead to larger grain sizes and fewer defects, both of which can improve luminescence intensity.

Location 5 also exhibited high luminescence emission. The intensity of the low energy excitation peak at location 5 is decreased compared to the high energy peak (figure 81a). Self-absorption has been observed in LPS due to overlap between the emission and the low energy excitation peak. Decreasing the low energy excitation peak will potentially decrease the degree of self-absorption. Location 5 is in the region with the highest at% of aluminum. Therefore, the shift in the intensity ratios of the two excitation peaks is attributed to the incorporation of aluminum into LPS. However, estimating the percentage of aluminum incorporated into the LPS is less straightforward. An estimation can be made by comparing the relative weight percentages of the present phases measured by XRD to the individual weight percentages of the elements from the composition model. As discussed above, due to the oxidation of the silicon target the WDS aluminum-silicon ratio is not considered accurate. Due to the alumina wafer, the percentage of Al_2O_3 in the film was not able to be measured. Normalizing the XRD values to the lutetium concentration of the composition model and basing the percent of Al_2O_3 in the film on the remaining stoichiometric oxygen yields an excess of 1.41 wt% aluminum. If it is assumed all of the excess aluminum is in the LPS phase this gives a doping range of 2.18 at% to 2.5 at%, depending on whether the aluminum sits in a lutetium, silicon, or is interstitial site.

Considering the ionic radius of aluminum (Al^{3+}, 0.535 Å) is much smaller than the ionic radius lutetium (Lu^{3+}, 0.861 Å) or cerium (Ce^{3+}, 1.02 Å), the aluminum is most likely sitting in an interstitial site or, more likely, a silicon site (Si^{4+}, 0.40 Å) . However, additional characterization would be required to confirm this.

Conclusion

The addition of a third component to the material system being explored complicates the sample processing and increases the time required to characterize the film. However, the potential benefits of exploring a ternary system increase dramatically. Using a serial method to identify the compositions of the brightest locations on the substrate with traditional crystal growth would be prohibitively time consuming.

The identified co-doping concentration of 2.5 at% aluminum in LPS:Ce appears to be a reasonable value. However, future work involving the growth of single crystal LPS:Ce co-doped with aluminum is required for confirmation of the present findings.

CHAPTER VI
CONCLUSION

In chapter 2, the thin film combinatorial technique successfully screened the binary Lu_2O_3-SiO_2 material system, identified the phases present and correlated the phases to the exhibited luminescence spectra. There are numerous physical differences between thin film and single crystal bulk samples, namely the morphology and sample thickness; however, the thin film photoluminescence spectra matched the single crystal spectra. Additionally, emission intensity for the LSO and LPS phases were in line with expectations based on single crystal behavior. Ultimately, the photoluminescence provided an accurate comparison and proved to be a valuable metric. XRD of the thin film also showed good results and clearly followed the expected phase diagram. The combination of XRD and photoluminescence can be employed to rapidly and successfully screen combinatorial thin film scintillation material libraries.

SEM imaging is not directly required for screening scintillation material systems, but it is helpful to confirm as deposited thickness (and therefore help confirm composition) and morphology of annealed samples. Photoluminescence and XRD are invaluable at each measurement location, but SEM imaging can be employed on an as-needed basis, which will increase the speed of understanding and interpreting the screening process.

In chapter 3, the effect of cerium concentration on single crystal LSO was investigated with temperature dependent steady-state and time-resolved luminescence spectroscopy. The results were used to determine the thermal quenching activation

energies and the phonon energies responsible for the thermal broadening of the luminescence spectra. The measured electron-phonon coupling values were shown to correspond to a Raman active Lu cation of the host LSO for small cerium concentrations. The measured phonon values were used to calculate CC diagrams of the luminescence centers. The observed broadening of the excitation spectra and narrowing of the emission spectra with increasing cerium was explained via a CC model. A combination of the CC model and concentration quenching explained the measured thermal quenching activation energies. Single crystal LSO experienced concentration at quenching due to self-absorption at relatively low cerium concentrations that was driven by a broadening of the configuration coordinate diagram (and PL spectra) and changes in the phonon modes affecting the cerium luminescence center.

Knowledge gained of the single crystal LSO cerium concentration dependent behavior in chapter 3 was used in conjunction with the results in chapter 4 to give a clear picture of the cerium concentration-dependent behavior of thin film LSO. It was found that the thin film LSO does not follow the single crystal concentration quenching mechanism because the 1 μm thick thin film is less susceptible to self-absorption. Additionally, the nano-crystalline nature of the film more easily accommodates the stresses induced by the cerium activator reducing the excitation spectrum broadening that is responsible for the increase in self-absorption. With the self-absorption quenching mechanism removed the ideal cerium concentration was found to increase to a level where additional

quenching mechanisms begin to dominate the luminescence behavior. In this case the mechanism that dominates is an increase in defect mediated non-radiative pathways.

In chapter 5 the ternary Lu_2O_3-SiO_2-Al_2O_3 material system was investigated. Three luminescent phases in the system where observed: LSO, LuAG and LPS. It was found that the addition of aluminum to LSO:Ce decreased the luminescence emission intensity. The LuAG present in the film exhibited very low luminescence due to either more dominant emission by the LSO and LPS, quenching by the addition or silicon, or possible quenching by the presence of non-luminescent phases such as $Lu_4Al_2O_9$. From the results it appeared that the addition of aluminum does improve the luminescence of LPS:Ce. The percentage of aluminum was estimated at 2.5 at%. Future work including the growth of single crystal LPS:Ce co-doped with aluminum is required for confirmation.

Outlook on combinatorial sputtering

The thin film combinatorial screening method was found to have some limitations in regards to optimizing the activator concentration. The binary and ternary studies had less limitations but were still subject to some complications. The main complications encountered are the film-substrate interaction, the degree of light out-coupling is sensitive to the film morphology and the inherent limited probe volume of a thin film. However, even with the complications the technique showed promise in exploring binary and ternary material systems. Additionally, based on the binary and ternary results, the technique shows promise for application to "alloying" systems such as (Lu_{1-}

$_x$Gd$_x$)$_2$SiO$_5$. If the above mentioned complications could be lessened the technique would be more robust.

The greatest advantage of the technique is the ability to rapidly produce a large number of compositions for each processing run. The potential number of compositions on one wafer (and therefore per processing run) is ultimately limited by the measurement spot size of the characterization method employed. This is illustrated in figure 82 by comparing the technique to a single crystal processing method such as Czochralski growth by setting the processing time for both methods to one week and plotting the number of potential compositions versus the measurement spot size. This was done for a binary gradient. The time advantage increase more dramatic for a ternary systems such as the one explored in chapter 5 where PL was measured for 35 different compositions.
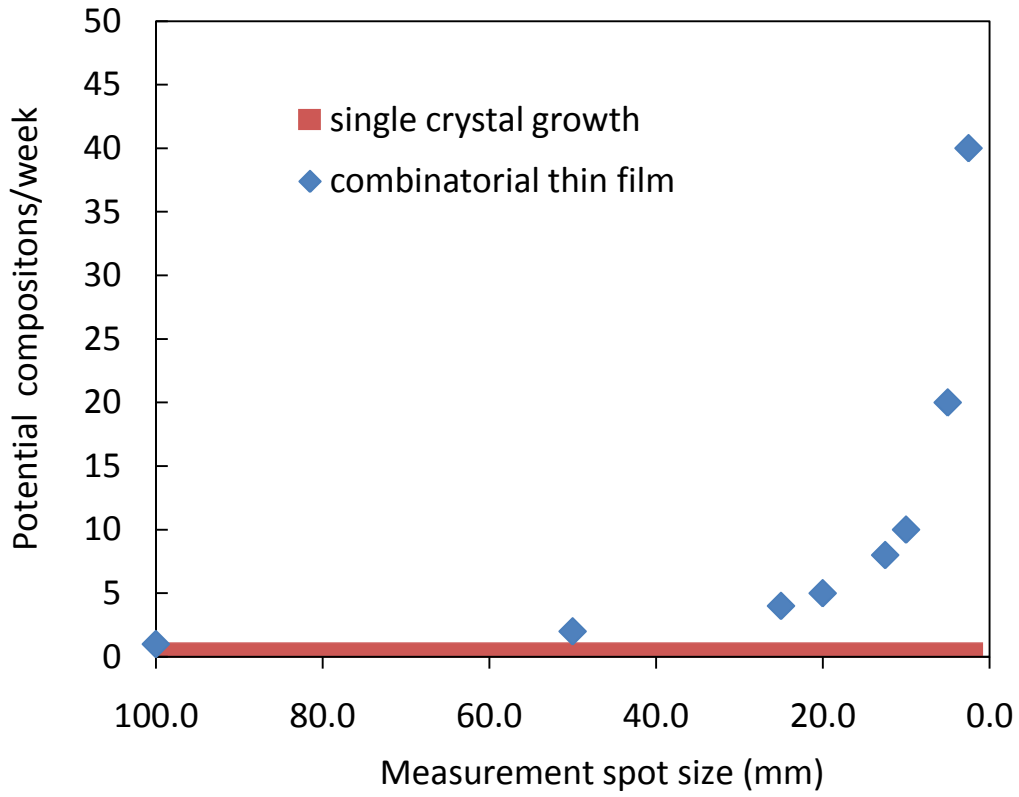
Figure 82. Measurement spot size versus number of potential compositions measured per week.

LIST OF REFERENCES

[1]   C. L. Melcher, "Perspectives on the future development of new scintillators," Nuclear Instruments & Methods in Physics Research Section A, vol. 537, pp. 6-14, (2005).

[2]   C. L. Melcher, "Scintillation Crystals for PET," The Journal of Nuclear Medicine, vol. 41, pp. 1051-1055, (2000).

[3]   B. R. Pamplin, *Crystal Growth*, 2nd ed. Oxford: Pergamon Press, (1980).

[4]   W. M. Yen, S. Shionoya, and H. Yamamoto, *Phosphor Handbook*, 2nd ed. Boca Raton: CRC Press, (2007).

[5]   P. D. Rack, "Optical Transitions in Alkaline Earth Sulfide Electroluminescent Phosphors," PhD Dissertation, Materials Science and Engineering, University of Florida, Gainesville, FL, (1997).

[6]   T. A. O'Brien, P. D. Rack, P. H. Holloway, and M. C. Zerner, "Crystal field and molecular orbital calculation of the optical transitions in Ce doped alkaline earth sulfide (MgS, CaS, SrS, and BaS) phosphors," Journal of Luminescence, vol. 78, pp. 245-257, (1998).

[7]   G. F. Knoll, *Radiation Detection and Measurement*, 2nd ed. New York: John Wiley & Sons, Inc., (1989).

[8]   A. Lempicki, A. J. Wojtowicz, and E. Berman, "Fundamental limits of scintillator performance," Nuclear Instruments & Methods in Physics Research Section A, vol. 333, pp. 304-311, (1980).

[9]   D. J. Robbins, "On predicting the maximum efficiency of phosphor systems excited by ionizing radiation," Journal of the Electrochemical Society, vol. 127, pp. 2694-2702, (1980).

[10]   H. Suzuki, T. A. Tombrello, C. L. Melcher, and J. S. Schweitzer, "Light Emission Mechanism of $Lu_2(SiO)_4O$:Ce," IEEE Transactions on Nuclear Science, vol. 40, pp. 380-383, August (1993).

[11]   H. Suzuki, T. A. Tombrello, C. L. Melcher, and J. S. Schweitzer, "UV and gamma-ray excited luminescence of cerium-doped rare-earth oxyorthosilicates," Nuclear Instruments and Methods in Physics Research Section A: Accelerators, Spectrometers, Detectors and Associated Equipment, vol. 320, pp. 263-272, (1992).

[12]   J. D. Naud, T. A. Tombrello, C. L. Melcher, and J. S. Schweitzer, "The role of cerium sites in the scintillation mechanism of LSO," IEEE Transactions on Nuclear Science, vol. 43, pp. 1324 - 1328, June (1996).

[13]   M. Ohring, *Materials Science of Thin Films*, 2nd ed. San Diego: Academic Press, (2002).

[14]   H. Koinuma and I. Takeuchi, "Combinatorial solid-state chemistry of inorganic materials," Nature Materials, vol. 3, pp. 429 - 438, July 2004 (2004).

[15]   K. Kennedy, T. Stefansky, G. Davy, V. F. Zackay, and E. R. Parker, "Rapid method for determining ternary-alloy phase diagrams," Journal of Applied Physics, vol. 36, pp. 3808-3810, (1965).

[16]   J. J. Hanak, "The "multiple-sample concept" in materials research: Synthesis, compositional analysis and testing of entire multicomponent systems," Journal of Materials Science, vol. 5, pp. 964-971, (1970).

[17]   X. D. Xiang, S. Xiaodong, G. Briceno, L. Yulin, W. Kai-An, C. Hauyee, W. G. Wallace-Freedman, C. Sung-Wei, and P. G. Schultz, "A combinatorial approach to materials discovery," Science, vol. 268, pp. 1738-40, (1995).

[18]   B. D. Milbrath, J. A. Caggiano, M. H. Engelhard, A. G. Joly, D. W. Matson, P. Nachimuthu, and L. C. Olsen, "Using thin films to screen possible scintillator materials," IEEE Transactions on Nuclear Science, vol. 56, pp. 1650-1654, (2009).

[19]   D. W. Matson, G. L. Graff, J. L. Male, B. R. Johnson, Z. Nie, A. G. Joly, and L. C. Olsen, "Synthesis and screening of thin films in the $CeCl_3$-$CeBr_3$ system for scintillator applications," Thin Solid Films, vol. 518, pp. 3194-3198, (2010).

[20]   Y. Zorenko, V. Gorbenko, A. Voloshinovskii, G. Stryganyuk, V. Mikhailin, V. Kolobanov, D. Spassky, M. Nikl, and K. Blazek, "Exciton-related luminescence in LuAG:Ce single crystals and single crystalline films," Physica Status Solidi (a), vol. 202, pp. 1113-1119, (2005).

[21]   Y. Zorenko, V. Gorbenko, E. Mihokova, M. Nikl, K. Nejezchleb, A. Vedda, V. Kolobanov, and D. Spassky, "Single crystalline film scintillators based on Ce- and Pr- doped aluminium garnets," Radiation Measurements, vol. 42, pp. 521-527, (2007).

[22]   P. Prusa, T. Cechak, J. A. Mares, M. Nikl, A. Beitlerova, N. Solovieva, Y. V. Zorenko, V. I. Gorbenko, J. Tous, and K. Blazek, "The α-particle excited scintillation response of the liquid phase epitaxy grown LuAG:Ce thin films," Applied Physics Letters, vol. 92, p. 041903, (2008).

[23]   T. Martin, P.-A. Douissard, M. Couchaud, A. Cecilia, T. Baumbach, K. Dupre, and A. Rack, "LSO-Based Single Crystal Film Scintillator for Synchrotron-Based Hard X-ray Micro-Imaging," IEEE Transactions on Nuclear Science, vol. 56, pp. 1412-1418, (2009).

[24]   Y. Deng, J. D. Fowlkes, J. M. Fitz-Gerald, and P. D. Rack, "Combinatorial thin film synthesis of Gd-doped $Y_3Al_5O_{12}$ ultraviolet emitting materials," Applied Physics A, vol. 80, pp. 787-789, (2005).

[25]   Y. Deng, J. D. Fowlkes, P. D. Rack, and J. M. Fitz-Gerald, "Thin film rf magnetron sputtering of gadolinium-doped yttrium aluminum garnet ultraviolet emitting materials," Optical Materials, (2005).

[26]   J. D. Fowlkes, J. M. Fitz-Gerald, and P. D. Rack, "Ultraviolet emitting ($Y_{1-x}Gd_x$)$_2O_{3-\delta}$ thin films deposited by radio frequency magnetron sputtering: Combinatorial modeling, synthesis, and rapid characterization," Thin Solid Films, vol. 510, pp. 68-76, (2006).

[27]   J. D. Fowlkes, J. M. Fitz-Gerald, and P. D. Rack, "Ultraviolet emitting (Y1-xGdx)2O3 - [delta] thin films deposited by radio frequency magnetron sputtering; structure-property-thin film processing relationships," Thin Solid Films, vol. 515, pp. 3488-3498, (2007).

[28]   P. D. Rack, J. D. Peak, C. L. Melcher, and J. M. Fitz-Gerald, "Scanning electron and cathodoluminescence imaging of thin film Lu_2SiO_5:Ce scintillating materials," Applied Physics Letters, vol. 91, (2007).

[29]   J. D. Peak, C. L. Melcher, and P. D. Rack, "Combinatorial Thin Film Synthesis of Cerium Doped Scintillation Materials in the Lutetium Oxide - Silicon Oxide System," IEEE Transactions on Nuclear Science, vol. 55, pp. 1480-1483, June (2008).

[30]   N. A. Toropov, I. A. Bondar, and F. Y. Galakhov, "Transactions of the 8th International Ceramics Congress," Copenhagen, Denmark, 1962, p. 87.

[31]   J. D. Peak, C. L. Melcher, and P. D. Rack, "Combinatorial thin film sputtering investigation of cerium concentration in Lu_2SiO_5 scintillators," Journal of Luminescence, vol. 130, pp. 1366-1370, (2010).

[32]   J. Felsche, "The crystal chemistry of the rare-earth silicates," in *Structure and Bonding*. vol. 13, ed: Springer-Verlag, 1973, pp. 99-197.

[33]   C. D. Brandle, A. J. Valentino, and G. W. Berkstresser, "Czochralski growth of rare-earth orthosilicates (Ln_2SiO_5)," Journal of Crystal Growth, vol. 79, pp. 308-315, (1986).

[34]   B. Henderson and G. F. Imbusch, *Optical Spectrosopy of Inorganic Solids*: Clarendon Press, (1989).

[35]   B. Di Bartolo, *Optical interactions in solids*. New York: Wiley, (1968).

[36]   C. L. Melcher and J. S. Schweitzer, "Cerium-doped Lutetium Oxyorthosilicate: A Fast, Efficient New Scintillator," IEEE Transactions on Nuclear Science, vol. 39, pp. 502-505, (1992).

[37]   R. Mao, L. Zhang, and R.-Y. Zhu, "Emission Spectra of LSO and LYSO Crystals Excited by UV Light, X-ray and γ–ray," IEEE Transactions on Nuclear Science, vol. 55, pp. 1759-1766, (2008).

[38]   Y. Chen, B. Liu, C. Shi, G. Ren, and G. Zimmerer, "The temperature effect of Lu_2SiO_5:Ce^{3+} luminescence," Nuclear Instruments & Methods in Physics Research Section A, vol. 537, pp. 31-35, (2005).

[39]   K. Yang, C. L. Melcher, P. D. Rack, and L. Eriksson, "Effects of Calcium Co-doping on Charge Traps in LSO:Ce Crystals," presented at the IEEE Nuclear Science Symposium, 2007.

[40]   K. Yang, C. L. Melcher, and M. Zhuravleva, "Luminescence Centers in Calcium Co-doped LSO:Ce Single Crystals," presented at the IEEE Nuclear Science Symposium, 2009.

[41]   N. Yamashita, Y. Michitsuji, and S. Asano, "Photoluminescence Spectra and Vibrational Structures of the SrS:Ce^{3+} and SrSe:Ce^{3+} Phosphors," Journal of the Electrochemical Society, vol. 134, pp. 2932-2934, (1987).

[42]   D. W. Cooke, B. L. Bennett, K. J. McClellan, J. M. Roper, M. T. Whittaker, and A. M. Portis, "Electron-lattice coupling parameters and oscillator strengths of cerium-doped lutetium oxyorthosilicate," Physical Review B, vol. 61, (2000).

[43]   J. Andriessen, P. Dorenbos, and C. W. E. van Eijk, "Calculation of energy levels of cerium in inorganic scintillator crystals," in *Scintillator and Phosphor Materials. Symposium, 6-8 April 1994*, Pittsburgh, PA, USA, 1994, pp. 355-65.

[44]   H. Merenga, J. Andriessen, and C. W. E. Van Eijk, "Positions of 4f and 5d energy levels of Ce3+ in the band gap of CeF3, YAG and LSO," in *LUMDETR '94. International Symposium on Luminescent Detectors and Transformers of Ionizing Radiation, 25-29 Sept. 1994*, UK, 1995, pp. 343-6.

[45]   A. Y. Kuznetsov, A. B. Sobolev, A. N. Varaksin, and O. A. Keda, "Embedded Cluster Calculations of the Electron Structure of the Ce^{3+} Impurity in Lu_2SiO_5 Crystals with Allowance for Crystal Lattice Relaxation and Polarization," Physica Status Solidi (b), vol. 204, pp. 701-712, (1997).

[46]   A. N. Varaskin, A. B. Sobolev, A. Y. Kuznetsov, and O. A. Keda, "Molecular-statics simulation of the cerium impurity of LSO crystals," Physics of the Solid State, vol. 39, pp. 426-427, (1997).

[47]   G. Blasse and B. C. Grabmaier, *Luminescent Materials*: Springer-Verlag, (1994).

[48]   B. Liu, M. Gu, Z. Qi, C. Shi, M. Yin, and G. Ren, "Laser-excited spectra of Lu_2SiO_5:Ce scintillator," Journal of Luminescence, vol. 127, pp. 645-649, (2007).

[49]   D. Chiriu, N. Faedda, A. G. Lehmann, and P. C. Ricci, "Structural characterization of $Lu_{1.8}Y_{0.2}SiO_5$ crystal," Physical Review B, vol. 76, pp. 1-8, (2007).

[50]   S. Campos, A. Denoyer, S. Jandl, B. Viana, D. Vivien, P. Loiseau, and B. Ferrand, "Spectroscopic studies of Yb3+-doped rare earth orthosilicate crystals," Journal of Physics: Condensed Matter, vol. 16, pp. 4579-4590, (2004).

[51]   P. C. Ricci, C. M. Carbonaro, D. Chiriu, R. Corpino, N. Faedda, M. Marceddu, and A. Anedda, "Ce^{3+}-doped lutetium orthosilicate crystals: Structural characterization," Materials Science and Engineering B, vol. 146, pp. 2-6, (2008).

[52]   P. Dorenbos, C. W. E. van Eijk, A. J. J. Bos, and C. L. Melcher, "Afterglow and thermoluminescence properties of Lu_2SiO_5:Ce scintillation crystals," Journal of Physics: Condensed Matter, vol. 6, pp. 4167-4180, (1994).

[53]   M. Raukas, "Luminescence Efficiency and Electronic Properties of Cerium," PhD, University of Georgia, Athens, GA, (1997).

[54]   W. M. Yen, M. Raukas, S. A. Basun, W. v. Schaik, and U. Happek, "Optical and photoconductive properties of cerium-doped crystalline solids," Journal of Luminescence, vol. 69, pp. 287-294, (1996).

[55]   U. R. Rodriquez-Mendoza, G. B. Cunningham, Y. Shen, and K. L. Bray, "High-pressure luminescence studies in Ce^{3+}:Lu_2SiO_5," Physical Review B, vol. 64, p. 195112, (2001).

[56]   C. L. Melcher, M. Schmand, M. Eriksson, L. Eriksson, M. Casey, R. Nutt, J. L. Lefaucheur, and B. Chai, "Scintillation Properties of LSO:Ce Boules," IEEE Transactions on Nuclear Science, vol. 47, pp. 965-968, (2000).

[57]   L. Pidol, O. Guillot-Noel, A. Kahn-Harari, B. Viana, D. Pelenc, and D. Gourier, "EPR study of Ce^{3+} ions in lutetium silicate scintillators $Lu_2Si_2O_7$ and Lu_2SiO_5," Journal of Physics and Chemistry of Solids, vol. 67, pp. 643-650, (2006).

[58]   F. H. Chung, "Quantitative Interpretation of X-ray Diffraction Patterns of Mixtures. I. Matrix-Flushing Method for Quantitative Multicomponent Analysis," Journal of Applied Crystallography, vol. 7, pp. 519-525, (1974).

[59]   X.-J. Liu, H.-L. Li, R.-J. Xie, Y. Zeng, and L.-P. Huang, "Spectroscopic properties of nano-sized cerium-doped lutetium aluminum garnet phosphors via

sol-gel combustion process," Journal of Luminescence, vol. 124, pp. 75-80, (2007).

[60]   H. A. M. v. Hal and H. T. Hintzen, "Compound formation in the Ce_2O_3-SiO_2 system," Journal of Alloys and Compounds, vol. 179, pp. 77-85, (1992).

[61]   W. C. Choi, H. N. Lee, E. K. Kim, Y. Kim, C.-Y. Park, H. S. Kim, and J. Y. Lee, "Violet/blue light-emitting cerium silicates," Applied Physics Letters, vol. 75, pp. 2389-2391, (1999).

[62]   L. Kepinski, D. Hreniak, and W. Strek, "Microstructure and luminescence properties of nanocrystalline cerium silicates," Journal of Alloys and Compounds, vol. 341, pp. 203-207, (2002).

[63]   P. Szupryczynski, M. A. Spurrier, C. J. Rawn, C. L. Melcher, and A. A. Carey, "Scintillation and optical properties of LuAP and LuYAP crystals," presented at the 2005 IEEE Nuclear Science Symposium, Puerto Rico, 2005.

[64]   A. J. Wojtowicz, W. Drozdowski, D. Wisniewski, K. Wisniewski, K. R. Przegietka, H. L. Oczkowski, and T. M. Piters, "Thermoluminescence and Scintillation of $LuAlO_3$:Ce," Radiation Measurements, vol. 29, pp. 323-326, (1998).

[65]   A. Lempicki and J. Glodo, "Ce-doped scintillators: LSO and LuAP," Nuclear Instruments & Methods in Physics Research Section A, vol. 416, pp. 333-344, (1998).

[66]   C. Mansuy, C. Dujardin, R. Mahiou, and J. M. Nedelec, "Characterization and scintillation properties of sol-gel derived Lu_2SiO_5:Ln^{3+} (Ln = Ce, Eu and Tb) powders," Optical Materials, vol. 31, pp. 1334-1336, (2009).

[67]   C. Mansuy, J. M. Nedelec, and R. Mahiou, "Molecular design of inorganic scintillators: from alkoxides to scintillating materials," Journal of materials Chemistry, vol. 14, pp. 3274-3280, (2004).

[68]   S. Ueno, H.-T. Lin, and T. Ohji, "Corrosion and recession mechanism of $Lu_2Si_2O_7$/mullite eutectic," Journal of the European Ceramic Society, vol. 28, pp. 2359-2361, (2008).

[69]   L. Pidol, A. Kahn-Harari, B. Viana, B. Ferrand, P. Dorenbos, J. T. M. d. Haas, C. W. E. v. Eijk, and E. Virey, "Scintillation propterties of Lu2Si2O7:Ce3+, a fast and efficient scintillator crystal," journal of Physics: Condensed Matter, vol. 15, pp. 2091-2102, (2003).

[70]   D. Pauwels, N. L. Masson, B. Viana, E. V. D. v. Loef, P. Dorenbos, and C. W. E. v. Eijk, "A Novel Inorganic Scintillator: Lu2Si2O7:Ce3+ (LPS)," IEEE Transactions on Nuclear Science, vol. 47, (2000).

[71]   L. Pidol, B. Viana, A. Galtayries, A. Bessiere, and P. Dorenbos, "Optical properties and energy levels of Ce3+ in lutetium pyrosilicate," Journal of Applied Physics, vol. 95, pp. 7731-7737, (2004).

[72]   C. W. E. van Eijk, "Inorganic-scintillator development," Nuclear Instruments & Methods in Physics Research Section A, vol. 460, pp. 1-14, (2001).

[73]   N. J. Cherepy, J. D. Kuntz, T. M. Tillotson, D. T. Speaks, S. A. Payne, B. H. T. Chai, Y. Porter-Chapman, and S. E. Derenzo, "Cerium-doped single crystal and transparent ceramic lutetium aluminum garnet scintillators," Nuclear Instruments & Methods in Physics Research Section A, vol. 579, pp. 38-41, (2007).

[74]   A. Lempicki, C. Brecher, D. Wisniewski, E. Zych, and A. J. Wojtowicz, "Lutetium Aluminate: Spectroscopic and Scintillation Properties," IEEE Transactions on Nuclear Science, vol. 43, pp. 1316-1320, (1996).

[75]   A. G. Petrosyan, V. F. Popova, V. V. Gusarov, G. O. Shirinyan, C. Pedrini, and P. Lecoq, "The Lu2O3-Al2O3 system: Relationships for equilibrium-phase and supercooled states," Journal of Crystal Growth, vol. 293, pp. 74-77, (2006).

[76]   A. K. Shirvinskaya and V. F. Popova, Doklady Akademii nauk SSSR, vol. 223, p. 1110, (1977).

APPENDIX

a.

b.

215
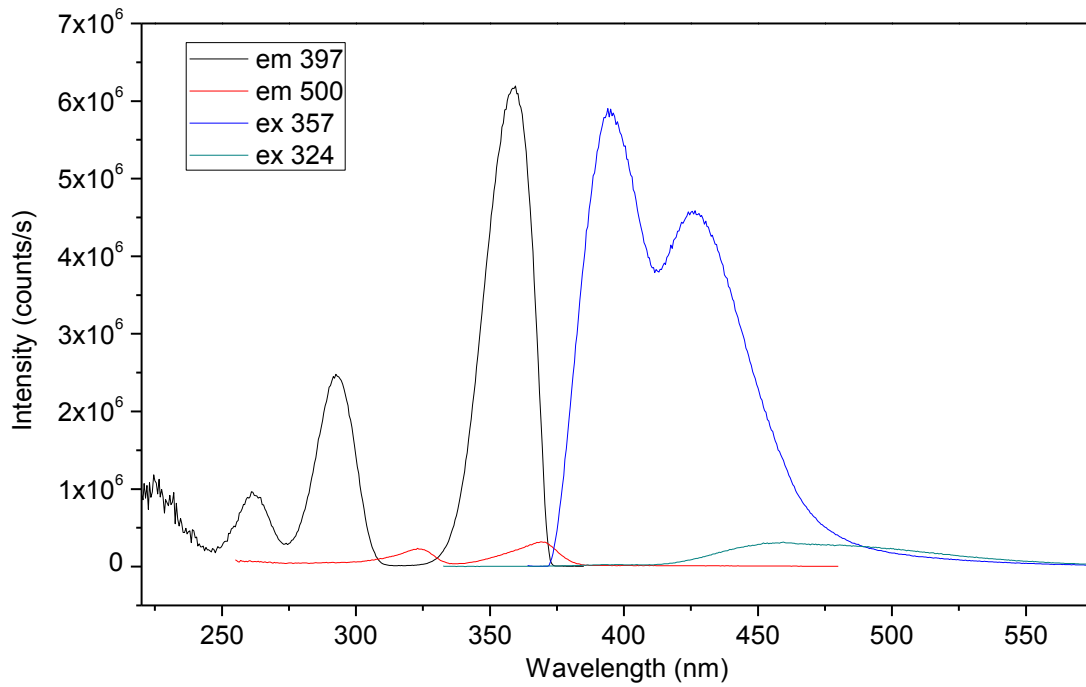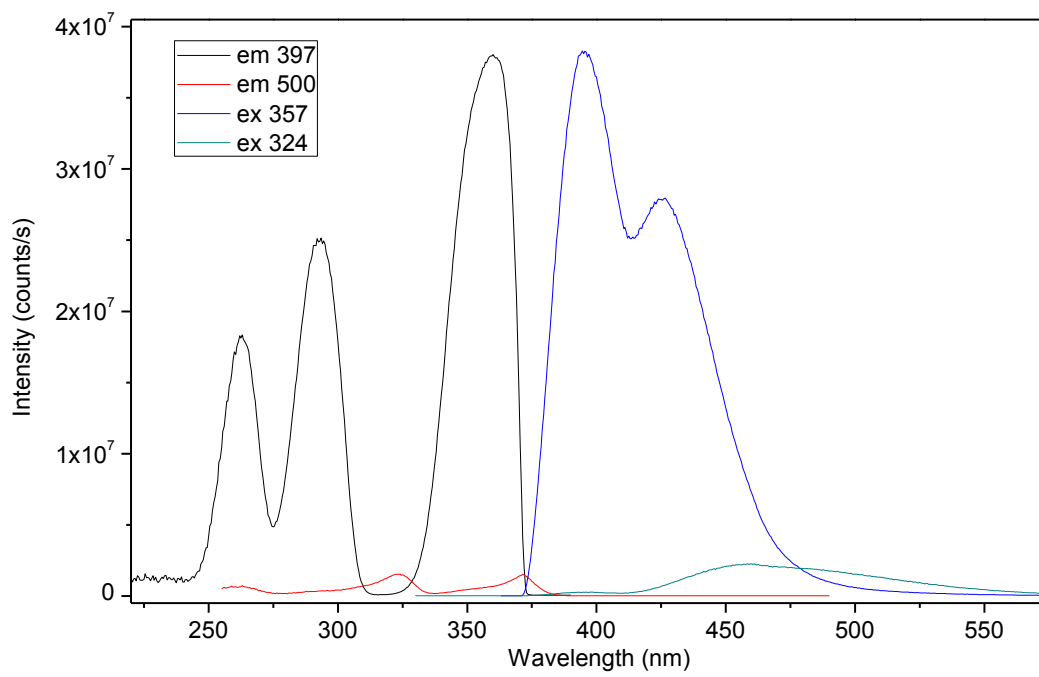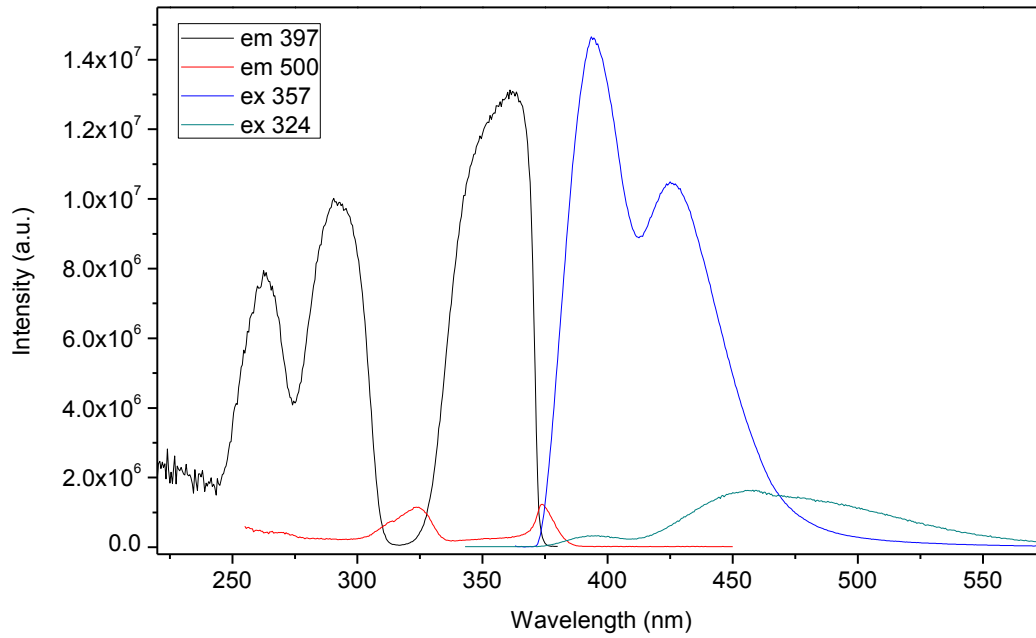
c.

Figure A-1. PL spectra for a) S-74, b) S-51 and c) S-75 at temperatures below 14 K.
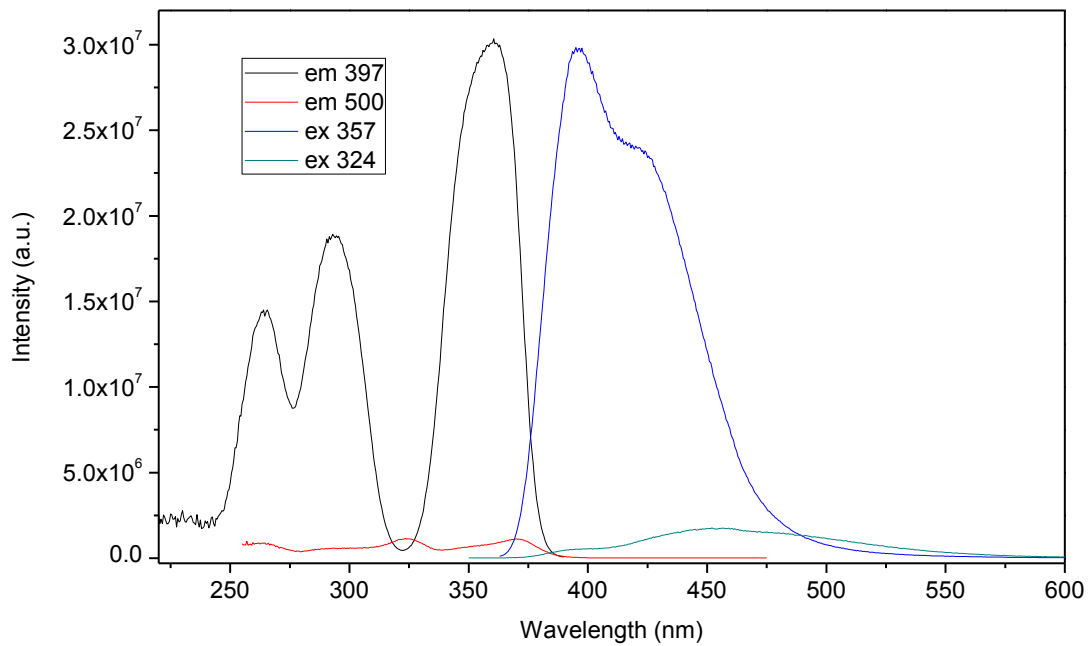
Figure A-2. PL spectra for S-51 at 200 K.
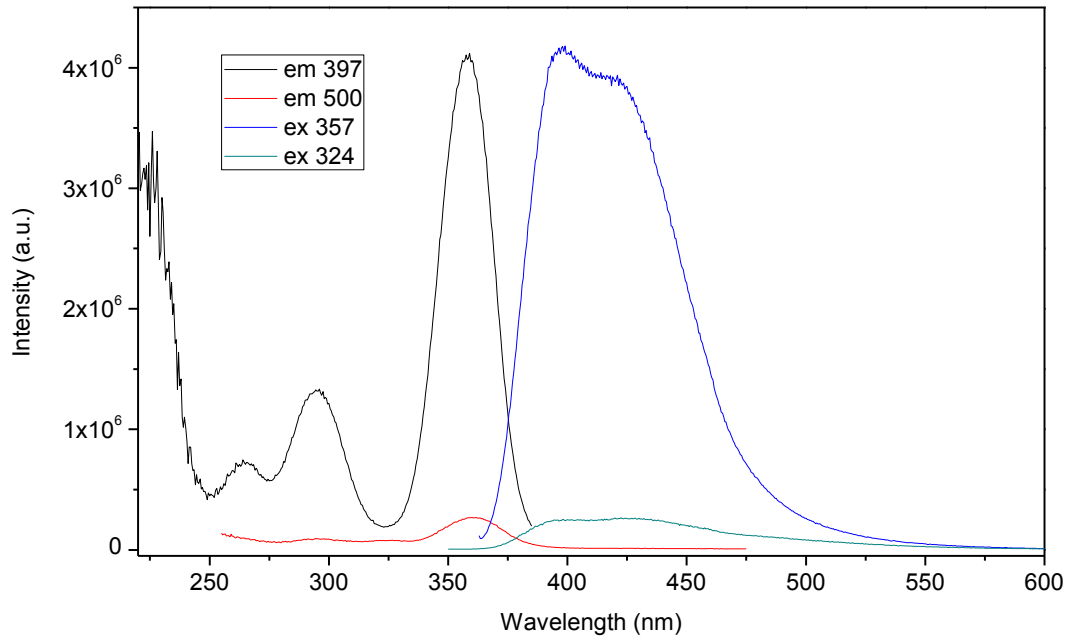
a.
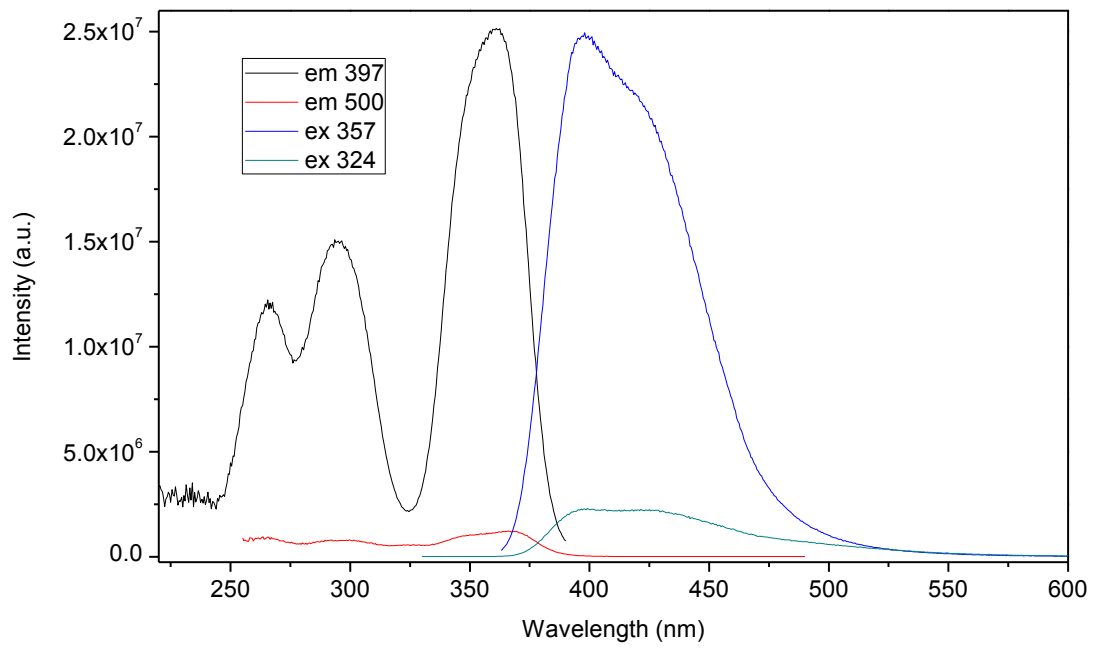
b.
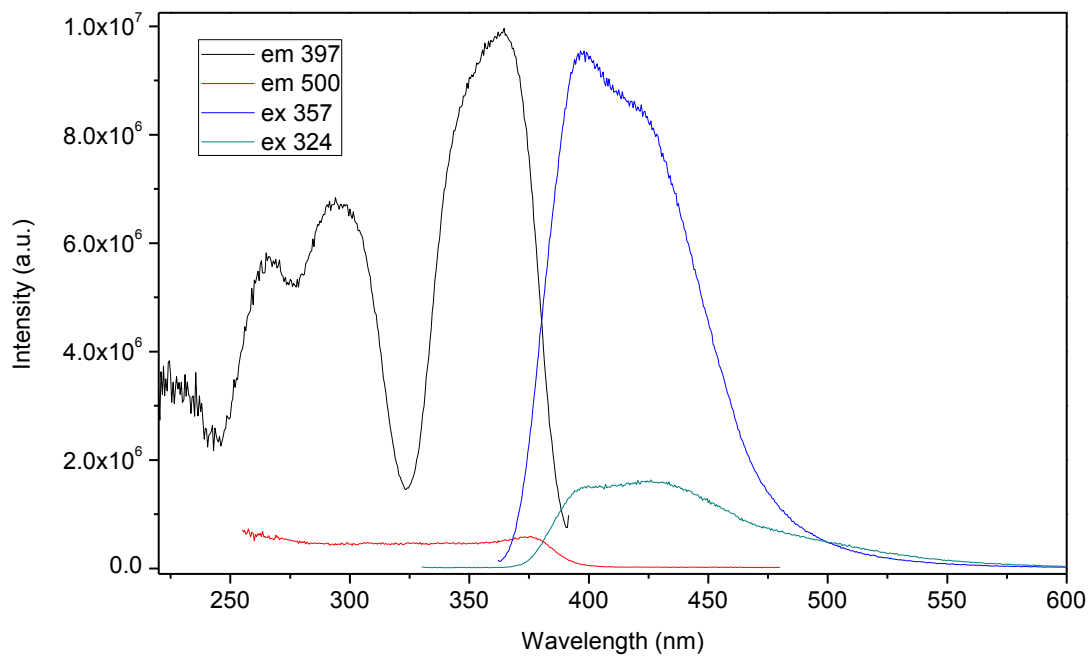
c.

A-3. PL spectra for a) S-74, b) S-51 and c) S-75 at 298 K.
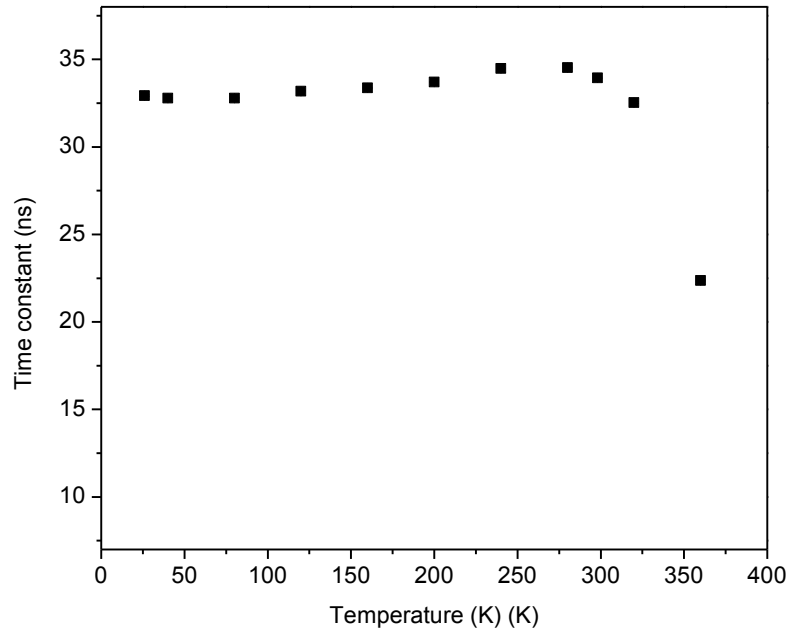
Figure A-4. S-51 time constant versus temperature.
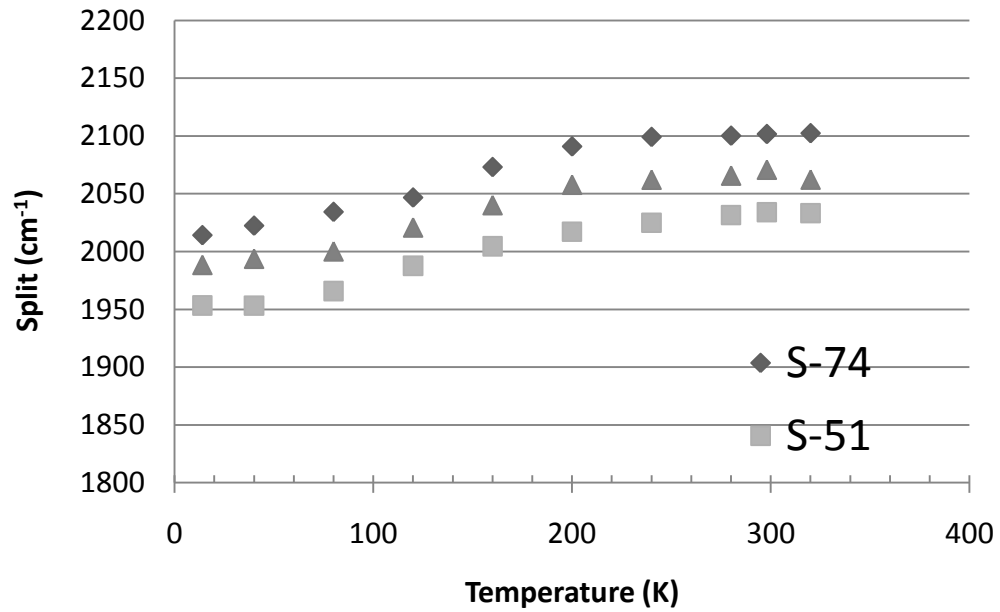
Figure A-5. a) 4f spin orbit-split based on 2 peak Gaussian fits with fixed amplitude ratios.
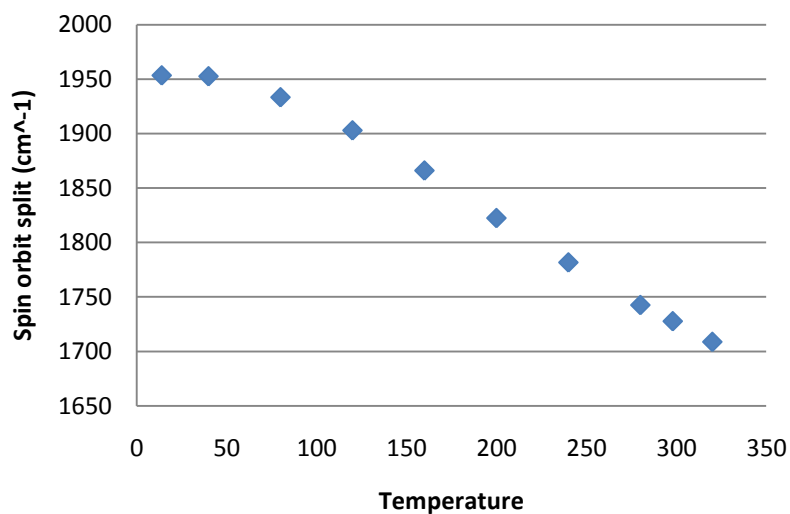
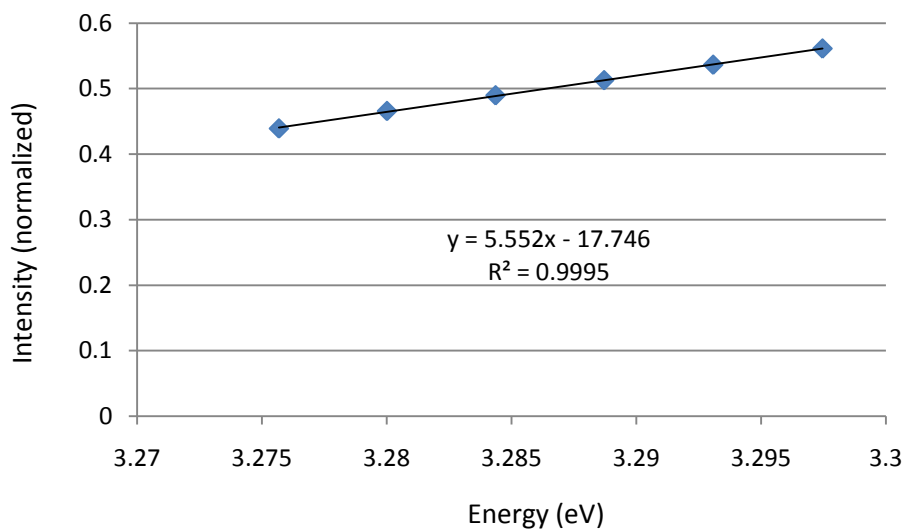Figure A-6. b) 4f spin orbit-split based on full floating two peak Gaussian fits of medium cerium (S-51) single crystal sample.

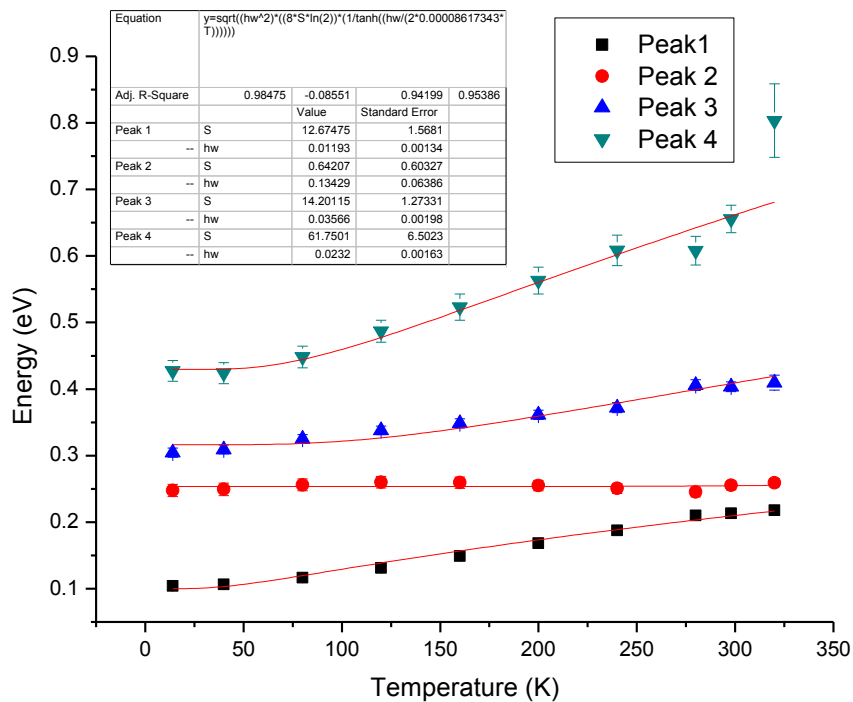Figure A-7. Example of the linear interpolation used to accurately measure the HWHM values.
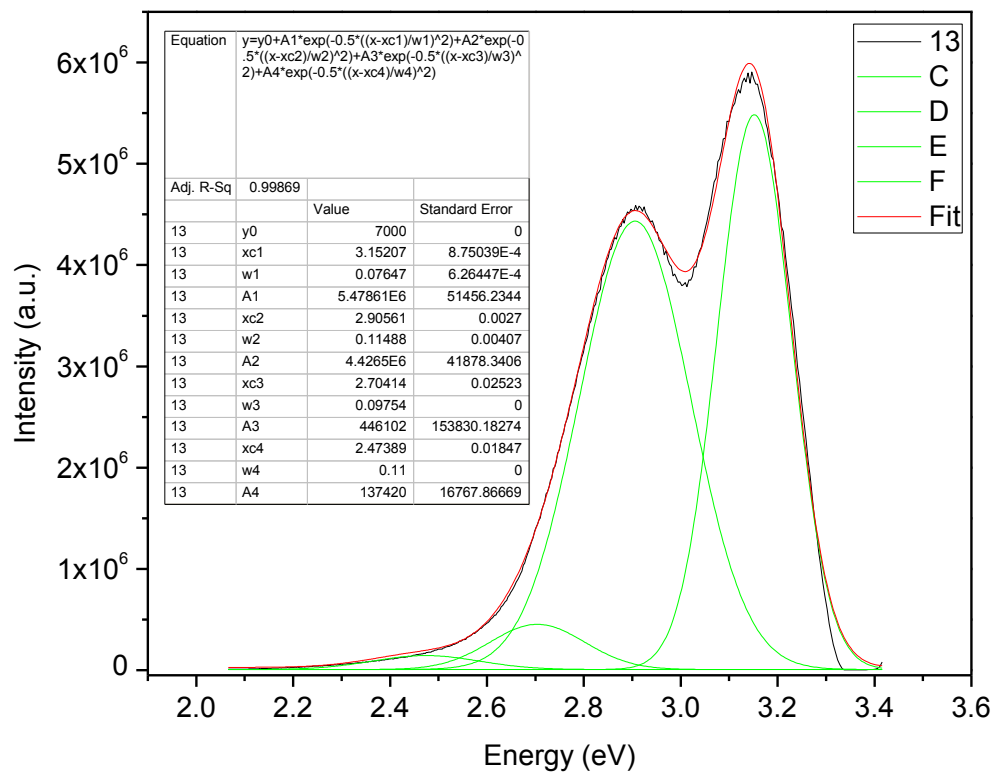
Figure A-8. An attempted four-peak Gaussian fit of the emission spectrum (357 nm excitation) of the low cerium (S-74) single crystal sample at 13 K.
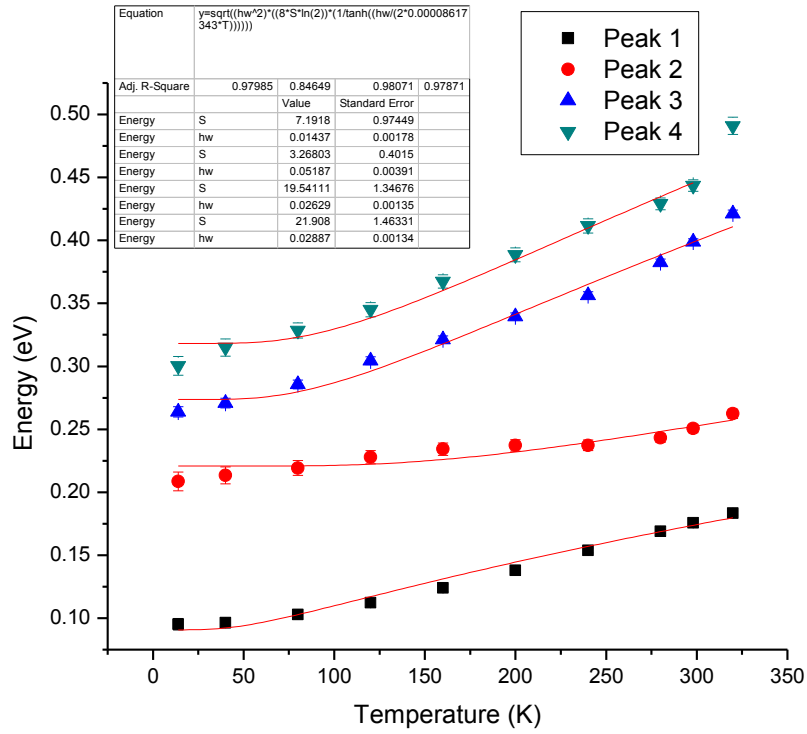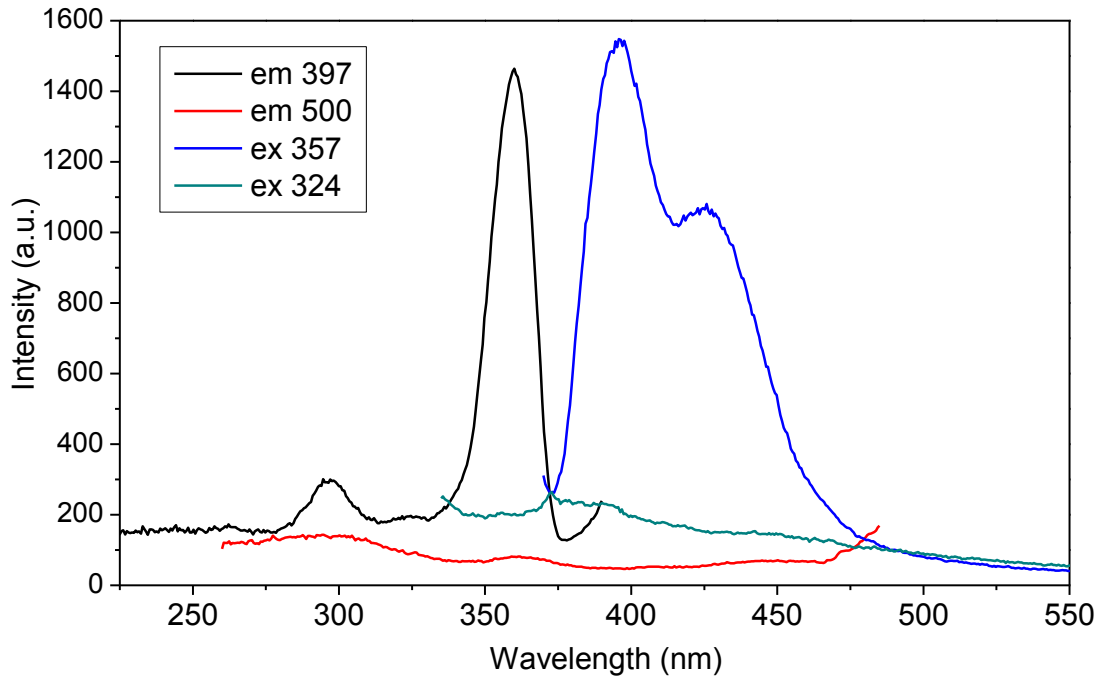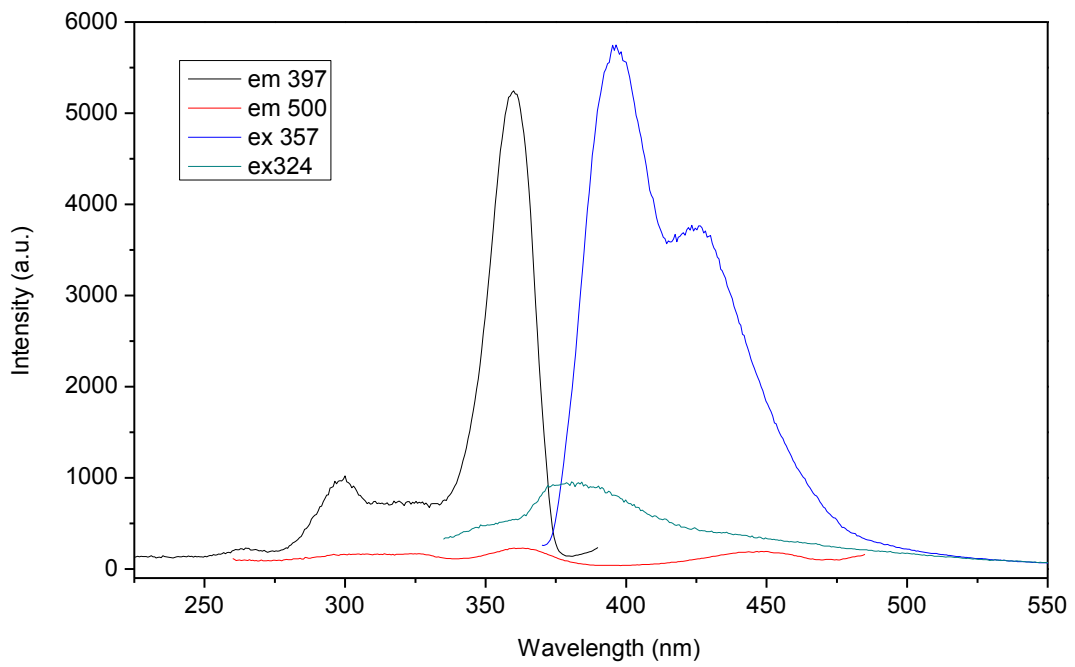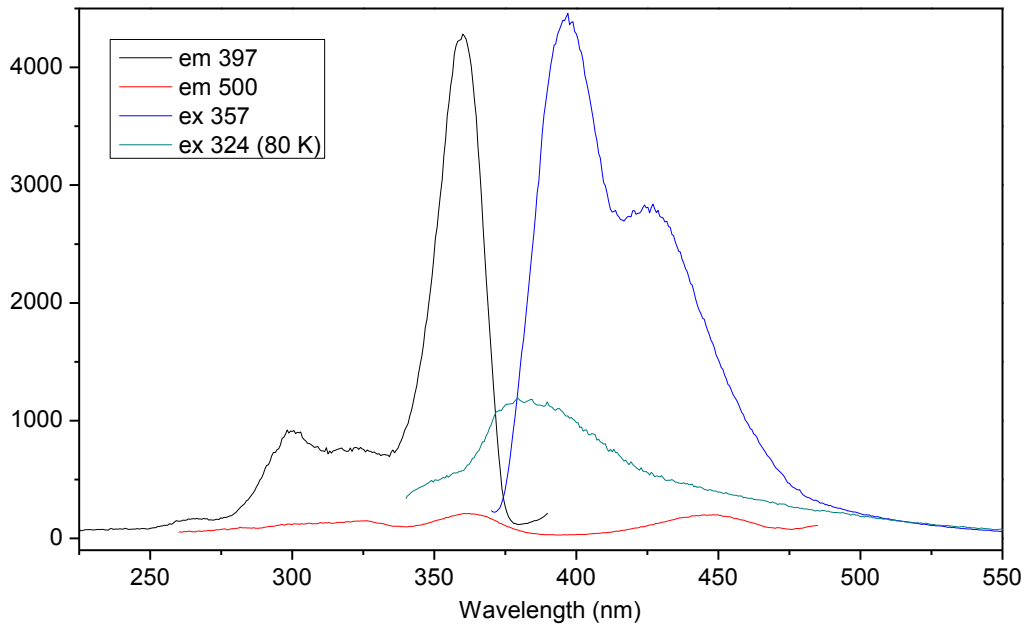
a.

b.

Figure A-9. HWHM of the excitation spectra (397 nm emission) measured by Gaussian fits for a) the medium cerium (S-51) and b) the high cerium (S-75) single crystal samples.
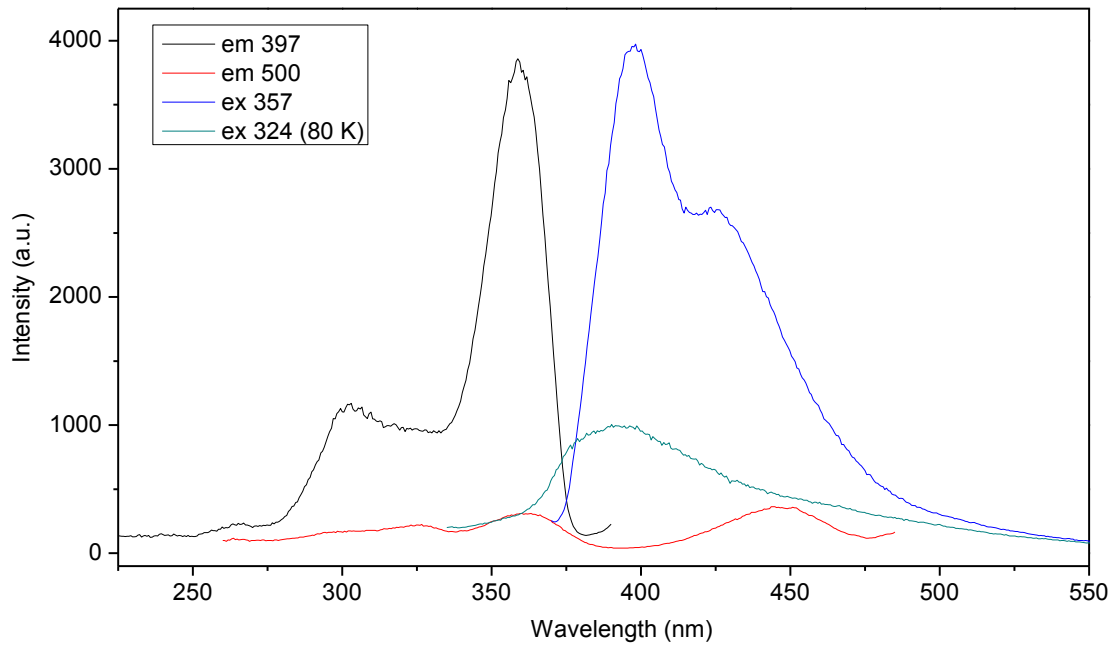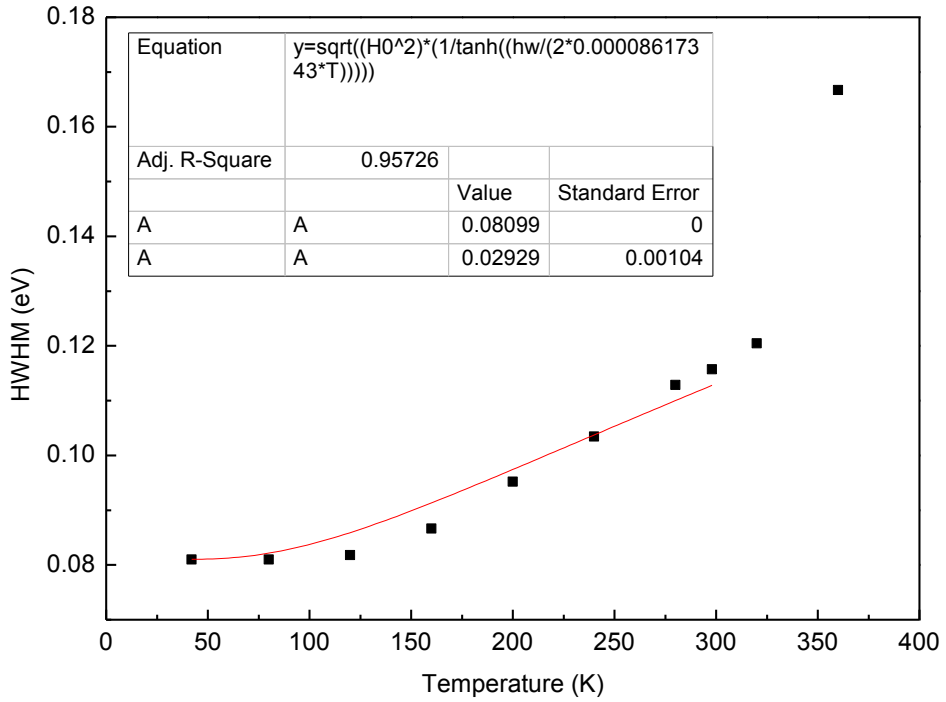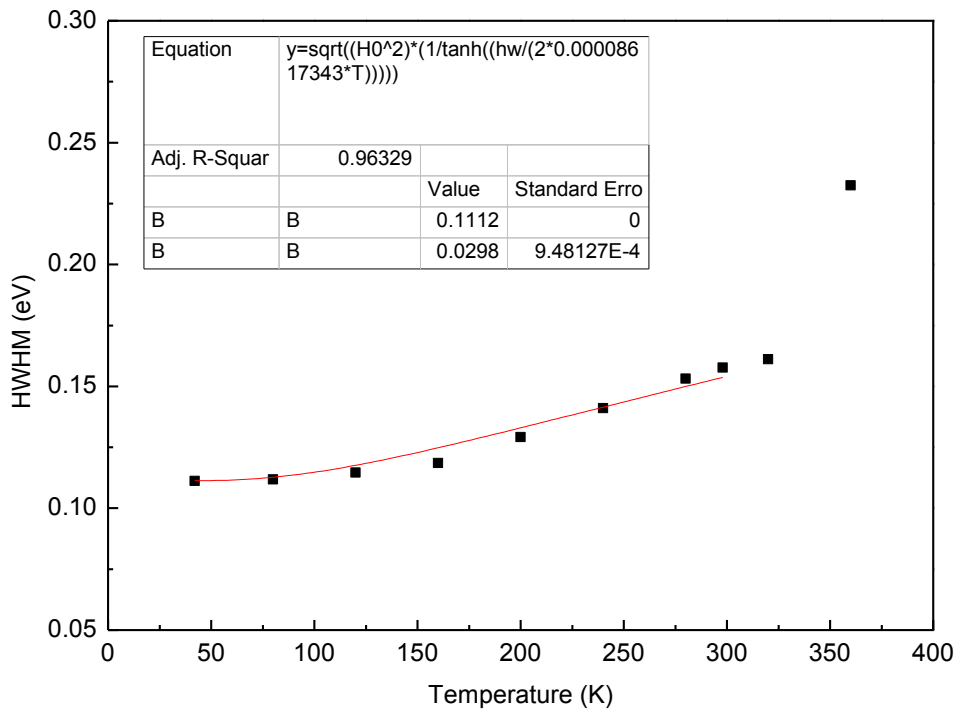
a.

b.

c.

d.

Figure A-10. Thin film LSO excitation and emission spectra for a) 0.06 at%, b) 0.23 at$, c) 0.34 at% and d) 0.86 at% cerium at 40 K (ex 324 at 80 K in c and d).

Equation	y=sqrt((H0^2)*(1/tanh((hw/(2*0.000086173 43*T)))))		
Adj. R-Square	0.95726		
		Value	Standard Error
A	A	0.08099	0
A	A	0.02929	0.00104

a.

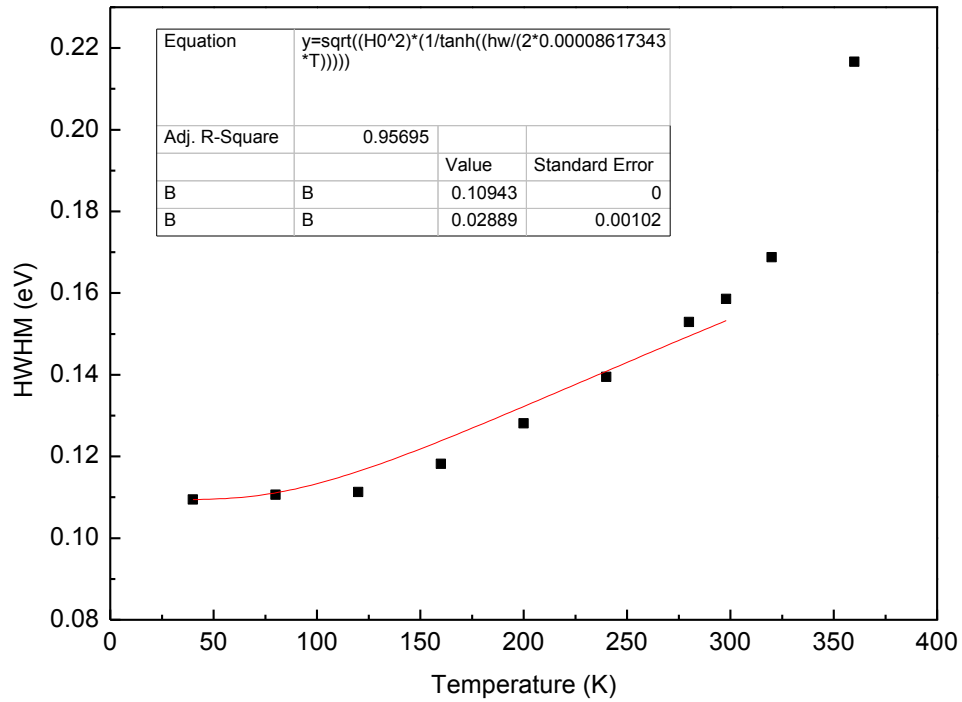| Equation	y=sqrt((H0^2)*(1/tanh((hw/(2*0.000086 17343*T)))))		
Adj. R-Squar	0.96329		
		Value	Standard Erro
B	B	0.1112	0
B	B	0.0298	9.48127E-4

b.

Figure A-11. HWHM values of a) excitation and b) emission spectra plotted versus temperature for thin film sample D6-1 with corresponding fits.
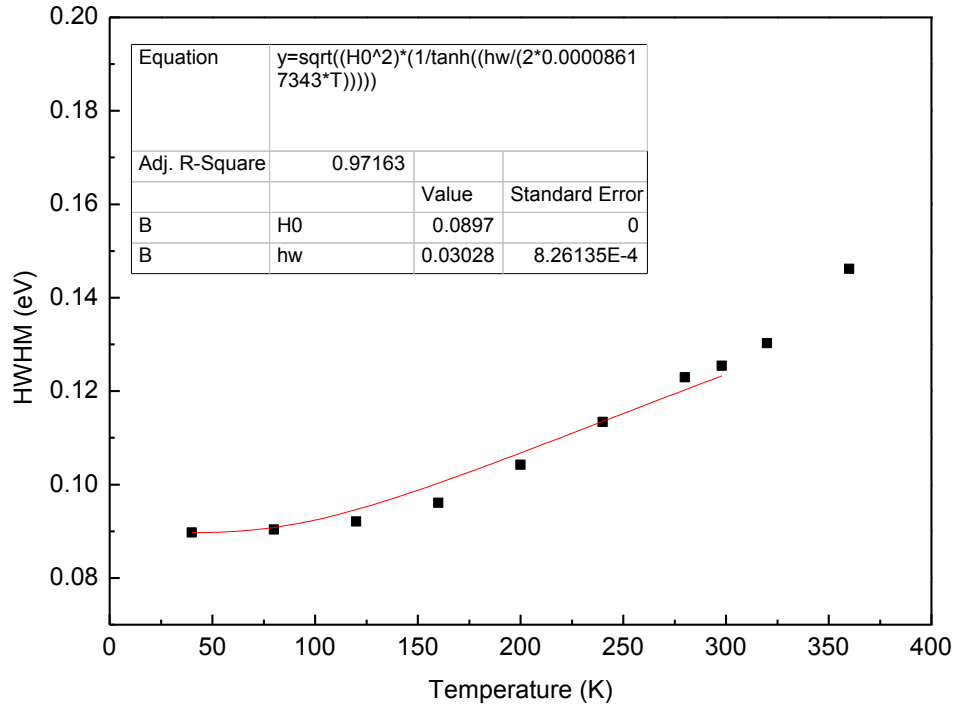
a.

b.

Figure A-12. HWHM values of a) excitation and b) emission spectra plotted versus temperature for thin film sample D6-3 with corresponding fits.

VITA

Jonathan Daniel Peak was born February 21, 1981 in Cincinnati, OH to Edwin and Joanne Peak where he was raised along with his younger sister, Kristin. In Cincinnati he attended St. Xavier high school. After graduation he enrolled at the Georgia Institute of Technology in Atlanta, GA where he studied Materials Science and Engineering. While there he researched carbon-black doped polymers and nano-silica doped epoxy composites under Professor C.P. Wong. During his undergraduate studies, Jonathan also completed internships at Alcoa, Inc. in Charleston, SC and at DBS manufacturing in Atlanta, GA. After earning his BS he moved to Gainesville, FL where he conducted graduate studies and worked as a teaching assistant in the department of Materials Science and Engineering at the University of Florida. After one year in Gainesville, he moved to Knoxville, TN and joined Professor Philip D. Rack's research group at the University of Tennessee. While there he also conducted research at the Scintillation Materials Research Center under Professor Charles L. Melcher. He completed his PhD in Materials Science and Engineering December 2010. Jonathan is to be married to his fiancée Nadya Michelle Vera January 29th, 2011.